WARWICK

Maximum-Entropy Mobility Spectrum of Two-Dimensional Hole Gas in Strained-$Si_{1-x}Ge_x$/Si Heterostructures

by

Somchai Kiatgamolchai

Thesis

Submitted to the University of Warwick

in partial fulfilment of the requirements

for admission to the degree of

Doctor of Philosophy

Department of Physics

June 2000

PAGE
MISSING
IN
ORIGINAL

Contents

List of Tables

List of Figures

Acknowledgments

First of all, I would like to thank my supervisors, Prof. T.E. Whall and Prof. E.H.C. Parker, for their valuable guidance and support during the course of the research. I am also very grateful to Dr. O.A. Mironov for his fruitful comments and technical support on the cryomagnetic system and Dr. B.M.M. McGregor for his guidance on device fabrication. Many thanks also go to Dr. R.A. Kubiak (former), Dr. P.J. Phillips, and Dr. C.P. Parry who grew the materials used in this research. I also would like to thank Dr. David Leadley, Abdullah Bin Chik, Prof. Robin Nicholas, and Kei Takashina, for carrying out the Hall measurement with the pulsed-magnet at Clarendon Laboratory, Oxford University. My thanks also go to J.C. Yeoh and T.J. Thornton from the Imperial College of Science, Technology & Medicine, London, for supplying the 2DEG sample. Also, I would like to acknowledge other members of the Advanced Semiconductor Research (ASR) group (present and former), who have helped with all my enquiries : Dr. N.L. Mattey, Dr. C.J. Emeleus. I also would like to thank T. Naylor and R. Morris for their essential technical support.

I would like to acknowledge the Institute for Promotion of Science and Technology Teaching (IPST) of Thailand for the financial support (DPST scholarship) during the years 1992–2000. And finally, I am the most grateful to my parents and my families for their support and encouragement.

Declarations

This thesis is the result of research carried out by the author in Department of Physics, University of Warwick between October 1995 and May 2000 and is submitted as partial fulfilment of the requirements for the award of the degree of Doctor of Philosophy. The work described below is all my own.

1. S. Kiatgamolchai, O.A. Mironov, E.H.C. Parker, and T.E. Whall, "Mobility Spectrum Technique for the measurement of the temperature-dependent mobility and carrier density in a modulation-doped p-$Si_{0.88}Ge_{0.12}$/Si heterostructure", Condensed Matter and Material Physics (CMMP'98), Manchester, UK, 21–23 December 1998.

2. S. Kiatgamolchai, M. Mironov, E.H.C. Parker, T.E. Whall, J.C. Yeoh, T.K. Fobelets, and T.J. Thornton, "Mobility Spectrum of 2DHG and 2DEG in SiGe-Si Heterostructures", 11^{th} General Conference of the European Physical Society (EPS-11 : Trend in Physics), London, UK, 6–11 September 1999.

3. S. Kiatgamolchai, O.A. Mironov, E.H.C. Parker, T.E. Whall, J.C. Yeoh, T.K. Fobelets, and T.J. Thornton, "Mobility Spectrum of high mobility 2DHG and 2DEG in Si-SiGe heterostructure", The 3^{rd} International Conference on Low Dimensional Structures Devices, Antalya, Turkey, 15–17 September 1999.

4. S. Kiatgamolchai, O.A. Mironov, Z. Dziuba, E.H.C. Parker, and T.E. Whall, "A Novel Mobility Spectrum Calculation using a Maximum Entropy Approach", submitted to Journal of Applied Physics.

Abstract

Magnetotransport properties of modulation-doped p-type $Si_{1-x}Ge_x/Si$ and $Si_{1-x}Ge_x/Si_{1-y}Ge_y$ heterostructures were studied, in the magnetic field range 0–12 T, and in the temperature range 0.35–300 K. The experimental data within the classical regime have been analysed by mobility spectrum analysis, in order to separate the influences of different parallel conduction paths. A new method of mobility spectrum analysis has been developed by the author, based on the concept of maximum-entropy, and this computation has been shown to overcome several drawbacks or limitations of previous mobility spectrum methods of calculation. The data have also been analysed by Beck&Anderson's analysis and the multicarrier fitting method for comparison. Analysis of the magnetic-field-dependent resistivity tensors reveals a two-dimensional hole gas (2DHG) in the Si/SiGe/Si quantum well, carriers in the boron-doped cap layer, and an unknown electron-like carrier. The carrier density of the 2DHG can either remain constant ($x = 0.1$), increase ($x = 0.13$), or decrease ($x \geq 0.2$), with increasing temperatures. Differences in the temperature dependences are partly attributed to different growth conditions. A decreasing carrier density with increase in temperatures may indicate the presence of acceptor-like defect states near the valence band edge of the SiGe channel. The mobility of the 2DHG between 100-300 K has the form $AT^{-\gamma}$ and γ has the bowl shape with the minimum at $x \sim 0.25$–0.3. These characteristics suggest a possible influence of alloy disorder scattering. The mobilities and activation energies of the carriers in the boron-doped cap vary between samples and this is believed to be due to boron-spike near the Si/Si-substrate interface, in some samples. The source of electron-like carrier is presently unknown.

Chapter 1

Introduction and Review of Previous Work

1.1 Introduction

Since the invention of the transistor by William Shockley in 1947 [Sze (1981)], the world has been transformed by electronics and engulfed by solid-state electronic devices that bring to people convenience, information and entertainment. The physics of such devices are based on the semiconducting properties of materials such as silicon (Si), germanium (Ge) and gallium arsenide (GaAs), the electrical properties of which can be controlled by adding other materials (dopants) to produce excessive holes (p-type) or electrons (n-type). Among those materials, silicon has been considered as the most attractive one due to its relative abundance and the existence of stable silicon-dioxide (SiO_2) insulator. Further advances in silicon technology have now taken place by incorporation of germanium to form a SiGe alloy which has better electrical transport than Si [Wang et al. (1995), Schaffler (1997), Whall and Parker (1998)].

Historically, Levitas (1955) studied the electrical properties of p-type bulk $Si_{1-x}Ge_x$ alloys grown by an isothermal solidification technique with x between 0 and 1. The materials were mostly polycrystalline with carrier concentration between

Table 1.1: Properties of Ge, Si, and GaAs at 300 K (after Sze(1981)).

Properties	Germanium	Silicon	GaAs
Crystal structure	Diamond	Diamond	Zincblend
Electron mobility ($cm^2V^{-1}s^{-1}$)	3900	1500	8500
Hole mobility ($cm^2V^{-1}s^{-1}$)	1900	450	400
Lattice constant (Å)	5.64613	5.43095	5.6533
Energy gap (eV)	0.66	1.12	1.424
Effective density of states in :			
valence band, N_V (cm^{-3})	6.0×10^{18}	1.04×10^{19}	7.0×10^{18}
conduction band, N_C (cm^{-3})	1.04×10^{19}	2.8×10^{19}	4.7×10^{17}
Dielectric constant	16.0	11.9	13.1
Intrinsic carrier concentration, n_i (cm^{-3})	2.4×10^{13}	1.45×10^{10}	1.79×10^{6}

10^{13}–10^{16} cm^{-3}. It was found that the room temperature intrinsic resistivity and energy gap of SiGe alloys decreased monotonically with increasing Ge composition while the hole mobility increased. These variations are as expected for the gradual transformation from pure Si to pure Ge (see table 1.1). In addition to well-known ionized impurity and phonon scattering, an alloy disorder scattering was observed from the temperature-dependence of mobility which was strongest at $x \sim 0.3$–0.4. Glicksman (1958) studied an n-type bulk $Si_{1-x}Ge_x$ single crystal with x between 0.74 - 1.00 with carrier concentration $\sim 10^{15}$ cm^{-3} and found that the room-temperature electron mobility also increased monotonically with increasing Ge compositions.

1.2 The Modulation-doped SiGe/Si Heterostructures

Advances in growth techniques took place in the mid-1970 when atomically controlled growth was achieved by a Molecular Beam Expitaxy (MBE). The MBE growth process is simply an evaporation process carried out in an ultrahigh vacuum (UHV) environment which gives a high quality single crystal structure. By using MBE, Ge

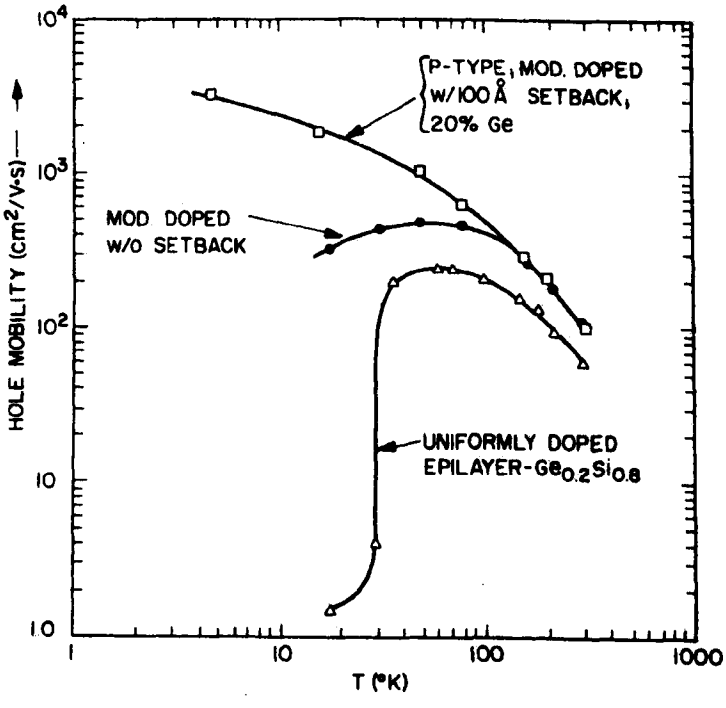

Figure 1.1: The Hall mobility versus temperature of a uniformly doped $Si_{0.8}Ge_{0.2}$, modulation-doped $Si_{0.8}Ge_{0.2}$ without setback, and modulation-doped $Si_{0.8}Ge_{0.2}$ with 100 angstrom setback (after People (1984)).

and other dopants can be alloyed into Si with high accuracy in composition and thickness. The first MBE-grown SiGe was accomplished by People et al. (1984) who grew 200 nm of $Si_{0.8}Ge_{0.2}$ pseudomorphically on an N^- Si substrate. In this manner, the SiGe layer is put under compressive strain because the lattice constant of Ge is approximately 4 % higher than that of Si (see table 1.1). Two different p-type doping schemes, uniform doping and modulation doping (MD), were investigated. Figure 1.2 shows the schematic picture of the MD structure. It was observed that the hole mobility of the MD structure was higher than that of a uniformly-doped structure at all temperatures (4-300 K) and the low-temperature mobility in the MD structure was enhanced by the introduction of an undoped Si layer (or "setback") between the doped layer and SiGe layer (see Fig. 1.1). An identical MD structure, but with n-type dopants, failed to sustain an enhancement of electron mobility at low temperature. This is because there is no conduction band offset for the electron confinement. Later, Abstreiter et al. (1985) showed that enhanced electron mobilities at low temperature can be obtained in a tensile strain Si grown on relaxed SiGe.

The schematic diagram of the MD p-SiGe/Si structure is shown in Fig. 1.2. The strained SiGe layer is sandwiched between pure silicon and provides a quantum well, due to the valence band offset, to carriers which transfer from the boron-doped silicon (B:Si). As more carriers move into the SiGe layer, the energy band profile of the whole structure also changes in such a way that the quantum well becomes a sharp triangular profile at the top SiGe/Si interface. The transferred carriers can be considered to transport in the two dimensional manner which is called the two-dimensional hole gas (2DHG). The 2DHG is separated from the parent acceptors in an irreversible manner [Dingle et al. (1978)]which gives rise to the higher low-temperature mobility due to less ionized impurity scattering.

The large application of SiGe/Si heterostructure lies in the area of Field-Effect-Transistor (FET) where the Si-FET has already dominated the market. The basic concept is to incorporate the strained SiGe channel into this Si-FET where the carrier

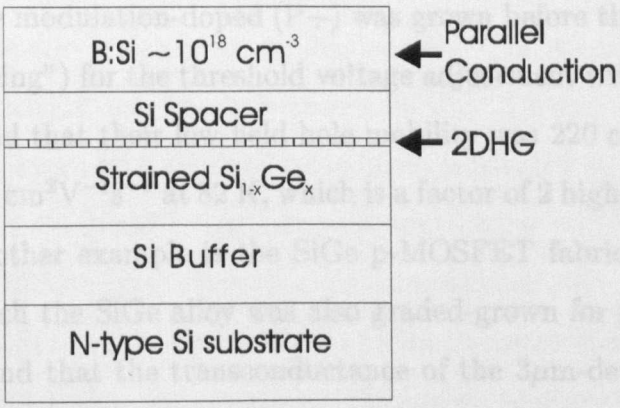

Figure 1.2: The modulation-doped SiGe/Si heterostructure contains 2DHG and a parallel conduction at temperatures above 77 K.

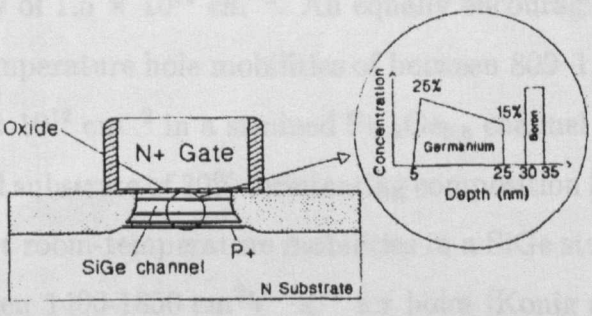

Figure 1.3: The schematic cross section of the modulation-doped SiGe p-channel MOSFET (after Verdonckt et al. (1991)).

transport takes place. The first fully working modulation-doped SiGe p-channel MOSFET was fabricated by Verdonckt et al. (1991), as shown in Fig. 1.3. The SiGe channel was graded-grown with the germanium content up to 25% for the maximum hole confinement and the modulation-doped (P+) was grown before the SiGe channel (so-called "inverted doping") for the threshold voltage adjustment without degrading the mobility. They found that their low-field hole mobility was 220 $cm^2V^{-1}s^{-1}$ at 300 K and increases to 980 $cm^2V^{-1}s^{-1}$ at 82 K, which is a factor of 2 higher than a submicron Si p-MOSFET. Another example is the SiGe p-MOSFET fabricated by Voinigescu et al. (1994) in which the SiGe alloy was also graded-grown for maximum hole confinement. They found that the transconductance of the 3μm-device with 0-40% Ge profiles is about 100 % higher than that of the corresponding Si p-MOSFET produced on the same chip. To achieve the SiGe strained layer with germanium content higher than 50%, this layer has to be grown on the SiGe virtual substrate. The virtual substrate is a relaxed SiGe alloy formed on the silicon substrate by grading the germanium composition from 0% at the substrate to a terminating composition. Konig and Schaffler (1993) fabricated a strained Ge channel Schottky gated p-type modulation doped FET, with the Ge grown on a graded SiGe virtual substrate of terminating composition 70%, and obtained a record 300 K Hall mobility of 1,300 $cm^2V^{-1}s^{-1}$ at a high carrier density of 1.5×10^{12} cm^{-2}. An equally encouraging result is the measurement of room-temperature hole mobilities of between 800–1,050 $cm^2V^{-1}s^{-1}$ for a carrier density of 3×10^{12} cm^{-2} in a strained $Si_{0.2}Ge_{0.8}$ channel grown on a graded 1 μm thick SiGe virtual substrate of 30% terminating composition [Ismail et al. (1994)]. With the current best room-temperature mobilities in a SiGe strained layer structure (not a device) between 1400-1850 $cm^2V^{-1}s^{-1}$ for holes [Konig and Dambkes (1995)] and 2600-3000 $cm^2V^{-1}s^{-1}$ for electrons [Nelson et al. (1993)], in comparison to the mobilies of 100 and 500 $cm^2V^{-1}s^{-1}$ respectively in a bulk Si FET, it sounds very promising that SiGe/Si heterostructures will be a key material to dominate the electronic market in years to come.

1.3 The Motivation of this Thesis

The carrier density and mobility are key parameters to explain the carrier transport within any semiconductor materials. Their room-temperature values are particularly important for the device design prior to fabrication. The schematic picture of the MD structure used within this thesis is shown in Fig. 1.2 and consists of a boron-doped silicon (B:Si) layer and a strained SiGe layer, separated by the undoped silicon layer (Si "spacer" or "setback"). At temperatures below ~77 K, conduction only occurs at the SiGe/Si interface where the two-dimensional hole gas is formed. The conduction within B:Si is relatively small due to the decrease of carrier concentration and mobility with decreasing temperatures. At higher temperatures, the B:Si layer conducts and provides a parallel conduction path to the two-dimensional hole gas. The standard Hall measurement, which is performed at a single low magnetic-field value, cannot determine the carrier density and mobility of two-dimensional hole gas accurately due to the contribution from the parallel conduction.

The conventional indicator of crystal quality is the mobility measured at liquid He temperature (~4K) where the phonon scattering is negligible and the mobility is much more sensitive to the SiGe crystal quality. However, Nelson et al. (1993) observed that it is not necessarily the case that the high low-temperature mobility structure will show high room-temperature mobility. This can be understood in terms of different dominant scattering mechanisms at different temperatures. At low temperature, the interface charge and surface roughness are the limiting factors for low and high carrier density, respectively, while the phonon scattering might be the main mechanism at room temperature [Whall (1997)].

A simple technique of chemical etching was used by Garchery et al. (1995) to remove the excessive dopants in a MD strained n-Si/$Si_{0.67}Ge_{0.33}$ sample. The sample was etched successively, with resistivity and Hall measurements performed at each step, until the measured mobility did not improve. At room temperature, the measured mobility increases monotonically from 1250 $cm^2V^{-1}s^{-1}$ to 2150 $cm^2V^{-1}s^{-1}$

while the measured carrier density decreased from 2.2×10^{12} cm^{-2} to 1.1×10^{12} cm^{-2}. The same technique was applied to a MD strained p-$Si_{0.8}Ge_{0.2}$/Si sample by McGregor et al. (1999) to obtain the maximum mobility of $\sim$ 200 cm^{2}V^{-1}s^{-1} with carrier density of 5×10^{11} cm^{-2}. However, the restrictions of using this technique to identify the mobility of 2D carriers are that (i) it is limited to a "normal" MD structure only, in which the B:Si layer is grown after the SiGe alloy, (ii) there must only be two conduction paths, and (iii) the 2D carriers should be unaffected by chemical etching.

It is well understood that the measured mobility from the Hall measurement differs from the drift mobility by a Hall factor. McGregor et al. (1993) measured the drift and Hall mobilities in heavily-doped strained $Si_{1-x}Ge_x$ ($0 < x < 0.2$) in the doping range of $(1.5\text{-}2.1)\times10^{19}$ cm^{-3} at room temperature and they found that the drift mobility increased with increasing Ge compositions while the Hall mobility decreased. A procedure to extract a drift mobility of two-dimensional electron gas (2DEG) from a MD strained n-Si/SiGe sample was proposed by Nelson et al. (1993), in which the drift mobility and carrier density of the doped layer was determined directly from an indentical MD structure but without a Si channel. This information was then subtracted from the MD structure to give the drift mobility and drift carrier density of 2DEG. However, this technique is only applicable where those two structures were grown under the same growth environment to ensure the same surface states. In practice, the carrier density of the doped layer in the MD structure will also be less than that obtained in the control because of charge transfer into the quantum well.

1.4 Mobility Spectrum Analysis

Mobility spectrum analysis is a new multicarrier characterization tool that employs the magnetic-field dependence of the resistivity and Hall coefficient. It is a non-destructive technique that is capable of identification of different groups of carriers

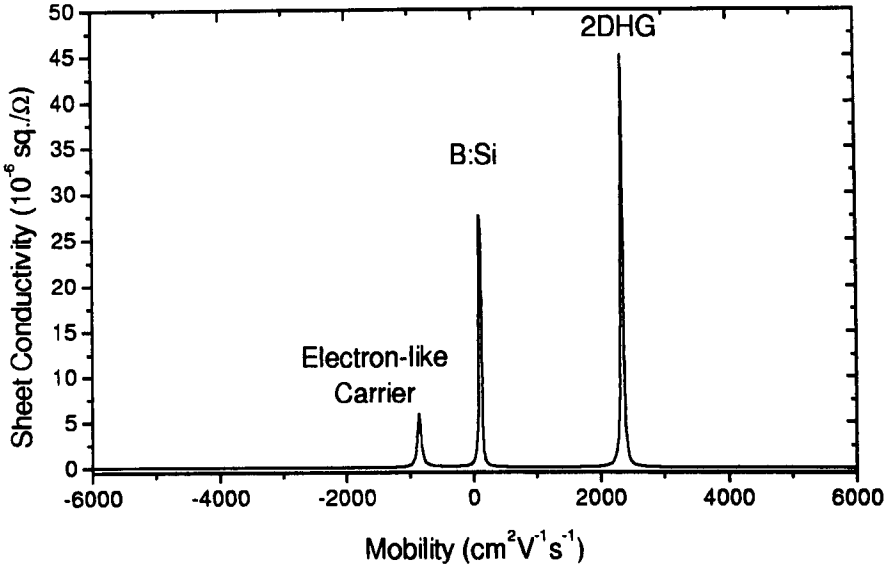

Figure 1.4: A typical Beck and Anderson mobility spectrum of the modulation-doped SiGe/Si heterostructure. Three carrier species are found, which are the two-dimensional hole gas (2DHG), the boron-doped silicon (B:Si), and an electron-like carrier. By the convention of Beck and Anderson mobility spectrum, hole carriers have positive mobilities and electron carriers have negative mobilities.

(carrier species) according to their different average mobilities, and hence different responses to the magnetic field. It was originally developed by Beck and Anderson (1987). The result of the analysis is a mobility-dependent conductivity, or "mobility spectrum", which consists of several peaks. A typical mobility spectrum of a modulation-doped SiGe/Si heterostrucutre at temperatures $\sim$ 77–100 K is shown in Fig. 1.4. From this spectrum, the number of electrically-active carrier species can be identified from the number of peaks within the mobility spectrum. Each peak also offers an estimation of mobility and conductivity when an appropriate averaging procedure is used. From the theoretical viewpoint, the broadening of each peak also indicates an energy-dependent relaxation time and the presence of harmonics in peak mobility would signal a nonspherical band structure [Beck and Anderson (1987)].

The original method of calculation by Beck and Anderson has been applied to a number of different semiconductor materials, for example bulk HgTe [Beck et al. (1988), Meyer et al. (1988)], bulk HgCdTe [Meyer et al. (1993)], thin film HgCdTe [Gui et al. (1998)], HgTe-CdTe superlattices [Hwang et al. (1991)], AlGaAs/GaAs heterostructures [Colvard et al. (1989)], Si-δ-doped GaAs [Panaev et al. (1993)], InGaAs [Svensson et al. (1991)], Si-δ-InSb [Panaev et al. (1996)], InP on a semi-insulating substrate [Achard et al. (1999)], and SiGe/Si [Hock et al. (1998)]. After several applications, it has later been realised that their calculation method is only qualitatively accurate. Nevertheless, it has been shown to provide good approximations to the mobility and carrier concentration of each carrier species. To obtain more accurate results, the estimated mobilities and carrier concentrations are further quantified by the multicarrier fitting technique [Colvard et al. (1989), Koser et al. (1994)].

The subsequent developments in the mobility spectrum approach over the last 10 years have involved new mathematical techniques in order to obtain a more accurate mobility spectrum. They are the iterative technique [Dziuba and Gorska (1992)], the quantitative mobility spectrum analysis (QMSA) [Antoszewski et al. (1995)], and the improved quantitative mobility spectrum analysis (i-QMSA) [Vurgaftman et al. (1998

The detail of each technique is discussed in chapter 3.

Despite all efforts to calculate the mobility spectrum efficiently and accurately, there are still disadvantages to overcome such as the instability and low-magnetic-field effect. The instability problem is that the mobility spectrum is extremely sensitive to the experimental error present in the measured data and the low-magnetic-field effect is when the range of the magnetic field is too low for the observation of the magnetic-field-dependent response. The difficulties of mobility spectrum calculation lie with the fundamental nature of the magnetoconductivity model in use. It will be shown later in chapter 3 that it resembles the well-known inverse problem of Fredholm integral equation of the first kind [Press et al. (1992)]. This topic has been studied extensively by mathematicians and yet is still under constant development. The mobility spectrum problem was studied from the inverse problem viewpoint and led the author to develop a new mobility-spectrum calculation which has numerous advantages, the detail of which is given in chapter 4.

1.5 The Structure of this thesis

This thesis is concerned with the investigation of the magnetoconductivity tensor in modulation-doped p-type SiGe/Si heterostructures in magnetic fields within the classical limit (i.e. before magnetic field quantization of energy bands sets in). It is especially concerned with experimental measurements and their interpretation in terms of so called mobility spectrum analysis. In chapter 2, the magnetotransport theory is explained which leads to the model used. The transport in high and low magnetic fields and the calculation of the Hall scattering factor from the mobility spectrum will also be explained. For completeness, scattering mechanisms in SiGe/Si will also be briefly discussed. Chapter 3 gives the review over various numerical techniques used to solve the magnetoconductivity model and other remedy techniques in order to recover the information about low mobility carrier. A newly developed

mobility spectrum technique based on the maximum entropy approach is explained in chapter 4. The experimental procedures and some aspect of the growth technique will be discussed in chapter 5. Chapter 6 contains the experimental data and results from the mobility spectrum analysis which includes result from 10%–65% Ge content samples. A summary of this thesis and the mobility spectrum analysis will be concluded in chapter 7, including suggestions for further investigations.

Chapter 2

Theoretical Concepts

2.1 Introduction

In this chapter, our current understanding of how the strain changes the band structure and effective masses in $Si_{1-x}Ge_x$ will be described. The charge transfer which occurs in a modulation-doped structure is then discussed briefly, followed by a review of the theoretical background on magnetotransport which leads to the mobility spectrum analysis given in Chapters 3 and 4 . The calculation of Hall factor, Hall mobility, and drift mobility, from the mobility spectrum are then developed. The theory of Shubnikov de-Haas oscillation and quantum Hall effect are also discussed as these phenomenon are employed to confirm the existence of 2D carriers. Finally, possible scattering mechanisms associated with 2D carriers are reviewed and particularly emphasized on their temperature dependences.

2.2 Electronic Properties of Si, Ge, and Strained $Si_{1-x}Ge_x$

2.2.1 Bandstructures of Si and Ge

The bandstructures of Si and Ge are shown in Fig. 2.1. The conduction band minima of Si are situated at about 85 % along the <100> directions, between the Γ-point (the centre of Brillouin zone) and the X-point, while those of Ge are at L-points which are along <111> directions. Due to lattice symmetry, there are 6 degenerate X-points and 8 degenerate L-points. The relationship between energy E and wave vector $\mathbf{k}$ at each point can be represented as an ellipsoidal constant energy surface :

$$E(\mathbf{k}) = \frac{\hbar^2 k_x^2}{2m_l^*} + \frac{\hbar^2\left(k_y^2 + k_z^2\right)}{2m_t^*}, \tag{2.1}$$

where m_l^* and m_t^* are the longitudinal and transverse effective masses, which are $0.98m_0$ and $0.19m_0$ for Si and $1.64m_0$ and $0.082m_0$ for Ge [Sze (1981)].

The valence band maxima of both Si and Ge lie at the Γ-point consisting of two subbands, a heavy-hole and a light-hole subband, degenerate at the Γ-point. A spin-orbit split-off subband lies 50 meV below in Si and 280 meV in Ge. The constant energy surfaces are so-called warped-spherical surfaces which have the following form [Dresselhaus et al. (1954)] :

$$E(\mathbf{k}) = \frac{-\hbar^2}{2m_0}\left\{Ak^2 \pm \left[B^2k^4 + C^2\sqrt{k_x^2k_y^2 + k_x^2k_z^2 + k_y^2k_z^2}\right]\right\}, \tag{2.2}$$

where the plus sign is associated with the light holes and the minus sign with the heavy holes. The effective masses can be computed from the parameters A, B, and C [Dresselhaus et al. (1955)] and are shown in table 2.1 for each subband near $\mathbf{k} = \mathbf{0}$.

2.2.2 Bandstructures of $Si_{1-x}Ge_x$

The valence bandstructure of an unstrained $Si_{1-x}Ge_x$ alloy is similar to that of Si for Ge compositions up to 85% (see Fig. 2.2b). The strain in $Si_{1-x}Ge_x$ alloys grown

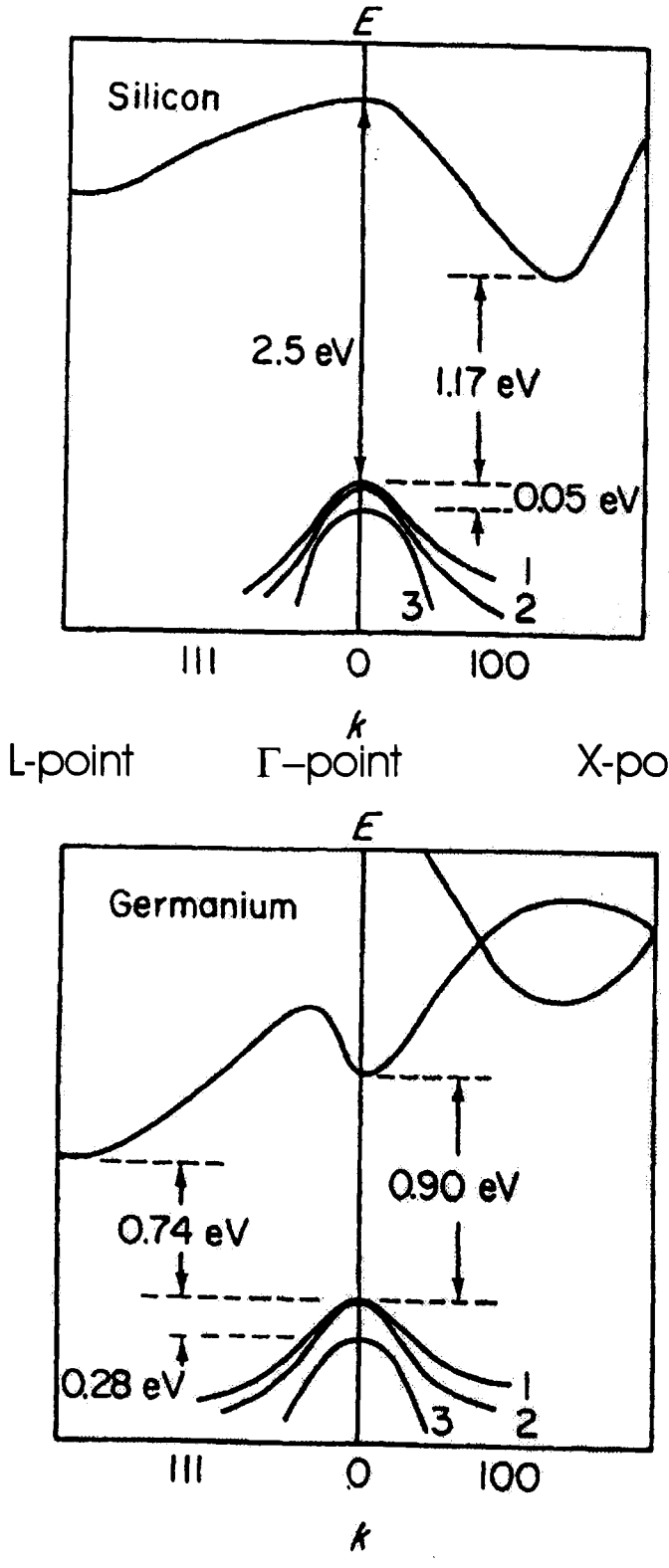

Figure 2.1: The band structures of unstrained Si and Ge (after Bube (1974)).

Table 2.1: Effective masses of heavy-hole, light-hole, and spin-orbit near the zone centre of Si and Ge.

Subband	Silicon	Germanium
Heavy-hole (HH) $\mid \frac{3}{2}, \pm\frac{3}{2} >$	0.5	0.3
Light-hole (LH) $\mid \frac{3}{2}, \pm\frac{1}{2} >$	0.16	0.04
Spin-orbit (SO) $\mid \frac{1}{2}, \pm\frac{1}{2} >$	0.234	0.095

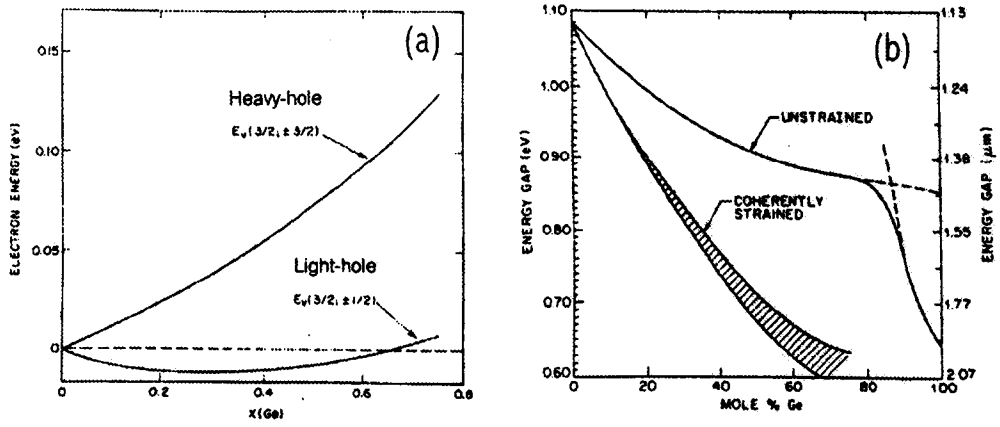

Figure 2.2: (a) The splitting of heavy-hole and light-hole bands and (b) reducing of energy gap of strain $Si_{1-x}Ge_x$ (after People (1985)).

lattice-matched on a Si substrate causes the separation between the heavy-hole and light-hole subbands [People (1985)] as well as the lowering of the spin-orbit subband [Hinckley et al. (1989)]. These reduce the intersubband and intraband scattering which limit the hole mobility. The in-plane heavy-hole mass under compressive strain is smaller than that of the light-hole mass. The heavy-hole subband is lifted above the light-hole subband and, therefore, holes will occupy the heavy-hole subband first and acquire a higher in-plane mobility which is advantageous in devices exploiting in-plane transport such as the Field-Effect-Transistor (FET). The in-plane effective mass is expected to decrease systematically with increasing Ge compositions from $0.40m_e$ at $x = 0.13$ to $0.29m_e$ at $x = 0.3$ [Cheng et al. (1994)].

In Fig. 2.3 the band structures and energy contour of heavy-hole and light-hole bands at a temperature of 300 K are shown.They are for unstrained and strained $Si_{0.7}Ge_{0.3}$ as calculated by Manku and Nathan (1991). The degeneracy lifting is clearly seen while the strained energy contour is less anisotropic than that of unstrained Si.

2.3 Charge Transfer in Modulation-doped Structures

The space charge distribution along the growth direction (z) within the modulation-doped structure can be obtained by solving Poisson's and Schrödinger's equation self-consistently. The importance of Schrödinger's equation is that it provides the energy levels and corresponding wave functions for 2D carriers. For a given potential energy profile $V(z)$, Schrödinger's equation is [Tan et al. (1990)] :

$$-\frac{\hbar^2}{2}\frac{d}{dz}\left(\frac{1}{m^*(z)}\frac{d}{dz}\right)\psi(z) + V(z)\psi(z) = E\psi(z), \tag{2.3}$$

where $m^*(z)$ is a z-dependent effective mass, $\psi(z)$ is the wave function with associated energy E. Computationally, there are as many eigenenergies as the number of mesh points on the z direction. However, only those energies which are within $10k_BT$ from the Fermi energy E_F are likely to be occupied. The 2D carrier density can be calculated, by assuming parabolic bands, from

$$n_k = \frac{m^*}{\pi\hbar^2}\int_{E_k}^{\infty}\frac{1}{1+e^{(E-E_F)/k_BT}}dE = \frac{m^*}{\pi\hbar^2}k_BT\ln\left(1+e^{\frac{E_k-E_F}{k_BT}}\right), \tag{2.4}$$

where E_k is the eigenenergy. The carrier concentration ($n(z)$) in m^3 unit, which will be used for the Poisson's equation, is obtained from

$$n(z) = \sum_k |\psi_k(z)|^2 n_k, \tag{2.5}$$

where ψ_k is the wave function corresponding to the eigenenergy E_k.

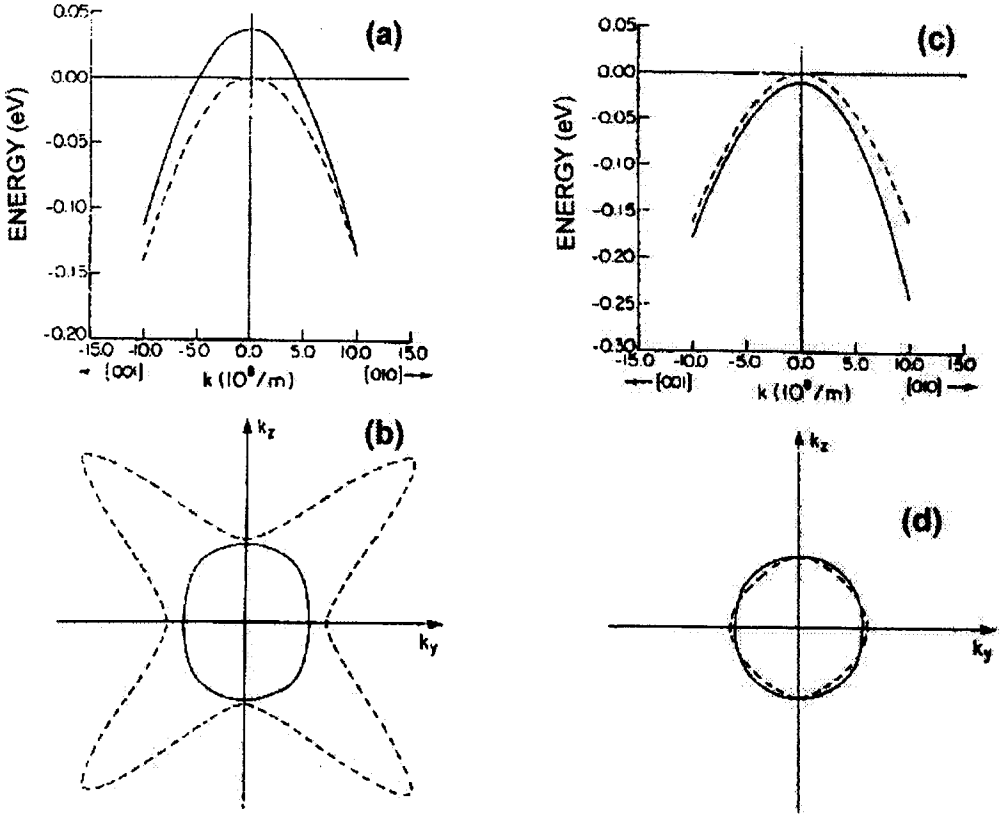

Figure 2.3: (a) Energy spectra and (b) constant energy contours for the heavy-hole band for x=0 (dashed) and x=0.3 (solid). (c) and (d) As (a) and (b) respectively, but for the light-hole band (after Manku and Nathan (1991)).

The Poisson's equation for a given charge distribution -$qN(z)$ is

$$\frac{d}{dz}\left(\varepsilon_s(Z)\frac{d}{dz}\right)\phi(z) = -q\frac{N(z)}{\varepsilon_0}, \tag{2.6}$$

where $\phi(z)$ is the potential profile and $\varepsilon_s(Z)$ is the dielectric constant function. $\phi(z)$ is related to the potential energy profile $V(z)$ by

$$V(z) = -e\phi(z). \tag{2.7}$$

Both Schrödinger and Poisson equations have to be solved self-consistently because the change in 2D carrier distribution affects the resultant potential in Poisson's equation while the change in potential profile also affects the 2D carrier distribution in Schrödinger's equation. In this thesis, the computer programme that performs this Schrödinger-Poisson calculation is that of Greg Snider which is made publicly available [Tan et al. (1990)] and widely used for many heterostructures.

Figure 2.4 is an example showing the valence band profile of a p-$Si_{0.87}Ge_{0.13}$/Si heterostructure at 10 K with one 2D subband, the lowest HH subband of energy minimum (E_0), occupied. Assuming that the energy gaps and valence band offset are temperature-independent, a typical scenario of what happens in the simulation as the temperature increases is as follows. At very low temperatures ($\sim$ 5–10 K) only one subband is occupied by 2DHG and its carrier density is almost temperature independent. As the temperature rises, the Fermi level starts to deviate from the valence bandedge (see Fig. 2.5) and hence from this subband, causing the decrease in carrier density associated with that subband (see the pHH1 curve in Fig. 2.6). However, this reduction is usually overcompensated by the increase in carrier density corresponding to higher subbands (pLH1–pHH5 curves in Fig. 2.6). The probability of carriers occupying higher subbands increases because the tail of Fermi-Dirac distribution smear out further away from the Fermi level, due to the thermal broadening. Usually, the subbands within $10k_BT$ from the Fermi level are taken into consideration and this results in the increase in the total 2DHG carrier density from 8×10^{10} cm^{-2}

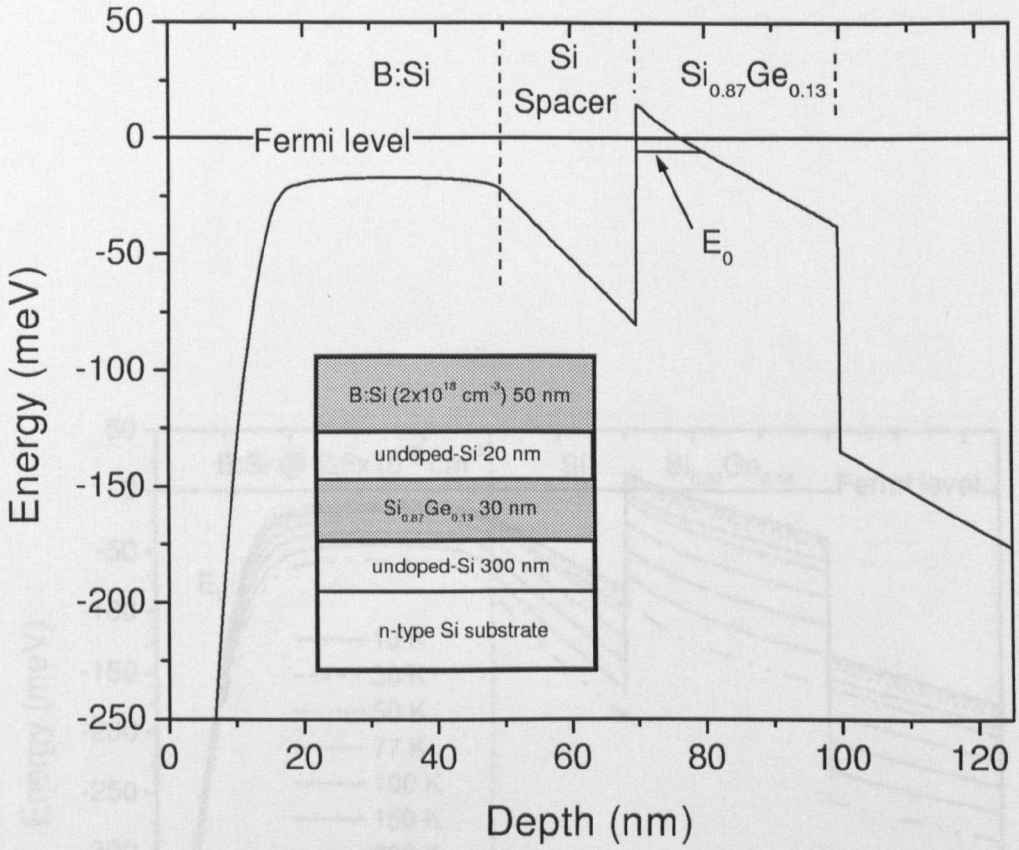

Figure 2.4: The band profile of a modulation-doped p-type $Si/Si_{0.87}Ge_{0.13}/Si$ heterostructure at 10 K by the Schrodinger-Poisson self-consistent calculation. Only one subband was found.

at 10 K to 1.5×10^{11} cm^{-2} at 300 K. Also, because more subbands are occupied, the carrier will distribute wider within the quantum well, as shown in Fig. 2.7.

2.4 The Magnetotransport Theory

Magnetotransport is the transport of charged carriers under the influences of both electric and magnetic fields. In this thesis, we consider only electric fields along the sample surface and magnetic fields perpendicular to the sample surface. Two phenomena are to be discussed, namely the magnetoresistance and Hall effect. The magnetoresistance is the change in resistance with the magnetic field while the Hall

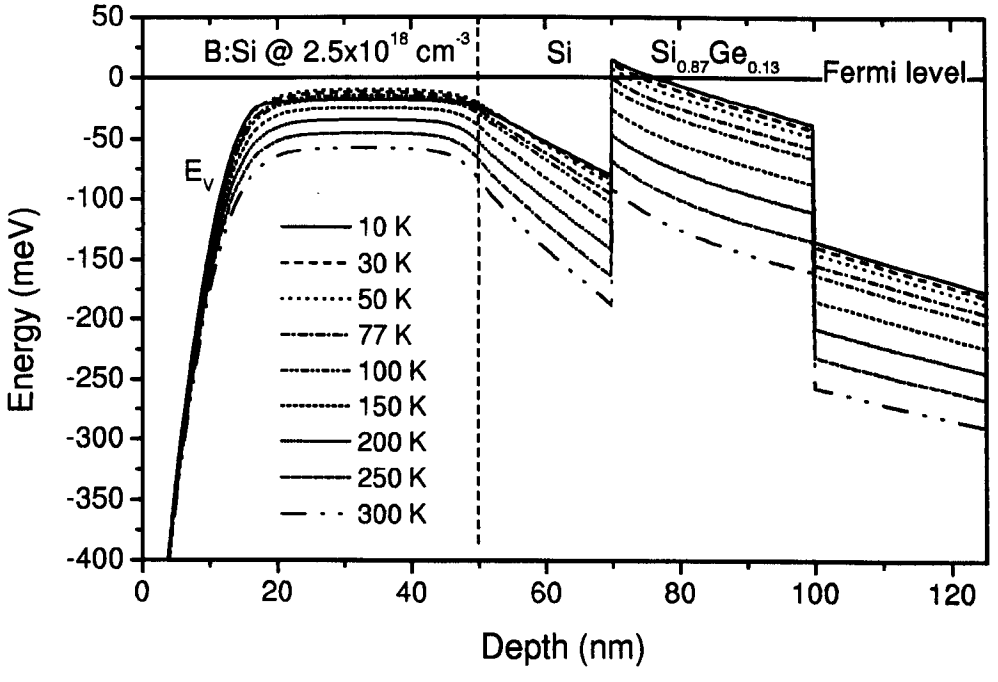

Figure 2.5: The band profile of the structure shown in Fig. 2.4 at temperatures between 10–300 K by the Schrodinger-Poisson self-consistent calculation.

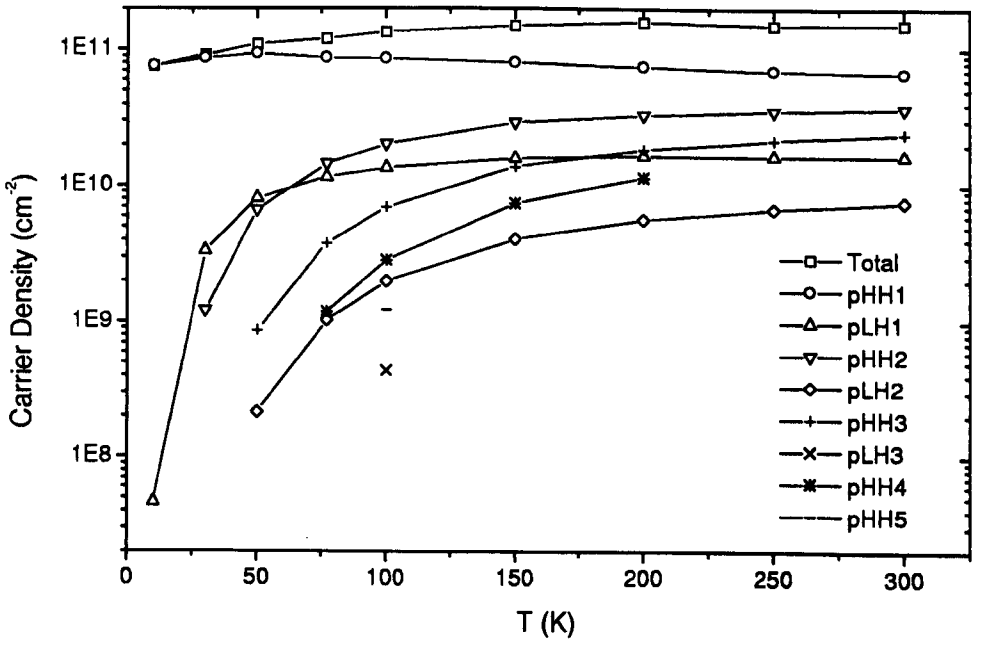

Figure 2.6: The carrier density in each subband of 2DHG as a function of temperature, for the structure shown in Fig. 2.4. The carrier density of all energy levels, except the HH1 level, increases with increasing temperature.

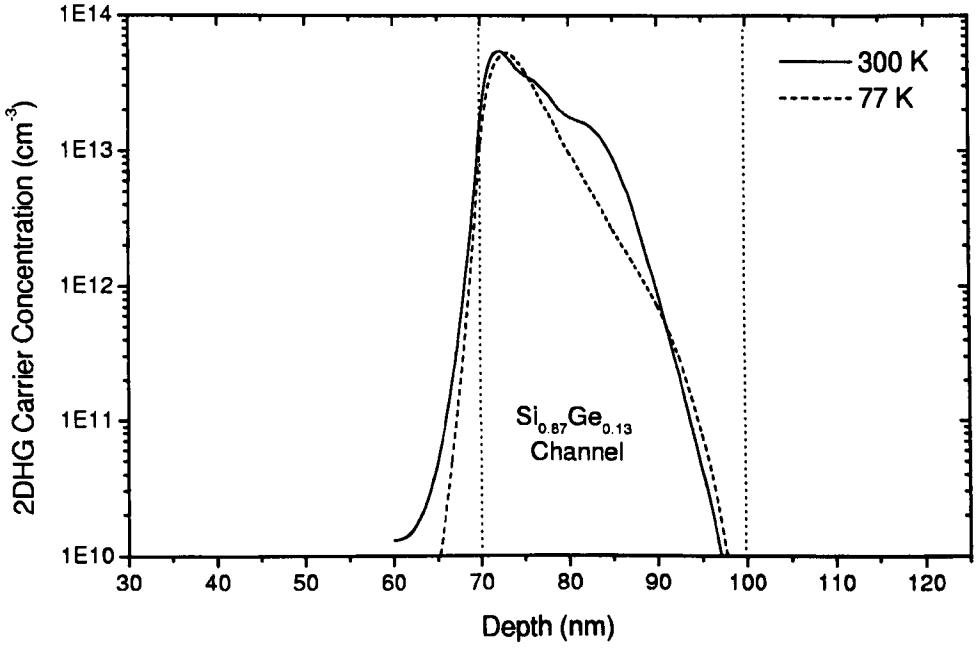

Figure 2.7: The 2DHG carrier distribution in the structure shown in Fig. 2.4 at 77 and 300 K.

effect is a development of a voltage in the direction perpendicular to the magnetic and electric field. From the theoretical viewpoint, it is customary to investigate the magnetoconductivity tensor components, i.e an inversion of the magnetoresistance and Hall resistance tensor elements, because the magnetoconductivity of many carrier species can be calculated from a summation of the effects over each carrier species. There are two approaches to the derivation of the magnetoconductivity, namely an equation of motion approach and a Boltzmann equation approach.

2.4.1 Equations of Motion

Consider a homogeneous sample with a uniformly distributed current parallel to the surface. For a single carrier with effective mass m^* and electronic charge e, travelling with the velocity $\mathbf{v}$ in an electric field ($\mathbf{E} = (E_x, E_y, 0)$) and a magnetic field ($\mathbf{B} =$

$(0, 0, B)$), the equation of motion can be written as :

$$m^*\mathbf{a} = e(\mathbf{E} + \mathbf{v} \times \mathbf{B}), \tag{2.8}$$

where $\mathbf{a}$ is the acceleration. By substitution of $\mathbf{a}$ with $\mathbf{v}'$ and solving this differential equation by using a complex variable method, the solution for the current density ($\mathbf{j}$) is given by

$$\begin{bmatrix} j_x \\ j_y \end{bmatrix} = \begin{bmatrix} \sigma_{xx} & -\sigma_{xy} \\ \sigma_{xy} & \sigma_{xx} \end{bmatrix} \begin{bmatrix} E_x \\ E_y \end{bmatrix}, \tag{2.9}$$

where

$$\sigma_{xx} = \frac{ne\mu}{1 + \mu^2 B^2}, \tag{2.10}$$

$$\sigma_{xy} = \frac{ne\mu^2 B}{1 + \mu^2 B^2}. \tag{2.11}$$

σ_{xx} and σ_{xy} are the longitudinal and transverse magnetoconductivity tensor components, respectively, n is the carrier concentration, and μ is the mobility. The magnetoresistivity (ρ_{xx}) and Hall coefficient (R_H) are obtained by inverting the magnetoconductivity tensor (Eq. 2.9) :

$$\rho_{xx} = \frac{\sigma_{xx}}{\sigma_{xx}^2 + \sigma_{xy}^2}, \tag{2.12}$$

$$R_H = \frac{\rho_{xy}}{B} = \frac{\sigma_{xy}}{B\left(\sigma_{xx}^2 + \sigma_{xy}^2\right)}, \tag{2.13}$$

where ρ_{xy} is a "Hall resistance". From the experimental viewpoint, we measure the magnetoresistivity and Hall coefficient, and the magnetoconductivity tensor components are calculated from these quantities following :

$$\sigma_{xx} = \frac{\rho_{xx}}{\rho_{xx}^2 + (BR_H)^2}, \tag{2.14}$$

$$\sigma_{xy} = \frac{(BR_H)^2}{\rho_{xx}^2 + (BR_H)^2}. \tag{2.15}$$

For an inhomogeneous or heterostructure sample, the magnetotransport consideration is slightly different. Consider two parallel slabs with different thickness,

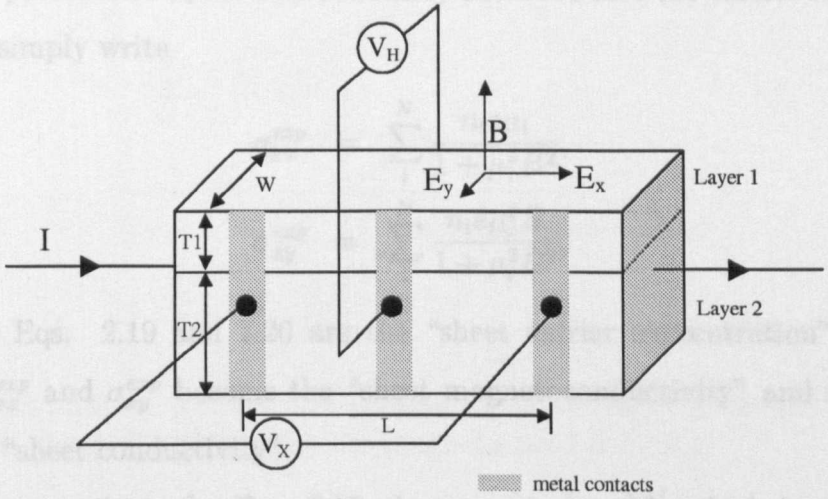

Figure 2.8: A two parallel slab model with different thickness, carrier concentration, and mobility. The current flow is uniform in x direction and parallel to the surface. The electric field E_x and E_y are common to both layers due to the use of metal contacts.

mobility, and carrier concentration, and assume that the current flow is everywhere parallel to x direction and is uniform within the individual slabs (see Fig. 2.8). If we can further assume that there is no interaction between them and the electric fields in the x and y directions are common to both layers, then we can establish Eq. 2.9 for each layer individually. From the conservation of the flowing current, it can be easily seen that

$$\begin{bmatrix} \overline{j_x}(T_1+T_2) \\ \overline{j_y}(T_1+T_2) \end{bmatrix} = \begin{bmatrix} \sum_{i=1}^{2} \frac{n_i e\mu_i T_i}{1+\mu_i^2 B^2} & -\sum_{i=1}^{2} \frac{n_i e\mu_i^2 B T_i}{1+\mu_i^2 B^2} \\ \sum_{i=1}^{2} \frac{n_i e\mu_i^2 B T_i}{1+\mu_i^2 B^2} & \sum_{i=1}^{2} \frac{n_i e\mu_i T_i}{1+\mu_i^2 B^2} \end{bmatrix} \begin{bmatrix} E_x \\ E_y \end{bmatrix}, \tag{2.16}$$

where $\overline{j_{xx}}$ and $\overline{j_{xy}}$ are average current densities in x and y directions and T_i is the thickness of layer i. We can generalise this equation for the N-layer sample and obtain

$$\overline{\sigma_{xx}} \sum_{i}^{N} T_i = \sum_{i}^{N} \frac{n_i e\mu_i T_i}{1+\mu_i^2 B^2}, \tag{2.17}$$

$$\overline{\sigma_{xy}} \sum_{i}^{N} T_i = \sum_{i}^{N} \frac{n_i e\mu_i^2 B T_i}{1+\mu_i^2 B^2}. \tag{2.18}$$

If any of the T_i is unknown, as is usually the case for the thickness of two-dimensional

carriers, the parameters T_i are conventionally absorbed into the carrier concentration and we can simply write

$$\sigma_{xx}^{exp} = \sum_{i}^{N} \frac{n_i e \mu_i}{1 + \mu_i^2 B^2}, \tag{2.19}$$

$$\sigma_{xy}^{exp} = \sum_{i}^{N} \frac{n_i e \mu_i^2 B}{1 + \mu_i^2 B^2}, \tag{2.20}$$

where n_i in Eqs. 2.19 and 2.20 are the "sheet carrier concentration" or "carrier density". σ_{xx}^{exp} and σ_{xy}^{exp} become the "sheet magnetoconductivity" and the quantity $n_i e \mu_i$ is the "sheet conductivity".

For one carrier only, Eq. 2.12 gives $\rho_{xx} = (ne\mu)^{-1}$ which is constant. In practice, most semiconductors exhibit the magnetoresistance effect which implies that at least two carriers are required. In the case where only one carrier exists and there is magnetoresistance, the energy dependence of relaxation time and/or the sample inhomogeneity are believed to be the cause.

2.4.2 The Quasi-Classical Boltzmann Equation

The Boltzmann equation has the form [Beer (1963)]

$$-\frac{e}{\hbar}(\mathbf{E} + \mathbf{v} \times \mathbf{B}) \cdot \nabla_{\mathbf{k}} f + \mathbf{v} \cdot \nabla_{\mathbf{r}} f = \left(\frac{\partial f}{\partial t}\right)_{coll}, \tag{2.21}$$

where $\mathbf{E}$ is the electric field, $\mathbf{v}$ is the velocity, $\mathbf{B}$ is the magnetic field. The solution to be obtained is for the departure of the carrier distribution function $f(\mathbf{k}, \mathbf{r}, t)$ from equilibrium. The third term in Eq. 2.21 is related to the spatial variation in f and is set to zero for a homogeneous sample with uniform temperature. The right-hand-side term is concerned with the collision of a carrier with either other carriers or the medium. If the energy of carrier does not change significantly compared to the thermal energy, this term can be approximated as

$$\left(\frac{\partial f}{\partial t}\right)_{coll} = -\left(\frac{f - f_0}{\tau}\right) \tag{2.22}$$

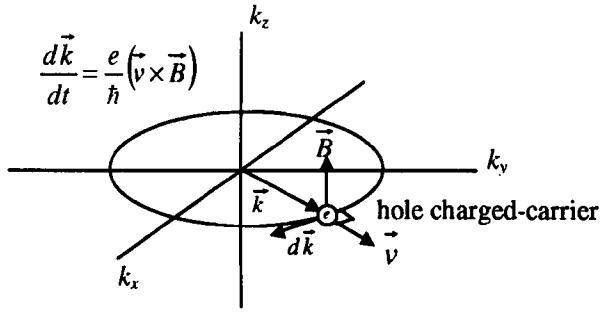

Figure 2.9: Illustration of a circular hodograph on the $k_x - k_y$ plane. The charged carrier moves along this path when the magnetic field is present.

which is called the relaxation time approximation. The proof of this approximation can be found in Wilson (1953).

The solution of Eq. 2.21 within the relaxation time approximation for a general energy band structure at an arbitrary magnetic field was given by McClure (1956). In his approach, he considers a charged carrier as it travels along a hodograph, an intersection path between a constant energy surface and a constant k_z plane (see Fig. 2.9) and shows that the velocity $\mathbf{v}$ of the carrier can be represented by a Fourier series :

$$\mathbf{v} = \sum_{m=-\infty}^{\infty} \mathbf{v}(m) \exp[im\omega s], \tag{2.23}$$

where $\mathbf{v}(m)$ is the Fourier coefficient, ω is the cyclotron angular frequency, and s is the time. For the simplification of the calculation, the relaxation time τ is assumed to be constant on the hodograph. The result is the magnetoconductivity tensor components (Eqs. 2.24-2.26) which are expressed as a Fourier series expansion in harmonics of the cyclotron frequency,

$$\sigma_{xx/xy} = \frac{e^2}{(2\pi)^3} \int d^3k \frac{\partial f_0}{\partial E} \tau S_{xx/xy}, \tag{2.24}$$

$$S_{xx} = \sum_{m=1}^{\infty} \frac{|B(m-1)|^2 + |B(-(m+1))|^2}{1 + (m\omega\tau)^2}, \tag{2.25}$$

Table 2.2: Finite terms in McClure's model for the majority hole-carriers with different hodograph rotation symmetries.

Rotation	n	m=n-1 (electron-like)	m=n+1 (hole-like)
1-fold	0	-1 (not exist)	1
	1	0 (not exist)	2
	2	1	3
2-fold	0	-1 (not exist)	1
	2	1	3
	4	3	5
3-fold	0	-1 (not exist)	1
	3	2	4
	6	5	7
4-fold	0	-1 (not exist)	1
	4	3	5
	8	7	9

$$S_{xy} = \sum_{m=1}^{\infty} \frac{m\omega\tau \left[|B(m-1)|^2 - |B(-(m+1))|^2\right]}{1+(m\omega\tau)^2}. \tag{2.26}$$

The coefficient B is related to $\mathbf{v}(m)$ in quite a complicated manner but McClure shows that only some B terms exist if the hodograph possesses specific rotation symmetry. This rotation symmetry can be derived directly from the crystal symmetry of the material, for example, silicon has a diamond structure and therefore has 4-fold rotation. In table 2.2 we show the terms which exist for hodographs with 1, 2, 3, and 4-fold rotation symmetry.

The use of this table can be demonstrated here for unstrained SiGe alloy in which the hodograph possesses the four-fold rotation symmetry due to the cubic lattice structure. Its tensor component (S_{xx} and S_{xy}) can be written as

$$S_{xx} = \frac{|B(0)|^2}{1+(\omega\tau)^2} + \frac{|B(-4)|^2}{1+(3\omega\tau)^2} + \frac{|B(4)|^2}{1+(5\omega\tau)^2} + \frac{|B(8)|^2}{1+(7\omega\tau)^2} + \ldots, \tag{2.27}$$

$$S_{xy} = \frac{\omega\tau\,|B(0)|^2}{1+(\omega\tau)^2} - \frac{3\omega\tau\,|B(-4)|^2}{1+(3\omega\tau)^2} + \frac{5\omega\tau\,|B(4)|^2}{1+(5\omega\tau)^2} - \frac{7\omega\tau\,|B(8)|^2}{1+(7\omega\tau)^2} + \ldots \tag{2.28}$$

If the majority carriers are holes, the third and seventh harmonics will behave like electrons because of their negative sign in Eq. 2.28. The detection of these harmonics was performed on the cyclotron resonant absorption measurement in which the third harmonic of p-type germanium disappears when the magnetic field is in the [111] direction, the direction which has a three-fold symmetry [Dexter (1955)]. It is questionable at present whether the Hall measurement would be sensitive enough to detect such harmonics.

The simplest example of McClure's formalism is a circular hodograph on which the tranverse velocity component is exactly sinusoidal. Consequently, there is only a single Fourier coefficient different from zero which means that only $B(0)$ exists in Eqs. 2.25 and 2.26. Eq. 2.24 is then similar to Eqs. 2.10 and 2.11. The rectangular hodograph was studied by Goldberg et al. (1957) who derived the Hall factor due to such band structure (see section 2.5) of 0.5, in coincidence with the value obtained from the geometrical technique by Allgaier (1967). The warped spherical surface of Si, Ge, and SiGe can be considered as an intermediate case between a spherical surface and cubic surface and therefore its Hall factor due to the energy surface is between 0.5 and 1.

The transformation of Eq. 2.24 from wave vector space into the mobility space was proposed by Beck and Anderson (1987) which gives

$$\sigma_{xx}(B) = \int_{-\infty}^{\infty} \frac{s(\mu)}{1+(\mu B)^2} d\mu, \tag{2.29}$$

$$\sigma_{xy}(B) = \int_{-\infty}^{\infty} \frac{s(\mu)\mu B}{1+(\mu B)^2} d\mu, \tag{2.30}$$

where $s(\mu)$ is the mobility-dependent conductivity density function or "mobility spectrum". These equations can be considered as the general forms of Eqs. 2.19 and 2.20 where the number of carriers is infinite. If this mobility spectrum is solved accurately, the interpretation of such mobility spectrum is as follows.

Assuming that there is only a 2DHG in a SiGe alloy heterostructure and no parallel conduction present (see Fig. 1.2), the mobility spectrum should be as shown

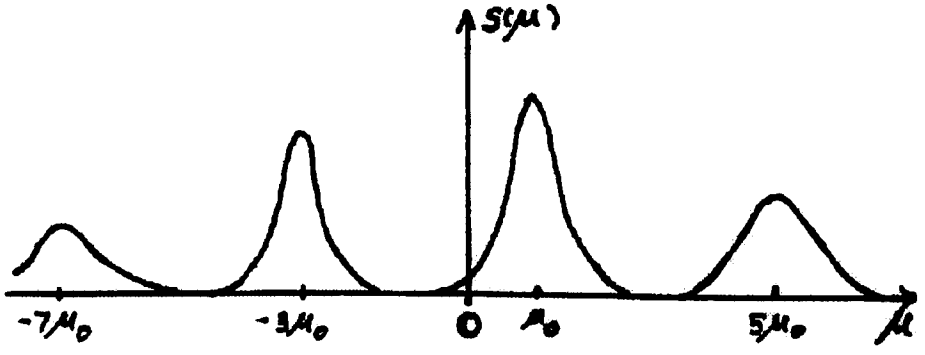

Figure 2.10: A possible mobility spectrum of SiGe alloy showing harmonics with broadening features due to the energy-dependence of relaxation time.

in Fig. 2.10. It consists of several peaks which are the third, fifth, and seventh harmonics. The height of each peak would indicate the magnitude of the Fourier coeffcient $B(m)$ while their broadening comes from the energy-dependence of the relaxation time. Qualitatively, more harmonics will appear if the constant energy contour deviates further away from a circular hodograph.

Another approach for the transformation of McClure's formalism was given by Kolodziejczak (1961) with assumptions that the constant-energy surface is spherical but the energy-wave vector dependence is nonparabolic. The magnetoconductivity tensor then has the form of

$$\sigma_{xx}(B) = \frac{e}{3\pi^2}\left\langle \frac{\mu(E)}{1+\mu^2(E)B^2} \right\rangle, \tag{2.31}$$

$$\sigma_{xy}(B) = \frac{eB}{3\pi^2}\left\langle \frac{\mu^2(E)}{1+\mu^2(E)B^2} \right\rangle, \tag{2.32}$$

$$\langle A \rangle = \int_0^\infty \left(-\frac{df_0}{dE}\right) Ak^D(E)dE, \tag{2.33}$$

where E is an energy, k is a wave-vector, and f_0 is the Fermi-Dirac function. D is the transport dimensionality which is 2 for a two-dimensional carrier gas. The mobility is dependent on the energy because the mobility is related to the relaxation time (τ) via

$$\mu(E) = \frac{e\tau(E)}{m^*}, \tag{2.34}$$

where m^* is an effective mass. Over a considerable range of energies, the relaxation time for many semiconductors can be approximated as

$$\tau(E) = \tau_0 \left(\frac{E}{k_B T}\right)^{-\alpha} \tag{2.35}$$

where τ_0 and α are constants [Smith (1978)]. Substitution of Eq. 2.35 into Eq. 2.34 gives

$$\mu(E) = \frac{e\tau_o \left(\frac{E}{k_B T}\right)^{-\alpha}}{m^*} \equiv \mu_0 \left(\frac{E}{k_B T}\right)^{-\alpha}. \tag{2.36}$$

If one assumes that the energy-wave vector dependence is quadratic :

$$E = \frac{\hbar^2 k^2}{2m^*}, \tag{2.37}$$

which is true for the wave vector near the zone centre,

$$-\frac{df_0}{dE} = \frac{-f_0(1-f_0)}{k_B T} \approx \frac{\exp\left(-\frac{E}{k_B T}\right)}{k_B T} \tag{2.38}$$

for nondegenerate carriers ($f_0 \ll 1$), and $D = 2$ for two-dimensional transport, the average mobility from Eq. 2.33 is :

$$\langle \mu \rangle = \frac{2m^* k_B T}{-\alpha \hbar^2} \int_0^\infty \exp\left(-\left(\frac{\mu_0}{\mu}\right)^{\frac{1}{\alpha}}\right) \left(\frac{\mu_0}{\mu}\right)^{\frac{2}{\alpha}} d\mu. \tag{2.39}$$

It follows that the mobility spectrum peaks can be described by the integrand :

$$s_0 \exp\left(-\left(\frac{\mu_0}{\mu}\right)^{\frac{1}{\alpha}}\right) \left(\frac{\mu_0}{\mu}\right)^{\frac{2}{\alpha}}, \tag{2.40}$$

where s_0, μ_0,and α are parameters to be optimised.

Figure 2.11 shows the transformation of the energy-dependent sheet conductivity into the mobility-dependent sheet conductivity. The energy-dependent sheet conductivity $s(E)$ (Eqs. 2.31–2.33) are combined with the energy-dependent wave vector $E(k)$ (Eq. 2.37) and with the scattering source $\mu(E)$ (Eq. 2.34).

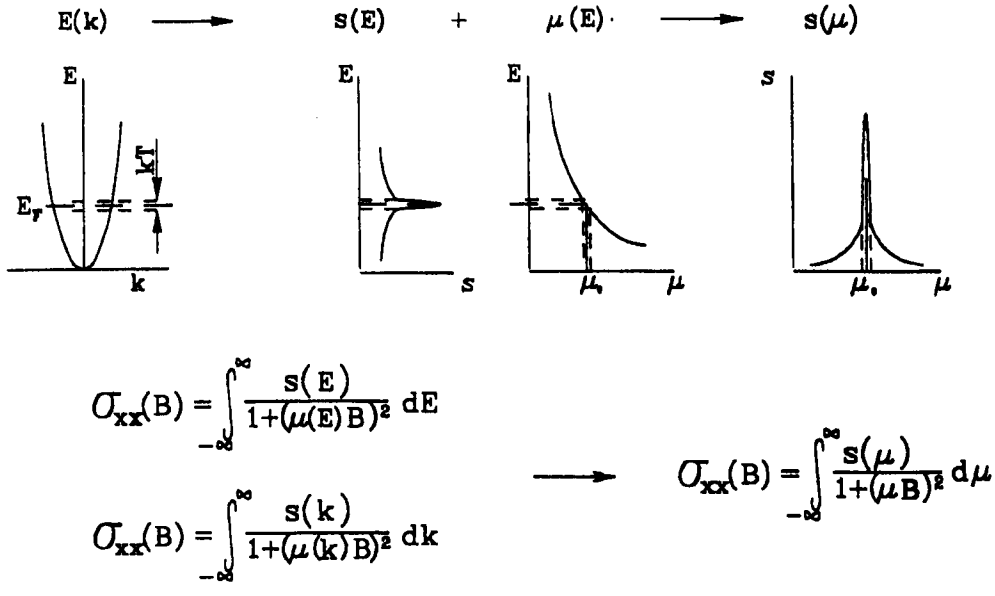

Figure 2.11: The transformation of the energy-dependent sheet conduction $s(E)$ into the mobility-dependent sheet conductivity $s(\mu)$. $E(k)$ is the band structure, which is parabolic in this case, E_F Fermi energy, k_BT thermal energy, and $\mu(E)$ the mobility associated with scattering mechanisms (after Dziuba (1996)).

2.5 Hall Factor

2.5.1 Conventional Approach

It is well known that the mobility measured by a low-field Hall measurement, or " the Hall mobility", and a measurement in an absence of magnetic field (e.g that of Haynes and Shockley experiment), or "drift mobility", differ by a Hall factor (r_H). The Hall mobility (μ_H) and drift mobility (μ_D) are related by [Bube (1974)]

$$\mu_H = r_H \mu_D = (K \cdot M)\mu_D, \tag{2.41}$$

and r_H usually deviates from unity which can be expressed as the product of factors K and M.

K is concerned with the energy dependence of the relaxation time in a non-degenerate gas which is

$$K = \frac{<\tau^2>}{<\tau>^2}. \tag{2.42}$$

Any quantity A (τ^2 or τ for this case) can be averaged according to their energy dependence as [Smith (1978)]

$$\langle A(E) \rangle = \frac{\int_0^\infty E \cdot N(E) \exp\left(-\frac{E}{k_B T}\right) A(E) dE}{\int_0^\infty E \cdot N(E) \exp\left(-\frac{E}{k_B T}\right) dE}, \tag{2.43}$$

where $N(E)$ is the density of states which has the form [Singh (1993)]

$$N(E) = \begin{cases} \frac{\sqrt{2} m^{3/2}}{\pi^2 \hbar^3} E^{1/2} & \text{, for 3-D system} \\ \frac{m}{\pi \hbar^2} E^0 & \text{, for 2-D system} \\ \frac{\sqrt{2} m^{1/2}}{\pi \hbar} E^{-1/2} & \text{, for 1-D system} \end{cases}. \tag{2.44}$$

Because $\langle \tau^2 \rangle$ is always greater than $\langle \tau \rangle^2$, K is therefore greater than unity. For example, phonon scattering mechanism has $\alpha = 0.5$ (see Eq. 2.35) which gives $K = 1.18$, while the ionized impurity scattering mechanism has $\alpha = -1.5$ which gives $K = 1.93$.

M is concerned with the anisotropy of the constant-energy surface (or contour for 2D system) and the non-parabolic nature of the energy dispersion $E(k)$. For the conduction band, this nonspherical surface can be modelled via effective masses m_1, m_2, m_3 along three main axes (see Eq. 2.1) and [Bube (1974)]

$$M = \frac{3(m_1 + m_2 + m_3)}{m_1 m_2 m_3 \left(\frac{1}{m_1} + \frac{1}{m_2} + \frac{1}{m_3}\right)^2}. \tag{2.45}$$

If the constant-energy surface is an ellipsoid of revolution so that $m_2 = m_3 = m_t$ and $m_1 = m_l$, and if $\gamma \equiv m_l/m_t$, we obtain

$$M = \frac{3\gamma(\gamma+2)}{(2\gamma+1)^2}, \tag{2.46}$$

which is always less than unity. For the valence band, the constant energy surface is too complex (see Eq. 2.2) to yield a simple form of M as Eq. 2.46 and we shall only give the conclusion that M for the valence band is also less than unity [Bube (1974)].

2.5.2 The Mobility Spectrum Approach

From Eq. 2.41, one can see that the Hall factor r_H is the ratio of Hall mobility to drift mobility. Because the Hall mobility is the mobility measured at the low-magnetic field ($\mu B \ll 1$) while the drift mobility is the mobility measured at the high-magnetic field ($\mu B \gg 1$) [Swanson (1955)], we then obtain

$$r_H = \frac{R_H(B \to 0)}{R_H(B \to \infty)} = \frac{\rho_{xy}(B \to 0)}{\rho_{xy}(B \to \infty)}. \tag{2.47}$$

By using Eqs. 2.13, 2.19, and 2.20 and using the notation $s_i = n_i e \mu_i$, we then obtain

$$\lim_{B\to 0} \rho_{xy} = \frac{\sum_i s_i \mu_i}{\left(\sum_i s_i\right)^2}, \tag{2.48}$$

$$\lim_{B\to \infty} \rho_{xy} = \frac{1}{\sum_i \frac{s_i}{\mu_i}}, \tag{2.49}$$

which gives

$$r_H = \frac{\left(\sum_i \frac{s_i}{\mu_i}\right)\left(\sum_i s_i \mu_i\right)}{\left(\sum_i s_i\right)^2}. \tag{2.50}$$

Notes that the sheet conductivity s_i is always positive and the mobility μ_i is positive for holes and negative for electrons. We shall now consider the range of this factor.

Case I : A group of carriers of only one type (i.e holes or electrons)

The Cauchy-Schwarz inequality states that

$$\left(\sum_{i=1}^{n} a_i^2\right)\left(\sum_{i=1}^{n} b_i^2\right) \geq \left(\sum_{i=1}^{n} a_i b_i\right)^2 . \tag{2.51}$$

If we set $a_i = \sqrt{\frac{s_i}{\mu_i}}$ and $b_i = \sqrt{s_i \mu_i}$, we then obtain

$$\left(\sum_{i=1}^{n} \frac{s_i}{\mu_i}\right)\left(\sum_{i=1}^{n} s_i \mu_i\right) \geq \left(\sum_{i=1}^{n} \left[\sqrt{\frac{s_i}{\mu_i}} \cdot \sqrt{s_i \mu_i}\right]\right)^2 \tag{2.52}$$

$$\geq \left(\sum_{i=1}^{n} s_i\right)^2 . \tag{2.53}$$

Therefore, the Hall factor of a group of one type of carriers is always not less than unity. This conclusion is found to be equivalent to that obtained from Eq. 2.42.

Case II : A group of mixed majority holes and minority electrons

Assuming that there are m holes, n electrons, and both mobilities are positive values (i.e. the following μ_i and $\mu_j > 0$), the Hall scattering factor is calculated step by step as follows :

$$r_H = \frac{\left(\sum_{i=1}^{m} \frac{s_i}{\mu_i} - \sum_{j=1}^{n} \frac{s_j}{\mu_j}\right)\left(\sum_{i=1}^{m} s_i \mu_i - \sum_{j=1}^{n} s_j \mu_j\right)}{\left(\sum_{k=1}^{m+n} s_k\right)^2} \tag{2.54}$$

$$= \frac{\left(\sum_{k=1}^{m+n} \frac{s_k}{\mu_k} - 2\sum_{j=1}^{n} \frac{s_j}{\mu_j}\right)\left(\sum_{k=1}^{m+n} s_k \mu_k - 2\sum_{j=1}^{n} s_j \mu_j\right)}{\left(\sum_{k=1}^{m+n} s_k\right)^2} \tag{2.55}$$

$$= \frac{\left(\sum_{k=1}^{m+n} \frac{s_k}{\mu_k}\right)\left(\sum_{k=1}^{m+n} s_k \mu_k\right)}{\left(\sum_{k=1}^{m+n} s_k\right)^2} - 2\frac{\sum_{i,j} \frac{s_i}{\mu_i} s_j \mu_j + \sum_{j,i} \frac{s_j}{\mu_j} s_i \mu_i}{\left(\sum_{k=1}^{m+n} s_k\right)^2} . \tag{2.56}$$

The first term in Eq. 2.56 is always greater than or equal to unity, which has the same effect as Eq. 2.42, while the second term, which is always greater than zero, reduces the Hall factor. This result suggests that the influence of band structure is similar to that of n-type minority carrier in a p-type medium. It is also true for the opposite case of p-type minority in an n-type medium.

In fact, electron-like behaviour in the valence band has been widely discussed in the literature. Consider the solution of Boltzmann's equation for the anisotropic band structure case at low-magnetic field, in which a current density (J) is expressed as a power series in magnetic field :

$$J_i = \sigma_{ij}\Sigma_j + \sigma_{ijl}\Sigma_j B_l + \sigma_{ijlm}\Sigma_j B_l B_m + \ldots, \tag{2.57}$$

where Σ is the electric field. For the current along the x-axis and B along the z-axis,

$$\sigma_{xx} = -e^2 \int \frac{dk}{4\pi^2} \tau v_x^2 \frac{\partial f_0}{dE}, \tag{2.58}$$

$$\sigma_{xyz} = -\frac{e^2}{\hbar} \int \frac{dk}{4\pi^2} \tau v_x^2 \frac{\partial f_0}{dE} \left[v_x \frac{\partial v_y}{\partial k_y} - v_y \frac{\partial v_y}{\partial k_x} \right]. \tag{2.59}$$

Fu et al. (1996) showed that the $\partial v_y/\partial k_x$ term is not zero for a nonparabolic non-spherical band structure. Because this term has a negative sign, it behaves as if electrons contribute to transport in the valence band.

2.6 The Calculation of Hall mobility and Drift mobility from the Mobility Spectrum

Consider the region of the mobility spectrum which contains only a single peak, for example, a peak at mobility μ_0 only in Fig. 2.10. The definition of Hall mobility is the mobility obtained from the ratio between the low-field Hall coefficient to the zero-field resistivity :

$$\mu_H = \frac{R_H(B \to 0)}{\rho_{xx}(B = 0)}. \tag{2.60}$$

By using Eqs. 2.12, 2.13, 2.19, and 2.20, one can easily obtain

$$\mu_H = \frac{\sum_i s_i \mu_i}{\sum_i s_i}. \tag{2.61}$$

By substitution of Eq. 2.50 into Eq. 2.41, we obtain the drift mobility

$$\mu_D = \frac{\sum_i s_i}{\sum_i \frac{s_i}{\mu_i}}. \tag{2.62}$$

Alternatively, we can calculate μ_D from the definition that

$$\mu_D = \frac{R_H(B \to \infty)}{\rho_{xx}(B=0)}, \tag{2.63}$$

because it is well known that the true carrier density (i.e when the Hall factor is unity) can be obtained from the Hall measurement if the magnetic field is high ($\mu B \gg 1$) [Swanson (1955)]. It must be emphasized here that Eq. 2.62 is only applicable for a single peak. The calculation of the drift mobility using all peaks in Fig. 2.10 will be incorrect because the third and seventh harmonics behave like electrons, resulting in an underestimated carrier density from the high-field Hall measurement.

From Eqs. 2.61 and 2.62, we can understand how to obtain these values graphically by considering asymptotes of magnetoconductivity tensor as shown in Fig. 2.12. The cross-over beween a zero-field σ_{xx} and low-field σ_{xy} yields the magnetic field which is an inverse of Hall mobility :

$$B_H = \frac{\sum_i s_i}{\sum_i s_i \mu_i} = \mu_H^{-1}, \tag{2.64}$$

while that between a zero-field σ_{xx} and high-field σ_{xy} is

$$B_D = \frac{\sum_i \frac{s_i}{\mu_i}}{\sum_i s_i} = \mu_D^{-1}. \tag{2.65}$$

The dimensions of Eqs. 2.64 and 2.65 may appear to be incorrect but it should be noted that the product μB is equal to $\tan(\theta_H)$, where θ_H is the Hall angle, which has no unit [Beer (1963)].

2.7 Shubnikov-de Haas Oscillation and Quantum Hall Effect

At a Si/SiGe heterojunction, the motion of carrier gases in the growth (z) direction are confined by an approximately triangular potentential well. In this direction, the carrier are in bound states of the well known discrete level "subbands" (E_n). When a

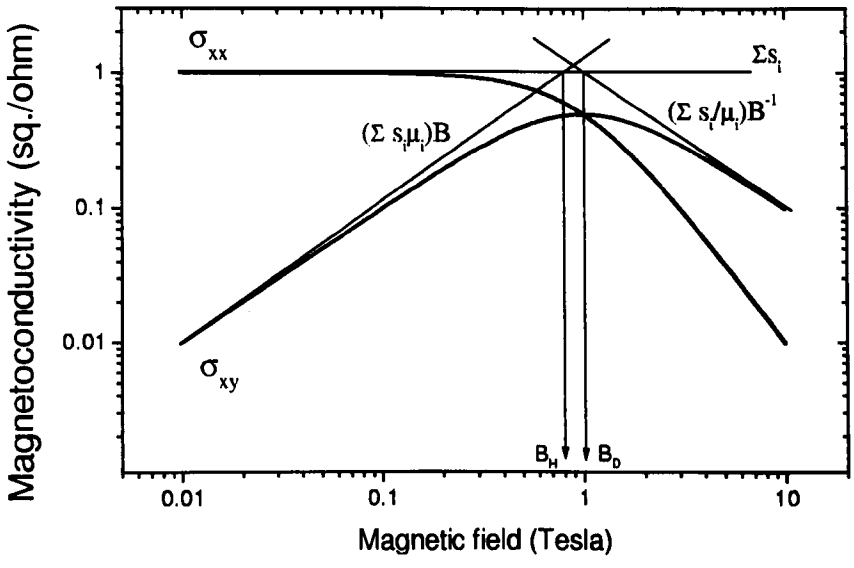

Figure 2.12: Asymptotes of σ_{xx} and σ_{xy} from which the Hall mobility, drift mobility, and Hall factor are deduced. The σ_{xx} and σ_{xy} are shown here as schematic picture only.

high-magnetic field is applied in the z-direction, perpendicular to the heterointerface, the motion of carrier gases in the $x-y$ plane will also become quantised into the Landau levels with energy $(l+\frac{1}{2})\hbar\omega_c$, where ω_c is the cyclotron angular frequency and $l = 1, 2, 3 \ldots$. Each Landau level can also be split further into two sublevels due to the interaction of the up-spin and down-spin (Zeeman splitting effect). Therefore, the total energy of carrier gases becomes

$$Energy = E_n + E_{Landau} \pm E_{spin}, \tag{2.66}$$

$$E_{Landau} = (l+\frac{1}{2})\hbar\omega_c, \text{l=0,1,2,...}, \tag{2.67}$$

$$E_{spin} = g\mu_B B, \tag{2.68}$$

where g is the effective g-factor and μ_B is the Bohr magneton.

Figure 2.13(a) shows the Landau levels which are a series of delta functions. In a real sample, the imperfection of the crystal and the presence of impurities cause the broadening of each Landau level (Fig 2.13(b) and (c)). When the magnetic field

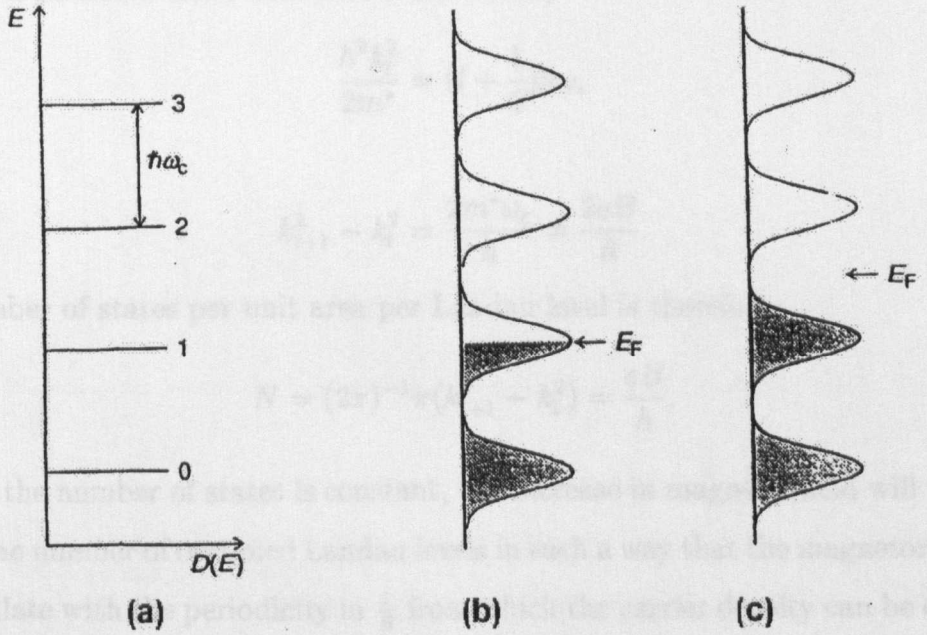

Figure 2.13: (a) The Landau level density of states with zero scattering (b,c) and in the presence of broadening due to scattering. The shaded region indicates filled with electrons. Two positions of the chemical potential (Fermi energy) are shown.

is increased, the energy $\hbar\omega_c$ will increase almost linearly ($\omega_c = eB/m^*$) and the Fermi level, which is roughly constant, will pass through these levels alternatively. At T $\sim$ 0 K where the Fermi-Dirac distribution is a step function, if the Fermi level lies at the minimum density of states (Fig. 2.13(c)), there is no empty state for conduction and therefore the conduction is minimum. On the other hand, when the Fermi level is at the maximum density of states (Fig. 2.13(b)), there are plenty of empty states for conduction and the conductivity will be maximum. As the temperature is increased, this will cause the Fermi-Dirac distribution function to become "smeared out" around the Fermi level. However, as long as $\hbar\omega_c \geq k_B T$, the general picture that the conductivities oscillates dramatically as the field is swept remains true.

The oscillation of magnetoresistance can be used to calculate the carrier den-

sity. For a parabolic band near zero wave vector,

$$\frac{\hbar^2 k_l^2}{2m^*} = (l + \frac{1}{2})\hbar\omega_c \tag{2.69}$$

or

$$k_{l+1}^2 - k_l^2 = \frac{2m^*\omega_c}{\hbar} = \frac{2eB}{\hbar}. \tag{2.70}$$

The number of states per unit area per Landau level is therefore

$$N = (2\pi)^{-1}\pi(k_{l+1}^2 - k_l^2) = \frac{eB}{h}. \tag{2.71}$$

Because the number of states is constant, the increase in magnetic field will therefore reduce the number of occupied Landau levels in such a way that the magnetoresistance will oscillate with the periodicity in $\frac{1}{B}$ from which the carrier density can be obtained:

$$\Delta\left(\frac{1}{B}\right) = \frac{e}{hn_s}. \tag{2.72}$$

Another feature associated with SdH oscillation is a quantum Hall plateau due to changing of Landau level. The Hall resistivity when the magnetoresistance goes to minimum is given by

$$\rho_{xy} = R_H B = \frac{B}{N_s e} = \frac{h}{je^2} = \frac{25812.8}{j}\Omega, \tag{2.73}$$

where j is a filling factor. A typical SdH oscillation and quantum Hall plateu are shown in Fig. 2.14. At low magnetic field, the decreasing magnetoresistance with increasing magnetic field is associated with the weak localisation and carrier-carrier interaction [Plews et al. (1997)] while at very high field a spin splitting can be observed. If the spin splitting is not observed, only even filling factors will be seen in Hall plateaux, otherwise both odd and even filling factor will be resolved.

A small signal SdH oscillation can be described as [Whall et al. (1994), Singh (1993)]

$$\frac{\Delta\rho_{xx}}{\rho_0(T)} = R_s V \frac{\Psi}{\sinh(\Psi)} \exp\left(\frac{-\pi\alpha}{\mu B}\right) \cos\left(\frac{2\pi^2\hbar n_s}{eB}\right), \tag{2.74}$$

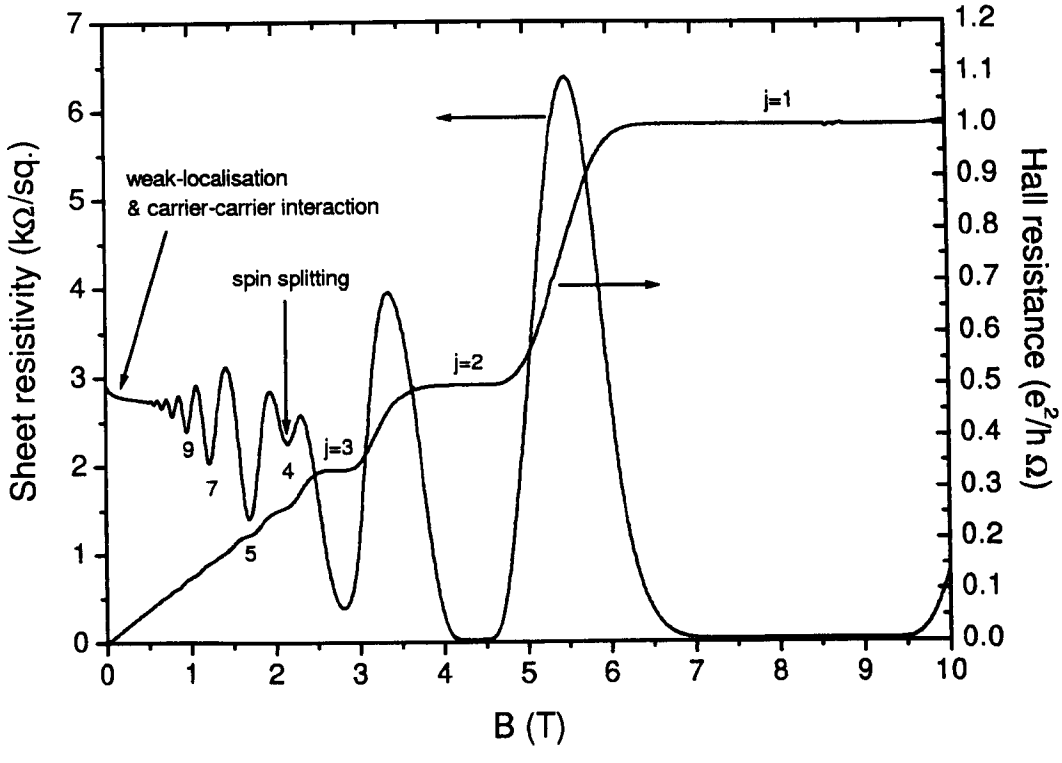

Figure 2.14: The Shubnikov de-Haas oscillation and quantum Hall plateaux of a modulation-doped p-type $Si/Si_{0.87}Ge_{0.13}/Si$ at 0.337 K.

where $\rho_0(T)$ is related to the Boltzman conductivity, the prefactor R_s is associated with Zeeman splitting, and V is usually set equal to 4 [Schoenberg (1984)]. The quantity Ψ is defined as

$$\Psi = \frac{2\pi kTm^*}{\hbar eB}. \tag{2.75}$$

Equation 2.74 can be viewed as an amplitude which increases with increasing magnetic field and decreases with increasing temperature and effective mass, multiplying a cosine wave whose frequency is determined by carrier density n_s and magnetic field. Within this thesis framework, the SdH oscillations are studied in the temperature range 0.3–1.5 K approximately and are theoretically scaled up to higher temperatures to estimate the temperature where classical transport commences. The effective mass m^* and α can be obtained by the following procedure :

1. Choosing a value of m^* to plot $\ln(\frac{\Delta\rho\sinh(\Psi)}{\rho_o(T)\Psi})$ against $\frac{1}{\mu B}$ for various magnetic fields. A straight-line fit yields a slope of $-\pi\alpha$.

2. Use preceding α to plot $\ln\left(\frac{\Delta\rho_{xx}}{\rho_0}\right)$ against $\ln\left(\frac{\Psi}{\sinh(\Psi)}\right) - \frac{\pi\alpha}{\mu B}$. If the chosen effective mass is correct, this plot will give a straight line with a slope of unity.

2.8 Scattering Mechanisms

The mobility is known to be affected by several scattering sources that perturb the potential from the ideal Bloch periodic form. Each scattering mechanism is known to have a certain dependence on the temperature and the carrier concentration or density. In table 2.3, we catagorize the known scattering mechanisms which occur in a bulk material. For our modulation-doped structure, the additional scatterings at the Si/SiGe interface are also of concern. These are studied in the form of interface roughness scattering and interface impurity scattering. Several scattering mechanisms can be combined according to the "Mathieson's rule", in which each mechanism is assigned a certain scattering rate $(\frac{1}{\tau_i})$ and these are summed linearly to yield a total

Table 2.3: The summary of scattering mechanisms present in bulk and 2D transport (after Nag (1980)).

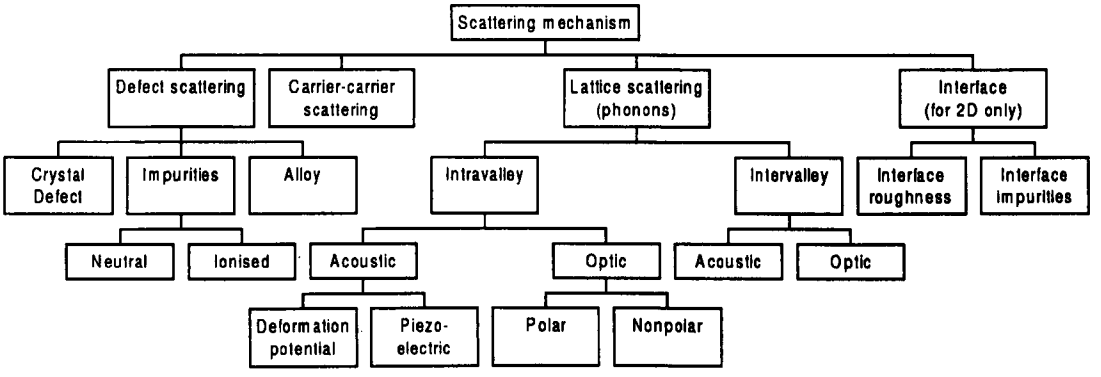

scattering rate ($\frac{1}{\tau_{total}}$). This rule applies exactly in the case of extremely degenerate carriers but is also often used for nondegenerate carriers. The mobility is related to the total scattering rate as $\mu = e < \tau_{total} > /m^*$, where the average function <> is defined in Eq. 2.43. It should be mentioned that the scattering rate is also energy dependant. If each scattering rate has the same energy dependence, the total mobility can be simplified further as

$$\frac{1}{\mu_{total}} = \sum_i \frac{1}{\mu_i}, \tag{2.76}$$

where μ_i is the mobility corresponding to each scattering mechanism. It can be seen that the total mobility μ_{total} will be limited by the scattering mechanism that has the least corresponding mobility. Therefore, the process of improving the total mobility of the material is to identify which mechanism limits the overall mobility. We shall only discuss the important scattering mechanism qualitatively and suggest the reader refers to the work done by Laikhtman and Kiehl (1993), Gold and Dolgopolov (1986), Ando et al. (1982), and Emeleus et al. (1993) for rigorous quantitative details.

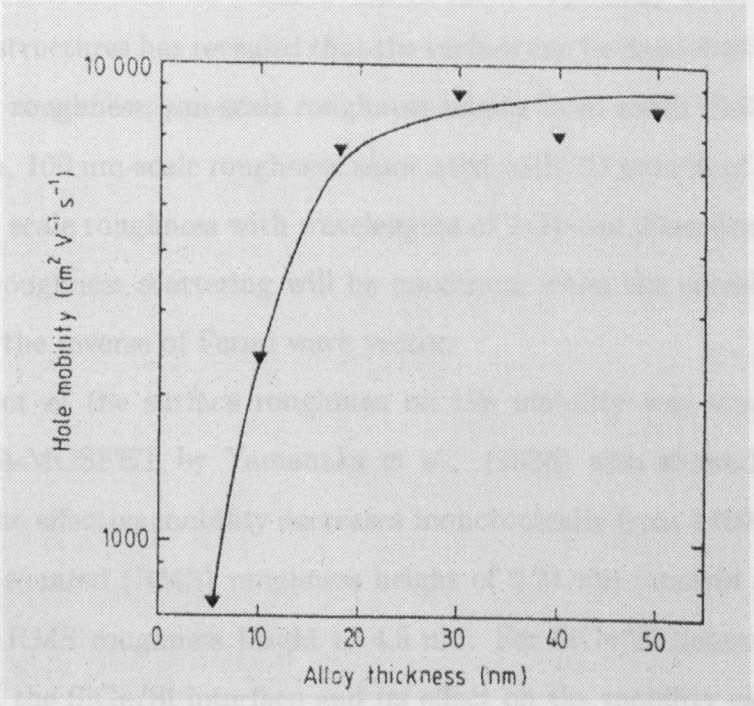

Figure 2.15: 4K Hall mobility versus alloy thickness of p-type modulation-doped $Si/Si_{0.87}Ge_{0.13}/Si$ heterostructure. The carrier density is approximately equal of mean value 2.5 $\pm 0.5\times$ 10^{11} cm^{-2} and a 40 nm setback (after Whall et al. (1993)).

2.8.1 Remote Impurity Scattering

The remote impurity scattering is caused by the ionized acceptors comprising the depleted part of the doped region near the quantum well. The strength of this scattering is reduced when the 2DHG carrier density and/or the spacer thickness is increased. It is now well-established that this kind of scattering does not limit the mobility.

2.8.2 Interface Roughness Scattering

The interface between SiGe alloy and Si is not completely flat because one or two monolayers of Ge are effectively random at the interface and the growth process can involve both 2D and 3D mode (see section 5.2.1). In theory, this roughness is characterised by the roughness height and the correlation length which are correlated into a

Gaussian distribution. A recent study on the surface morphology of modulation doped Si/SiGe heterostructures has revealed that the surface can be described by three different wavelength roughness; μm-scale roughness arising from misfit dislocation formed to relieve strain, 100 nm-scale roughness associated with 3D growth of channel layers, and the atomic scale roughness with wavelengths of 1–10-nm [Feenstra et al. (1995)]. The interface roughness scattering will be maximum when the correlation length is approximately the inverse of Fermi wave vector.

The effect of the surface roughness on the mobility was studied in the inversion layer Si-MOSFET by Yamanaka et al. (1996) who showed that at room temperature, the effective mobility decreases monotonically from 1400 $cm^2V^{-1}s^{-1}$ for the root-mean-squared (RMS) roughness height of 0.21 nm (control sample) to 600 $cm^2V^{-1}s^{-1}$ for RMS roughness height of 4.5 nm. For SiGe/Si heterostructures, the roughness is at the SiGe/Si interface and its effect on the mobility can be indirectly linked to the quantum well width. The scattering will increase when the well width is reduced because the carriers are forced closer to the interface. It has been predicted that at temperatures below 20 K the interface roughness scattering will be dominant when the well width is 4 nm or less [Gold (1987), Penner et al. (1998)]. The experimental result of the Hall mobility versus alloy thickness of p-type modulation-doped $Si/Si_{0.87}Ge_{0.13}/Si$ heterostructure at 4 K, as shown in Fig. 2.15, confirmed that the mobility decreases with decreasing well width and drops abruptly when the alloy thickness is less than $\sim$ 18 nm [Whall et al. (1993)]. A similar study but of modulation-doped n-type strain Si on relaxed $Si_{0.8}Ge_{0.2}$ also shows that the mobility monotonically decreases from 50,000 $cm^2V^{-1}s^{-1}$ for 20-nm well width to 100 $cm^2V^{-1}s^{-1}$ for 1.3-nm well width [Yutani and Shiraki (1996)]. This decreasing trend also occurs for 2DEG in AlAs/GaAs in thin quantum well thickness ($<$ 6 nm) where the electron mobility decreases proportionally to the well width to the power of 6 [Sakaki et al. (1987)]. It should be noted that even though thicker quantum well will decrease this scattering, there is a limit in quantum well thickness for a given

germanium composition to maintain the strain within SiGe alloy (see section 5.2.1).

2.8.3 Phonon Scattering

Phonon or lattice vibration scattering is an intrinsic property of materials which is very important at high temperature. It can be expected to cause three different types of electronic transitions, i.e. transitions between states within a single valley via acoustic phonon (intravalley acoustic-phonon scattering) and optical phonon (intravalley optical-phonon scattering), and transitions between different valleys (intervalley scattering). The intravalley acoustic-phonon scattering involves phonons with low energies and is almost an elastic process while the intravalley optical-phonon scattering is induced by optical phonons of low momentum and high energy, which is negligible in silicon. The intervalley scattering can be induced by high-momentum, high-energy phonons, which can be of either acoustic or optical-mode nature.

The temperature dependence of lattice-scattering mobility in pure bulk germanium is $T^{-1.66}$ for electrons and $T^{-2.33}$ for holes in the temperature range 100–300 K [Morin (1954)] while in pure bulk silicon it is $T^{-2.42}$ for electrons and $T^{-2.2}$ for holes. Kawaji (1969) formulated the theory of two-dimensional lattice scattering for electrons or holes in a semiconductor inversion layer and predicted that its mobility will have the temperature dependence of T^{-1} instead, due to the reduced transport dimensionality. Experimentally, the power of temperature in the range -1– -1.5 has been observed for the acoustic phonon and less than -2 for the optical phonon [Ando et al. (1982)]. Even though the quantum confinement enhances the low temperature mobility, at room temperature, Bhaumik et al. (1993) investigated the interaction between holes confined in a strained $Si_{1-x}Ge_x$ quantum well and acoustic and optical phonons theoretically and suggested that the confinement of holes does not provide any significant reduction in carrier scattering over bulk-pseudomorphic SiGe layers. This is because in the former case the large number of subbands available to the carrier into the quantum well while the latter case considers only the

heavy-hole to light-hole and heavy-hole to heavy-hole scattering.

2.8.4 Alloy Scattering

The distribution of Si and Ge atoms in SiGe alloy is typically in a random manner. This random process gives rise to fluctuations in the potential which decreases the alloy-limited mobility. The addition of Ge into pure Si decreased the low temperature mobility from exceeding 30,000 $cm^2V^{-1}s^{-1}$ to less than 3000 $cm^2V^{-1}s^{-1}$ for $Si_{0.88}Ge_{0.12}$ alloy [Venkataraman et al. (1993)]. The alloy scattering is described by two main parameters, the composition and the alloy potential. According to the theory, the alloy scattering is maximum for $Si_{0.5}Ge_{0.5}$ and, at high temperature where the screening is negligible, the alloy scattering has no temperature dependence. The value of alloy potential ranging from 0.2 to 0.9 eV has been reported in the past but is believed not to be higher than 0.6 eV [Kearney and Horrell (1998)]. The difference between band gap energies of Si and Ge of 0.43 eV has also been adopted [Emeleus et al. (1993)].

2.8.5 Interface Impurity Scattering

The interface impurity scattering is important for low carrier density ($\sim 10^{11}$ cm-2) and at low temperature. Basaran et al. (1994) reported the high mobility of 19,820 $cm^2V^{-1}s^{-1}$ at 7 K in $Si_{0.93}Ge_{0.07}$ and 11,100 at 4 K in $Si_{0.87}Ge_{0.13}$, employing the high growth temperature which was primarily to reduce interface charge scattering. A value of interface impurity density between -7 to 2×10^{10} cm^{-2} was obtained by CV profiling technique in the sample grown under our MBE [Brighten et al. (1993)].

Chapter 3

A Critical Review of Mobility Spectrum Analysis

3.1 Introduction

This chapter describes the numerical analyses that can be used to solve the mobility spectrum problem. In section 3.2, the mathematical form of the magnetoconductivities are explained in analogy with an inverse problem. This is followed by a discussion of a conventional multicarrier fitting method, the limitations of which are explained. Then, the calculation method proposed by Beck and Anderson (1987), an iterative technique by Dziuba and Gorska (1992), a Quantitative Mobility Spectrum Analysis (QMSA) by Antoszewski et al. (1995), and an improved Quantitative Mobility Spectrum Analysis (i-QMSA) by Vurgaftman et al. (1998) are discussed.

3.2 Mathematical Considerations

3.2.1 Inverse Problem

Solving for $s(\mu)$ from Eq. 2.29 and 2.30 is mathematically known as an inverse problem of the Fredholm integral of the first kind which has the general form [Press et al. (1992)]

$$F(y) = \int K(x,y) \cdot G(x) dx, \tag{3.1}$$

where $K(x,y)$ is a kernel function. The general difficulty in this inverse problem is that this equation is often extremely ill-conditioned, i.e the solution $G(x)$ obtained by inverting the kernel is extremely sensitive to small changes or errors in $F(y)$. Moreover, because the kernel smooths function $G(x)$ over a specific range of x, without having $F(y)$ covering sufficient range in y, the inversion procedure will lead to lost information in $G(x)$.

From a mathematical viewpoint, four aspects should be considered before attempting to calculate $G(x)$, namely the existence, uniqueness, construction, and stability of the solution [Parker (1977)]. The proof of existence of the solution is generally omitted by physicists because the quantity $G(x)$ is usually a physical parameter. The uniqueness of the solution is also ignored but it can be empirically tested by the simulation of synthetic data where $G(x)$ is known. The questions of construction and stability are of most concern, because the solution could be in disagreement with any prior assumption and the error could destabilise the solution.

3.2.2 Kernel Functions

There are two limiting cases that should be firstly considered, viz. a constant and delta function kernel. For the former case, $F(y)$ is constant because there is no y-dependency and there are infinite solutions $G(x)$. For the latter case, $F(y)$ is just $G(x)$ due to the property of delta function, i.e. $\delta(x,y) = 1$ when $x = y$.

Consider the kernel functions in the magnetoconductivity problem which are denoted by $K_{xx}(\mu, B)$ and $K_{xy}(\mu, B)$ and have the following forms :

$$K_{xx}(\mu, B) = \frac{1}{1+(\mu B)^2}, \tag{3.2}$$

$$K_{xy}(\mu, B) = \frac{\mu B}{1+(\mu B)^2}. \tag{3.3}$$

The quantities μ and B are mutual and therefore can be regarded as one parameter (μB). The plot of the K_{xx} and K_{xy} functions against μB is shown in Fig. 3.1. Four asymptotic lines associated to the high and low-field limits of σ_{xx} and σ_{xy} are also shown. The cross-over between asymptotes indicates the region where the dependency of the kernel on μB is strongest and that is the region around $\mu B = 1$, which will be called a "unity condition". This means that, for our 12-Tesla system, the minimum mobility that the mobility spectrum will resolve is ~ 833 cm^{2}V^{-1}s^{-1}, an inversion of 12 T. It has been suggested that the lowest mobility that can be resolved for 12 T can be as low as ~ 300 cm^{2}V^{-1}s^{-1} because the unity condition is the situation where a carrier deviates one radian of arc before scattering, but the applied magnetic field can exert an influence on a carrier as soon as it begins to spiral or, in other words, at much lower value of μB than unity [Antoszewski and Faraone (1996)].

3.3 Physical Limitations

Mathematically, the magnetic field should be as high as possible so that the kernel functions can cover a sufficient range. However, there are two physical limitations that should be considered. Firstly, the relaxation-time approximation (Eq. 2.22) is generally applicable when the energy transfer per scattering is zero or small compared with the Fermi energy. This includes elastic scattering such as ionized impurity scattering which involves no energy transfer, and acoustic-phonon scattering which involves a small energy transfer. Optical-phonon scattering is an inelastic process associated with a large energy transfer per scattering event and therefore the relaxation-time

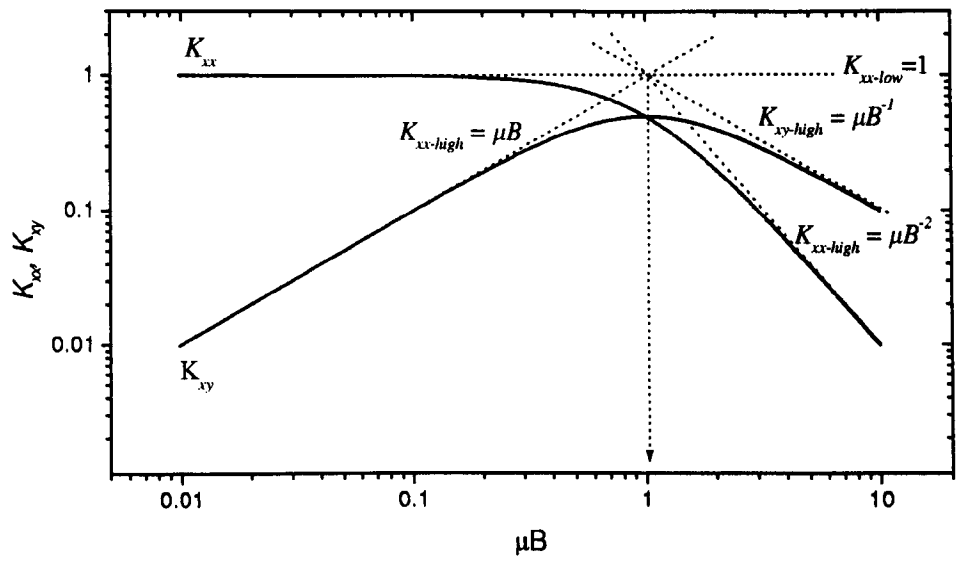

Figure 3.1: The kernel functions of magnetoconductivity $\sigma_{xx}$and σ_{xy}.

approximation may not hold [Kim et al. (1993)].

Secondly, the magnetic field might affect the carrier density, mobility, or the relaxation time. Panaev et al. (1993) suggested that the influence of magnetic field on the transport relaxation time occurs when the Lamor radius is comparable to the effective range of interaction with scatterers. In other words, in the mobility spectrum problem, the magnetic field should not bend the electron trajectory within the scattering range. Another example is a report on a carrier freezout effect, observed in a lowly-doped narrow gap HgTe sample, in which an additional peak in the mobility spectrum occurs closely to the mobility of inversion of freezout field. This peak compensates for the reduction in carrier density because of the widening gap with increasing magnetic field [Beck et al. (1988)]. In addition, in δ-doped GaAs, the δ-well may also be changed by the magnetic field when the depopulation of the highest subband occurs when $E_F - E_i \leq \hbar\omega_c/2$ [Panaev et al. (1993)].

The mobility spectrum problem is obviously inapplicable where Shubnikov-de Haas oscillation emerges or, according to Beck and Anderson (1987), when there is a negative magnetoresistance. However, recently, Dziuba et al. (1999) demonstrated

that the mobility spectrum can be used to analyse the negative-magnetoresistance in $In_{0.53}Ga_{0.47}As/InP$ heterostructures by assuming that there is a magnetic field dependent mobility.

3.4 Numerical Analyses

3.4.1 Multicarrier Fitting

By using Eqs. 2.12 and 2.13,or Eqs. 2.19 and 2.20, with predefined number of carrier species, each μ_i and n_i can be identified by using a standard fitting procedure such as the Levenberg-Marquardt algorithm [Marquardt (1963)]. The merit of fit determined by a chi-square test is defined as [Press et al. (1992)]

$$\chi^2 \equiv \sum_{i=1}^{M} \left[\frac{y_i - y(x; a_1 ... a_{2N})}{\sigma_i} \right]^2, \tag{3.4}$$

where y_i is sheet resistivity, Hall coefficient, longitudinal magnetoconductivity, or transverse magnetoconductivity, and a_i's are a set of sheet carrier density and mobility.

The choice of quantities which should be used for the fitting depends on the range of mobilities and magnetic fields available. When considering the kernel K_{xx} and K_{xy}, one can obviously see that it is mathematically impossible to use magnetoconductivity tensor components (Eqs. 2.19 and 2.20) directly for the carrier with $\mu B_{max} < 1$ because the data is virtually "incomplete". It should be noted that in the modulation-doped structure, the 2DHG mobility is much higher than the supply layer and therefore the data which is considered "incomplete" for the supply layer is not necessarily "incomplete" for the 2DHG, for the same magnetic field range. To increase the sensitivity, their derivatives with respect to the magnetic field might be used but the problem will be harder to solve because it become non-linear with respect to the mobility and carrier density.

3.4.2 Beck and Anderson Mobility Spectrum (BA)

Beck and Anderson (1987) developed a mobility spectrum calculation by applying the theorem of Krein [Krein (1962)] to Eqs. 2.29 and 2.30. The calculation consists of two steps namely a "physical test" and the determination of the envelope function. The physical test checks the validity of the data by calculating the eigenvalues of an associated matrix of the data, which have to be non-negative. These eigenvalues and corresponding eigenfunctions are then used to calculate the envelope function or "mobility spectrum", a mobility-dependent sheet conductivity. In the spectrum, each carrier species exhibits itself as a peak and a peak coordinate directly gives the mobility and sheet conductivity, and hence the carrier density. Because the calculation is rather mathematically complex, we shall leave the numerical details to Appendix A and only concentrate on the application from the experimental viewpoint.

An example of the BA analysis is presented in Fig. 3.2 for a synthetic data set having 2 carrier species ($n_1 = 10^{12}$ cm^{-2}, $\mu_1 = 1500$ cm^{2}V^{-1}s^{-1}, $n_2 = 10^{12}$ cm^{-2}, $\mu_2 = 2500$ cm^{2}V^{-1}s^{-1}). The synthetic data is generated at 8 magnetic field values (see Figs. 3.2(a) and (b)). From the synthetic sheet resistivity and Hall coefficient, the magnetoconductivity tensor components (σ_{xx}, σ_{xy}) are calculated, using Eqs. 2.14 and 2.15. Before performing the BA analysis, all 8 data points are further grouped combinatorially to form 56 data subsets, each consisting of 3 data points. It will be shown later that a data subset of $N + 1$ data points is optimum for N carrier species. The BA analyses are then applied to all 56 data subsets. We found that not all, but 50, data subsets pass the physical test. This is quite astonishing because even this case where there is no uncertainty involved, the BA analysis already rejects some data subsets which are considered being "unphysical". And finally, we obtain 50 mobility spectra and the one which best fits all 8 data points is shown in Fig. 3.2(c). When this spectrum is converted into a mobility versus carrier density plot, the peak coordinates remarkably yield the correct mobilities and carrier density of carrier species we use for this simulation. It should be noted that when a data subset

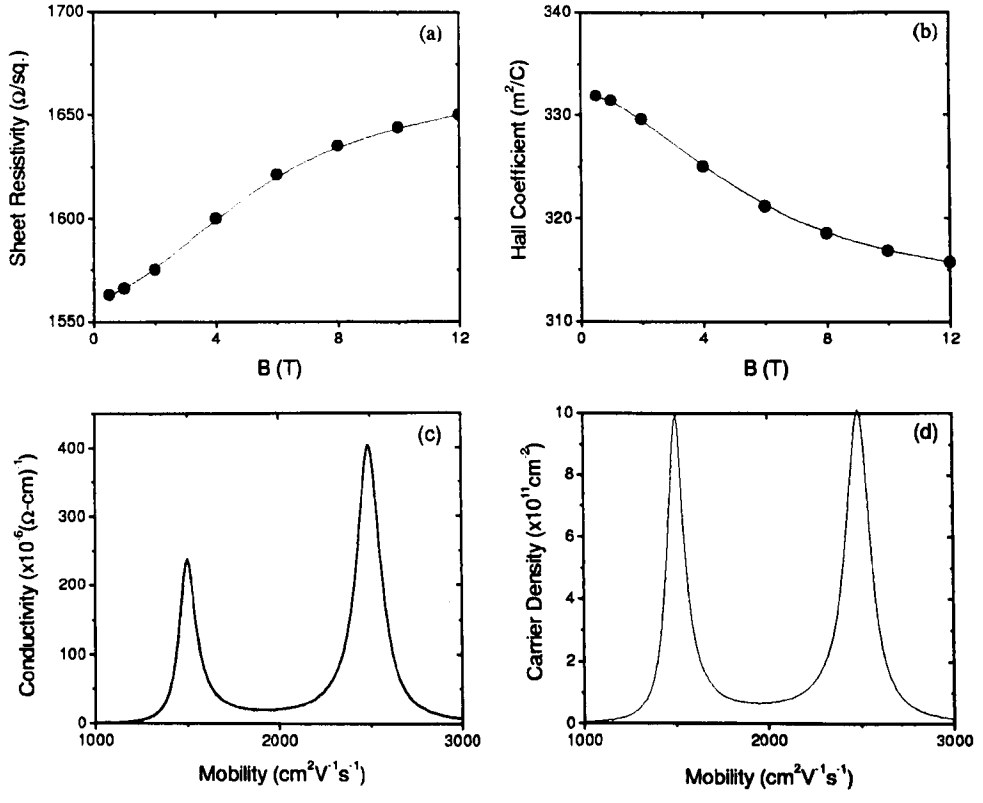

Figure 3.2: Typical calculation procedure for Beck and Anderson mobility spectrum analysis. (a) and (b) are synthetic data generated from two carrier species: $n_1 = 10^{12}$ cm^{-2} , $\mu_1 = 1,500$ cm^{2}V^{-1}s^{-1} and $n_2 = 10^{12}$ cm^{-2}, $\mu_2 = 2,5000$ cm^{2}V^{-1}s^{-1}. The spectrum after calculation is displayed in (c) and the carrier density is calculated and displayed in (d).

is "unphysical" in the BA analysis, it does not mean that this data subset contains unreal data. It merely says that it is impossible to calculate the mobility spectrum for a given data subset. The characteristic of this data subset is inconsistent with the magnetoconductivity model used (Eqs. 2.19 and 2.20).

To show that the data subset of 3 data points is optimum for 2 carrier species, we perform the physical test of a data set of 25 data points using the same carrier species. We use 25 data points, instead of 8, because this gives a higher number of data subsets to be tested. Different numbers of data points per data subset are tested and the result is shown in table 3.1. It reveals that when the number of data points

Table 3.1: The physical tests for different set of data points selected from 25 data points.

Data points	Data Subsets	Physical	Percentage(%)
2	276	276	100
3	2024	1895	94
4	10626	263	3
5	42504	15	~ 0

used per data subset increase from 3 to 4, the number of data subsets that pass the physical test decreases rapidly from 94% to 3% and almost none of data subsets of 4 data points pass the test. Data subsets that use 2 data points also pass the test entirely (100%) but we found that the spectra from these data subsets contain only a single peak. In general, it is observed that the spectrum which is generated from the data subset of $N+1$ data points, after passing the physical test, contains N peaks at most. Therefore, we can conclude that the use of $N+1$ data points per data subset is optimum for the BA analysis of N carrier species and the number of carrier species can be obtained by increasing the number of data points per data set, performing the physical test, and checking when the physical percentage decreases dramatically.

The next simulation is to investigate the influence of the experimental error. We use previous synthetic data set (25 data points) and perform the BA analysis of 3-data-point subsets. Prior to the BA analysis, randomly Gaussian-distributed errors are mixed into the synthetic data. Because there are $\sim$ 1900 spectra, the plot of all spectra would be difficult to observe. Instead, we produce a histogram plot of all mobilites, associated to the peaks, of all spectra so that the consistency of the spectra can be checked. The histogram at different errors are shown in Fig. 3.3. Without intentional error (0%), the histogram consists of 2 main peaks having the mobility windows very close to the expected values of 1500 and 2500 $cm^2V^{-1}s^{-1}$. Because the histogram peaks are very narrow, this implies that most spectra have the same peak

at very close mobilities. As the error increases, an intermediate histogram peak at mobility $\sim$ 2100 $cm^2V^{-1}s^{-1}$ starts to dominate while the original 2 histogram peaks start to disappear. It can be postulated that this intermediate peak occurs because some data subset does not cover sufficient magnetic-field range, i.e. these 3 data points are adjacent to each other on the magnetic field axis, and therefore only 1 peak can be obtained from the spectrum.

The histogram plot at 0% error is particularly of interest. It is conceivable that, in principle, all mobility spectra should be the same for this case because they are calculated from the same set of carrier species (the intentional error is equivalent to the perturbation to carrier species and therefore randomly produces different sets of carrier species). However, the width of each histogram peak is about 2–4 times the window width (40 $cm^2V^{-1}s^{-1}$) which means that the spectra are not the same. There must be some uncertainty present in the synthetic data. Indeed, this uncertainty comes entirely from the round-off effect of the computer, the limitation of the number of the digits the computer can handle, which can cause the error at the magnitude of 10^{-14} %. This round-off error is also believed to be responsible for an intermediate histogram peak in the 0%-error case.

In summary, the BA analysis is regarded as a qualitative technique that yields the number of carrier species and the estimate of mobility of each carrier species. The mobility spectrum is not unique and extremely sensitive to the uncertainty in the data.

3.4.3 Well-defined Mobility Spectrum Problem

The mobility spectrum problem is regarded as a well-defined problem when the number of mobility points is equal to the number of magnetic field points. The linear-

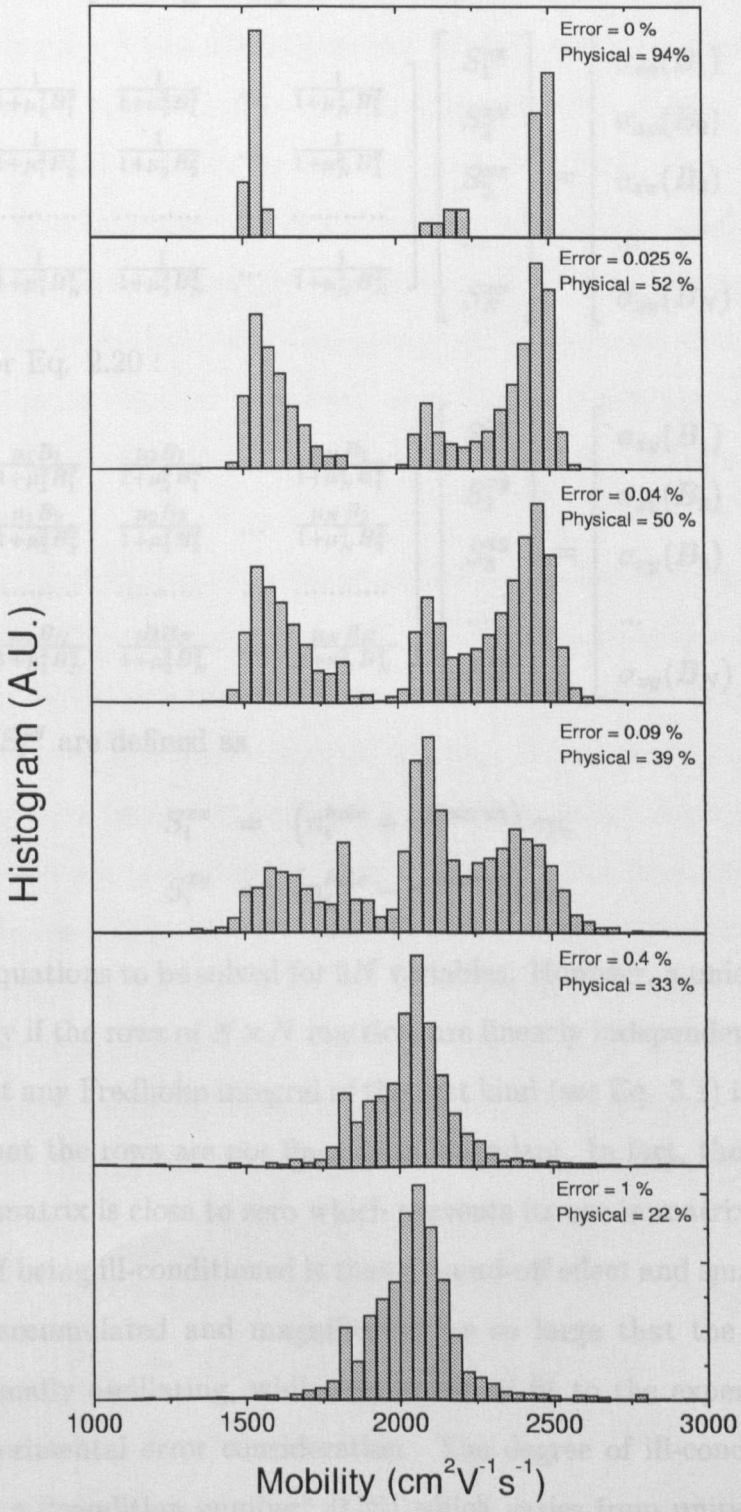

Figure 3.3: The histogram of mobilities at the peaks of all mobility spectra for different errors. The window width is 40 $cm^2V^{-1}s^{-1}$.

equation sytem corresponding to Eq. 2.19 is then :

$$\begin{bmatrix} \frac{1}{1+\mu_1^2 B_1^2} & \frac{1}{1+\mu_2^2 B_1^2} & \cdots & \frac{1}{1+\mu_N^2 B_1^2} \\ \frac{1}{1+\mu_1^2 B_2^2} & \frac{1}{1+\mu_2^2 B_2^2} & \cdots & \frac{1}{1+\mu_N^2 B_2^2} \\ \cdots\cdots & \cdots\cdots & \cdots & \cdots\cdots \\ \frac{1}{1+\mu_1^2 B_N^2} & \frac{1}{1+\mu_2^2 B_N^2} & \cdots & \frac{1}{1+\mu_N^2 B_N^2} \end{bmatrix} \begin{bmatrix} S_1^{xx} \\ S_2^{xx} \\ S_3^{xx} \\ \cdots \\ S_N^{xx} \end{bmatrix} = \begin{bmatrix} \sigma_{xx}(B_1) \\ \sigma_{xx}(B_2) \\ \sigma_{xx}(B_3) \\ \cdots \\ \sigma_{xx}(B_N) \end{bmatrix}, \tag{3.5}$$

and similarly for Eq. 2.20 :

$$\begin{bmatrix} \frac{\mu_1 B_1}{1+\mu_1^2 B_1^2} & \frac{\mu_2 B_1}{1+\mu_2^2 B_1^2} & \cdots & \frac{\mu_N B_1}{1+\mu_N^2 B_1^2} \\ \frac{\mu_1 B_2}{1+\mu_1^2 B_2^2} & \frac{\mu_2 B_2}{1+\mu_2^2 B_2^2} & \cdots & \frac{\mu_N B_2}{1+\mu_N^2 B_2^2} \\ \cdots\cdots & \cdots\cdots & \cdots & \cdots\cdots \\ \frac{\mu_1 B_N}{1+\mu_1^2 B_N^2} & \frac{\mu 2 B_N}{1+\mu_2^2 B_N^2} & \cdots & \frac{\mu_N B_N}{1+\mu_N^2 B_N^2} \end{bmatrix} \begin{bmatrix} S_1^{xy} \\ S_2^{xy} \\ S_3^{xy} \\ \cdots \\ S_N^{xy} \end{bmatrix} = \begin{bmatrix} \sigma_{xy}(B_1) \\ \sigma_{xy}(B_2) \\ \sigma_{xy}(B_3) \\ \cdots \\ \sigma_{xy}(B_N) \end{bmatrix}, \tag{3.6}$$

where S_i^{xx} and S_i^{xy} are defined as

$$S_i^{xx} = \left(n_i^{hole} + n_i^{electron}\right) e\mu, \tag{3.7}$$

$$S_i^{xy} = \left(n_i^{hole} - n_i^{electron}\right) e\mu. \tag{3.8}$$

There are $2N$ equations to be solved for $2N$ variables. However, a unique solution will be obtained only if the rows of $N \times N$ matrices are linearly independent of other rows. It turns out that any Fredholm integral of the first kind (see Eq. 3.1) is ill-conditioned which means that the rows are not linearly independent. In fact, the determinant of ill-conditioned matrix is close to zero which prevents its use in matrix inversion. The adverse effect of being ill-conditioned is that a round-off effect and small experimental errors can be accumulated and magnified to be so large that the result becomes meaningless, usually oscillating, whilst the merit of fit to the experimental data is within the experimental error consideration. The degree of ill-conditioning can be determined via a "condition number" (CN) which varies from unity for an identity matrix, which has completely linearly independent rows, to infinity (see Appendix B). The bigger the condition number is, the higher the ill-conditioning is.

To improve the condition of the matrix (reducing the condition number), one might use a "Singular Value Decomposition (SVD)" technique (see Appendix C) which discards some equations that are linear combination of other equations and hence reduces the condition number (see Fig. 3.4), or a Philips-Twomey regularisation, which smoothly improves the condition of the matrix via a single parameter (λ) (see Fig. 3.5). The combination between SVD and Phillip-Twomey regularisation was also proposed by Rothwell and Drachman (1989) which allows more freedom in locating the optimum solution. However, even though significant improvements in the spectrum is observed, the negativity in conductivity, and hence carrier density is still unavoidable.

It is known that an iterative technique gives a more accurate result than any direct technique (i.e. all preceding techniques). The iterative technique is self-correcting and usually used to smooth the result from a direct technique. Shaw (1953) stated that it is unlikely that an iterative method will lead to incorrect solution even for an ill-conditioned matrix because there is no matrix manipulation involved. All coefficients in the matrix are used directly. This is in contrast to Rice (1981) who argued that if the problem is ill-conditioned, then no amount of effort, trickery, or talent used in the computation can produce accurate answers except by chance. In addition to avoiding the matrix manipulation in the iterative technique, one can also acquire a capability to directly impose a nonnegativity constraint for the conductivity variable.

Dziuba and Gorska (1992) were the first to solve the mobility spectrum problem by the iterative technique. The mobility spectrum obtained by this technique is unique because it exploits all data points. The iteration takes the form

$$S_{i,k}^{xx} \Leftarrow S_{i,k-1}^{xx} + \left(\sigma_{xx}^{\exp}(B_i) - \sigma_{xx}(B_i)\right)\alpha_{xx}, \tag{3.9}$$

$$S_{i,k}^{xy} \Leftarrow S_{i,k-1}^{xy} + \left(\frac{\sigma_{xy}^{\exp}(B_i) - \sigma_{xx}(B_i)}{B_i}\right)\alpha_{xy}, \tag{3.10}$$

where k represents the number of iteration and α_{xx} and α_{xy}, which are less than 1, control the convergence speed. The plot of conductivities versus μ_i was found to oscillate around zero partial conductivity with the biggest positive partial conductivity

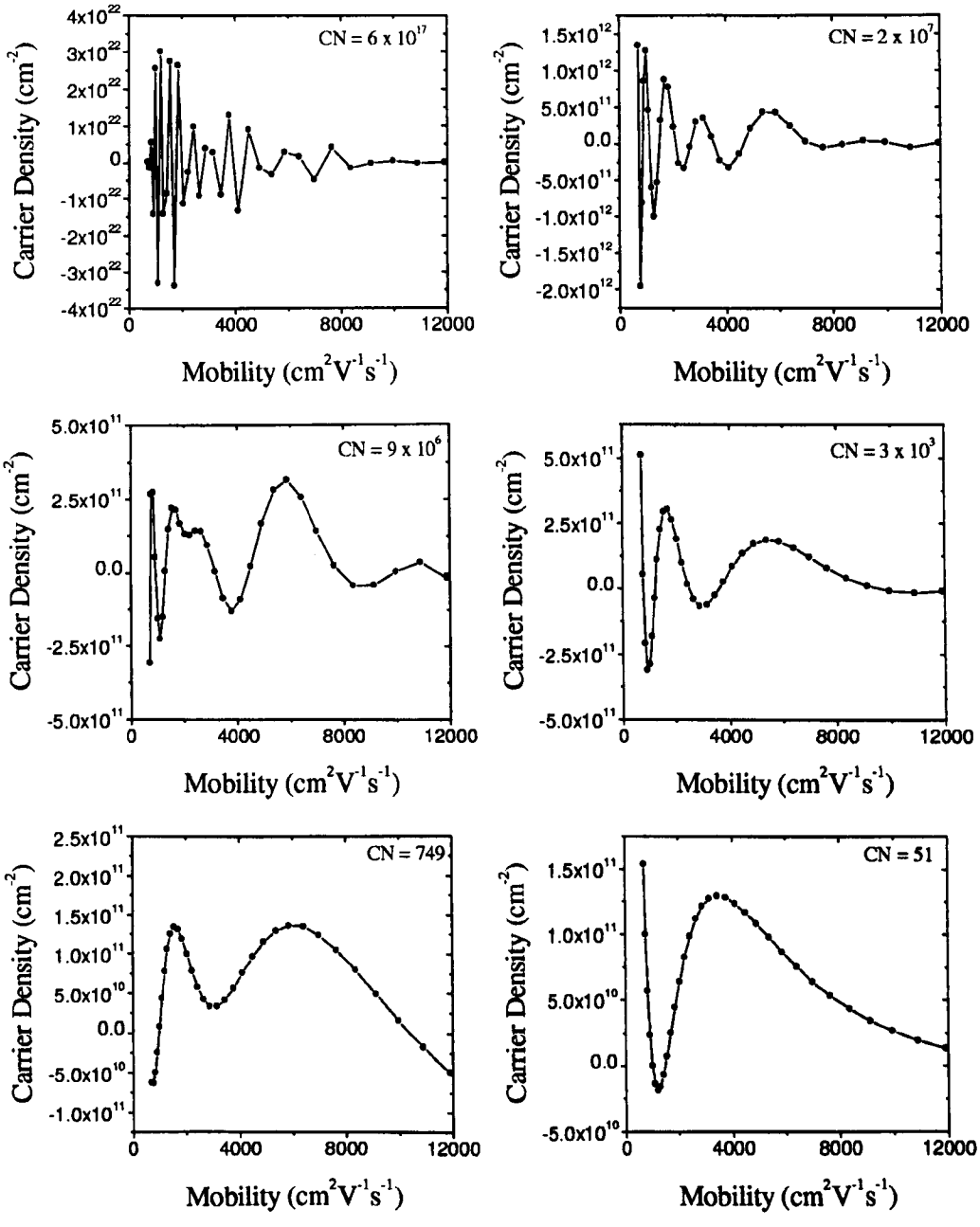

Figure 3.4: The carrier density as a function of mobility, obtained from the Singular Value Decomposition (SVD) technique applied to σ_{xx} tensor. The synthetic data of two carriers species : $n_1 = 10^{12}$ cm^{-2}, $\mu_1 = 2,000$ cm^{2}V^{-1}s^{-1} and $n_2 = 10^{12}$ cm^{-2}, $\mu_2 = 6,000$ cm^{2}V^{-1}s^{-1}. As the condition number (CN) is reduced, the spectrum becomes less fluctuated.

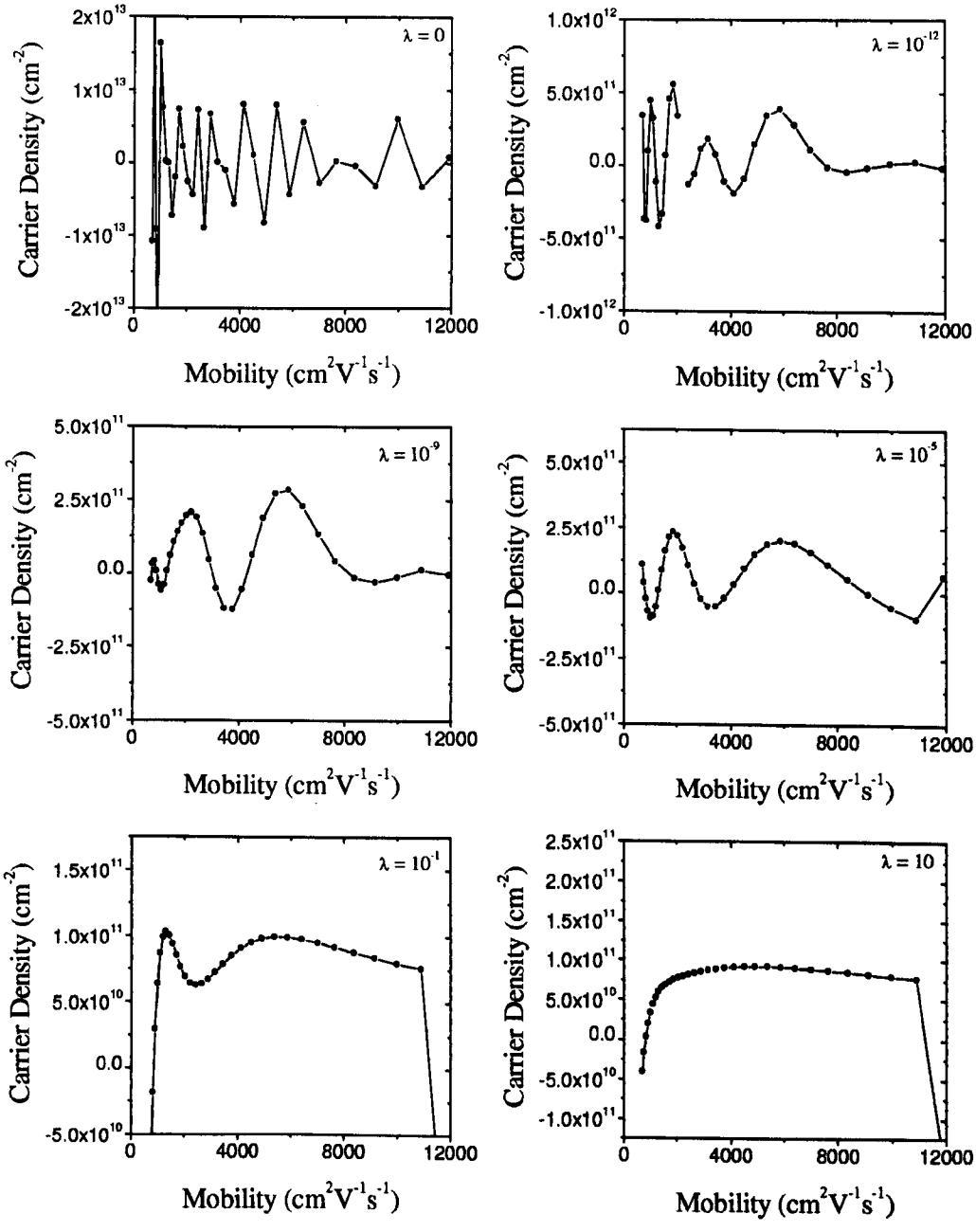

Figure 3.5: The carrier density as a function of mobility by Phillip-Twomey regularisation at various control parameters (λ) for σ_{xx} tensor.

occurring at the mobility corresponding to the actual average mobility of the majority group of carriers in the material. The oscillation means that some of the partial conductivity is negative which is unphysical. An additional "smoothing procedure" has been proposed to minimize this effect but it is found that the negative partial conductivity cannot be entirely suppressed while maintaining an acceptable fit to the data. In this iterative technique, a set of mobility points μ_i is arbitrarily chosen in the range B_{min}^{-1} to B_{max}^{-1} $\text{m}^2\text{V}^{-1}\text{s}^{-1}$ where B_{min} and B_{max} are the minimum and maximum measured magnetic fields. The number of mobility points is then limited by the number of measured magnetic field points and the lowest mobility is set by the maximum magnetic field available.

Antoszewski et al. (1995) later used a Gauss-Siedel sussessive over-relaxation method, which has been named a quantitative mobility spectrum analysis (QMSA), which has the form

$$S_i^{xx} \Leftarrow S_i^{xx} + \varpi_{xx}(1+\mu_i^2 B_i^2)\left[\sigma_{xx}^{\text{exp}}(B_i) - \sum_{j=1}^{N} \frac{S_j^{xx}}{1+\mu_j^2 B_i^2}\right] \tag{3.11}$$

$$S_i^{xy} \Leftarrow S_i^{xy} + \varpi_{xy}\frac{(1+\mu_i^2 B_i^2)}{\mu_i B_i}\left[\sigma_{xy}^{\text{exp}}(B_i) - \sum_{j=1}^{N} \frac{S_j^{xy}\cdot \mu_j B_i}{1+\mu_j^2 B_i^2}\right] \tag{3.12}$$

where ϖ_{xx} and ϖ_{xy} are convergence parameters. Mathematically, the convergence speed is improved because S_i^{xx} and S_i^{xy} are used as soon as they become available [Press et al. (1992)]. Examples of QMSA applications are for GaAs/AlGaAs HBT and HEMT structures [Antoszewski et al. (1997)], AlGaN/GaN [Dziuba et al. (1997)] and HgCdTe [Gui et al. (1997)]. The mobility range has been extended to values of μ less than B_{max}^{-1} by the extrapolation of experimental data to higher fields than the maximum measured magnetic field [Meyer et al. (1997)]. Meyer et al. (1997) showed the extrapolation to higher field by reproducing the known high-field asymptotic forms for $\sigma_{xx}(B)$ and $\sigma_{xy}(B)$ at $\mu B \gg 1$ and join smoothly with the magnitudes, first derivatives, and second derivatives of $\sigma_{xx}(B)$ and $\sigma_{xy}(B)$. Nonetheless, this cannot be applied to the general case where μB never exceeds the unity and σ_{xy} never reaches the maximum A higher number of mobility points is also obtained by spline

interpolation between the experimental data points. Even though these procedures seem to overcome problems inherent in the iterative technique, the use of interpolation and/or extrapolation of experimental data is questionable because there are several interpolation and extrapolation techniques available and the modification of original data prior to calculation is subject to investigator bias and error.

An improved quantitative mobility spectrum (i-QMSA) has removed the limitation in the number of mobility points by not confining these to the value $\mu_i = B_i^{-1}$ [Vurgaftman et al. (1998)](see "unity condition" in section 3.2.2). The range of mobilities and the number of mobility points are then independent of the range and the number of points of measured magnetic field. i-QMSA differs from the iterative technique and QMSA in that it minimizes the least square deviation of both conductivity tensor and its derivative with respect to magnetic field, and updates only one carrier for each iteration. In addition, empirical procedures (two/three-point swapping and point elimination) for manipulating the mobility spectrum are introduced and shown to improve the fits while smoothing the spectrum and making it "more physically reasonable". Despite these refinements, it must be said that empirical procedures are likely to be case-specific and are dependent on individual bias. Moreover, the unity condition is still necessary in spite of their ignorance. This can be seen when they realise that it is mostly the carrier according to the unity condition that to be updated, because its modification produces the most fit within that iteration.

3.5 Conclusion

The mobility spectrum problem is equivalent to the inverse problem of the Fredholm integral of the first kind. The mobility spectrum has been solved for so far by 4 different techniques namely the Beck and Anderson analysis, the iterative technique, the Quantitative Mobility Spectrum Analysis (QMSA), and the improved QMSA (i-QMSA). The difficulties in the problem can be divided into two main catagories; the

low carrier-mobility and the number of magnetic field points. The low carrier-mobility requires the magnetic field data at very high field in order to fulfil the unity condition while the experimental data needs the interpolation to make the number of magnetic field points match the number of mobility points of the mobility spectrum. Both requirements are lifted with the development of i-QMSA but its empirical procedures are currently questionable.

Chapter 4

Development of a Maximum-Entropy Mobility Spectrum (MEMS)

4.1 Introduction

In chapter 3, the development of the mobility spectrum problem is reviewed and it is discovered that the mobility spectrum problem is equivalent to an inverse problem of the Fredholm integral of the first kind. The inverse problem is, in general, a problem in which one deduces the underlying information from an incomplete data. In the mobility spectrum problem, the underlying information is a quasi-continuous mobility spectrum and the incomplete data is the magnetoconductivity tensor components obtained in discrete magnetic field. One of the most versatile tools in inverse problem solving is a "maximum entropy" concept. It has been applied to many physics problems, for example, the enhanced resolution of secondary ion mass spectroscopy (SIMS) [Chu and Dowsett (1997)] and the image processing [Skilling (1984)]. In this chapter, we will use this to solve the mobility spectrum and compare it to existing mobility spectrum calculation techniques.

4.2 Entropy and Information Theory

An "entropy" is a quantity used to measure the order of the system. By the law of thermodynamics, any system will naturally change from order to disorder state. For example, an sugar cube put into a glass of water will diffuse until its concentration everywhere is equal - the disorder state. In the information theory, that sugar cube is equivalent to 'knowledge'. The knowledge is only useful when it is in order or definite. In other words, the uncertainty associated with that knowledge must be sufficiently small. We can use the same entropy to describe the uncertainty of the knowledge quantitatively.

Consider a real variable X that can have a set of outcomes $\{x_1, x_2, x_3, \ldots, x_n\}$ with probabilities $\{p_1, p_2, p_3, \ldots, p_n\}$, where all $p_i > 0$ and $\sum_{i=1}^{n} p_i = 1$. We can define the entropy (uncertainty) of this variable as

$$H(X) = -\sum_{i=1}^{n} p_i \ln p_i. \tag{4.1}$$

Jaynes (1957) proved that the entropy is a unique way to measure the amount of uncertainty represented by this probability distribution and if many distributions are "equally possible", the one with maximum entropy is the least biased estimate possible on the given information, i.e, it is maximally noncommittal with regard to unmeasured (missing) information.

Consider a coin-tossing experiment in which the outcomes can be either "head" (H), or "tail" (T). If we perform 100 tosses for 2 coins (coins A and B) and the possibility of the outcomes are shown in table 4.1. The question is "what will be the next outcome (H or T) for coin A and B?" Instinctively, we will be more confident to predict the outcome of coin B as a head, than the outcome of coin A. This is because the knowledge about coin B is more definite or has less uncertainty. In Fig. 4.1 we plot the entropy of all possible outcomes using Eq. 4.1, from which we can see that the entropy is maximum when the probabilities for head and tail are equal, i.e. 0.5.

Table 4.1: The probabilities of the outcomes of two different coins.

Coin	H	T
A	0.48	0.52
B	0.96	0.04

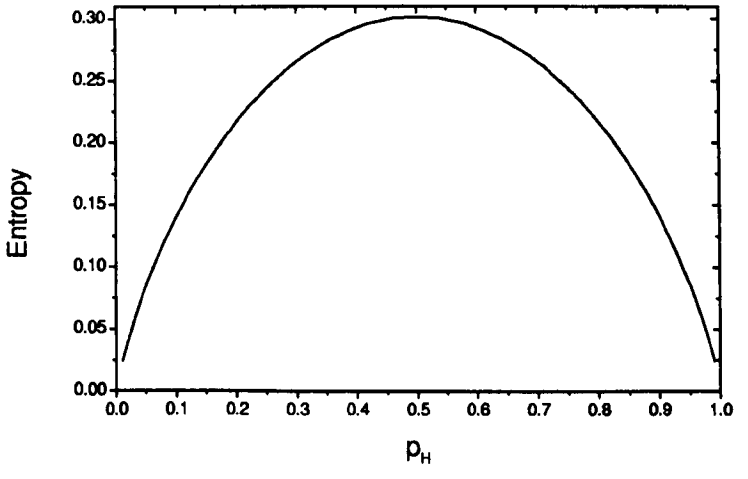

Figure 4.1: The entropy as a function of head probability (p_H).

4.3 Maximum-Entropy Mobility Spectrum (MEMS)

The strategy is to consider the mobility spectrum in a form of a probability distribution of several events. The probability is proportional to the partial conductivity s_i and each event is associated with a mobility μ_i. From the information theory viewpoint, prior to the measurement, there are no measured data and the most probable distribution is justifiably an equal distribution among all events. As we start to obtain the first few data points, they allow us to adjust the probability distribution in such a way that the modified probability distribution produces a good fit to the measured data. However, at this early stage, there are not enough data points to produce a unique probability distribution because the number of the data points is much less than the number of events. Consequently, there are many feasible probability distributions that agree well with all the data points. Rationally, one would prefer to choose the probability distribution which is maximally noncommittal with regard to unavailable (unmeasured) data. Examples of unavailable data are those between two adjacent measured data points on the magnetic field axis and data at higher magnetic fields than are available. Jaynes (1957) has shown that the most likely probability distribution among feasible distributions can be found by assigning an "entropy" to each probability distribution and choosing the one with the highest entropy. Therefore, a new approach to mobility spectrum calculations is to combine a minimization of deviation of the fit from measured data with entropy-maximization.

In analogy with the entropy defined in information theory, for the first time, one can define the entropy of the mobility spectrum as

$$H(\mathbf{s}) = -\sum_{i}^{N} p_i \ln p_i, \tag{4.2}$$

$$p_i = \frac{s_i}{\sigma_0}, \tag{4.3}$$

where $\mathbf{s}$ is a set of partial conductivities s_i, p_i is a probability of s_i, and σ_0 is the conductivity at zero magnetic field. Within this formalism, holes and electrons have nonnegative partial conductivities and their mobilities are positive and negative, re-

spectively. Assume that the resistivity and Hall coefficient are measured at M different magnetic fields, the summation of Eqs. 2.19 and 2.20 can be written in a matrix form as

$$\mathbf{K} \cdot \mathbf{s} = \sigma^{tot}, \tag{4.4}$$

$$K_{ij} = \frac{1 + \mu_i B_j}{1 + \mu_i^2 B_j^2}, \tag{4.5}$$

$$\sigma_j^{tot} = \frac{\sigma_{xx}(B_j) + \sigma_{xy}(B_j)}{\sigma_0}, \tag{4.6}$$

where $\mathbf{p}$ is a set of probabilities p_i, $i = 1 \ldots N$, and $j = 1 \ldots M$. The probabilities of mobility spectrum having maximum entropy is obtained from the method of Lagrangian multipliers [Jaynes (1957)] which gives

$$p_i = \exp\left(-\lambda_0 - \sum_{j=1}^{M} \lambda_j K_{ji}\right), \tag{4.7}$$

where λ_j is a Lagrangian multiplier. Because $\sum_{i=1}^{N} p_i = 1$, λ_0 can be represented in terms of other λ_i's as

$$\exp(\lambda_0) = \sum_{i=1}^{N} \exp\left(-\sum_{j=1}^{M} \lambda_j K_{ji}\right). \tag{4.8}$$

By substitution of Eq. 4.7 into Eq. 4.4 and using Eq. 4.8, one arrives at an implicit set of M nonlinear-equations

$$\sum_{i=1}^{N} \left\{ \left(K_{ji} - \sigma_j^{tot}\right) \exp\left(-\sum_{j=1}^{M} \lambda_j K_{ji}\right) \right\} = 0, \tag{4.9}$$

which have M unknown Lagrangian multipliers.

Agmon et al. (1979) showed that these nonlinear equations can be solved by recasting the problem of determining the Lagrangian multipliers as a variational problem. The set of Lagrangian multipliers which satisfies Eq. 4.9 can be obtained indirectly by finding a minimum of a concave function

$$F = \ln\left(\sum_{i=1}^{N} \exp\left(-\sum_{j=1}^{M} \lambda_j \left[K_{ji} - \sigma_j^{tot}\right]\right)\right). \tag{4.10}$$

Using successive approximations [Hollis et al. (1992)], the maximum-entropy mobility spectrum is achieved by iteration of Eq. 4.7 and the following equation :

$$\lambda_j^{(new)} = \lambda_j^{(old)} - \beta \left(\sigma_j^{tot} - \sum_{i=1}^{N} K_{ji} p_i \right), \tag{4.11}$$

where β is an adjusting parameter, until the set of probabilities p_i converges. The advantages of using the maximum-entropy approach are as follows.

1. The partial conductivity is guaranteed to be nonnegative according to Eqs. 4.3 and 4.7.

2. The number of mobilities can be higher than the number of magnetic fields.

3. A mobility μ_i does not necessitate a measurement at a field of $B = \mu_i^{-1}$. Consequently, no interpolation or extrapolation is required, as QMSA does, in order to extend the range of mobilities to higher values than $B_{\min}^{-1}$ or lower values than $B_{\max}^{-1}$.

In the following sections, MEMS is compared to the QMSA and i-QMSA. The comparison with Beck and Anderson analysis is unnecessary because BA analysis is a qualitative technique while MEMS is a quantitative technique.

4.4 Comparisons between QMSA and MEMS

To demonstrate the MEMS technique, a synthetic data set is generated and MEMS and QMSA analyses are performed. The synthetic data set is calculated for two carriers with $n_1 = 1 \times 10^{11}$ cm^{-2}, $\mu_1 = 2000$ cm^{2}V^{-1}s^{-1}, $n_2 = 1 \times 10^{11}$ cm^{-2}, and $\mu_2 = 6000$ cm^{2}V^{-1}s^{-1}, and with 30 magnetic fields equally spaced from 0 to 10 tesla. The mobilities in synthetic data are chosen to be high enough ($\mu_i B_{\max} > 1$) so that QMSA does not require extrapolation of the synthetic data. The number of mobility points in the spectrum is 200 which are spaced equally in log-scale for QMSA and linear-scale for MEMS. The QMSA uses a cubic spline interpolation to

obtain 200 data points while MEMS uses only the available 30 data points. The mobility range is between 10^3 and 10^4 $cm^2V^{-1}s^{-1}$ for holes, and between -10^3 to -10^4 $cm^2V^{-1}s^{-1}$ for electrons, and the iteration continues until the spectrum does not change significantly which is typically around 100,000 iterations for QMSA and 20,000 iterations for MEMS. The number of iterations is presently not a serious issue because only the number of resolved peaks from QMSA and MEMS will be compared, not the shape of the peaks (see section 6.3.3 for further details). The adjustable parameter (β) for all MEMS analyses is 0.2 which gives smooth and stable convergence.

Figure 4.2 shows the normalised mobility spectrum obtained from both techniques for synthetic data sets with different errors in resistivity and Hall coefficient. For the "no error" case, both techniques yield the same spectra consisting of two well-separated peaks, corresponding to two carrier species having mean mobilities of μ_1 and μ_2. As the errors increase, each peak in the QMSA spectrum splits into two sharp peaks while MEMS comfortably maintains its initial two peaks. Consequently, the number of carrier species obtained from MEMS will be much more accurate. For higher values of error (0.5 and 1.0 %), MEMS also starts to show an artifact around the electron mobility of -1000 $cm^2V^{-1}s^{-1}$. It should be noted that the initial peaks continue to dominate while the artifact is easily spotted as an incomplete peak.

Figure 4.3 demonstrates how the MEMS calculation evolves when the true mobility spectrum corresponds to Gaussian distributions. The ratio of the standard deviation to mean mobility of the Gaussian distributions is set to be 0.1 and the true distributions are shown as solid lines. After 300,000 iterations, which takes around 5 minutes on a computer running a 450 MHz Pentium III processor, the MEMS closely resembles the true distribution. The smoothness of MEMS is a very interesting feature that cannot be achieved by any other existing mobility spectrum techniques. The shape of MEMS should provide information about the energy dependence of the relaxation time and the wave vector dependence of the constant energy "surface" as

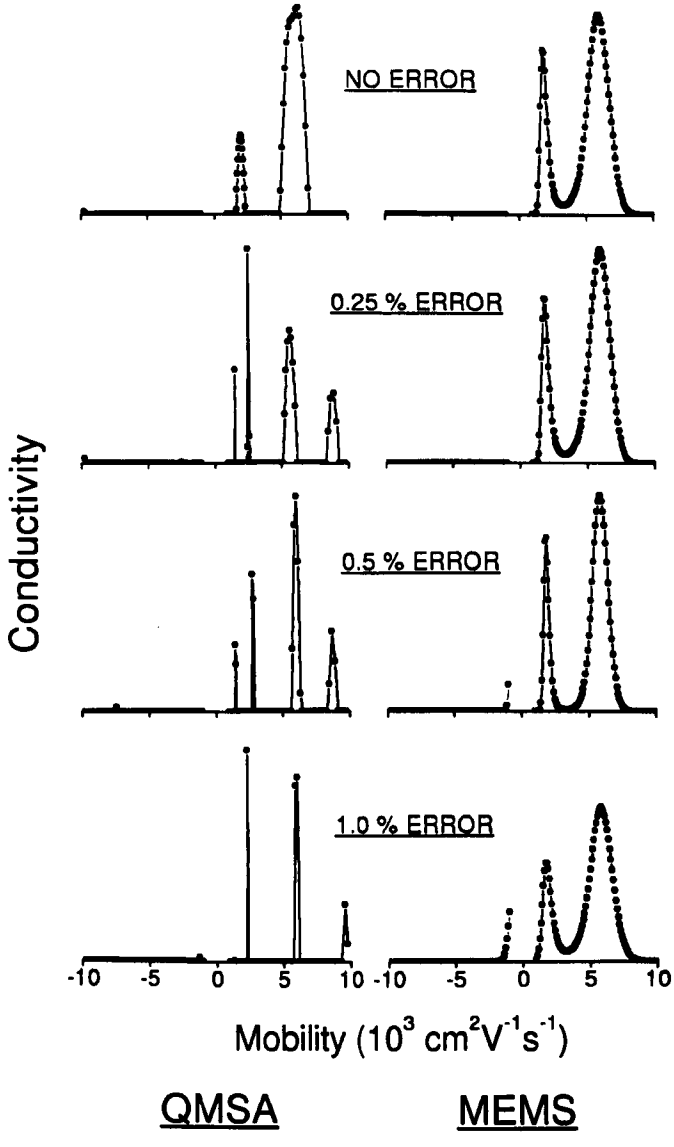

Figure 4.2: Comparisons between QMSA and MEMS spectra of synthetic data sets for two carrier species ($n_1 = 1 \times 10^{11} \mathrm{cm}^{-2}$, $\mu_1 = 2000\ \mathrm{cm}^2\mathrm{V}^{-1}\mathrm{s}^{-1}$, $n_2 = 1 \times 10^{11}\ \mathrm{cm}^{-2}$, $\mu_2 = 6000\ \mathrm{cm}^2\mathrm{V}^{-1}\mathrm{s}^{-1}$), subject to various errors in ρ_{xx} and R_H. Conductivity ranges of each spectrum are scaled differently for clearer comparisons.

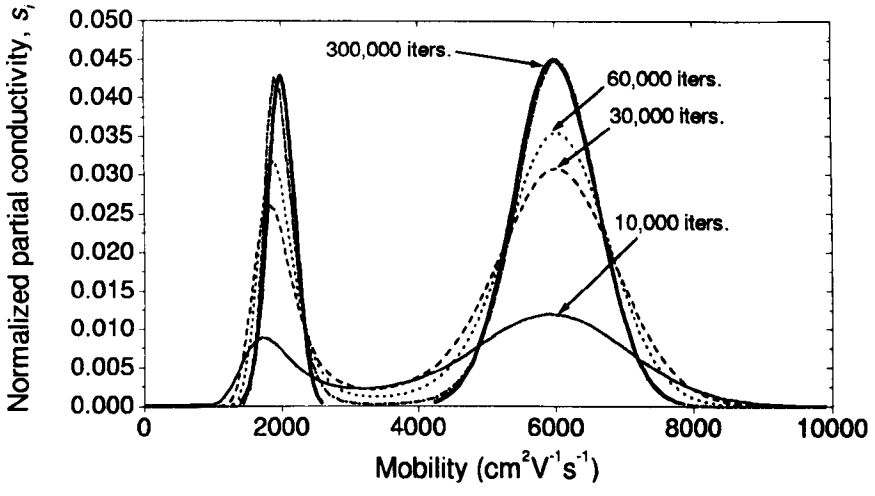

Figure 4.3: The MEMS for a synthetic data set corresponding to two carrier species : $n_1 = 1 \times 10^{11}\text{cm}^{-2}$, $\mu_1 = 2000\ \text{cm}^2\text{V}^{-1}\text{s}^{-1}$, $n_2 = 1 \times 10^{11}\ \text{cm}^{-2}$, $\mu_2 = 6000\ \text{cm}^2\text{V}^{-1}\text{s}^{-1}$. Each carrier species is assumed to have a Gaussian distribution of mobilities with a fractional standard deviation of 0.1, which is represented by the thick solid line.

first postulated by Beck and Anderson (1987).

Another attractive feature of MEMS is the ability to recover the conductivity of low-mobility carriers below the limitation set by B_{max}^{-1}, without any modifications to the main calculation and without the need for empirical procedures. To demonstrate this, the synthetic data set is generated for two carriers having $n_1 = 1 \times 10^{13}\text{cm}^{-2}$, $\mu_1 = 200\ \text{cm}^2\text{V}^{-1}\text{s}^{-1}$, $n_2 = 1 \times 10^{12}\text{cm}^{-2}$, and $\mu_2 = 1500\ \text{cm}^2\text{V}^{-1}\text{s}^{-1}$, with 0.1 % error in ρ_{xx} and R_H, and 30 magnetic field points equally spaced from 0 to 10 tesla. The MEMS is carried out for 500,000 iterations and the result is shown in Fig. 4.4. Two peaks at the mobilities μ_1 and μ_2 are clearly resolved. It should be noted that we choose mobilities which are distributed equally on logarithmic scale so that the low-mobility peak does not overlap the high-mobility peak.

To summarize, the MEMS technique can produce a mobility spectrum accurately, revealing the correct number of carrier species, and is less sensitive to experimental error. A good fit can be obtained within a reasonable calculation time and the low-mobility (μ_{low}) carrier contribution with $\mu_{low}B_{\text{max}} < 1$ can be extracted

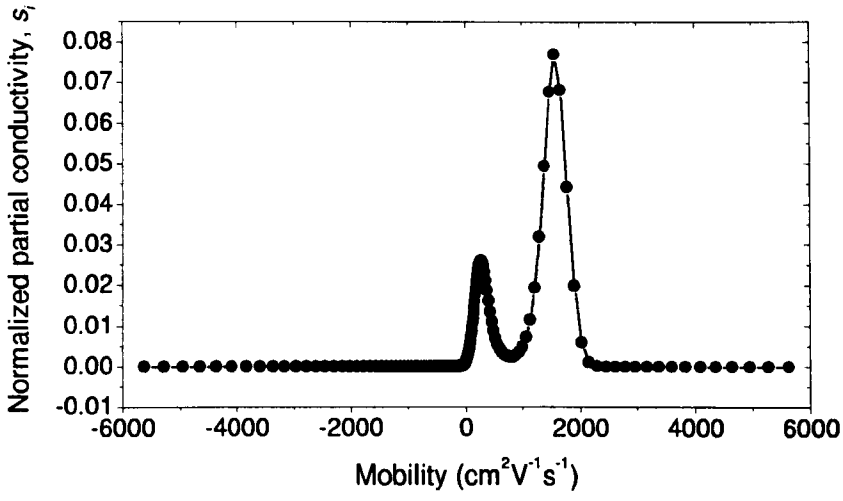

Figure 4.4: A MEMS of two carriers ($n_1 = 1 \times 10^{13}\text{cm}^{-2}$, $\mu_1 = 200$ $\text{cm}^2\text{V}^{-1}\text{s}^{-1}$, $n_2 = 1 \times 10^{11}$ cm^{-2}, $\mu_2 = 1500$ $\text{cm}^2\text{V}^{-1}\text{s}^{-1}$) subject to 0.1% error in ρ_{xx} and R_H.

successfully, provided the higher-mobility (μ_{high}) carrier has $\mu_{high}B_{max} \geq 1.5$.

4.5 Comparisons between i-QMSA and MEMS

In this section, we will compare the mobility spectra which are obtained from i-QMSA and MEMS techniques. The i-QMSA analysis was performed by using the computer programme developed at Lakeshore Cryogenic Ltd, the detail of which can be found in Vurgaftman et al. (1998).

The first comparison is to consider the i-QMSA spectrum for the synthetic data that was previously used to produce MEMS in Fig. 4.2. The i-QMSA for "no-error" and "0.5%-error" cases are shown in Fig. 4.5. For the "no-error" case, i-QMSA yields the same result as MEMS but MEMS is slightly smoother. For "0.5%-error", i-QMSA still maintains its two original peaks quite well but with the appearance of one unknown electron peak at the mobility around 15,000 $\text{cm}^2\text{V}^{-1}\text{s}^{-1}$, which can be mistaken as the third carrier. This again emphasizes the benefit of using MEMS that it is less likely to give a wrong number of peaks (the number of carriers). We have also

noticed that both i-QMSA and MEMS for "0.5%-error" generate the same artefact peak near the electron mobility of 1,000 $cm^2V^{-1}s^{-1}$. In MEMS, when this happens, it informs us that there might be a real peak outside the mobility range considered. If this peak remains stationary when the mobility range is increased, it is then the real peak, otherwise just an artefact.

Two more comparisons were made on the the room-temperature experimental data from bulk GaN and a p-type High Electron Mobility Transistor (p-HEMT) GaAs/AlGaAs heterostructure provided by Lakeshore Cryogenic Ltd as the test data. For the GaN sample, we found that i-QMSA and MEMS yield quite similar peaks but with the exception that MEMS is much smoother (see Fig. 4.6). Moreover, MEMS for hole and electron join smoothly at zero mobility, the feature that cannot be achieved by any other existing mobility spectrum calculation techniques.

For p-HEMT sample, we expect to see two peaks which correspond to the high-mobility 2DEG and the low-mobility supply layer. However, because the product μB_{max} for this sample is very low (0.5), MEMS can only reveal one broad asymmetric peak (see Fig. 4.7). This means that MEMS cannot separate them due to having insufficient data ($\mu B < 1$). It has been observed by the author in numerous cases, without showing them here, that MEMS peak is symmetric, we then can try to extract those two overlapped peaks by fitting 2-Gaussian peaks to the unsymmetrical MEMS peak, which yields the mobilites at the peak of 4,500 and 700 $cm^2V^{-1}s^{-1}$. These mobilites are quite close to those obtained from the i-QMSA spectrum, which are 4,000 and 550 $cm^2V^{-1}s^{-1}$.

4.6 Conclusion

A new approach to the mobility spectrum technique, based on maximum entropy, has been developed. In contrast to all other existing methods of calculation, this new technique does not require any supporting procedures or "unity condition" to

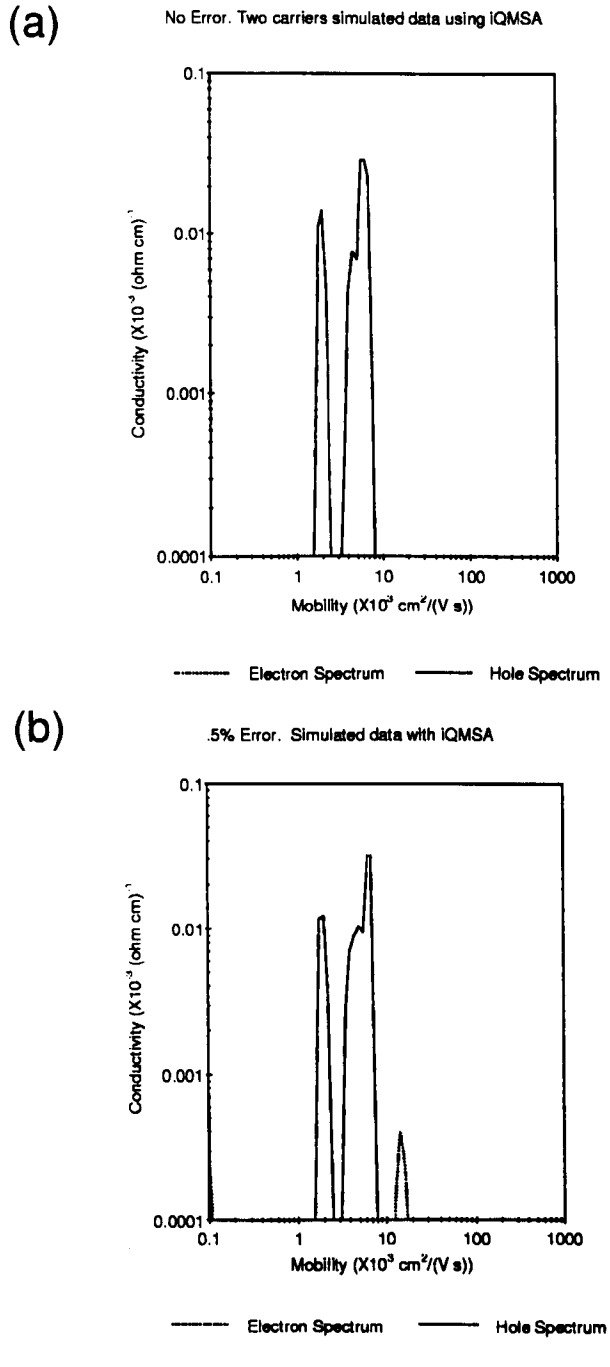

Figure 4.5: i-QMSA mobility spectrum of synthetic data sets for two carrier species ($n_1 = 1\times10^{11}\text{cm}^{-2}$, $\mu_1 = 2000\,\text{cm}^2\text{V}^{-1}\text{s}^{-1}$, $n_2 = 1\times10^{11}\ \text{cm}^{-2}$, $\mu_2 = 6000\,\text{cm}^2\text{V}^{-1}\text{s}^{-1}$), subject to (a) 0% and (b) 0.5% errors in ρ_{xx} and R_H.

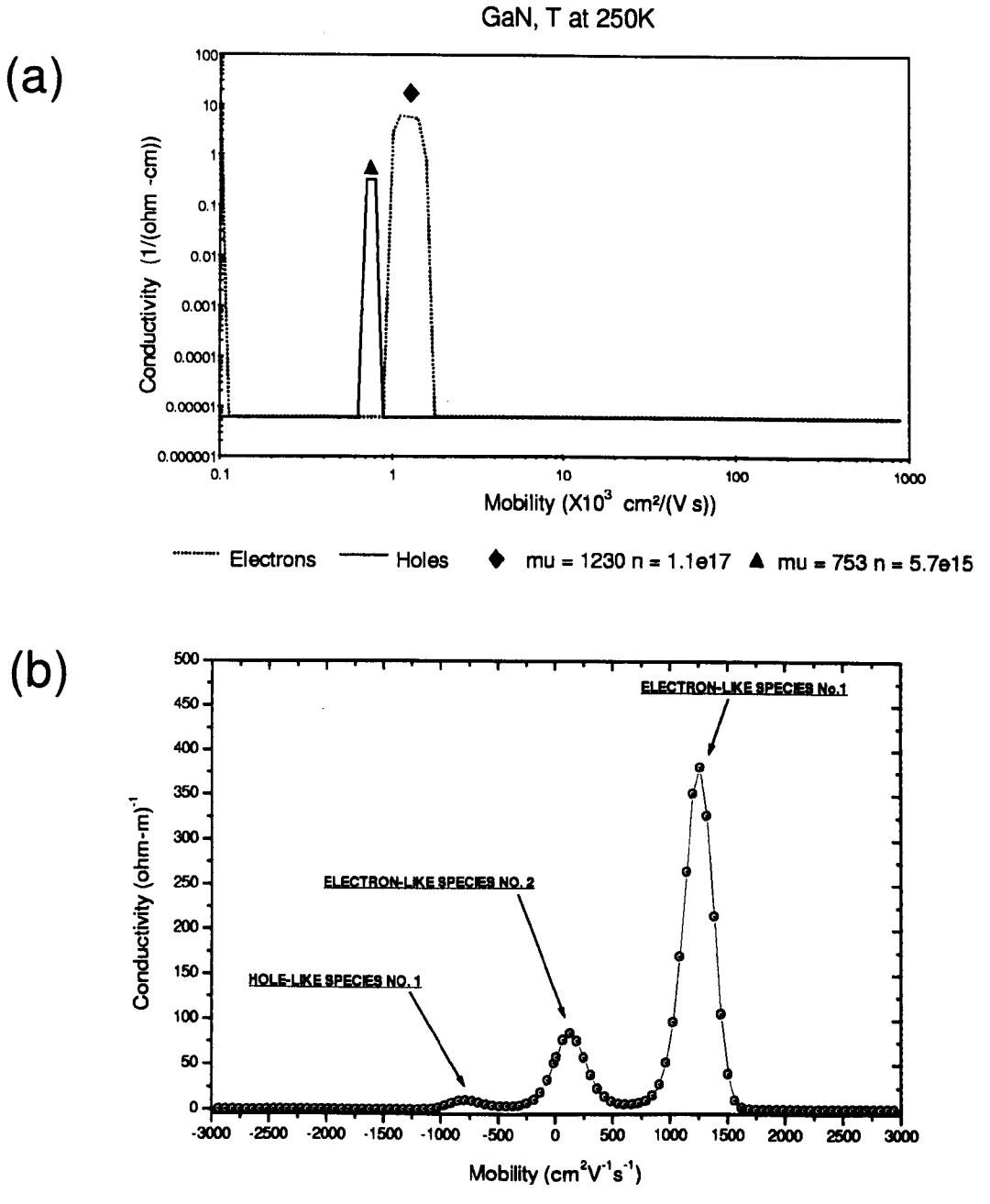

Figure 4.6: (a) i-QMSA and (b) MEMS mobility spectra of bulk GaN at 250 K, with $\mu B_{max} = 2$.

(a)

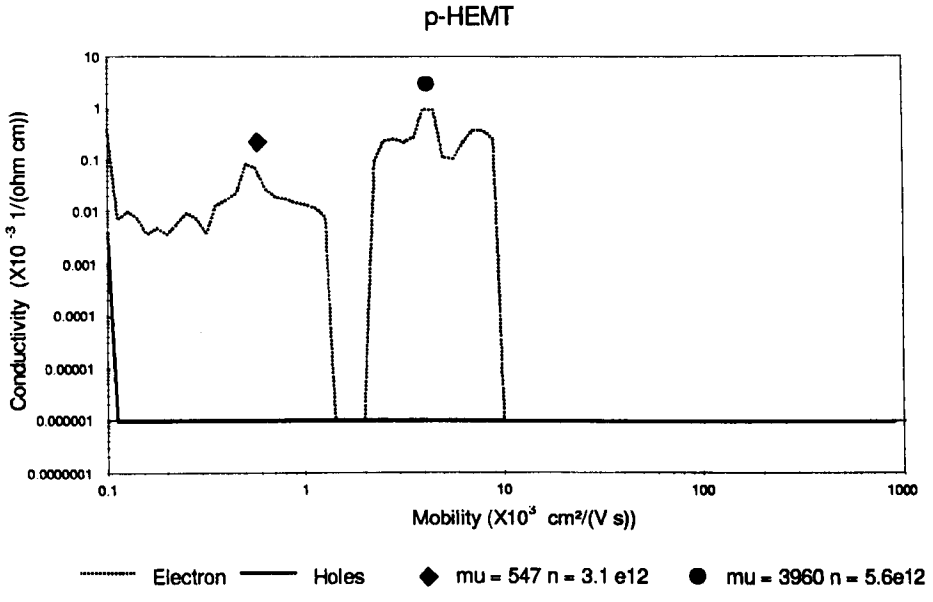

(b)

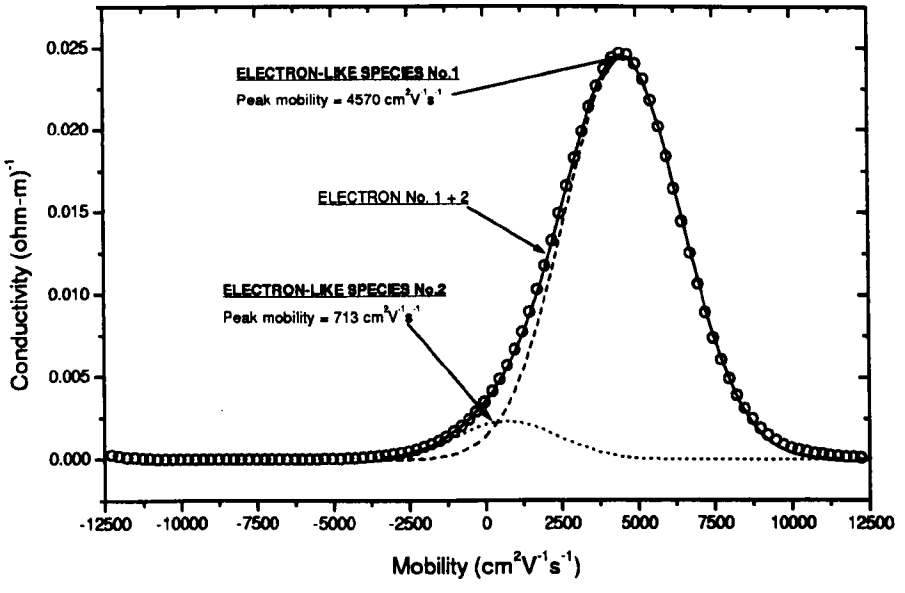

Figure 4.7: (a) i-QMSA and (b) MEMS mobility spectra of p-HEMT with μB of 0.5.

be satisfied. The number of data points on the magnetic field axis can be much less than the number of mobility points. The low-mobility carrier species can also be determined successfully provided a higher-mobility (μ_{high}) carrier has $\mu_{high}B_{\max} \geq 1.5$. It is demonstrated that the present procedure yields useful results when the maximum measurement-error in resistivity and Hall coefficient is less than 0.25%, which is attainable in most laboratories. Table 4.2 summarises the advantages and disadvantages of each mobility spectrum calculation technique. Because the resultant mobility spectrum is extremely smooth, we expect that this new technique will serve as a suitable tool for the study of energy-dependent relaxation times and band structures as predicted by Beck and Anderson (1987). The comparison between MEMS and i-QMSA are made for both synthetic and experimental data and both techniques are found to yield similar results. However, as MEMS uses less data points than i-QMSA and without interpolation of experimental data, we can conclude that MEMS outperforms i-QMSA in this manner.

Table 4.2: The summary of advantages and disadvantages of each mobility spectrum calculation technique.

METHOD	ADVANTAGES	DISADVANTAGES
Beck and Anderson Analysis (MSA)	• high sensitivity to low-mobility carrier. • require a few data points, typically between 2-6.	• No unique spectrum if there are high number of data points, from which 2-6 data points are to be chosen. • The spectrum is an envelop, an upper bound of all possible spectra.
Iterative technique and Quantitative Mobility Spectrum Analysis (QMSA)	• produces a unique spectrum which is not an envelop. • use all available data points.	• interpolation/extrapolation of data points are required. • low sensitivity to low-mobility carrier. • negative conductivity could occur. • mirror/ghost peak effect. • peak breaking due to experimental errors.
improved - Quantitative Mobility Spectrum Analysis (i-QMSA)	• improves the fit over QMSA method.	• empirical manipulation procedures are likely to be case-specific and difficult to implement. • peak breaking due to experimental errors.
Maximum-Entropy Mobility Spectrum Analysis (MEMS)	• no inter/extrapolation is required. • gives smoother spectrum. • less sensitivity to experimental error, higher sensitivity to low-mobility carrier. • conductivity is always positive. • no empirical manipulation procedure. • produces a unique spectrum which is not an envelop. • use all available data points.	• the fit to the function $\sigma_{xx} + \sigma_{xx}$ is always good but the fits to σ_{xx} and σ_{xx} individually are sometimes poor. Further investigation is needed.

Chapter 5

Experimental Methods

5.1 Introduction

This chapter contains information about the experiments that were carried out during the present Ph.D. course at The University of Warwick. The general principles of MBE are given first in Section 5.2 which includes a discussion of how the strained SiGe and boron-doped Si samples were grown (Sections 5.2.1 and 5.2.2). The device fabrication procedures for the van der Pauw and Hall bar are then given in Section 5.3, followed by the details of the cryostats in Section 5.4, and how the resistivity and Hall coefficent are measured and calculated in Section 5.5.

5.2 Molecular Beam Epitaxy (MBE)

The MBE machine used to grow the pseudomorphic SiGe structures is a commercial Vacuum Generator V90S machine shown schematically in Fig. 5.1. It consists of two main chambers which are connected via an isolation valve. Clean silicon substrates are loaded into the first preparation chamber via the fast entry load-lock (FEL) and stored there at a pressure of 10^{-9}-10^{-10} mbar. The FEL avoids the entire system being vented each time the new set of substrates is loaded. For the growth, the substrate

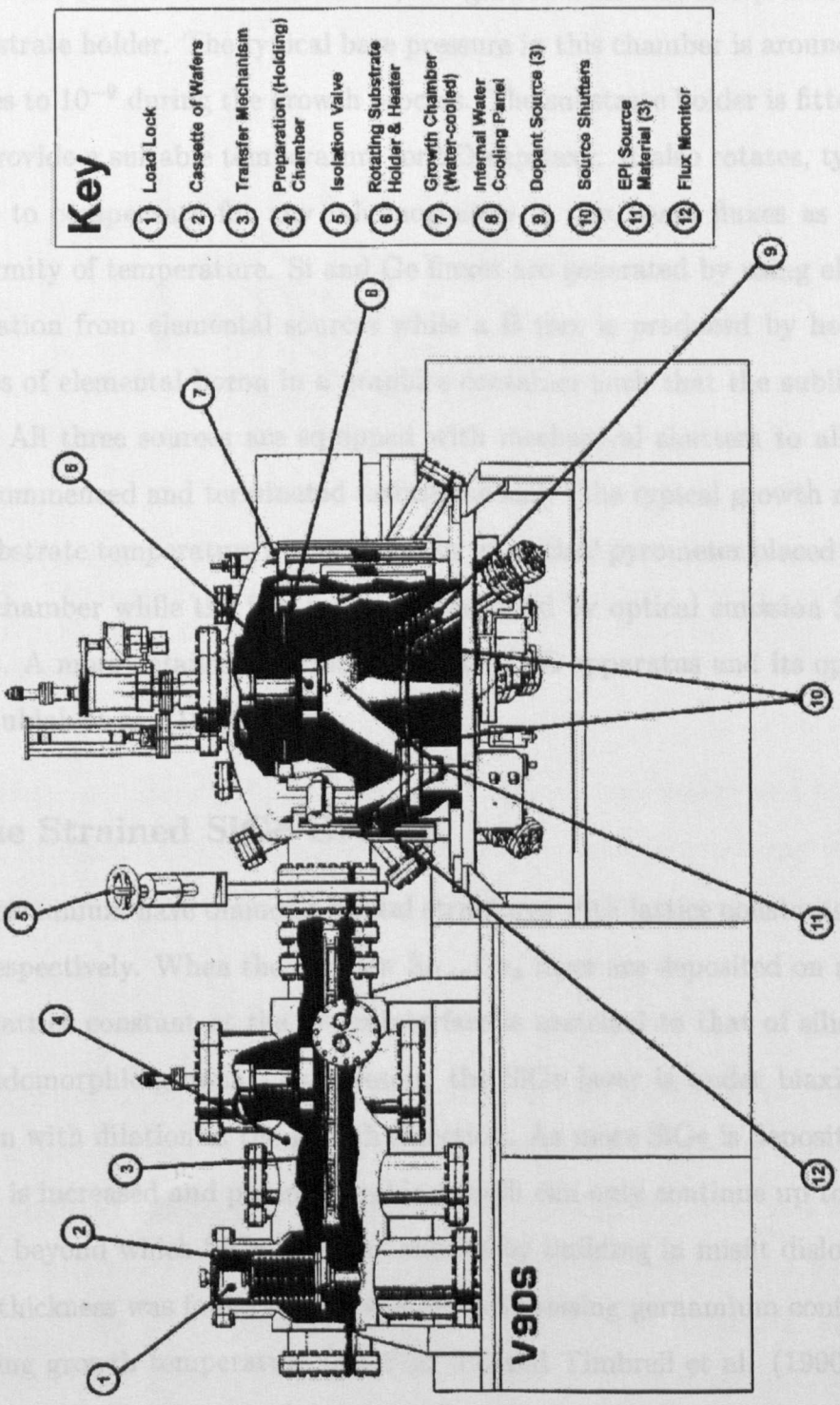

Figure 5.1: The schematic picture of the V90S solid source molecular beam epitaxy system used at The University of Warwick.

is then transferred into the second chamber, the growth chamber, and placed on the rotatable substrate holder. The typical base pressure in this chamber is around 10^{-11} mbar and rises to 10^{-9} during the growth process. The substrate holder is fitted with a heater to provide a suitable temperature for 2D expitaxy. It also rotates, typically at 60 r.p.m., to compensate for any inhomogeniety in the beam fluxes as well as the nonuniformity of temperature. Si and Ge fluxes are generated by using electron-beam evaporation from elemental sources while a B flux is produced by heating a small granules of elemental boron in a graphite container such that the sublimation of B occurs. All three sources are equipped with mechanical shutters to allow the fluxes to be commenced and terminated instantaneously (the typical growth rate is 1 Å/s). The substrate temperature is monitored by an optical pyrometer placed outside the vacuum chamber while the flux rates are measured by optical emission Sentinel flux monitors. A more detailed description of this MBE apparatus and its operation is given by Kubiak et al. (1988).

5.2.1 The Strained SiGe Growth

Silicon and germanium have diamond crystal structures with lattice constants of 5.43 and 5.66 Å respectively. When the first few $Si_{1-x}Ge_x$ layer are deposited on a silicon surface, the lattice constant at the heterointerface is matched to that of silicon - so called a pseudomorphic growth. As a result, the SiGe layer is under biaxial compressive strain with dilation in the growth direction. As more SiGe is deposited, this strain energy is increased and pseudomorphic growth can only continue up to a critical thickness, beyond which SiGe becomes relaxed by building in misfit dislocations. This critical thickness was found to increase with decreasing gernamium content and with decreasing growth temperature (see Fig. 5.2 and Timbrell et al. (1990)). The low temperature also causes a reduction in the adatom mobility on the substrate surface which prevents the formation of 3D islands (see Fig. 5.3), the minimum surface energy configuration [Snyder et al. (1992)]. However, it should not be too low

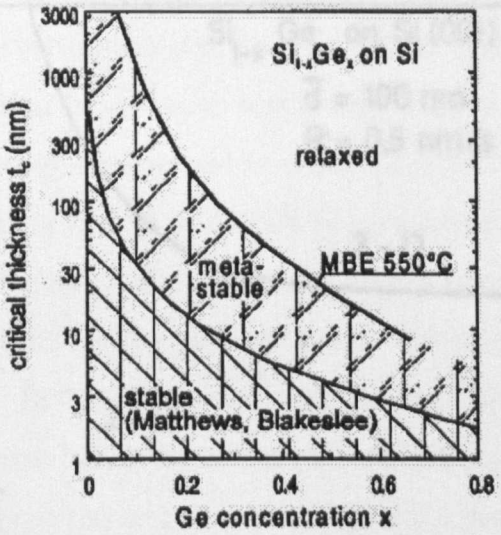

Figure 5.2: The critical thickness for strain relaxation plotted against composition for $Si_{1-x}Ge_x$ on Si. The lowest curve is the theoretical calculation for themal equilibrium whereas the experimental curve for layers grown at 550°C by MBE is shown as an upper curve (after Schaffler F. (1997)).

as vacancy defects will start to form, resulting in poor crystal quality and hence low charge carrier mobility. In Si, the minimum growth temperature was found to be 450 $°C$, below which a defect density of 10^{18} cm^{-3} occurs [Gossman et al. (1992)].

5.2.2 Boron-doped Silicon Growth

The incorporation of boron into Si MBE was studied intensively by Parry (1991) who found that all boron atoms are electrically active even at low growth temperature. One problem observed was the segregation of boron atoms up to the surface when the growth temperature was higher than 600 °C and the boron concentration was higher than 10^{19} cm^{-3}. This is a serious problem especially for the "inverted" structure, where the boron-doped layer is grown before the SiGe alloy, because the segregation decreases the spacer and contaminates the SiGe quantum well.

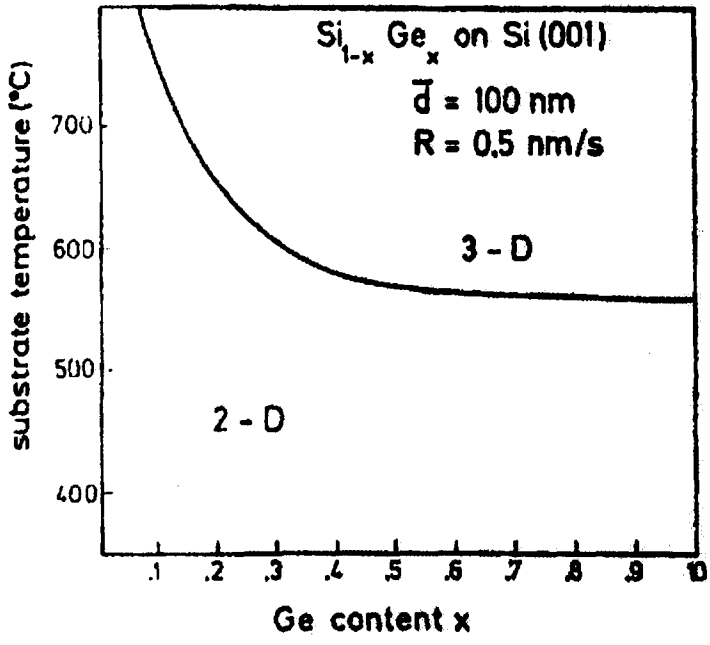

Figure 5.3: Temperature dependence of the 2D and 3D growth mode, predicted by Bean et al. (1984).

5.3 Device Fabrication

5.3.1 Van der Pauw Device

The standard technique for measuring the resistivity and Hall mobility of arbitary laminar shape was proposed by Van der Pauw (1958). In order to use this technique, the following requirements must be applied:

1. The contacts must be on the circumference of the sample and be sufficiently small.

2. The sample is homogeneous in thickness.

3. The sample does not have isolated holes inside.

The recommended shape was a "clover- leaf" shape where the contact influences are minimal. The Greek-cross shape was used in the present work because it was much

simpler to make and the error in measurement of ρ_{xx} and ρ_{xy} was small ($< 0.5\%$) for a sample width less than half of the length [Versnel (1979)]. From the starting wafer, the sample is cleaved by diamond scribe into a small square (1.5×1.5 cm^2) along [100] direction. Nitrogen gas is used to remove any small particles on both sides of the sample before loading into an ION TECH Microvac 350 magnetron sputterer, where several aluminium (1%Si) discs 1mm in diameter and $\sim 1\mu$m in thickness are deposited onto the sample via a shadow mask. The sample is then annealed at temperatures 450–550 °C for 30–45 minutes under flowing Nitrogen gas, depending on the depth of the 2D channel below the surface, to achieve ohmic contacts. Black wax is subsequently painted onto the surface in the shape of a cross having an aluminium contact at each end. After drying, the sample is etched for 10–12sec in a Si etchant, a mixture of (70%)HNO_3, CH_3 COOH and (50%) HF in the volume ratio 75:17:8. The etch depth is $\sim 1\mu$m which is enough for the structure whose epilayer thickness is only 0.3–0.4 μm. Finally, the wax is dissolved away using xylene and the sample is rinsed thoroughly in deionised water.

5.3.2 Hall Bar Device

The Hall bar is more favourable than a van der Pauw device for the magnetic-field-dependence measurements because its geometry is much simpler to analyse and the latter requires the calculation of the f factor. The geometry of Hall bar should be designed in such a way that current flow is uniform within the measuring region and there is minimal current passing through the Hall contacts. The design is in accordance with the published ASTM standard (1976).

The fabrication procedure is quite similar to that for the van der Pauw device, except that the black wax is replaced by a standard photolithography procedure. This requires well designed masks and a mask aligner. Two masks were designed by using EasyCAD for Windows^{TM} as shown in Fig. 5.4. The pictures are printed on high quality A4 papers and photographed onto high resolution Kodalith Ortho 6556 black

and white film with the reduction ratio of 10:1.

The Hall bar fabrication starts by sputtering aluminium all over the sample surface. The sample is then hard baked under atmospheric air at 120–130 °C for 30 minutes to ensure that the surface is completely dry. Then, a thin film of Microposit^{TM} S1815 photoresist is deposited on the top of the sample and soft baked under atmospheric air at 90-100 °C for 30 minutes. Next, the mesa pattern is transferred onto the photoresist by means of ultra-violet exposure for 50 seconds. The pattern is developed by using Microposit MF-319 developer which removes the UV-exposed photoresist. This is followed by dipping the sample in aluminium etchant (H_2PO_4+HNO_3+H_2O), rinsing in deionized water, dipping in the silicon etchant (HF+CH_3COOH+H_2O), and rinsing again in deionized water. It was observed that the photoresist can sometimes come off the surface during the silicon etch. If this has happened and aluminium has not been sputtered onto the surface before, this would have led to damages to the surface and loss of the sample. The remaining photoresist is removed by Microposit Remover 1165. The whole process of photolithography, starting from the hard baking, is then repeated for the contact definition mask. Once the mask is developed, the sample is dipped in aluminium etchant to remove the unwanted aluminium, leaving aluminium contacts. Finally, the sample is cut into the individual Hall bar devices and it is annealed to yield ohmic contacts. The device is glued onto a chip carrier and sample contacts are connected to the gold pads of the chip carrier by gold wires. Typical Hall bars are 1.7 mm in channel length and 0.5 mm in width, with a 4.4 mm separation between current-source probes.

5.4 Cryostat Equipment and Operations

5.4.1 Close-cycled Cryostat System (10-300 K)

The schematic picture of the Air Products close-cycled cryostat is shown in Fig. 5.5. After the sample mounting, the pressure is reduced to 10^{-5} Torr to provide a

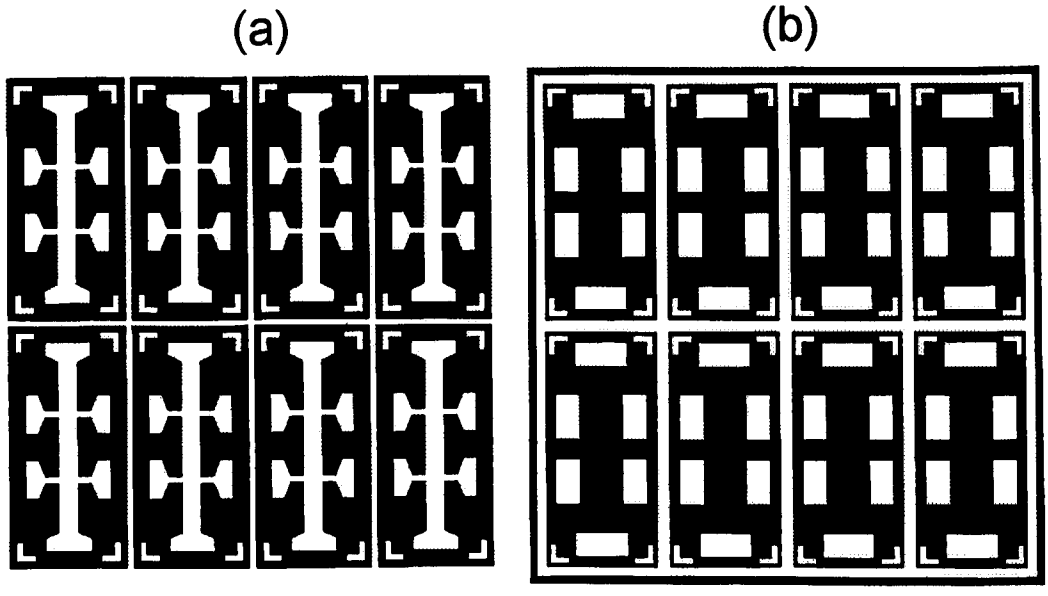

Figure 5.4: The negative printout of masks for (a) mesa patterning and (b) for contact definition.

good thermal shield. The temperature of the sample is reduced by means of the Helium compressor to a base temperature of 10 K before starting the resistivity and Hall measurement. High pressure helium, supplied by the compressor at $\sim$ 310 psi, entered the expander module where it was cooled to the refrigeration temperature. The work done by the high pressure gas expansion, as it left the expander matrix as the much lower pressure of $\sim$ 85psi, caused the gas temperature to drop and provided refrigeration. The refrigeration cycle was repeated sixty times per minute causing rapid cooling of the copper expander assembly.

To increase the temperature, a metal film heater is used and the temperature can be monitored via a Chromel/Gold thermo-couple. The temperature was maintained stable within 1 K at all temperatures between 10 K and 300 K by an Air Products Ltd. temperature controller.

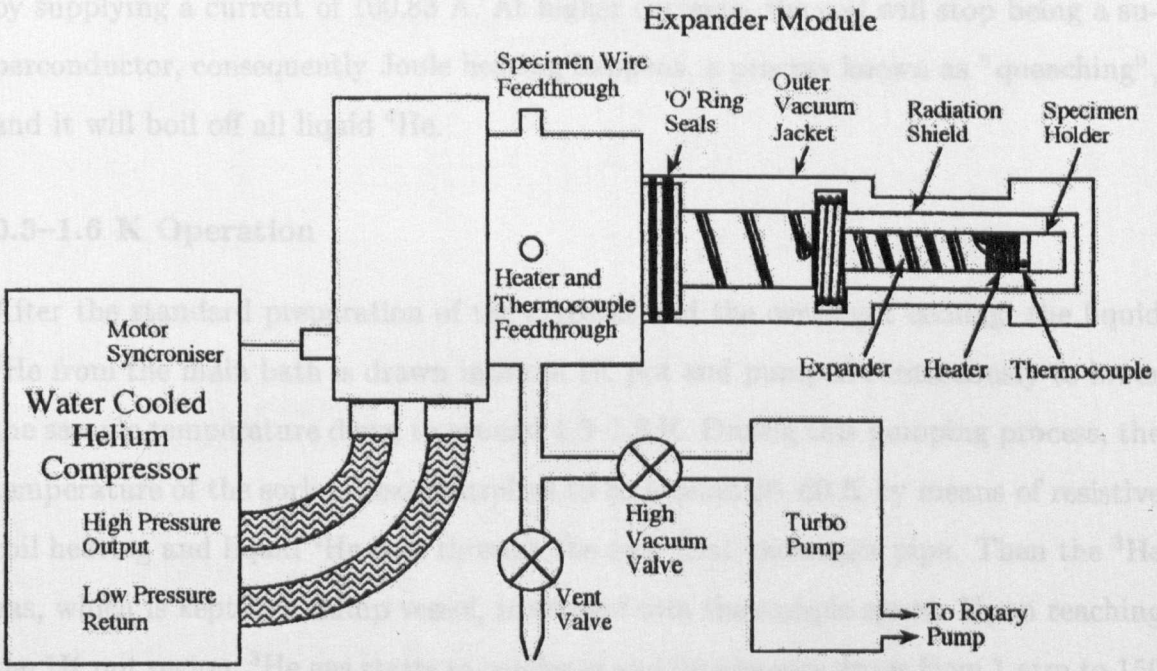

Figure 5.5: The schematic diagram of close-cycled cryostat for resistivity and low-field Hall measurement at temperatures between 9 and 300 K (after McGregor (1997)).

5.4.2 Superconducting Electromagnet System (0.35-300 K)

Measurements of the magnetic-field-dependence of resistivity and Hall coefficient were carried out in an Oxford Instruments ^{3}He cryomagnetic system with a base temperature of 0.3 K. Magnetic fields up to 12 T were generated by a superconducting solenoid submerged in liquid ^{4}He. The schematic cross-section diagram of the central part of this cryostat is shown in Fig. 5.6. The magnetic field is generated by passing a d.c. current through the superconducting coil which can be swept continuously to 12 T by supplying a current of 100.83 A. At higher currents, the coil will stop being a superconductor, consequently Joule heating happens, a process known as "quenching", and it will boil off all liquid ^{4}He.

0.3–1.6 K Operation

After the standard preparation of the cryostat and the overnight cooling, the liquid ^{4}He from the main bath is drawn into the 1K pot and pumped continuously to lower the sample temperature down to around 1.3–1.6 K. During this pumping process, the temperature of the sorb is also controlled to be around 50–60 K by means of resistive coil heating and liquid ^{4}He flow through the sorb heat exchanger pipe. Then the ^{3}He gas, which is kept in a dump vessel, is allowed into the sample space. Upon reaching the 1K pot region, ^{3}He gas starts to condense and its pressure drops from 1 atm to 150 mbar. Then, the sorb temperature is gradually decreased manually. The sorb contains a charcoal which acts as a pump when it is cooled down below $\sim$ 35 K. As the sorb temperature decreases below this temperature, the sorb starts to pump the liquid ^{3}He and this process lowers the temperature of the sample, which is now submerged under this liquid, to the lowest temperature of $\sim$ 0.3 K. The higher temperatures can be achieved by increasing the sorb temperature which causes less pumping of liquid ^{3}He. The sample temperature was read from a doped Ge resistance thermometer (Lake Shore Cryotronics), calibrated in the range 0.3-6K, when in a stable condition and in the absence of a magnetic field. In Shubnikov-de Haas experiments temperature

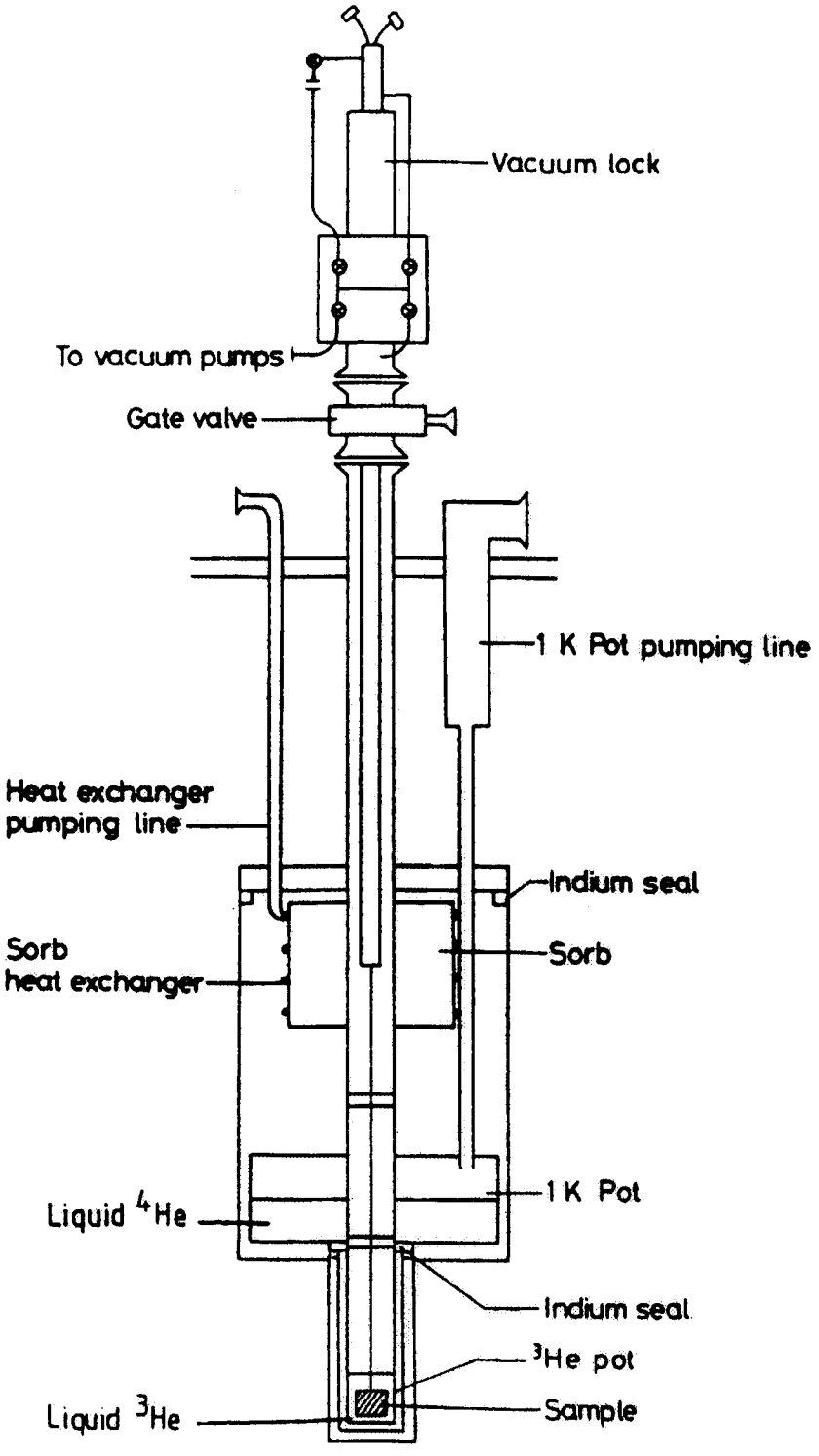

Figure 5.6: Central part of ^{3}He cryomagnetic system (12T).

measurements were taken at the start and finish of the run to check the stability and were averaged.

10–300 K Operation

This cryostat was originally designed for the low-temperature (0.3-1.6K) measurement which has a very poor heat sink due to the use of a fiber glass insert for the sample holder. This means that only the gas inside the sample space will act as a heat transfer medium which is by far less stable than a standard metal medium. To achieve the high temperature measurement with sufficient temperature stability, the following work-around solutions were developed without modifying the cryostat. A heater wire and a Lakeshore capacitance sensor (CS-500) were installed onto the sample holder. This sensor has a very low magnetic-field dependence and high sensitivity especially at 77–300 K. The Lakeshore temperature controller (CA-91CA) was used in conjunction with this sensor. To achieve a stable temperature below 30 K, the 1K pot was pumped with an only slightly opened pumping-valve together with the use of the sample heater. Temperature control is more difficult than that at higher temperature because the sensitivity of the capacitance sensor is comparatively lower. To obtain stable temperatures higher than 30 K but less than 150 K, only the sample heater is used. For higher temperatures, the sorb temperature is controlled to be around 50–60 K so that the accumulating heat at the top of the insert can be drawn out effectively. The temperature is measured using a silicon diode thermometer (Institute of Cryogenic, Southamton University) calibrated in the range 1.5–300 K with an uncertainty of $\pm$30mK. The optimum operation was achieved with the temperature stability of $\pm$0.5K for at least 1 hour at all temperatures (10–300 K).

5.5 Resistivity and Hall Measurements

5.5.1 Van der Pauw Device

The main component is a lock-in amplifier (EG&G Instruments, Model 5209 and 5210) which acts both as an a.c. voltage source and phase sensitive voltage detector. A signal frequency of 7 Hz was used to avoid the main power supply frequency of 50 Hz. The current to the sample was limited by a series resistor of 10 MΩ and the typical current supplied is 0.5 μA. The higher supply current could heat up the sample while the lower one will reduce the Hall voltage , for a given magnetic field of 0.41 T, to below the measurable level of the lock-in amplifier. The current is deduced from the voltage developed across high precision series resistor of 10kΩ. The schematic arrangements of electrical wires for the resistivity and Hall measurements are shown in Fig. 5.7. The resistivity can be measured in different 8 configurations, 4 for each magnetic field polarity. The resistivity can be calculated from :

$$\rho = \frac{\pi d}{\ln 2} \cdot \frac{\overline{V_\rho}}{I} \cdot f, \tag{5.1}$$

where $\overline{V_\rho}$ is an average voltage, I is the current, and d is the thickness of the measured sample. d is usually unknown but conventionally set to unity and the resistivity is therefore the "sheet resistivity". The correction factor f is geometry-dependent which is found to be close to unity due to the symmetry in the Greek cross sample.

Low-field Hall measurements were performed by using a 0.41 T permanent magnet. The Hall voltage were measured in 4 different configurations; 2 configurations for each magnetic field polarity. The Hall coefficient can then be calculated from :

$$R_H = \frac{\overline{V_H} d}{BI}, \tag{5.2}$$

where $\overline{V_H}$ is an average Hall voltage and B is the magnetic field. The thickness d is unknown and set to unity in the case of the modulation-doped samples. From Eqs. 5.1 and 5.2 the carrier density (n_s) and Hall mobility (μ_H) can be obtained from :

$$n_s = (eR_H)^{-1} \times 10^{-4}\text{cm}^{-2}, \tag{5.3}$$

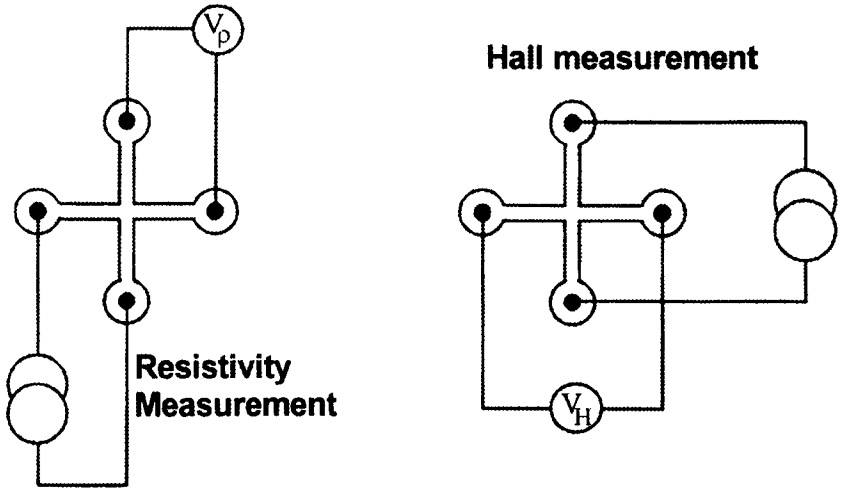

Figure 5.7: Electrical wire arrangement for the van der Pauw device (after Van der Pauw (1958)).

$$\mu_H = \frac{R_H \times 10^4}{\rho} \mathrm{cm^2 V^{-1} s^{-1}} \tag{5.4}$$

5.5.2 Hall Bar Device

Three lock-in amplifiers were used to measure the resistivity, Hall, and current voltage simultaneously while the magnetic field is continuously swept. The schematic diagram of the apparatuses is shown in Fig. 5.8. The signal from a lock-in amplifier is used as a reference signal for another two lock-in amplifiers and also as the current supply to the sample. The current limited series resistance can be changed to provide the supply current between 20–100 nA. 20 nA is used for the Shubnikov de-Haas measurement to ensure that it does not heat up the sample. The resistivity as a function of magnetic field can be calculated as

$$\rho(B) = \frac{V_\rho(B)}{I} \cdot \frac{w}{l} \tag{5.5}$$

where w/l is the width to length ratio. The Hall coefficient is calculated according to Eq. 5.2. Because the magnetic field is changed continuously and the lock-in amplifier has a time delay, hysteresis will occur which can be removed by averaging the up and

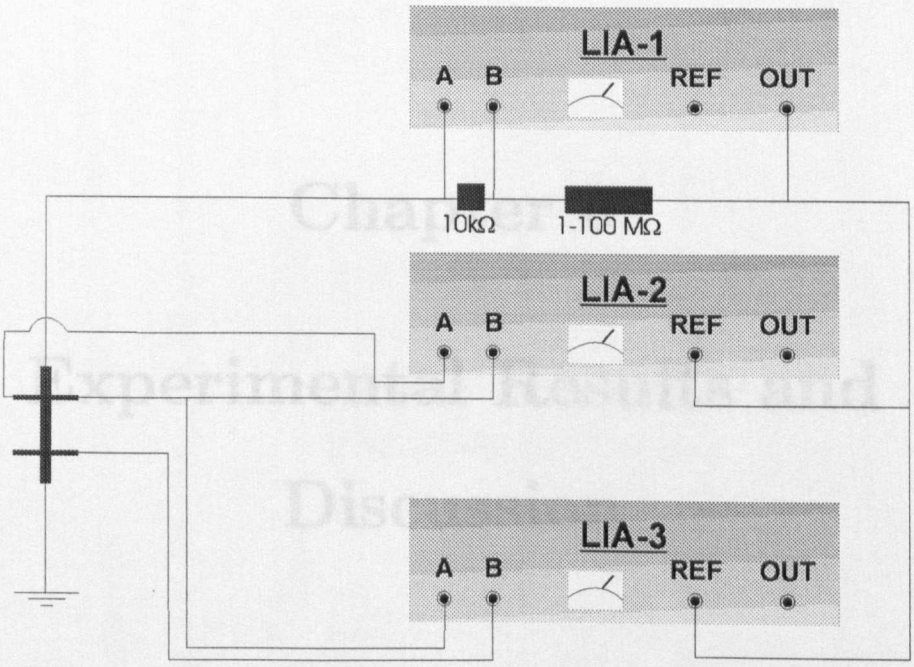

Figure 5.8: The electrical apparatus arrangement for the Hall bar device measurement.

down-sweeping signal.

Chapter 6

Experimental Results and Discussion

6.1 Introduction

In this chapter, measurements of the magnetic-field-dependent sheet resistivity and Hall coefficient, in the temperature range 0.3–300 K and in the magnetic field range 0–12 T, are reported. The materials for the measurements are modulation-doped p-type $Si_{1-x}Ge_x$/Si heterostructures with $0.10 \leq x \leq 0.65$. The schematic diagram of the modulation-doped p-type $Si_{0.9}Ge_{0.1}$/Si heterostructure (or $Si_{0.9}Ge_{0.1}$/Si sample for short) is illustrated in Fig. 6.1 as an example. In this structure, the SiGe alloy is sandwiched between pure Si which produces the quantum well confinement. The hole carriers transfer from the boron-doped silicon (Si:B) cap layer to this quantum well and are confined within the vicinity near the top Si/SiGe interface. The carriers are constrained to transport approximately along the plane parallel to the interface, the so-called "two-dimensional hole gas (2DHG)". For all samples, their electrical and nominal structural parameters are summarised in table 6.1. These samples were selected with different objectives which are explained as follows.

1. Samples 33.26 and 31.17 were chosen because their Hall mobilities at 0.3 K

Table 6.1: Electrical and nominal structural parameters of the modulation-doped $Si_{1-x}Ge_x/Si$ heterostructures discussed in this thesis.

Sample No.	0.3K μ ($cm^2V^{-1}s^{-1}$)	n_{SdH} ($\times 10^{11}$ cm^{-2})	Boron-Doping ($\times 10^{18}$ cm^{-3})	Cap thickness (nm)	Spacer (nm)	QW thickness (nm)	x
33.26	7385	1.57	2.5	70	20	25	0.10
31.17	11,920	2.11	2.5	50	20	30	0.13
54.49	2888	6.64	2.0	25	7	15	0.20
55.41	2217	6.46	2.0	20	25	8	0.36 (a)
59.22	2329	4.42	2.0	50	25	10	0.36 (b)
59.53	1737	10.40	2.0	50	15	7	0.45
60.46	N/A	N/A	2.0	10	5	4	0.65 †
50.36	—	—	2.0	25	—	—	0.00

† on $Si_{0.65}Ge_{0.35}$ virtual substrate and after annealing.

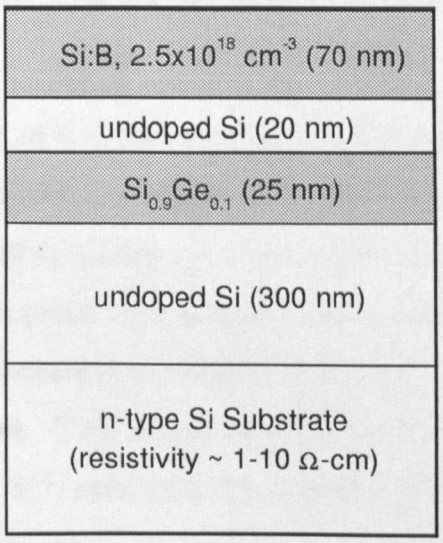

Figure 6.1: Cross-sectional schematic view of the modulation-doped p-$Si_{0.9}Ge_{0.1}$/Si heterostructure.

are very high. This will help enhance the 2DHG mobility spectrum peak and separation between Si:B and 2DHG peak.

2. Sample 54.49 was chosen mainly for the validation of Hall factor calculation proposed in section 2.5.2. The validation was made possible because the Hall factor of $Si_{0.8}Ge_{0.2}$/Si was previously measured in the temperature range 10–300 K by Hall and Strip technique [McGregor et al. (1999)] and by a combination between the Capacitance-Voltage and Hall measurements [Lander et al. (1997)]. However, we expect to obtain the Hall factor only at temperatures up to 100 K because the mobility at higher temperature is less than 1,000 $cm^2V^{-1}s^{-1}$, the minimum resolvable mobility spectrum peak for the maximum magnetic field of 10 T.

3. Samples 55.41 and 59.22 were selected because of their high germanium contents (36% Ge). In particular, sample 59.22 was grown by a new approach so-called Low-Growth-Temperature-Post-Grown-Annealing (LGTPGA) to achieve highly planar Si/SiGe interface [Grasby et al. (1999)]. It is therefore very in-

teresting to investigate whether the 2DHG mobility is improved by this new technique.

4. Samples 59.53 and 60.46 were measured mainly because of their high germanium contents, of 45% and 65% Ge respectively. For sample 59.53, we also have the result from Hall and Strip technique [Prest (2000)] which can be compared with the magnetotransport result. For sample 60.46, it was measured at temperatures down to 220 K only because it was highly resistive (> 100 kΩ) and unmeasurable at lower temperatures. This sample has the room temperature Hall mobility around 1,000 $cm^2V^{-1}s^{-1}$, even with the presence of the parallel conduction.

5. Sample 50.36 was used as a control sample, i.e. without SiGe channel.

The experimental data were examined using Beck and Anderson analysis (BA), multicarrier fitting (MCF), and maximum-entropy mobility spectrum analysis (MEMS). BA was used to determine the number of carrier species and approximate values of the mobility and carrier density of each carrier species. This result was then further optimised by MCF. MEMS was employed independently to yield the mobility spectrum. From the mobility spectrum, the number of peaks indicates the number of carrier species and each peak can be used to determine the mobility and carrier density of the corresponding carrier species. The results from BA, MCF, and MEMS, are discussed in Section 6.4–6.7. Furthermore, the Hall factor and the power of the energy dependence of the relaxation time will be extracted.

6.2 Characteristics of Experimental Data

The samples were firstly measured by van der Pauw measurement in the temperature range 10–300 K in order to investigate the temperature dependence of sheet resistivity (ρ_{xx}), Hall mobility (R_H), and carrier density (n_s). We found that the results of all samples are very similar and therefore only a typical result will be shown in Fig. 6.2.

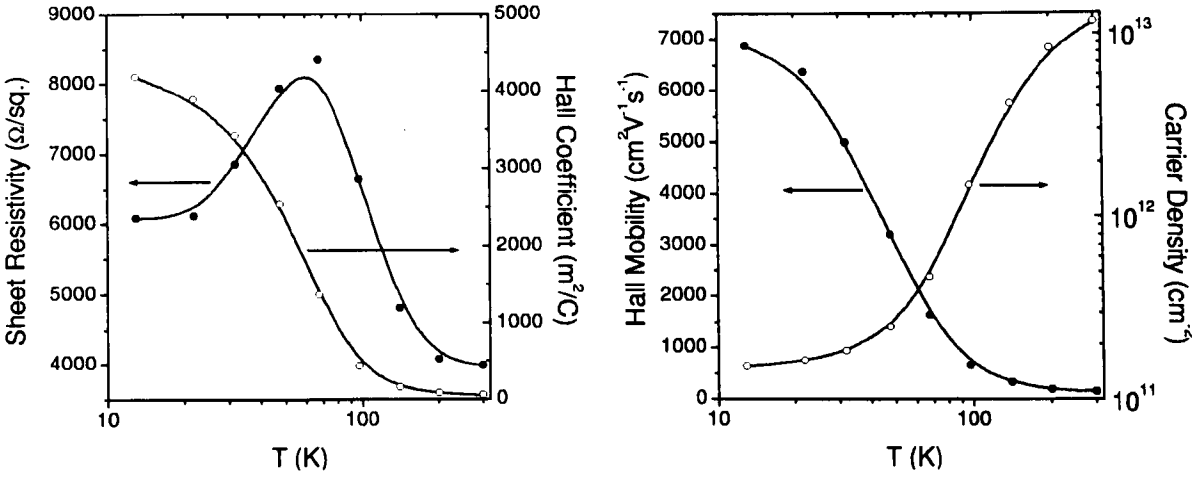

Figure 6.2: The sheet resistivity, Hall coefficient, Hall mobility, and carrier density as functions of temperature of $Si_{0.9}Ge_{0.1}/Si$ sample from van der Pauw measurement at the magnetic field of 0.41 Tesla.

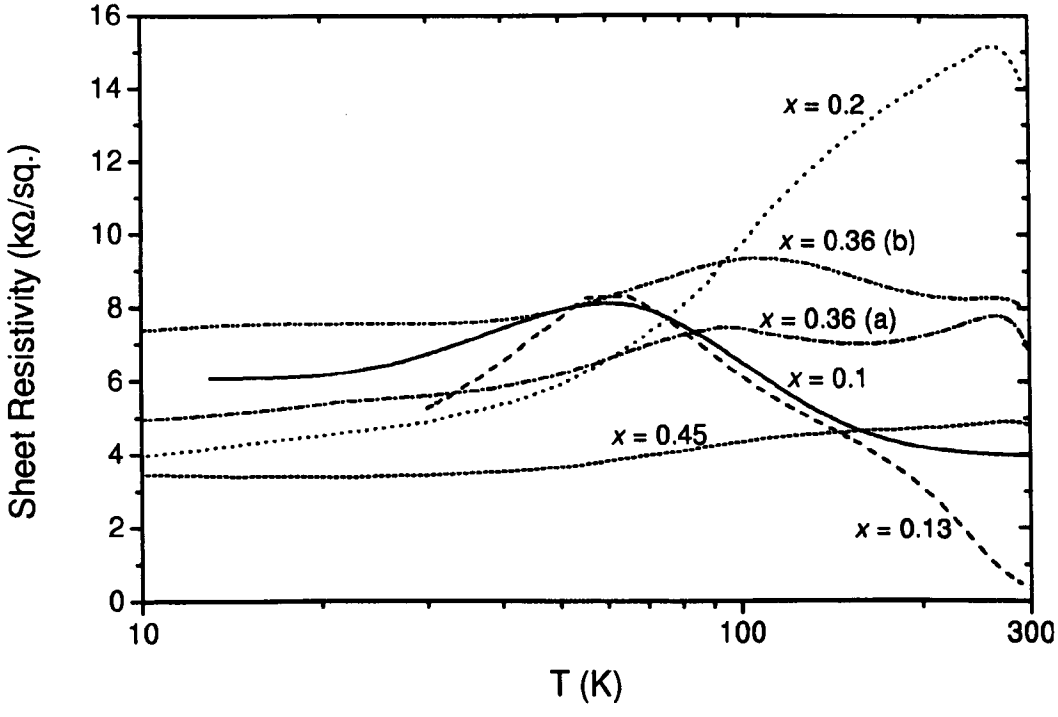

Figure 6.3: The sheet resistivity as a function of temperature for various $Si_{1-x}Ge_x/Si$ samples ($0.1 \leq x \leq 0.45$).

The characteristics of carrier density and mobility are similar for all samples in that the carrier density is constant at low temperature and starts to rise slowly as the temperature is increased. At temperatures above 70 K, it increases exponentially due to the ionisation of the Si:B supply layer. The Hall mobility always decreases with increasing temperatures. The sheet resistivity of all samples decreases with decreasing temperature at temperatures below 50 K. However, at higher temperatures, it can either have one or two maxima or no maximum at all (see Fig. 6.3). It will be shown later in section 6.8 that this is due to the balancing between the increasing sheet resistivity of 2DHG and decreasing sheet resistivity of Si:B, with increasing temperatures.

The magnetic-field dependence of the sheet resistivity and Hall coefficient in the temperature range 0.3–300 K were measured at $\sim$ 1,000 magnetic field points as the magnetic field was swept continuously in the range 0–12 T. The data were measured at 10–35 temperature points. The typical characteristic of sheet resistivity is that, at low temperature (0.3–1.5 K), it exhibits the Shubnikov de-Haas (SdH) oscillations with or without the negative magnetoresistance at low magnetic fields ($B < 3$ T). As the temperature increases, the SdH oscillations become smaller and disappear, usually in the temperature range 10–30 K but varying from sample to sample. Then, the classical transport takes place where the sheet resistivity increases monotonically with increasing magnetic field. The Hall coefficient in the classical transport regime decreases monotonically with increasing magnetic field in the range 1.5–12 T. Below 1.5 T, we observe that it can either decrease monotonically with decreasing field down to 0 T, or go through the minimum at $\sim$ 1 T and increase, or remain approximately constant. For a fixed magnetic field within the range 1.5–12 T, the Hall coefficient always decreases with increasing temperatures.

6.3 Numerical Analyses

6.3.1 Beck and Anderson Analysis

The data set for each sample consists of 30 data points which are equally distributed on the magnetic field axis. Each data set is used to form data subsets of 2–6 data points which are validated by "physical test" and their Beck and Anderson mobility spectra are subsequently calculated. In table 6.2, we show a typical physical test result for the $Si_{0.9}Ge_{0.1}$/Si sample. These physical percentages can be treated as the probability of having N carrier species if $N + 1$ data points are used. What we shall look for from this table for each temperature is the data-point configuration where its corresponding physical percentage is between 50–80%. This data-point configuration will be the most sensitive to be used for the calculation of the Beck and Anderson mobility spectrum. After the Beck and Anderson (BA) mobility spectrum calculation, we plot the histogram of mobility at all peaks of all BA mobility spectra in Figs. 6.4-6.10. If the histogram peak is sharp, for example the Si:B peak at 73 K in the $Si_{0.9}Ge_{0.1}$/Si sample, it means that this carrier species is not influenced by the experimental error and/or by the magnetic field, and vice versa. We recall that each spectrum is calculated from different data subset, which consists of a few data points combinatorially selected from a data set.

We found that there are 3 carrier species at most in all samples from the Beck and Anderson analysis, which are the 2DHG, Si:B, and the unknown electron-like carrier species. The 2DHG can be clearly seen in all samples as the histogram peak with highest positive mobility. The Si:B and $Si_{0.65}Ge_{0.35}$:B are also distincly observed at lower mobilities between 0–800 $cm^2V^{-1}s^{-1}$. In this thesis, the term " the electron-like carrier species" will be used for the unknown carrier species which behaves like the electron-type carrier. It could be either the n-type substrate, the minority carrier in Si:B, the background doping (phosphorus), or the band structure (see section 2.5.2). The unknown electron-like carrier species is the most pronounced in $Si_{0.9}Ge_{0.1}$/Si

Table 6.2: The physical percentage of $Si_{0.9}Ge_{0.1}/Si$ using 2–6 data points per data subset.

T(K)	Data points				
	2	**3**	**4**	**5**	**6**
10	100	0	0	0	0
15	100	0	0	0	0
16	100	0	0	0	0
19	100	10	0	0	0
26	100	87	63	0	0
31	100	95	38	2	0
36	100	96	52	7	0
51	100	98	70	15	0
61	100	90	61	25	2
62	100	92	68	32	3
73	100	95	77	41	7
76	100	98	77	23	1
80	100	93	60	12	0
81	100	100	94	52	6
91	100	100	95	73	19
96	100	100	94	63	12
110	100	100	93	56	11
111	100	100	74	16	0
115	100	100	78	18	0
120	100	95	61	3	0
126	100	100	82	27	2
135	100	100	95	56	12
142	100	100	93	42	5
145	100	99	81	12	0
160	100	100	93	42	5
172	100	98	73	7	1
180	100	100	95	50	7
200	100	100	91	29	1
211	100	100	87	34	2
220	100	100	81	20	1
241	100	97	65	8	0
283	99	87	40	3	0

sample at temperatures between 91–110 K and in $Si_{0.35}Ge_{0.65}/Si_{0.65}Ge_{0.35}$ sample. In $Si_{0.8}Ge_{0.2}$/Si and $Si_{0.64}Ge_{0.36}$/Si-(b) samples, the Si:B and electron-like carrier species are unseparable and we obtain the average peak. As the temperature is increased, the average peak moves closer to the Si:B because of its increasing sheet conductivity due to the thermal ionisation.

6.3.2 Multicarrier Fitting

The multicarrier fitting (MCF) was performed using the commercial MULTAN HL5600s software of the Bio-Rad. The principle of the calculation is to assume the number of carrier species and perform a nonlinear modified-Marquardt optimization of mobilities and carrier densities [Koser et al. (1994)]. The initial values were usually obtained from Beck and Anderson analysis by using the sharpest-peak spectrum. During the "physical test", there are many data subsets that pass the test, and each data subset generates one BA mobility spectrum. The author has observed that the sharpest-peak spectrum is produced from the data subset which has the least positive eigenvalue (λ_i in Appendix A). It should be noted that MCF uses the sheet resistivity and Hall coefficient, rather than the magnetoconductivity tensor components, because they are more sensitive to low-mobility carrier species.

The mobility obtained from MCF is neither Hall mobility nor drift mobility. For a sample with only one carrier species, it is well known that the carrier density obtained from Hall measurements at very high magnetic field ($\mu B_{max} \gg 1$) is the real value and is different from that at very low magnetic field ($\mu B_{max} \ll 1$) by the Hall factor. For MCF of 1 carrier species, the magnetic field usually covers both high and low magnetic fields and, therefore, the mobility will be just the average value. This mobility will be roughly between Hall and drift mobilities and corresponds to the inverse of the magnetic field at the σ_{xy} peak (see Fig. 2.12). For MCF of multicarrier species, we estimate that the meaning of mobility for each carrier species will be the same as MCF of one carrier species. The result from the multicarrier fitting for each

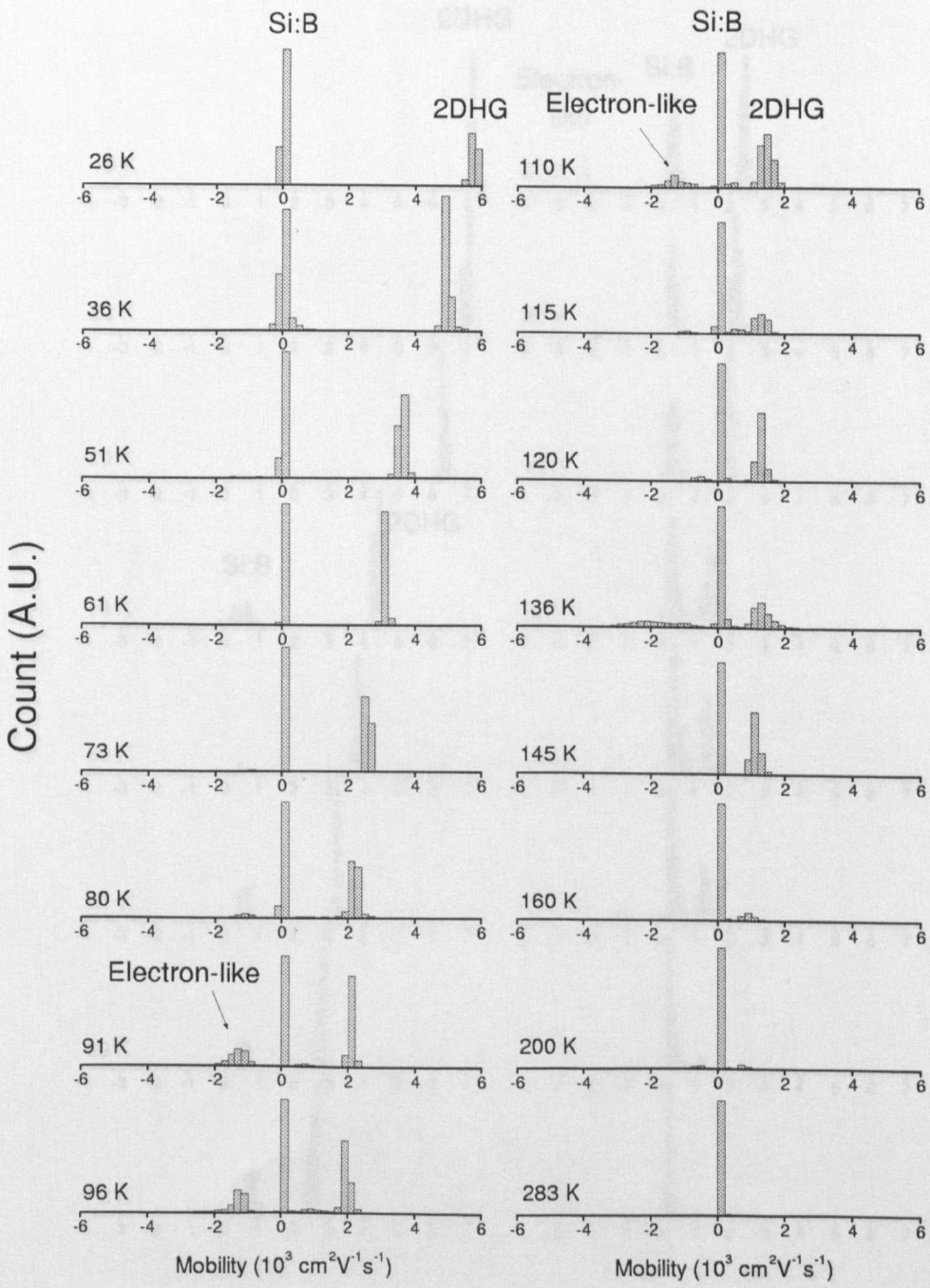

Figure 6.4: The histogram of peak abscissa of BA mobility spectra of $Si_{0.9}Ge_{0.1}$/Si sample in the temperature range 26–283K. The mobility range is between -10,000 $cm^2V^{-1}s^{-1}$ and 10,000 $cm^2V^{-1}s^{-1}$ with a resolution of 40 $cm^2V^{-1}s^{-1}$. The histogram window width is 200 $cm^2V^{-1}s^{-1}$.

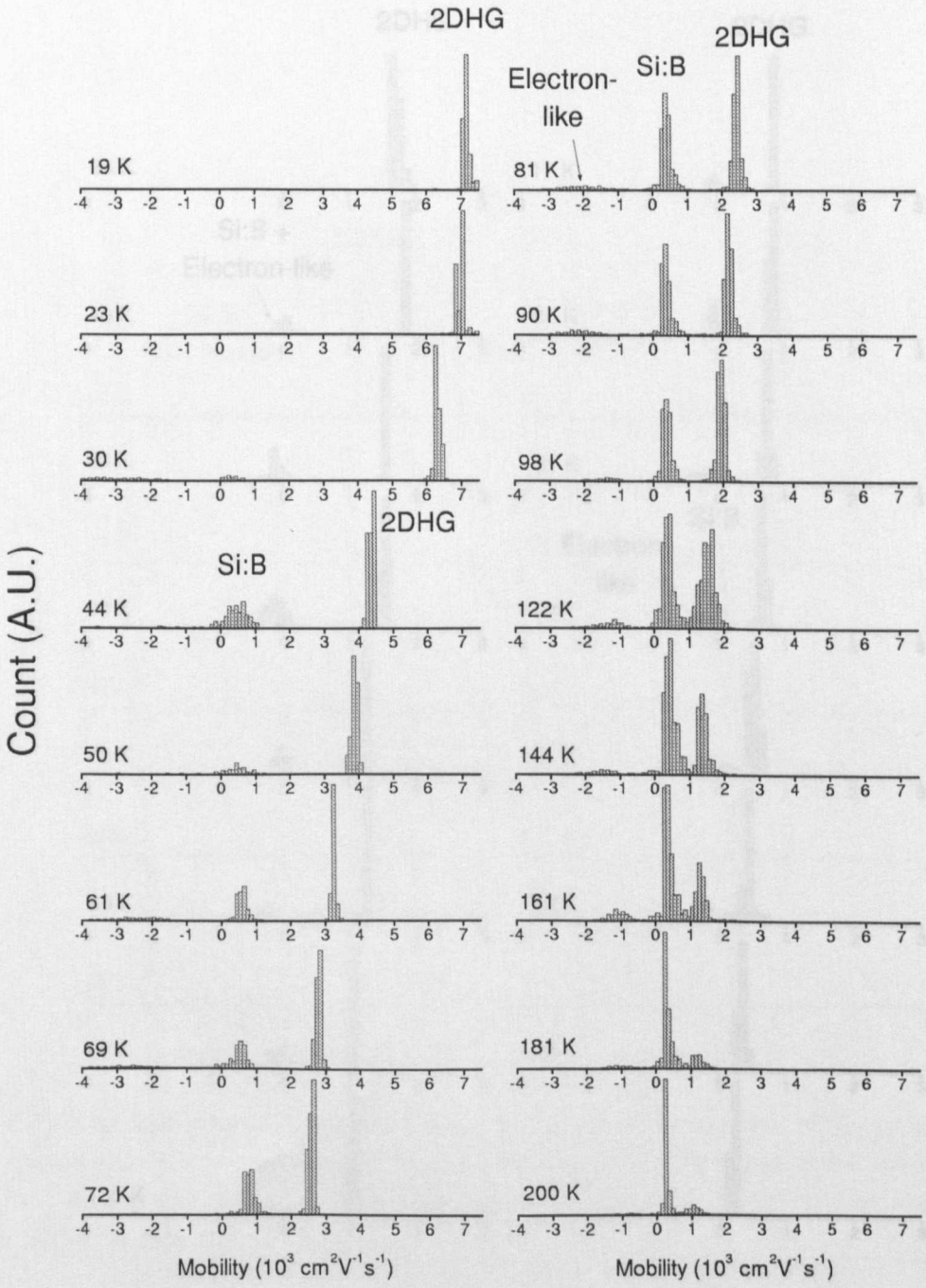

Figure 6.5: The histogram of peak abscissa of BA mobility spectra of $Si_{0.87}Ge_{0.13}/Si$ sample in the temperature range 19–200 K. The mobility range is between -10,000 $cm^2V^{-1}s^{-1}$ and 10,000 $cm^2V^{-1}s^{-1}$ with a resolution of 40 $cm^2V^{-1}s^{-1}$. The histogram window width is 100 $cm^2V^{-1}s^{-1}$.

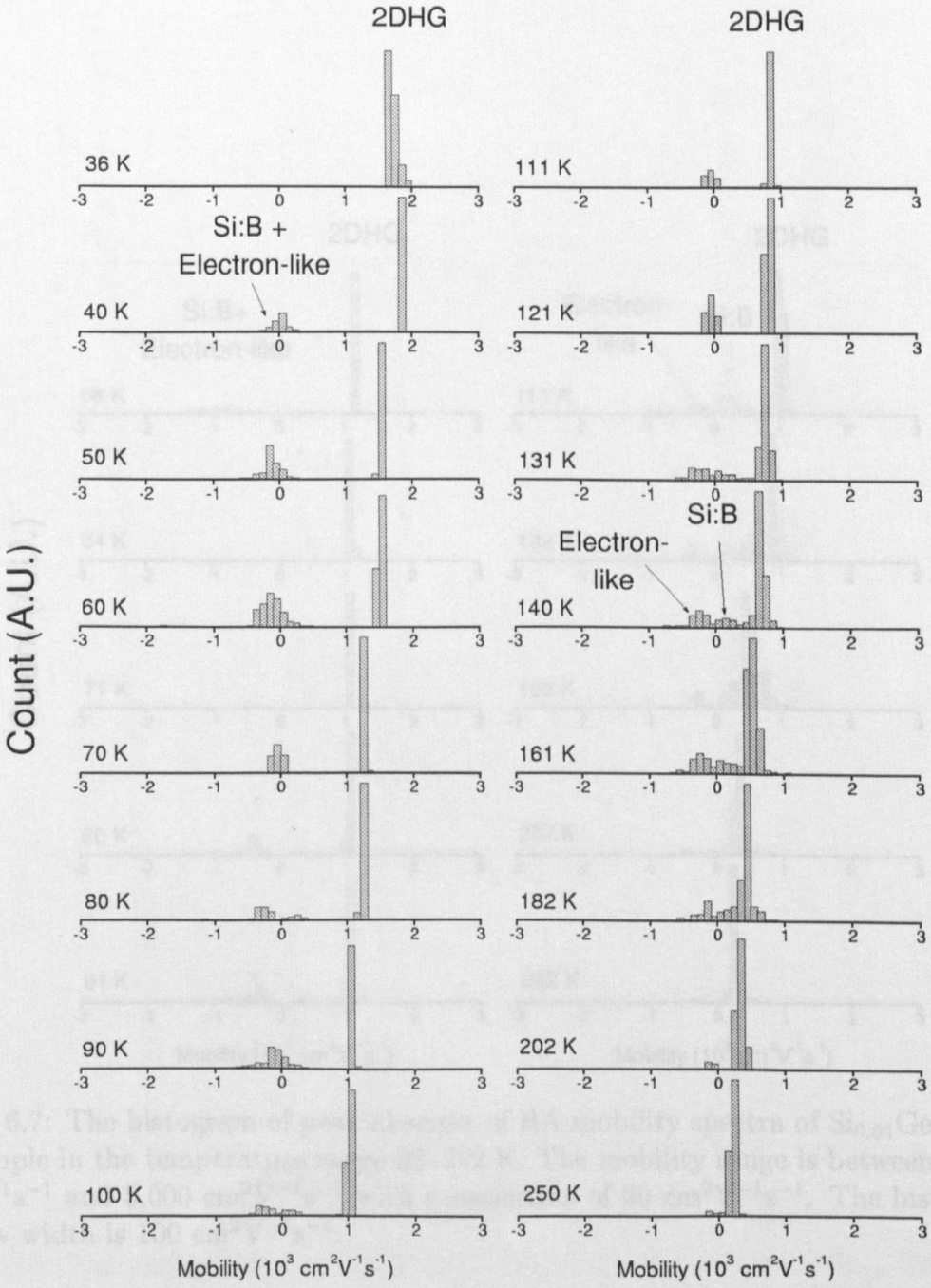

Figure 6.6: The histogram of peak abscissa of BA mobility spectra of $Si_{0.8}Ge_{0.2}/Si$ sample in the temperature range 36–250 K. The mobility range is between -5,000 $cm^2V^{-1}s^{-1}$ and 5,000 $cm^2V^{-1}s^{-1}$ with a resolution of 20 $cm^2V^{-1}s^{-1}$. The histogram window width is 100 $cm^2V^{-1}s^{-1}$.

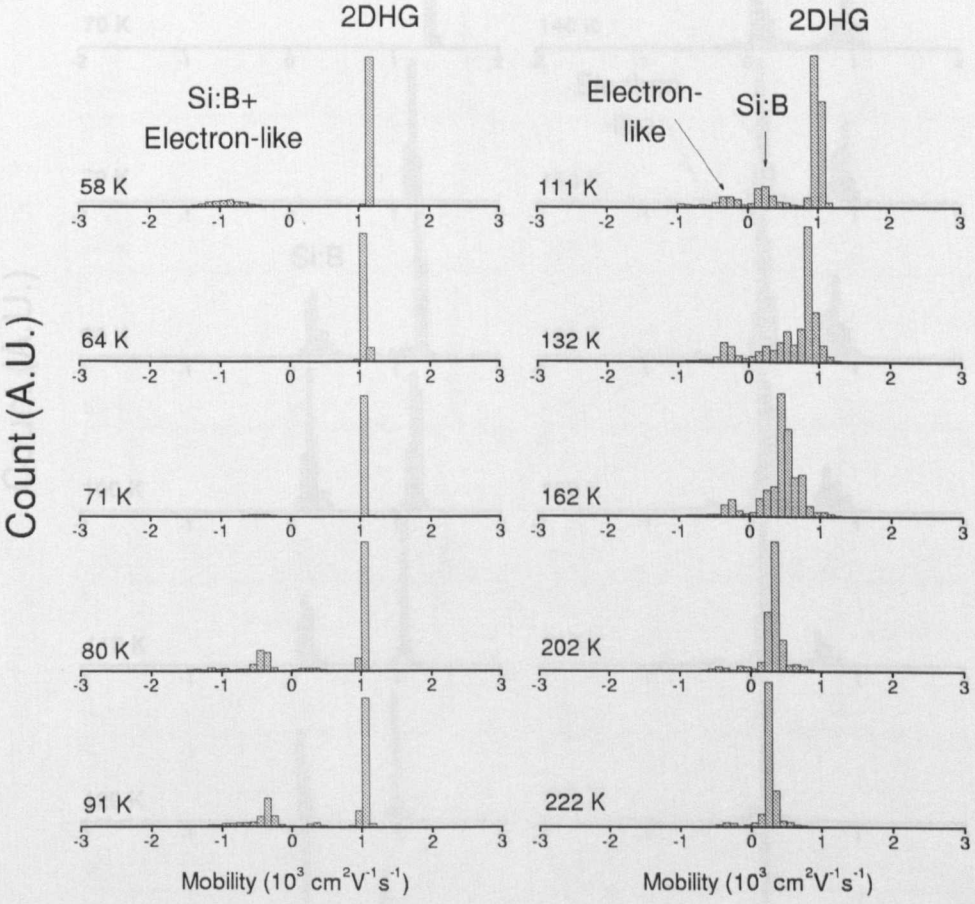

Figure 6.7: The histogram of peak abscissa of BA mobility spectra of $Si_{0.64}Ge_{0.36}/Si$-(a) sample in the temperature range 58–222 K. The mobility range is between -5,000 $cm^2V^{-1}s^{-1}$ and 5,000 $cm^2V^{-1}s^{-1}$ with a resolution of 20 $cm^2V^{-1}s^{-1}$. The histogram window width is 100 $cm^2V^{-1}s^{-1}$.

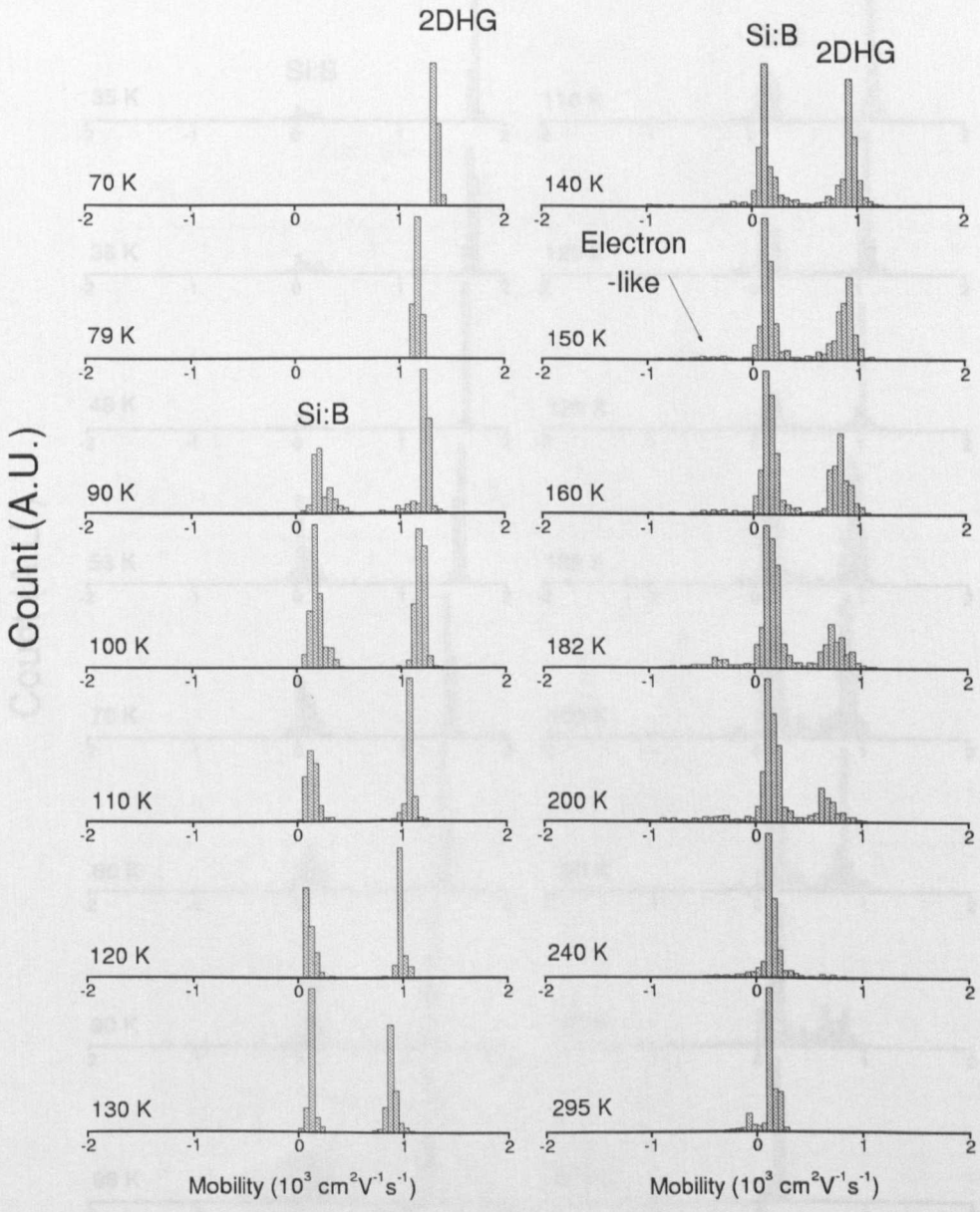

Figure 6.8: The histogram of peak abscissa of BA mobility spectra of $Si_{0.64}Ge_{0.36}$/Si-(b) sample in the temperature range 70–295 K. The mobility range is between -5,000 $cm^2V^{-1}s^{-1}$ and 5,000 $cm^2V^{-1}s^{-1}$ with a resolution of 20 $cm^2V^{-1}s^{-1}$. The histogram window width is 50 $cm^2V^{-1}s^{-1}$.

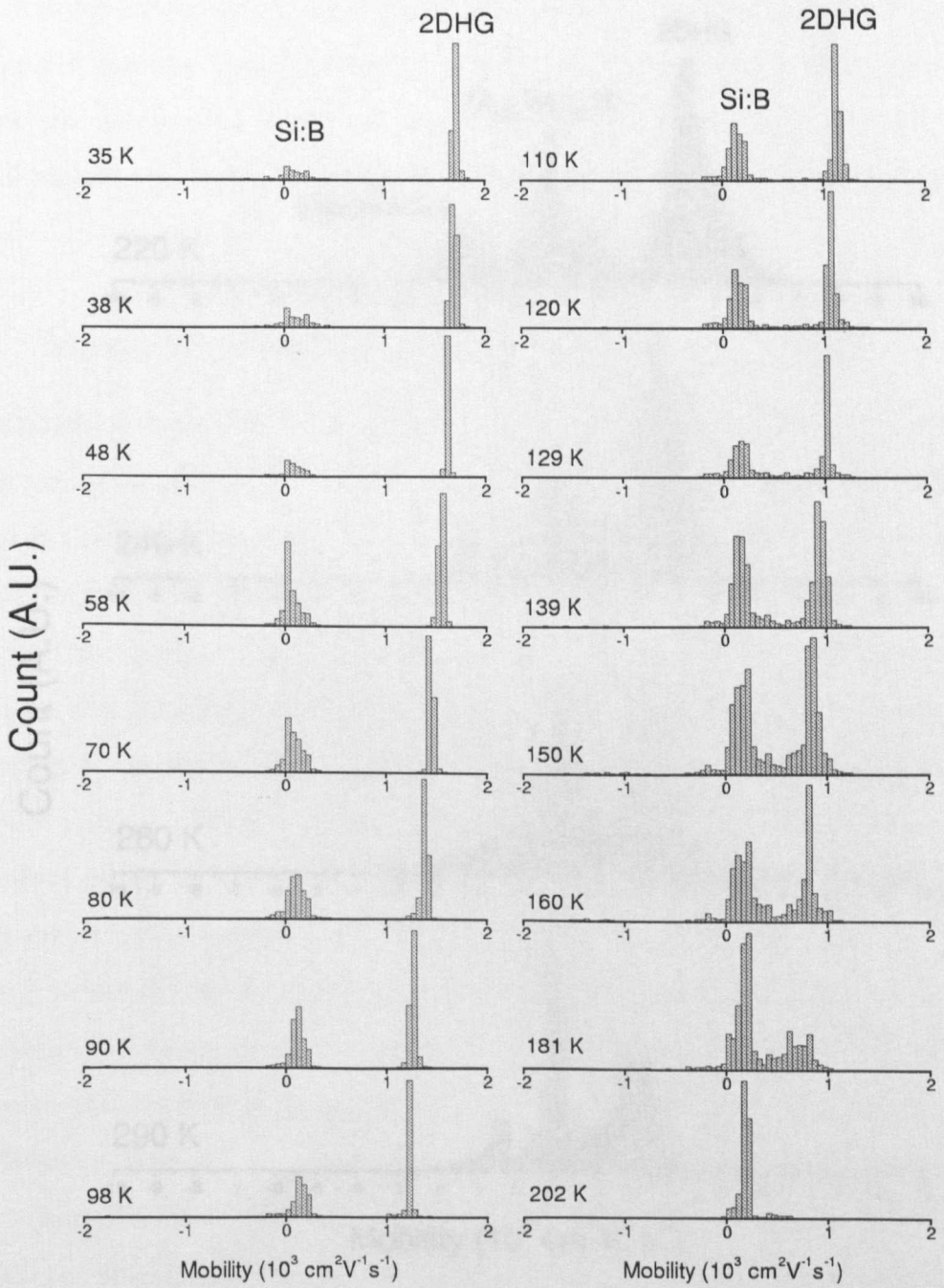

Figure 6.9: The histogram of peak abscissa of BA mobility spectra of $Si_{0.55}Ge_{0.45}/Si$ sample in the temperature range 35–202 K. The mobility range is between -5,000 $cm^2V^{-1}s^{-1}$ and 5,000 $cm^2V^{-1}s^{-1}$ with a resolution of 20 $cm^2V^{-1}s^{-1}$. The histogram window width is 50 $cm^2V^{-1}s^{-1}$.

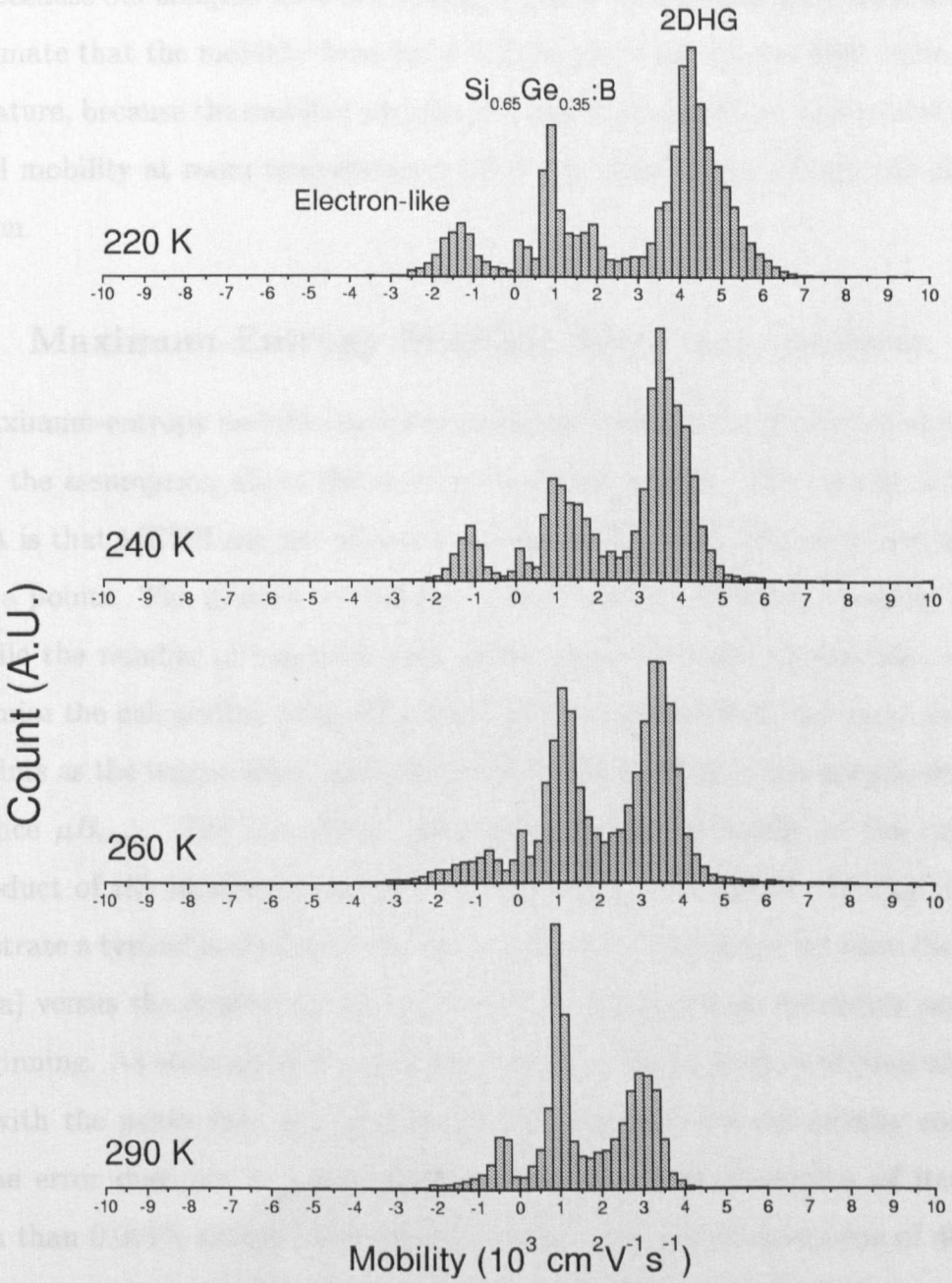

Figure 6.10: The histogram of peak abscissa of BA mobility spectra of $Si_{0.35}Ge_{0.65}/Si_{0.65}Ge_{0.35}$ sample in the temperature range 220–290 K. The mobility range is between -10,000 $cm^2V^{-1}s^{-1}$ and 10,000 $cm^2V^{-1}s^{-1}$ with a resolution of 40 $cm^2V^{-1}s^{-1}$. The histogram window width is 200 $cm^2V^{-1}s^{-1}$.

sample will be presented in sections 6.4–6.7.

Because our samples have decreasing mobility with increasing temperature, we can estimate that the mobility from MCF will be very close to the drift value at low temperature, because the mobility satisfies the high field condition, and moves toward the Hall mobility at room temperature, where the mobility only fulfils the low-field condition.

6.3.3 Maximum-Entropy Mobility Spectrum Analysis

The maximum-entropy mobility spectrum analyses (MEMS) were performed without making the assumption about the number of carrier species. The benefit of MEMS over BA is that MEMS can use all available data points while BA only uses between 2–6 data points. The number of mobility points used in MEMS is typically around 200 while the number of magnetic field points varies between 36 and 300 in order to optimise the calculation time. The trend is that one needs to use more magnetic field points as the temperature increases because the mobility of the sample decreases and hence μB_{max}. The calculation time increases proportionally to the square of the product of the number of mobility and mangetic field points. In Fig. 6.11 we demonstrate a typical evolution of MEMS and the error (deviation between the fit and the data) versus the number of iterations. The iteration process converges rapidly at the beginning. As soon as all the peaks emerge, the convergence continues at slower speed with the peaks only getting sharper. The calculations are usually continued until the error does not decrease significantly over a certain number of iterations, i.e. less than 0.001% change after 200 iterations. The typical iterations of 400,000–1,000,000 is tested to yield the correct MEMS within the experimental error.

MEMS of all samples are shown in Figs. 6.12–6.18. The typical change in MEMS with temperature is that at very low temperature the 2DHG peak is dominant. As the temperature increases, the Si:B peak becomes relatively more important while the 2DHG peak moves toward the Si:B peak. At sufficiently high temperatures, these

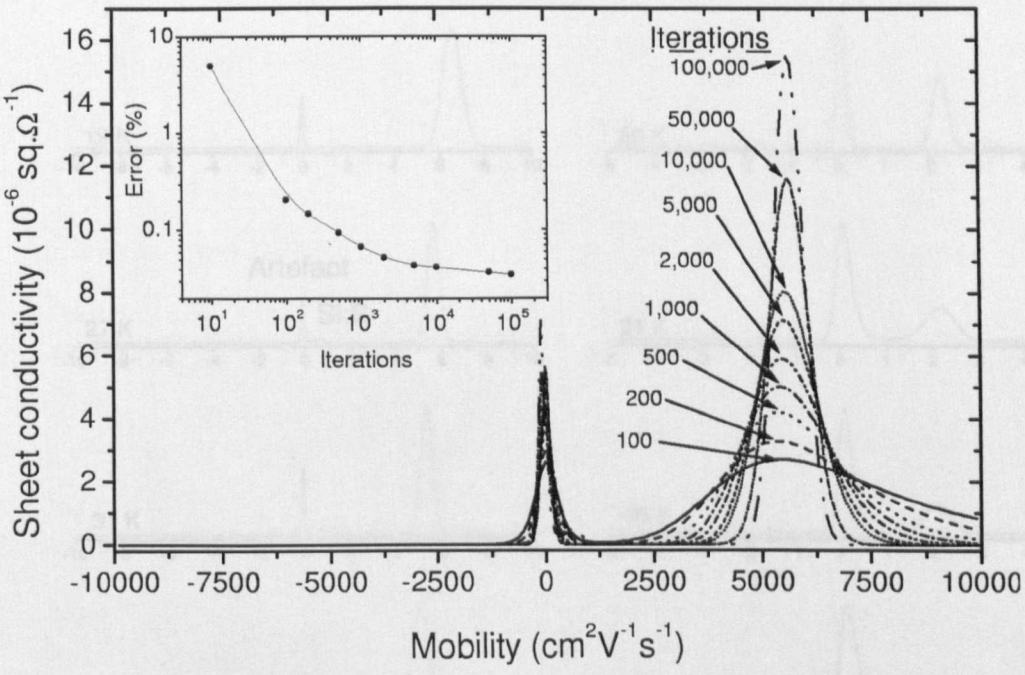

Figure 6.11: MEMS of $Si_{0.9}Ge_{0.1}$/Si sample at 27 K as a function of iterations. An inset shows the total standard error of the fits from the experimental data at each iteration.

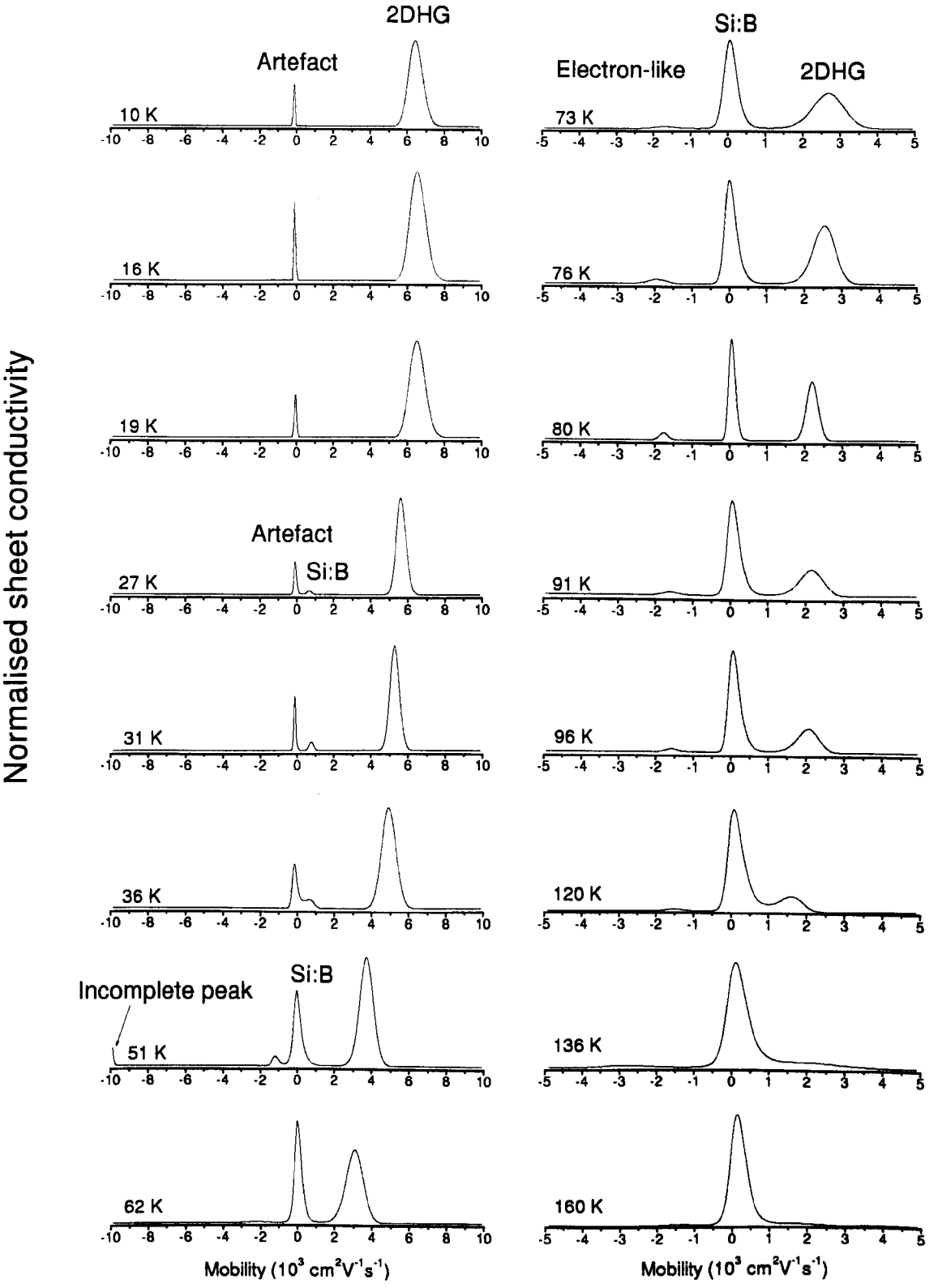

Figure 6.12: MEMS of $Si_{0.9}Ge_{0.1}$/Si sample in the temperature range 10–160 K.

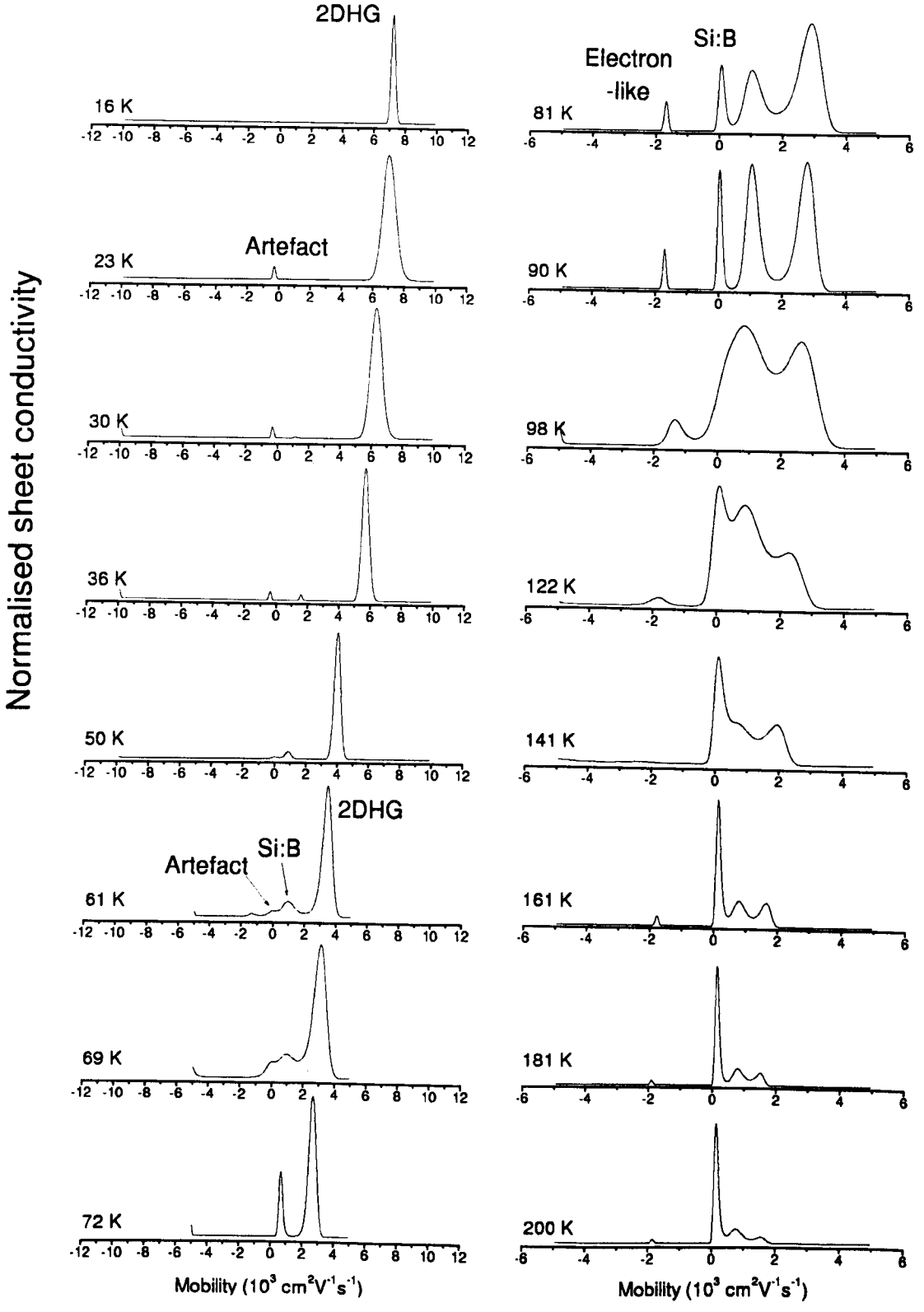

Figure 6.13: MEMS of $Si_{0.87}Ge_{0.13}$/Si sample in the temperature range 16-200 K.

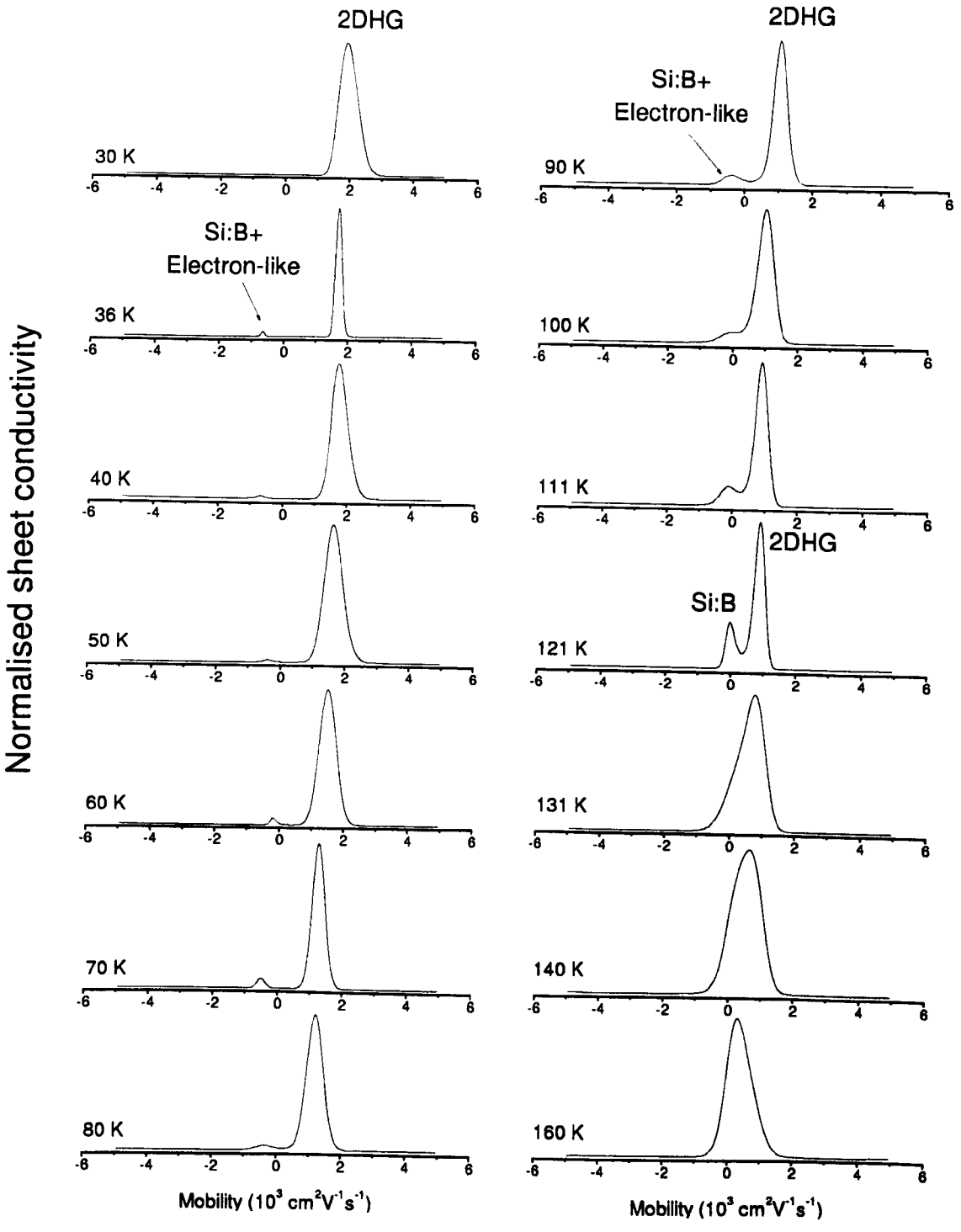

Figure 6.14: MEMS of $Si_{0.8}Ge_{0.2}$/Si sample in the temperature range 30–160 K.

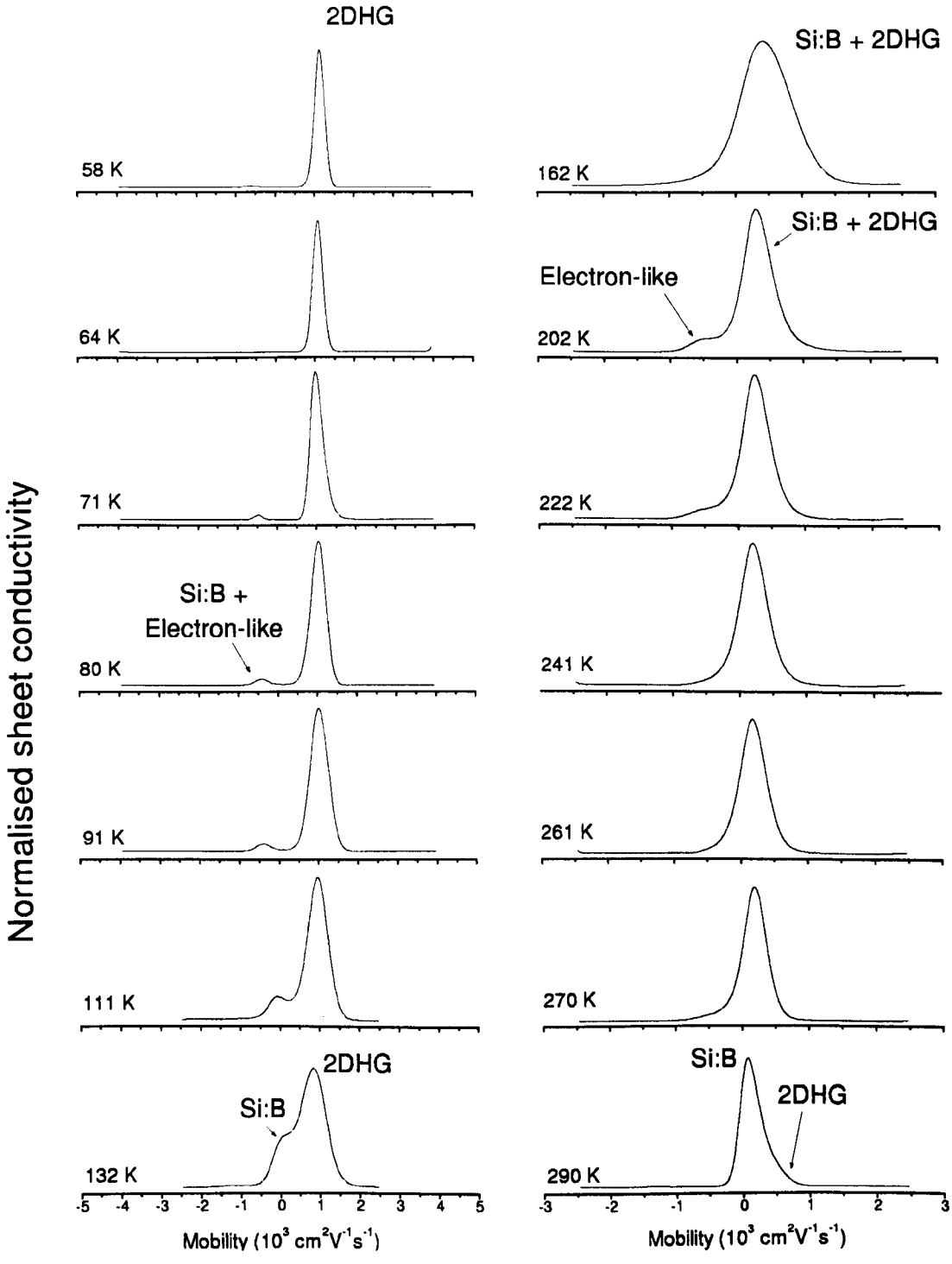

Figure 6.15: MEMS of $Si_{0.64}Ge_{0.36}$/Si-(a) sample in the temperature range 58–290 K.

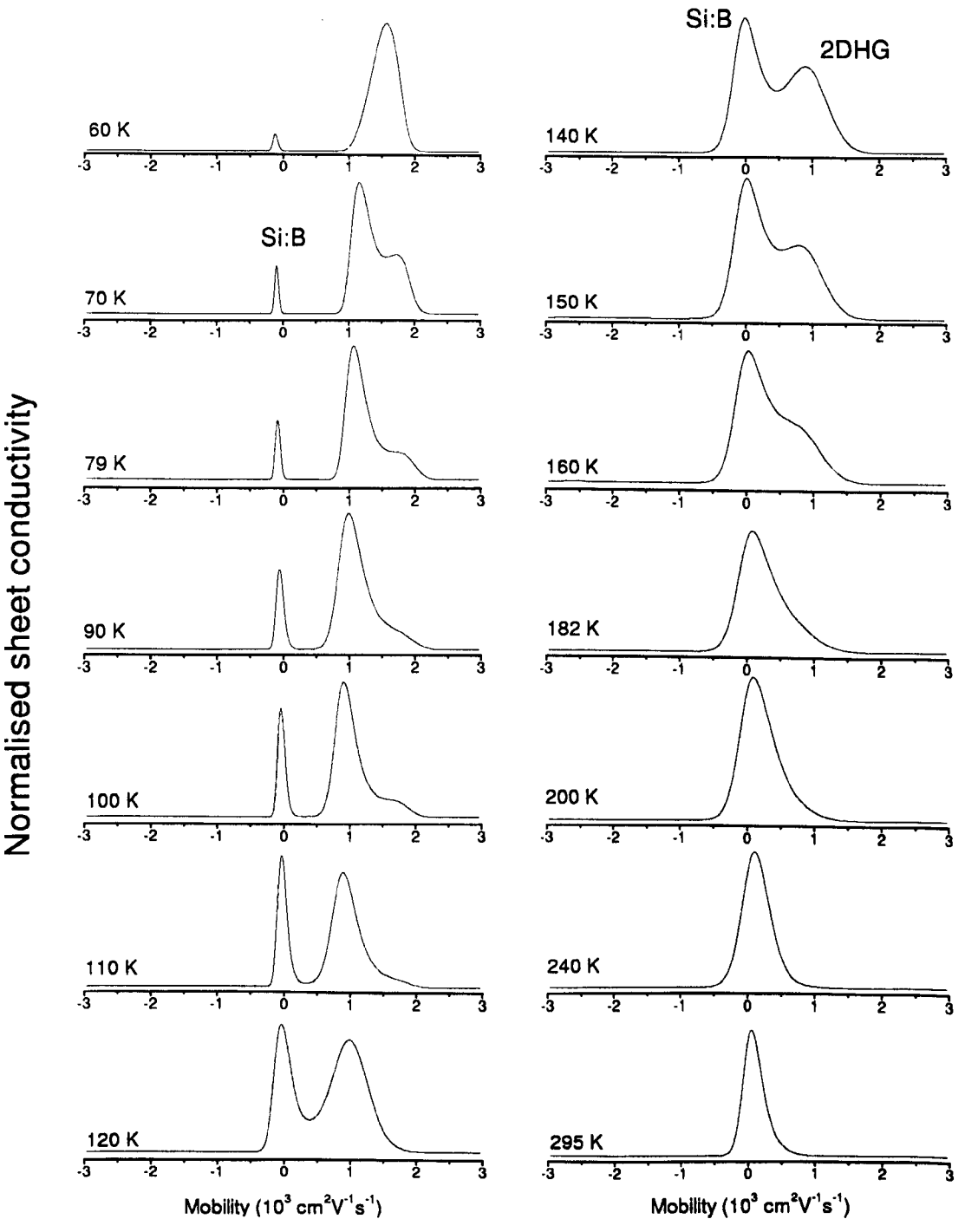

Figure 6.16: MEMS of $Si_{0.64}Ge_{0.36}$/Si-(b) sample in the temperature range 60-295 K.

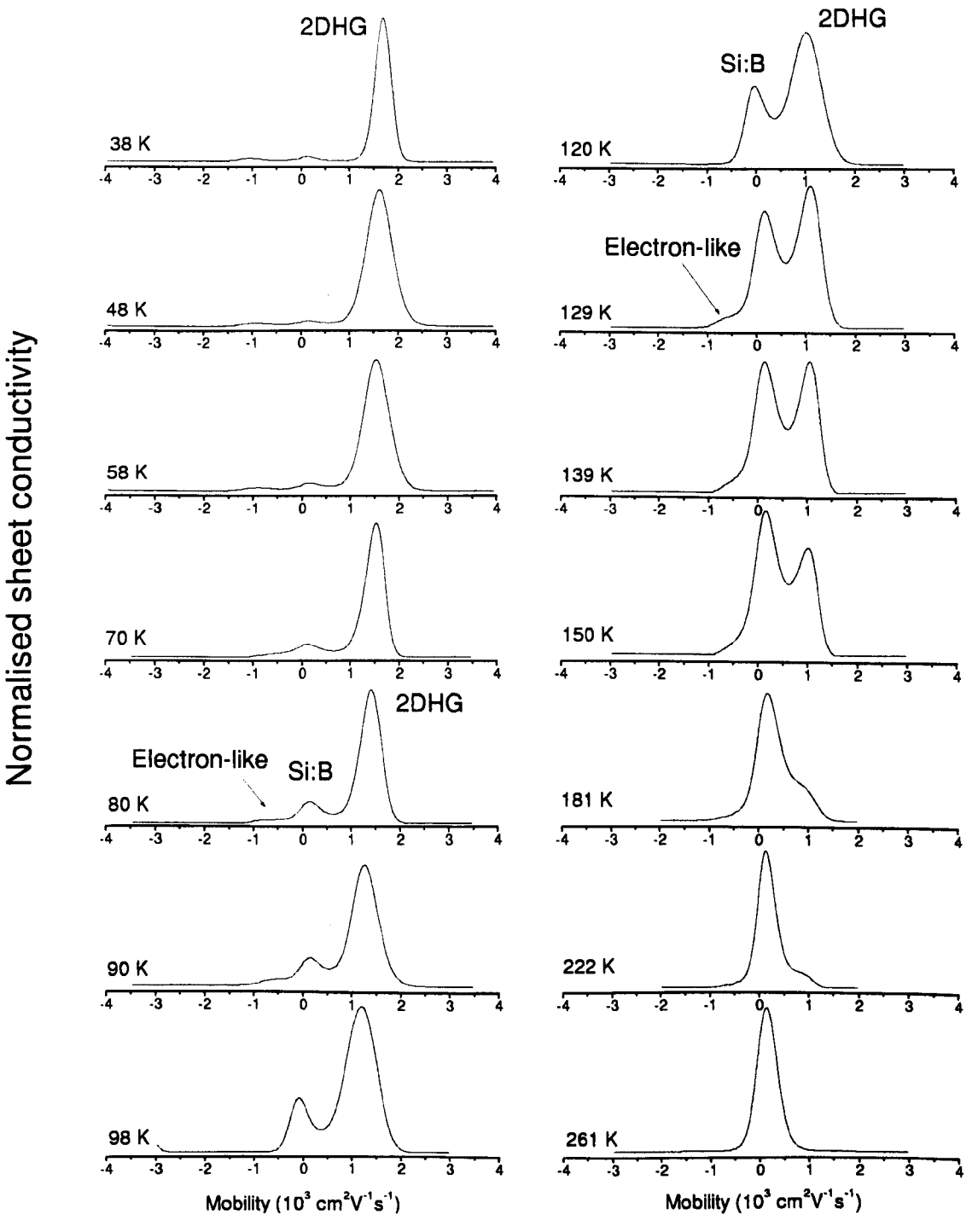

Figure 6.17: MEMS of $Si_{0.55}Ge_{0.45}$/Si sample in the temperature range 38-261 K.

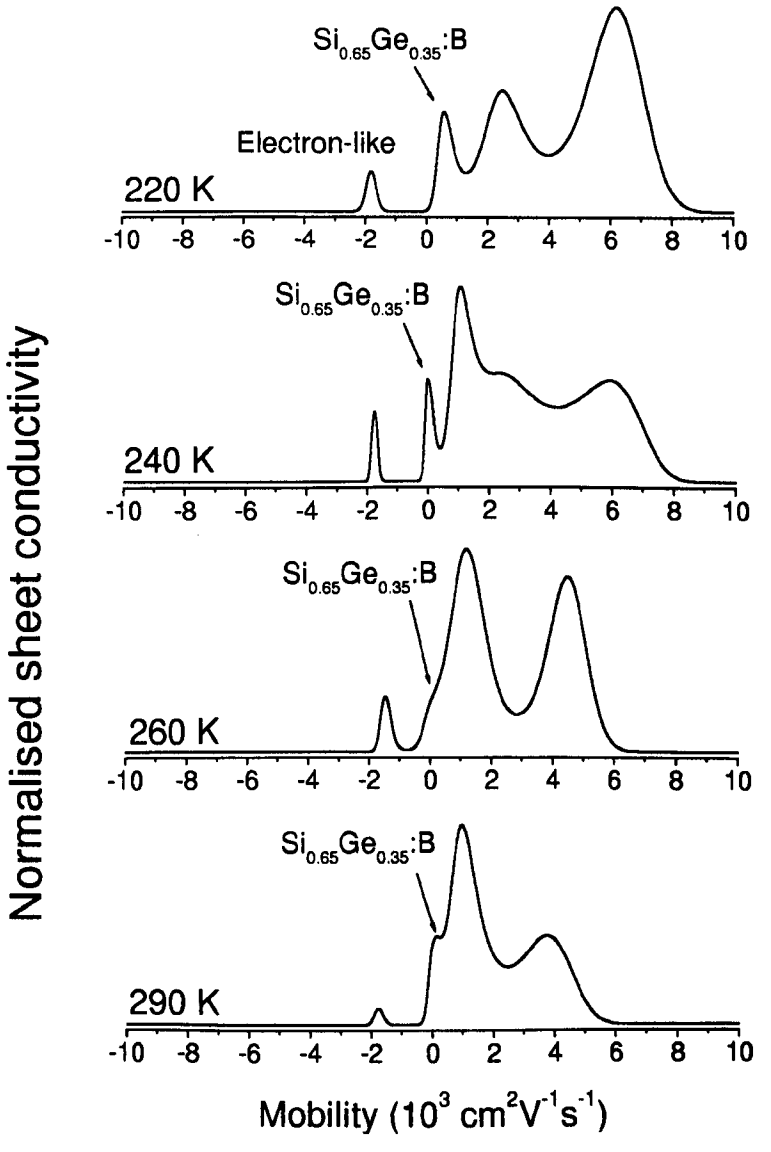

Figure 6.18: MEMS of $Si_{0.35}Ge_{0.65}/Si_{0.65}Ge_{0.35}$ sample in the temperature range 220-290 K.

two peaks merge and only one peak can be resolved. The electron-like and Si:B carrier species are also unresolveable in $Si_{0.8}Ge_{0.2}$/Si and $Si_{0.64}Ge_{0.36}$/Si-(a) samples because Si:B sheet conductivity is too low. With increasing temperatures, the combination of Si:B and electron-like carrier species results in the average peak which moves closer to the real Si:B (positive mobility) peak due to more ionization of Si:B than electron-like carrier species. For example, in $Si_{0.8}Ge_{0.2}$/Si samples, the average peak moves from the mobility of $\sim$ -500 $cm^2V^{-1}s^{-1}$ towards 0 and change to positive as the temperature is increased.

The issue concerning the well-defined Si:B peak is how to calculate its mobility and carrier density. The mobility cannot be obtained by using Eq.2.61 for Hall mobility or Eq.2.62 for drift mobility, because the Si:B peak spreads over positive and negative mobilities. In theory, this spreading is impossible because the spectrum must converge to the origin (see Eq.2.40) and it is undefined at zero mobility. In practice, the broadening in Si:B peak is mainly due to the insufficient magnetic-field dependency ($\mu_{Si:B}B_{max} \sim 0.2$). Having low magnetic field dependency means that the convergence process for this peak will be extremely slow and the calculation has to be performed with large number of iterations, which is impractical. As a result, the peak shape of Si:B is incorrect to be used for the calculation of Hall or drift mobility. In this thesis, we will take the mobility at the peak as the mobility of Si:B and the carrier density will be calculated by using the total sheet conductivity of the Si:B peak.

Another problem to be solved is the overlaping between Si:B and 2DHG peaks which occurs at high temperatures (> 200 K). In order to separate them, we might try to fit Eqs. 2.40 twice to the overlapped peaks. However, as Eq. 2.40 cannot be used for the broad Si:B peak, we must choose another way to separate them. One simple method is to use the Gaussian function which takes the form

$$s(\mu) = G \exp\left(-0.5\left[\frac{\mu - \mu_0}{w}\right]^2\right), \tag{6.1}$$

where G is a constant, μ_0 is a mobility at the centre of the peak, and w is a standard

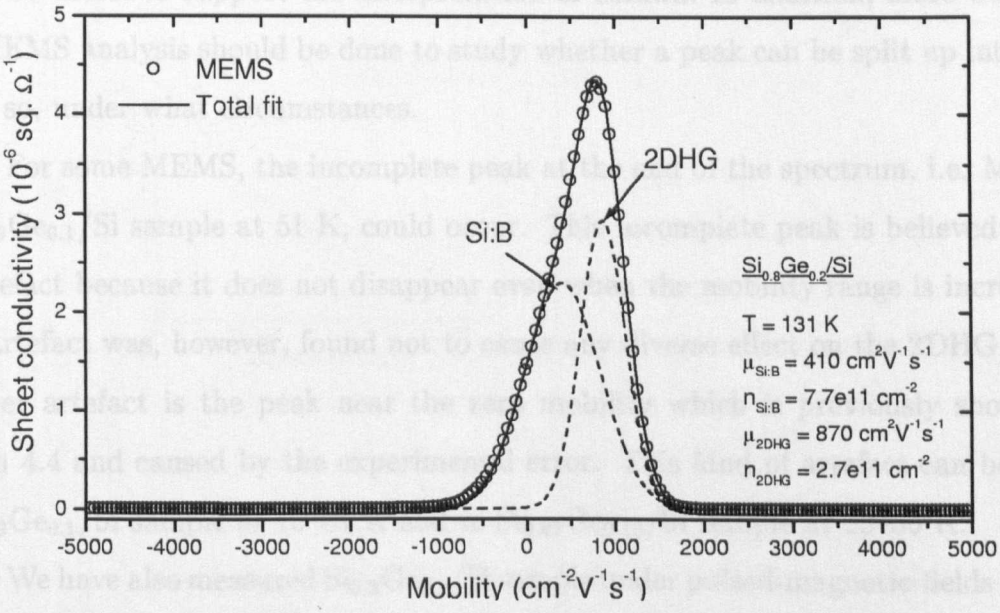

Figure 6.19: MEMS of $Si_{0.8}Ge_{0.2}/Si$ sample at 131 K fitted by 2 Gaussian functions. Each Gaussian function yields the mobility and total sheet conductivity, and hence the carrier density.

deviation. We found that the use of 2 Gaussian functions can fit MEMS very well. The μ_0 is used as the mobility of the corresponding carrier species and the total sheet conductivity is employed to yield the carrier density. An example is shown in Fig. 6.19 which features MEMS at 131 K of the $Si_{0.8}Ge_{0.2}/Si$ sample. The mobility of Si:B and 2DHG obtained by this approach can be consistent with those obtained from MCF assuming 3 carrier species, provided that the conductivity of the additional electron carrier species is relatively small.

The MEMS which consist of more than 2 hole-like peaks, i.e. in $Si_{0.87}Ge_{0.13}/Si$ at 81–200 K, $Si_{0.67}Ge_{0.36}/Si$-(b) at 70–110 K, and $Si_{0.35}Ge_{0.65}/Si_{0.65}Ge_{0.35}$ at 220-290 K, are very difficult to analyse. It is unclear at present whether there is an additional carrier species transporting in parallel to the known carrier species (Si:B, 2DHG, electron-like) or if these peaks belong to either Si:B or 2DHG. At this stage, we can only suggest that the boron profile from the secondary ion mass spectroscopy (SIMS)

would be useful to support the interpretation of MEMS. In addition, more work on this MEMS analysis should be done to study whether a peak can be split up into two and if so, under what circumstances.

For some MEMS, the incomplete peak at the end of the spectrum, i.e. MEMS of $Si_{0.9}Ge_{0.1}$/Si sample at 51 K, could occur. This incomplete peak is believed to be an artefact because it does not disappear even when the mobility range is increased. This artefact was, however, found not to cause any diverse effect on the 2DHG peak. Another artefact is the peak near the zero mobility which is previously shown in section 4.4 and caused by the experimental error. This kind of artefact can be seen in $Si_{0.9}Ge_{0.1}$/Si sample at 10–31 K and in $Si_{0.87}Ge_{0.13}$/Si sample at 23–36 K.

We have also measured $Si_{0.8}Ge_{0.2}$/Si sample under pulsed-magnetic-fields (Clarendon Laboratory, Oxford University) up to 41 T at 77 and 202 K. The principle of the pulsed-magnet is to energise the superconducting solenoid by a massive current from a capacitor bank over a short period of time ($\sim$ 20 ms) [Jones et al. (1994)]. A DC current through the sample was employed and the Hall measurement was performed for both polarity of magnetic fields and current directions in order to remove the hysterisis effect in the signals. The base temperature is 77 K (liquid nitrogen) and the temperature can be raised by a heater coil, situated near to the sample.

The MEMS was calculated using 400 mobility points, 400 magnetic field points, and 10^6 iterations. The result at 77 K and the final fit are shown in Fig. 6.20. Three peaks are resolved which are marked as 2DHG, Si:B, and the electron-like carrier species. We have noticed that the fit to $\sigma_{xx} + \sigma_{xy}$ is very good with average error of less than 0.01% while the fits to σ_{xx} and σ_{xy} separately are poorer with errors $\sim$ 5% (see an inset in Fig. 6.20). There are two possibilities that might lead to this result. The first possibility lies in the use of Eq.4.6 in the closeness of fit optimization. If $\frac{d\sigma_{xx}}{dB}$ and $\frac{d\sigma_{xy}}{dB}$ are nearly equal, the function $\sigma_{xx}+\sigma_{xy}$ cannot represent the true fits to σ_{xx} and σ_{xy} independently. For the experimental data shown, we estimate that this would occur at magnetic fields higher than 20 T. However, the result for $Si_{0.9}Ge_{0.1}$/Si

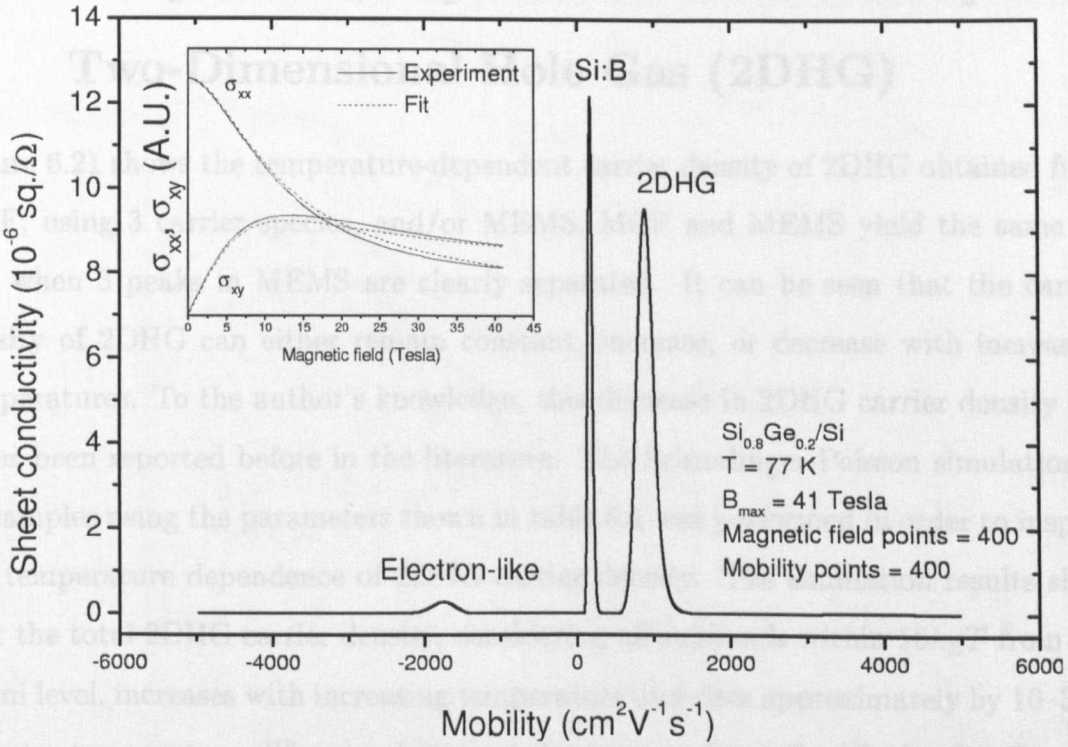

Figure 6.20: MEMS of $Si_{0.8}Ge_{0.2}$/Si at 77 K using the maximum magnetic field of 41 Tesla.

sample at 73 K (which correspond to same μB_{max} value) shows that MEMS can fit σ_{xx} and σ_{xy} individually very well, especially near the maximum in σ_{xy}. Therefore, it is not caused by failure of the calculation method.

A second possible explanation is the Shubnikov de-Haas oscillation effect. From the SdH oscillations measured in the magnetic field range 0–10 T and in the temperature range 0.3–1.5 K, we have estimated that the maximum SdH amplitude at 77 K would be around 3% of the maximum measured magnetoresistance which is close the resultant error of 5%. As a result, we can conclude that the error is mostly due to the SdH oscillations. For MEMS at 200 K, we found that only a single peak, which is an average between Si:B and 2DHG, can be obtained and therefore is not useful for further discussion.

6.4 Temperature-Dependent Carrier Density of the Two-Dimensional Hole Gas (2DHG)

Figure 6.21 shows the temperature-dependent carrier density of 2DHG obtained from MCF, using 3 carrier species, and/or MEMS. MCF and MEMS yield the same result when 3 peaks in MEMS are clearly separated. It can be seen that the carrier density of 2DHG can either remain constant, increase, or decrease with increasing temperatures. To the author's knowledge, this decrease in 2DHG carrier density has never been reported before in the literature. The Schrodinger-Poisson simulation of all samples using the parameters shown in table 6.1 was performed in order to inspect the temperature dependence of 2DHG carrier density. The simulation results show that the total 2DHG carrier density, considering all subbands within $10k_BT$ from the Fermi level, increases with increasing temperature and rises approximately by 10–30% at room temperature. The simulation results agree quite well with the $Si_{0.9}Ge_{0.1}$/Si and $Si_{0.87}Ge_{0.13}$/Si samples but disagree with other samples which have a germanium composition of $x = 0.2$ and higher.

A possible source that affects the 2DHG carrier density is the surface states. It is well known for our samples that around 20 nm of the sample surface is depleted of free carriers, and when this depletion region gets closer to the channel it also starts to deplete the 2DHG [McGregor (1997)]. Let's consider the surface depletion width (l_s) as a function of temperature. The surface depletion width can be calculated by solving Poisson's equation for a bulk carrier concentration N_A as [Chandra et al. (1979)]

$$l_s = \sqrt{\frac{2\epsilon_0\epsilon_r}{qN_A}\left(\phi_B - \frac{k_BT}{q}\ln\left(\frac{N_V}{N_A}\right)\right)}, \tag{6.2}$$

where ϵ_0 is the permitivity of free space, ϵ_r is the dielectric constant of silicon, ϕ_B is the pinned Fermi level at the surface, T is the temperature, and N_V is the effective density of states at the valence band edge. This N_V is also temperature dependent

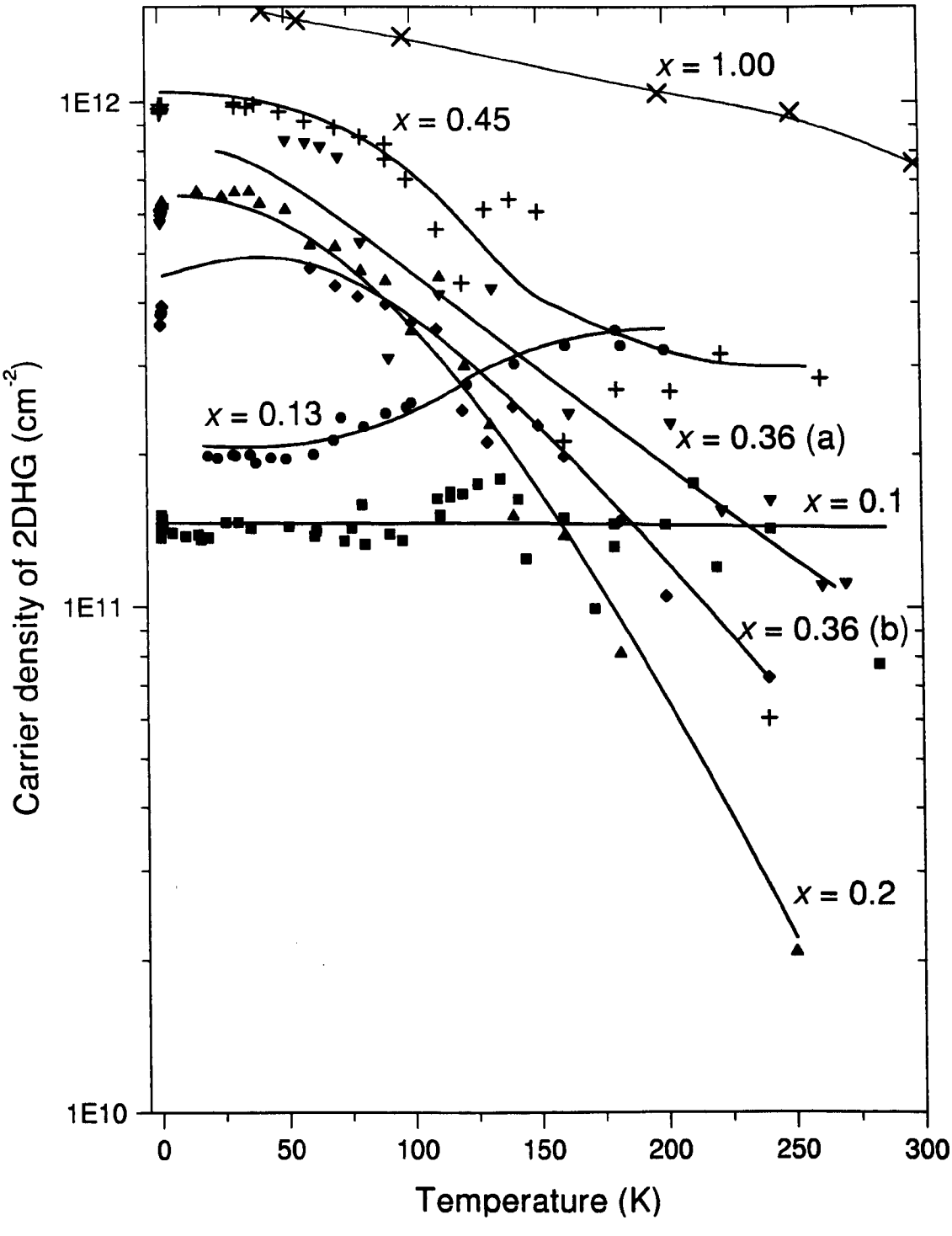

Figure 6.21: The carrier density of the two-dimensional hole gas (2DHG) versus temperature of the modulation-doped p-$Si_{1-x}Ge_x$/Si heterostructures with $0.10 \leq x \leq 0.45$. For $x = 1.00$, the data is provided by Morris (2000) which is for a pure strained Ge channel on a relaxed $Si_{0.3}Ge_{0.7}$ virtual substrate.

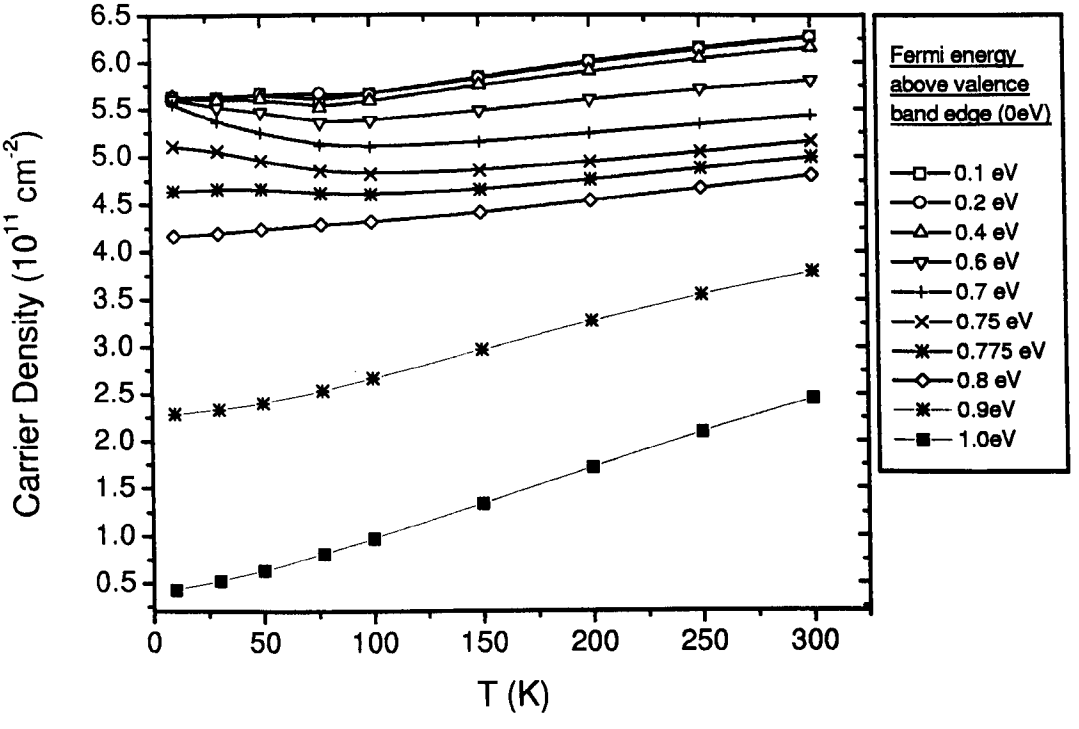

Figure 6.22: The carrier density of 2DHG as a function of temperature in $Si_{0.8}Ge_{0.2}/Si$ sample for different Fermi energy levels, obtained from Schrodinger-Poission simulation. The Fermi level is pinned at the surface by the use of Schottky contact and a fixed applied gate voltage.

which is [Sze (1981)]

$$N_V = 1.04 \times 10^{19} \left(\frac{T}{300}\right)^{\frac{3}{2}}. \tag{6.3}$$

From Eqs.6.2 and 6.3, one can see that if other parameters are fixed, the depletion width l_s can only decrease with increasing temperatures. This means that the higher the temperature, the less the influence of surface states on the 2DHG.

The samples usually come into contact with the hydrofluoric acid (HF) solution during the device processing, i.e. for the surface cleaning. The Fermi level on HF etched silicon surface, studied by photoelectron spectroscopy, is found to be pinned at about 0.2 eV or less below the conduction band, independent of the concentration of the HF solution in the range of 1-50 % and independent of the temperature in the range of 200–300 K [Schlaf et al. (1999)]. In Fig. 6.22, we show the Schrodinger-Poisson simulation result of $Si_{0.8}Ge_{0.2}$/Si for different pinned Fermi levels at the surface. It can be seen that none of pinning levels within the bandgap (0–1.1 eV) could account for the change in the 2DHG carrier density of $Si_{0.8}Ge_{0.2}$/Si sample. In addition, it seems that there is no correlation between the change in 2DHG carrier density and the Si:B thickness. For example, $Si_{0.87}Ge_{0.13}$/Si and $Si_{0.55}Ge_{0.45}$/Si have the same Si:B thickness but the carrier density of the 2DHGs change in opposite directions with temperature.

The decrease in 2DHG carrier density might indicate the lost of quantum confinement within the well when the temperature is increased, especially for a very thin SiGe channel. Let's consider the solution of Schrodinger's equation for a square potential well. The solution is that when the well width is reduced, the ground-state energy level is pushed further away from the valence bandedge and the separation between adjacent energy levels is increased. This is experimentally confirmed by photoluminescence (PL) measurement in strained $Si_{0.8}Ge_{0.2}$/Si [Xiao et al. (1992)]. Their results at 4 K and 77 K also showed that, for a fixed quantum well width, the energy levels actually shift toward the valence bandedge as the temperature is increased. The room temperature confinement in strained $Si_{0.84}Ge_{0.16}$/Si was studied

by Chen et al. (1993) by photothermal deflection spectroscopy. Their result gives the similar well-width dependence and shows that it is only important when the width is less than $\sim$ 10 nm. The ground-state enegy level is found not to shift significantly different from that at 77 K as obtained from the PL measurement, taken into accout the difference in germanium content. The hole confinement within a pure Ge layer sandwiched between pure Si has been recently studied by Cyca et al. (1997) by fabricating a Si/Ge/Si p-MOSFET, with 1-nm-thick pure Ge channels grown pseudomorphically on Si substrate, and capped by 10-nm pure Si. The room temperature result by a Capacitance-Voltage technique showed that this pure Ge channel provides a good confinement to 2DHG with the carrier density up to 2.5×10^{12} cm^{-2} before the surface conduction at the cap/oxide interface becomes more important. A similar structure but with a narrow triangular Ge profile, graded to a peak of pure Ge with rise and fall lengths of just 2 nm, was also produced by Pawlowicz et al. (1998) who showed that the channel provides a good hole confinement to 2DHG and acheived slightly higher carrier density of $(3.4\text{–}5)\times10^{12}$ cm^{-2}. However, they found that the degradation in peak mobility with decreasing well width can be lower than that from the bulk Si control device. By taking all this evidence into consideration, it is unlikely that the decrease in our 2DHG carrier density is caused by the degradation in quantum confinement with either temperature or the well width.

A recent Hall and Strip technique on the $Si_{0.55}Ge_{0.45}$/Si sample [Prest (2000)] has confirmed that the decrease in carrier density is genuine. Figure 6.23 shows the Hall mobility and carrier density measured by low-field van der Pauw measurement as the surface was chemically etched for different times. At 8-minute etch, the carrier density dips slightly from 1×10^{12} cm^{-2} to 8.5×10^{11} cm^{-2} as the temperature increases from 10 to 70 K. This is in remarkably good agreement with the result shown in Fig. 6.21 for $x = 0.45$. The increase in carrier density at higher temperatures is merely due to Si:B parallel conduction. For 10-mintute etch, the sample is critically etched so that the low temperature carrier density drops to 6.5×10^{11} cm^{-2}. At this stage,

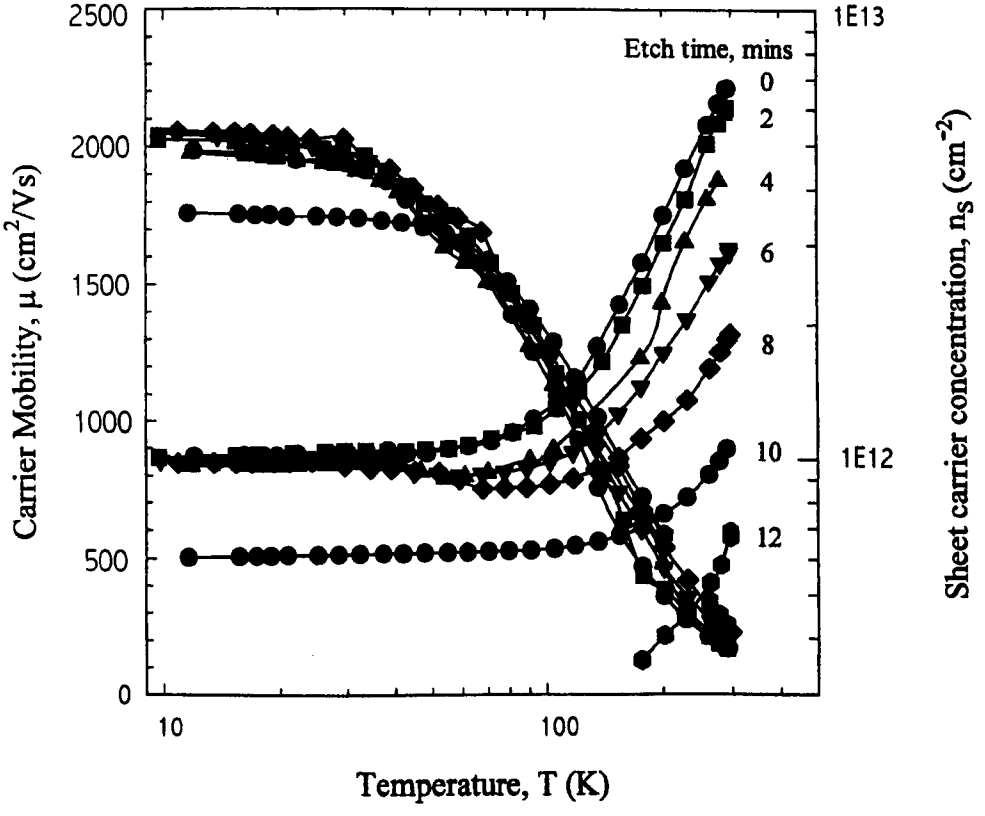

Figure 6.23: The Hall and Strip technique for $Si_{0.55}Ge_{0.45}/Si$ sample reveals that 2DHG carrier density (sheet carrier concentration) can decrease with increasing temperature. This is seen in 8-minute etch as a small dip in carrier density at temperatures around 80–100 K (after Prest (2000)).

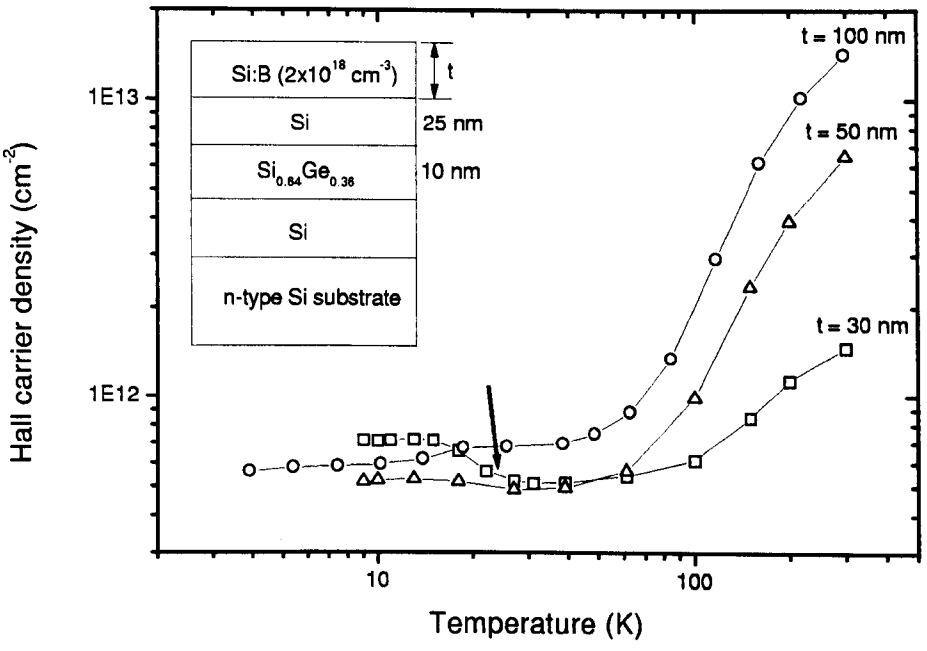

Figure 6.24: The Hall carrier density of the modulation-doped p-$Si_{0.64}Ge_{0.36}$/Si heterostructure with different Si:B cap thicknesses (after Grasby (2000)). An arrow indicates the decrease in Hall carrier density for the cap thickness of 30 nm.

the carrier density does not show any drop which cannot be explained from our MCF or MEMS result. For 12-minute etch, the 2DHG is completely depleted and only the parallel conduction can be measured at temperatures above 200 K.

A similar result was also obtained for $Si_{0.64}Ge_{0.36}$/Si samples grown with different Si:B thickness by Grasby (2000). The results are shown in Fig. 6.24 in which the sample with the thinnest Si:B layer (30 nm) shows a dip in carrier density around 70–100 K. This behaviour cannot be seen if the Si:B layer is thick (50 and 100 nm) because the Si:B carrier density will be so high that the decrease in 2DHG carrier density is overcompensated by the increasing ionised Si:B carrier density. Only when the 2DHG density is approximately twice the cap density will the decrease in measured carrier density be observed.

6.5 Temperature-Dependent Mobility of the Two-Dimensional Hole Gas (2DHG)

Figure 6.25 shows the temperature-dependent mobility of 2DHG for different samples. The mobility is essentially constant at low temperature and decreases with increasing temperature. During the decrease, the mobility might go through a minimum (for $Si_{0.9}Ge_{0.1}$/Si, $Si_{0.87}Ge_{0.13}$/Si, and $Si_{0.64}Ge_{0.36}$/Si-(a) samples) or a kink, as marked by arrows in Fig. 6.25. This minimum characteristic is quite similar to that which has been previously observed in GaAs/AlAs quantum wells by Sakaki et al. (1987) who suggested that this is primarily due to the reduction of the screening effect of the 2DHG, with increasing temperature, and upon further increase of temperature, the mobility increases because of the increase of the carrier kinetic energy. In this thesis, we shall not attempt to explain the scattering mechanisms quantitatively but only investigate the temperature dependence in the temperature range 100–300 K where the phonons are known to be dominant and the analysis is important for the room temperature device application.

The mobility in the temperature range 100–300 K shows the form of $\mu = AT^{-\gamma}$. γ and A as functions of germanium content are shown in Fig. 6.26(a) and (b), respectively. It is clear that for pure silicon or germanium channels, the phonon scattering is dominant due to $\gamma \sim 1$. For the strained SiGe alloy, we found that the curves in Fig. 6.26(a) and (b) are very similar to those reported for bulk p-type relaxed SiGe alloy, in which the minima in γ and A indicate the strong influence of alloy scattering [Levitas (1955)]. However, the minima for our samples occur at lower germanium content (~ 0.3). Moreover, due to the two-dimensional transport in the modulation-doped structure, γ is found to be less than that of the bulk SiGe alloy, and theoretically by 0.5 [Shik (1997)].

Having seen the alloy scattering influence does not mean that it is the second limiting factor to the phonon scattering. For 2D transport, the additional interface

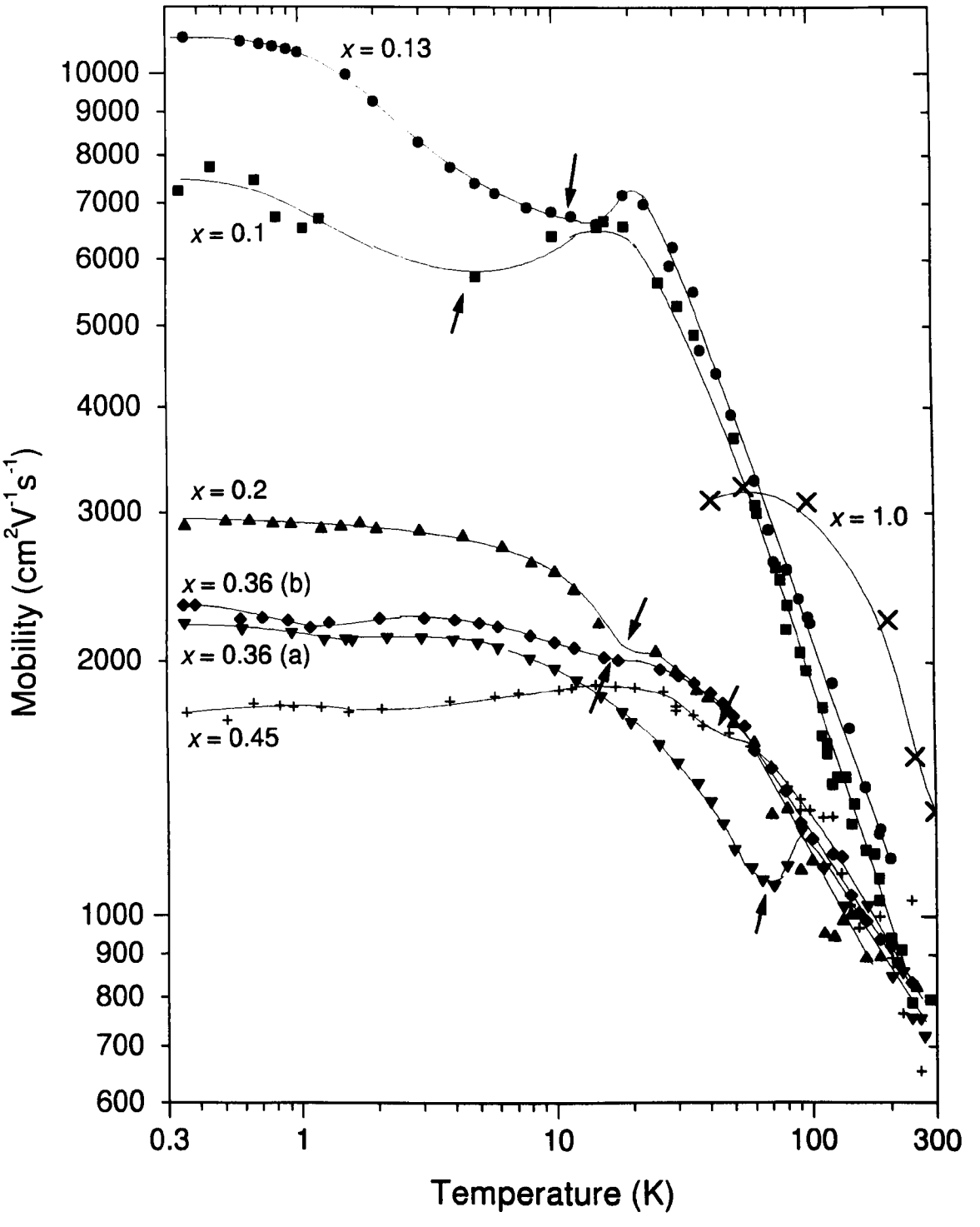

Figure 6.25: The mobility of the two-dimensional hole gas versus temperature of the modulation-doped p-$Si_{1-x}Ge_x$/Si heterostructures ($0.10 \leq x \leq 0.45$). For $x = 1.0$, the sample consists of the strained pure Ge grown on the relaxed $Si_{0.3}Ge_{0.7}$ virtual substrate (after Morris (2000)).

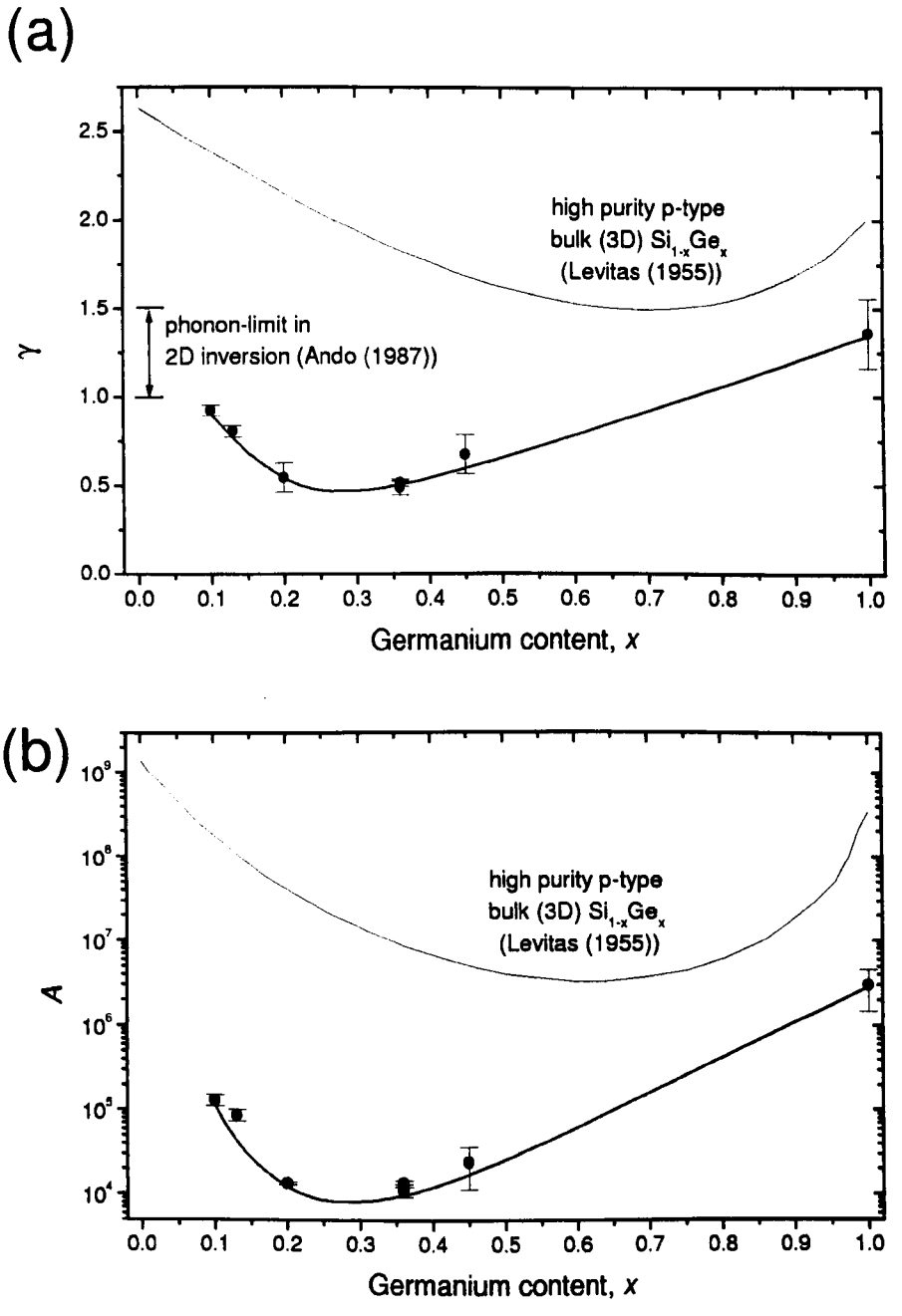

Figure 6.26: (a) The exponent γ and (b) the coefficient A versus the germanium composition x ($0.1 \leq x \leq 1.0$). The mobility in the temperature range 100–300 K is fitted by the form $\mu = AT^{-\gamma}$. The data for $x = 1.0$ is the strained pure Ge channel grown on the relaxed $Si_{0.3}Ge_{0.7}$ virtual substrate (after Morris (2000)).

roughness and interface charge scattering will also have to be taken into consideration. The interface roughness is usually studied by considering the the mobility as a function of carrier density, not temperature. Kearney and Horrell (1998) have theoretically predicted that the alloy scattering will not be the significant limiting factor for 300K mobility. Whall and Parker (1999) also supported this by giving an example that the mobility of a modulation-doped $Si/Si_{1-x}Ge_x/Si$ sample, which has the alloy scattering, and a modulation-doped $Si/Si_{10x}Ge_{10(1-x)}/Si$ short period superlattice, which has no alloy scattering, does not differ by as much as the value predicted. Furthermore, a recent study on a coherently strained $Si/Si_{0.5}Ge_{0.5}/Si$ p-channel field effect transistor has shown that the most significant scattering is due to the surface roughness, not the alloy [Fischer et al. (2000)].

The room temperature mobility of all samples are found to lie somewhere between 700 and 900 $cm^2V^{-1}s^{-1}$. This mobility agrees with the effective mobility of 600 $cm^2V^{-1}s^{-1}$ extracted from the $Si_{0.8}Ge_{0.2}/Si$ p-channel MOSFET at room temperature for the low carrier density of 10^{11} cm^{-2} [Lander et al. (1997)].

6.6 The Boron-doped Silicon Supply Layer

The carrier density of the boron-doped silicon supply layer, obtained from the MCF, versus temperature is shown in Fig. 6.27. From this data, we can extract the activation energy E_A by fitting [Blakemore (1974)]

$$\frac{p_0\,(N_d + p_0)}{(N_a - N_d - p_0)} = \left(\frac{N_V}{\beta}\right) \exp\left(\frac{-E_A}{k_B T}\right), \tag{6.4}$$

where p_0 is the carrier concentration, N_d is the donor concentration, N_a is the acceptor concentration, N_V is the effective density of states in the valence band (see Eq.6.3), and β is the hole degeneracy. Because we obtain the carrier density from the experiment, the carrier concentration has to be estimated by calculating the effective thickness of the cap layer. We will estimate this thickness at room temperature and assume that it is temperature-independent. The effective thickness (t_{eff}) in the Si:B

Table 6.3: The effective thickness of boron-doped silicon layer at 300 K.

x	300 K n_s ($\times 10^{12}$ cm^{-2})	n_{2DHG} ($\times 10^{11}$ cm^{-2})	t_{eff} (nm)	t_{nom} (nm)	E_A (meV)
0.10	11.60	1.57	40	70	12 ± 1
0.13	30.30	2.11	105	50	57 ± 1
0.20	2.98	0.10	13	25	24 ± 1
0.36(a)	5.55	1.00	24	25	37 ± 1
0.36(b)	7.12	0.30	31	50	25 ± 3
0.45	9.20	3.00	39	50	17 ± 7

layer at 300 K is estimated by

$$t_{eff} = 0.7 \left(\frac{n_s - n_{2DHG}}{0.8 \times N_a} \right) \times 10^7, \tag{6.5}$$

where n_s is the measured carrier density and n_{2DHG} is the 2DHG carrier density. The prefactor 0.7 is the Hall factor and the factor 0.8 comes from the fact that 80% of boron is ionised at room temperature [Li (1978)]. The result is shown in table 6.3 in which the effective thickness of all samples, except $x = 0.13$, are less than the nominal thicknesses. This is in good agreement with the presence of surface depletion in our samples. For sample $x = 0.13$, the effective thickness is about twice the nominal thickness and this is very unusual. We have carried out a chemical etching experiment in which the surface of the $Si_{0.87}Ge_{0.13}$/Si sample was chemically etched slightly and this was followed by the Hall measurement. We found that the carrier density increases after the chemical etching at temperatures higher than 200 K. This indicates that this sample has the strong leakage current through the substrate.

The background doping in our MBE system is known to be primarily n-type, possibly the phosphorus of $\sim 10^{15}$ cm^{-3}. For the acceptor concentration, the nominal boron-doping concentration as shown in table 6.1 will be used. The hole degeneracy is set to 4 because each acceptor impurity level can accept one hole of either spin and the impurity level is doubly degenerate as a result of the two degenerate valence

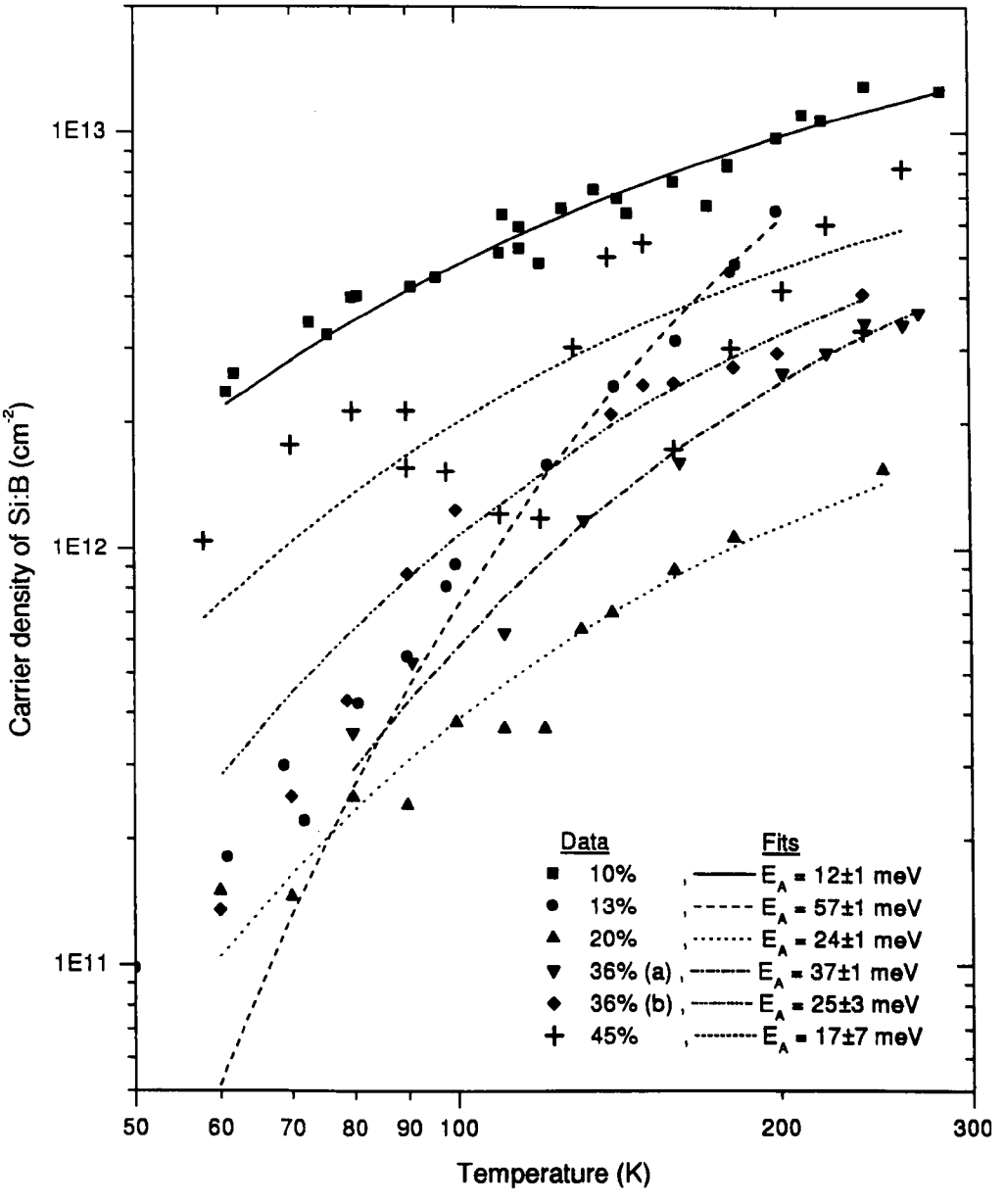

Figure 6.27: The temperature-dependent carrier density of the boron-doped silicon supply layer (2–2.5×10^{18} cm^{-3}) in several modulation-doped p-$Si_{1-x}Ge_x$/Si heterostructures ($0.10 \leq x \leq 0.45$). The fits are shown as solid lines.

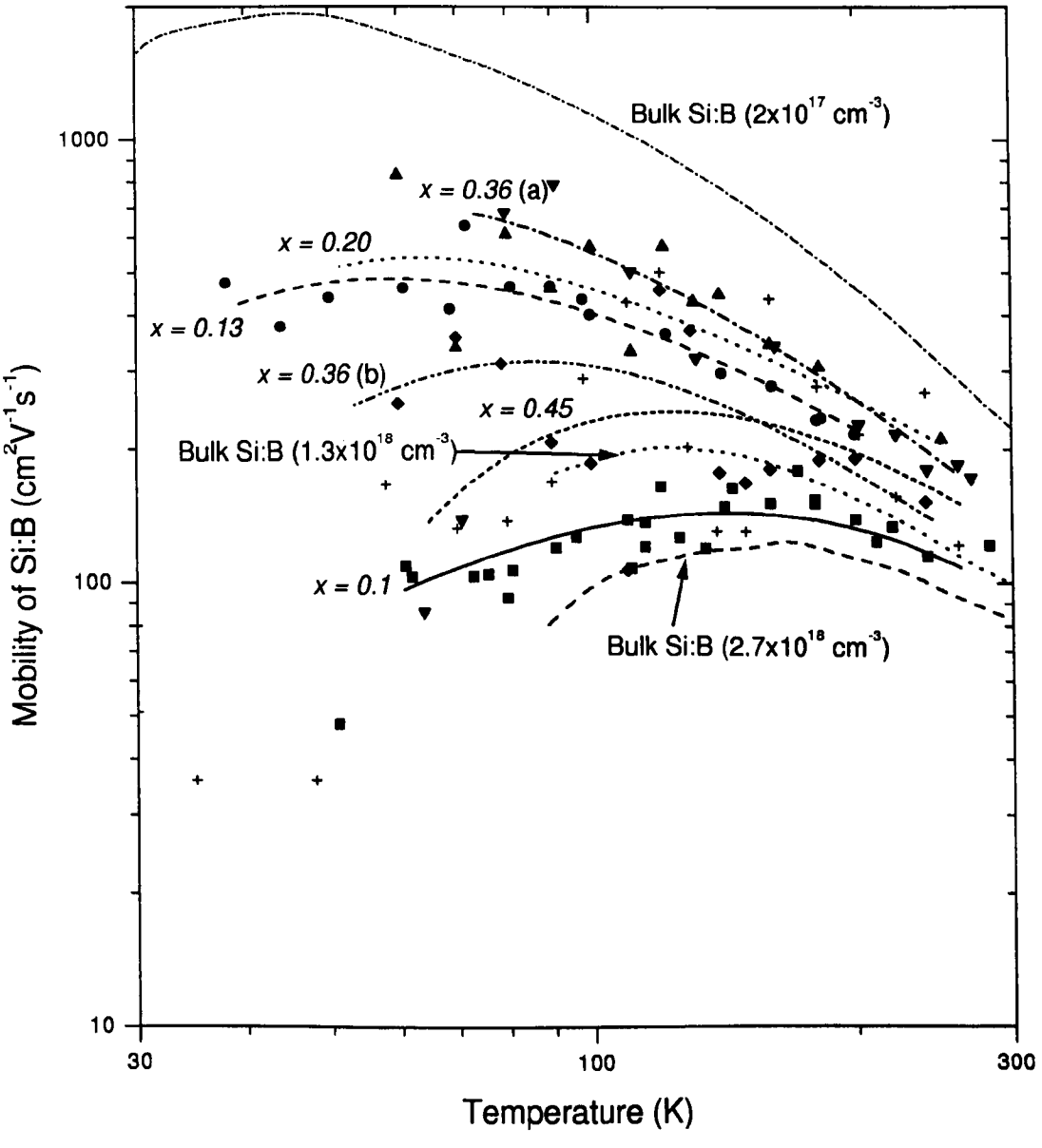

Figure 6.28: The temperature-dependent carrier mobility of the boron-doped silicon supply layer (2–2.5×10^{18} cm^{-3}) in several modulation-doped p-$Si_{1-x}Ge_x$/Si heterostructures ($0.10 \leq x \leq 0.45$). The solid lines are guides to the eyes. The mobility of boron-doped bulk silicon is taken from Pearson and Bardeen (1949) for 1.3×10^{18} and 2.7×10^{18} cm^{-3}, and from Morin and Maita (1954) for 2×10^{17} cm^{-3}.

band at $\mathbf{k} = 0$ (see Section 2.2.1). The final fits are shown in Fig. 6.27 as solid lines in which the activation energies range from 12 to 57 meV. These activation energies are much higher than those in bulk silicon, which are between 3–8 meV, for the same doping concentration [Manzini and Modelli (1989), Li (1978)]. In Fig. 6.29, we plot our activation energies on the well established $N_a vs. E_A$ curve which yields the doping concentration between 2×10^{16} and 2×10^{18} cm^{-3}.

The doping concentration of less than 2×10^{18} cm^{-3} seems to be possible when the temperature-dependent mobility of Si:B is taken into account. The temperature-dependent mobility of Si:B, as shown in Fig. 6.28, indicates that the doping concentration varies between 2×10^{17} and 2.7×10^{18} cm^{-3}. One possibility that decreases the boron doping concentration is that there is usually a boron-spike near the silicon buffer-silicon substrate interface and what we obtain from our analysis is the average between this boron spike and Si:B cap. In Fig. 6.30, the SIMS profile of boron in $Si_{0.64}Ge_{0.36}$/Si-(a) is shown in which the boron-spike is clearly seen over 12-nm full-width-half-maximum with the sheet concentration of 4×10^{11} cm^{-2}. The average concentration is around 5×10^{17} cm^{-3}. We can roughly combine these 2 carrier species at the low magnetic field using [Garchery et al. (1995)]

$$\overline{n} = \frac{(n_1\mu_1 + n_2\mu_2)^2}{(n_1\mu_1^2 + n_2\mu_2^2)}, \tag{6.6}$$

$$\overline{\mu} = \frac{(n_1\mu_1^2 + n_2\mu_2^2)}{(n_1\mu_1 + n_2\mu_2)}, \tag{6.7}$$

where $\overline{n}$ and $\overline{\mu}$ are the average carrier density and mobility, respectively. We can easily show that

$$\min(\mu_1, \mu_2) < \overline{\mu} < \max(\mu_1, \mu_2), \tag{6.8}$$

and

$$\min(n_1, n_2) < \overline{n} < n_1 + n_2. \tag{6.9}$$

In Fig. 6.31 we calculate $\overline{n}$ and $\overline{\mu}$ as functions of the ratio of n_{spike} to $n_{Si:B}$ using the parameters extracted from $Si_{0.64}Ge_{0.36}$/Si-(a) sample at 77 K. Because the mobility of

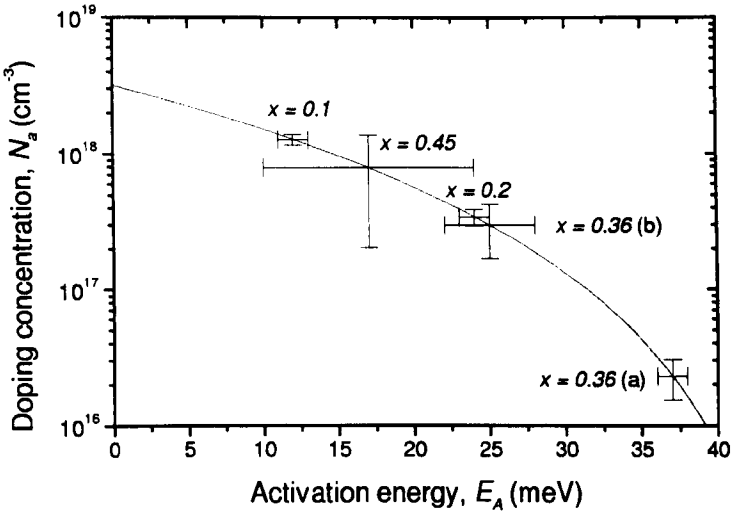

Figure 6.29: The activation energies of Si:B in various $Si_{1-x}Ge_x$/Si samples (horizontal error bar) plotted on the well established doping concentration versus the activation energy in bulk silicon (solid line) (after Li (1978), and Manzini and Modelli (1989)). The vertical error bars represent the range of doping concentrations, corresponding to the range of activation energy, for each sample.

boron-spike is currently unknown, it will be taken from the bulk silicon at the same doping concentration, which is $\sim$ 1,000 $cm^2V^{-1}s^{-1}$ [Morin and Maita (1954)]. At 77 K, the Si:B mobility is 100 $cm^2V^{-1}s^{-1}$ and the its carrier density is 1.2×10^{12} cm^{-2}, assuming that 30% of borons are ionised [Li (1978)]. For $Si_{0.64}Ge_{0.36}$/Si-(a) sample at 77 K, the $n_{spike}/n_{Si:B}$ ratio is 0.33 and the $\overline{\mu}$ is 780 $cm^2V^{-1}s^{-1}$, which agrees with the mobility of $x = 0.36$(a) shown in Fig. 6.28.

6.7 Electron-Like Carrier Species

6.7.1 General Considerations

The puzzle in the modulation-doped samples is the presence of the electron-like carrier species. Its mobility obtained by MCF scatters between that of boron-doped silicon and of the 2DHG, and tends to decrease with increasing temperatures. Its carrier

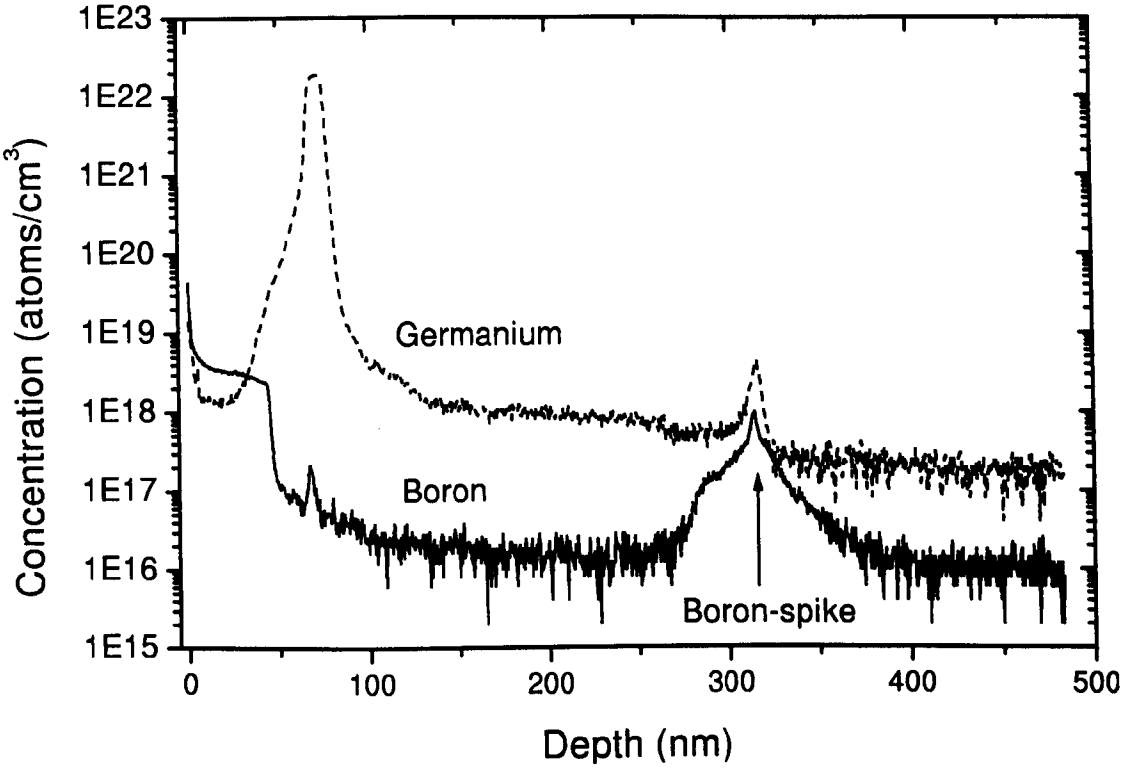

Figure 6.30: The boron and germanium profiles of $Si_{0.64}Ge_{0.36}$/Si-(a) sample. The boron-spike is located at about 20 nm above the Si/Si-substrate interface (after Grasby (2000)).

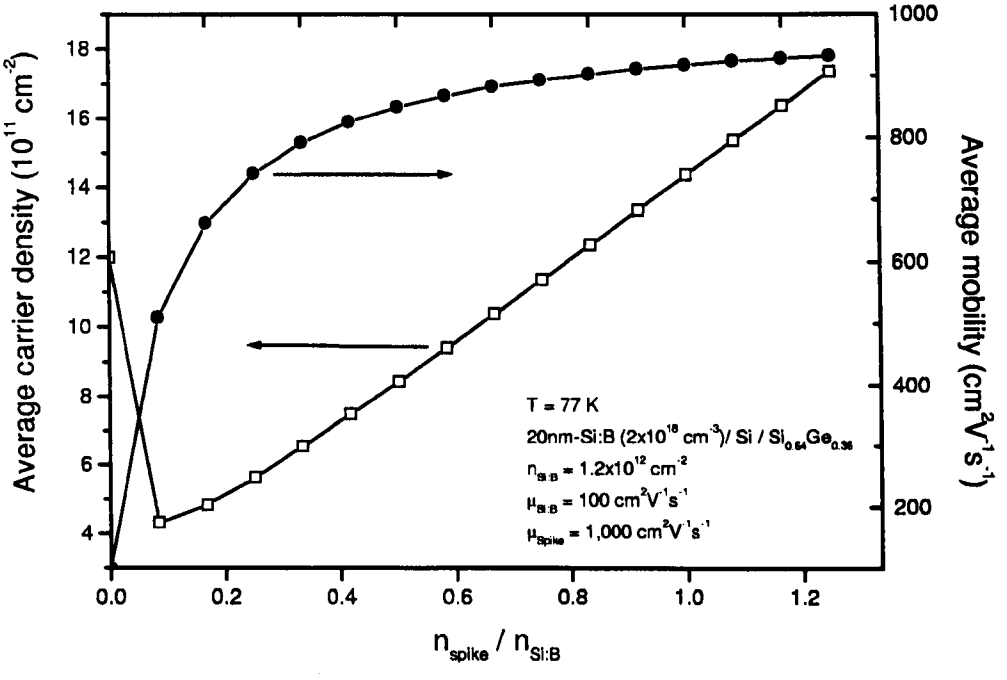

Figure 6.31: The average carrier density and mobility between Si:B and boron-spike in $Si_{0.64}Ge_{0.36}$/Si sample at 77 K.

density scatters between 3 $\times 10^{10}$–3×10^{11} cm^{-3} and tends to increase with increasing temperatures. The sheet conductivity of the electrons is found to be around 6–16% of the total sheet conductivity.

The source of this electron-like carrier species is presently unknown. The possible causes are :

1. It might come from the n-type substrate which is arsenic-doped at $\sim 10^{14}$-10^{15} cm^{-3}. However, the mobility of bulk arsenic-doped silicon at 2.1×10^{15} cm^{-3} is about an order of magnitude higher [Morin and Maita (1954)], and the carrier density due to the substrate with full ionisation and thickness (500 μm) should be 5 times lower. Two factors needs to be taken into account when considering this unknown electron-like carrier species from the substrate. Firstly, if the aluminium contacts diffuse deeper than the mesa thickness, the electron transport from the substrate is not only along the Hall bar but also unpredictably within the larger substrate. We have carried out a simple leakage-current-through-the-substrate test by making a back contact with indium-gallium paste on the scratched surface and measuring the current across front and back contacts. The leakage current was measured to be less than 1 nA at temperatures below 200 K for the applied voltage of 0.5 V. This leakage current cannot compare with the supplied current through the Hall bar which is typically 100 nA or higher. Secondly, the interface between aluminium contacts (p-type) and substrate (n-type) behaves in a nonohmic manner, producing a nonlinear I-V curve. With such a low leakage current, non-Hall bar geometry, and nonohmic contacts, it might be possible that the mobility and carrier density extracted could be much different from the bulk properties.

2. It might be the background doping which is phosphorus at the concentration of $\sim 10^{15}$ cm^{-3}. However, the mobility of bulk phophorus at this concentration is almost the same as the arsenic-doped [Norton et al. (1973)] which makes it unlikely to be responsible.

3. This electron-like carrier might be the minority carrier in the boron-doped silicon. Such minority carriers are reported to have a mobility of 300 and 100 $cm^2V^{-1}s^{-1}$ at 77 and 300 K respectively, for the boron doping concentration of 2.5×10^{18} cm^{-3} [Leu and Neugroschel (1993)]. Even though, these mobilities are not equal to our result, but at least they are in the same order of magnitude.

4. The unknown electron-like carrier might be the mobility harmonics as predicted by McClure's formalism. However, if the harmonics are to be observed via the spectrum, it is questionable that why only one peak, instead of two (harmonics of SiGe and Si:B), is observed. From the calculation viewpoint, the harmonics of 2DHG should be easier to obtain than of Si:B because the mobility of 2DHG is much higher than Si:B and higher than the inverse of maximum magnetic field. Therefore, the electron-like carrier observed may entirely represent the harmonics of 2DHG. For a slightly warped energy contour (2D), we expect to see this electron peak at a mobility 3 times the mobility of 2DHG if SiGe alloy possesses the 4-fold rotation symmetry. However, this predicted value is higher than the observed value which is around $0.8\mu_{2DHG}$ at all temperatures. Two possible explanations for obtaining the value of $0.8\mu_{2DHG}$, instead of $3\mu_{2DHG}$, is that i) if SiGe alloy is grown in such a way that it has 2-fold or 1-fold symmetry, we then expect to see the electron-like carriers at the same mobility as that of 2DHG, the value which is closer to $0.8\mu_{2DHG}$, and ii) the electron-like carrier of 2DHG and Si:B may be too close to be separated within the spectrum and MEMS can only yield a combined peak.

The observation of minority carriers in heterostructures grown on opposite-type substrates was often found in literature. For example, Colvard et al. (1989) pointed out in their multicarrier fitting of high electron mobility transistor structures (HEMTs) $Al_xGa_{1-x}As/GaAs$ that quality of the final fit shows significant improvement if a third layer is included which is p-type and has an unrealistic mobility close

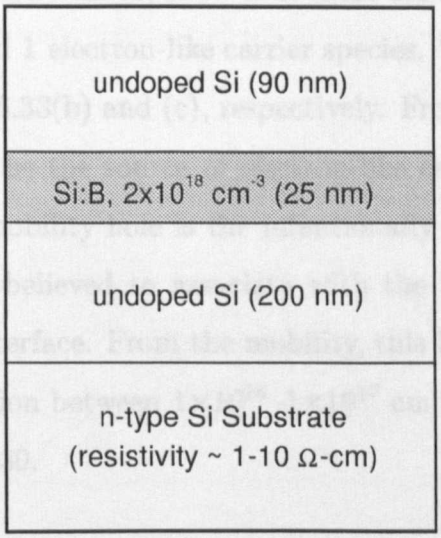

Figure 6.32: The cross-section schematic view of the expitaxial boron slab on the n-type substrate.

to that of the 2DEG. The source of this p-type carrier was not proved in their work and only was suspected to be the p-type substrate.

6.7.2 Boron Slab on an N-Type Silicon Substrate

To clarify whether the electron-like carrier species come from the SiGe alloy, a boron-doped silicon sample grown on an n^- substrate without the SiGe channel (Sample 50.36) was measured in the magnetic fields up to 12 Tesla, from 66 to 243 K, and with the number of magnetic field points between 10 and 30. Its schematic picture is shown in Fig. 6.32 and its low-field result is shown in Fig. 6.33(a). Unpredicatably, the Hall mobility reaches a maximum value of 1,000 $cm^2V^{-1}s^{-1}$ at 66 K, which is about an order of magnitude higher than the mobility of boron-doped bulk silicon at 2×10^{18} cm^{-3} (see Fig. 6.28). Its room temperature carrier density is also very much higher than the nominal value of 4×10^{12} cm^{-2} (2×10^{18} cm^{-3} $\times$ 25 nm $\times$ 0.8 (ionization percentage)). Furthermore, the activation energy was calculated to be 51 meV which is much higher than the expected value of 6–8 meV. The calculations by Beck and

Anderson analysis, MCF, and MEMS, show that there are 3 carrier species present in this sample, 2 hole-like and 1 electron-like carrier species. Their mobility and carrier density are shown in Fig. 6.33(b) and (c), respectively. From this result, we can only conclude that there must be the source of electron-like carrier species which is not the SiGe alloy. The low mobility hole is the intentionally boron-doped silicon while the high mobility hole is believed to associate with the boron-spike at the silicon buffer/silicon substrate interface. From the mobility, this boron-spike must have the average doping concentration between 1×10^{16}–1×10^{17} cm^{-3} which is consistent with the value shown in Fig. 6.30.

6.7.3 The Chemical Etching Experiment

This experiment was performed at the early stage of PhD. course in which the sample was fabricated into a greek-cross bar and the measurements were taken at between 10–12 data points in the magnetic field up to 12 Tesla. The gold wires and all aluminium contacts were protected by black wax which was painted carefully onto the sample and chip package. The measurement was done at 77 K with different chemical etching times. After a 7-minute-15-second etch, the carrier density of 2DHG decreases dramatically and the measurement was taken in the temperature range 40–220 K to check the temperature dependence of each carrier species. The magnetic-field-dependent sheet resistivity and Hall coefficient were fitted by the multicarrier fitting using 3 carrier species.

It was found that chemical etching alters every carrier by reducing their carrier density while their mobilities were held essentially constant. In Fig. 6.34 we plot the sheet conductivity, i.e. the product of mobility and carrier density, of boron-doped silicon against that of electron and 2DHG. In Fig. 6.34(a), the sheet conductivity of electron tends to decrease with decreasing sheet conductivity of the Si:B. This means that there is a corelation between the electron-like carrier and the Si:B. Figure 6.34(b) shows that sheet conductivity of the 2DHG is independent of boron-doped silicon as

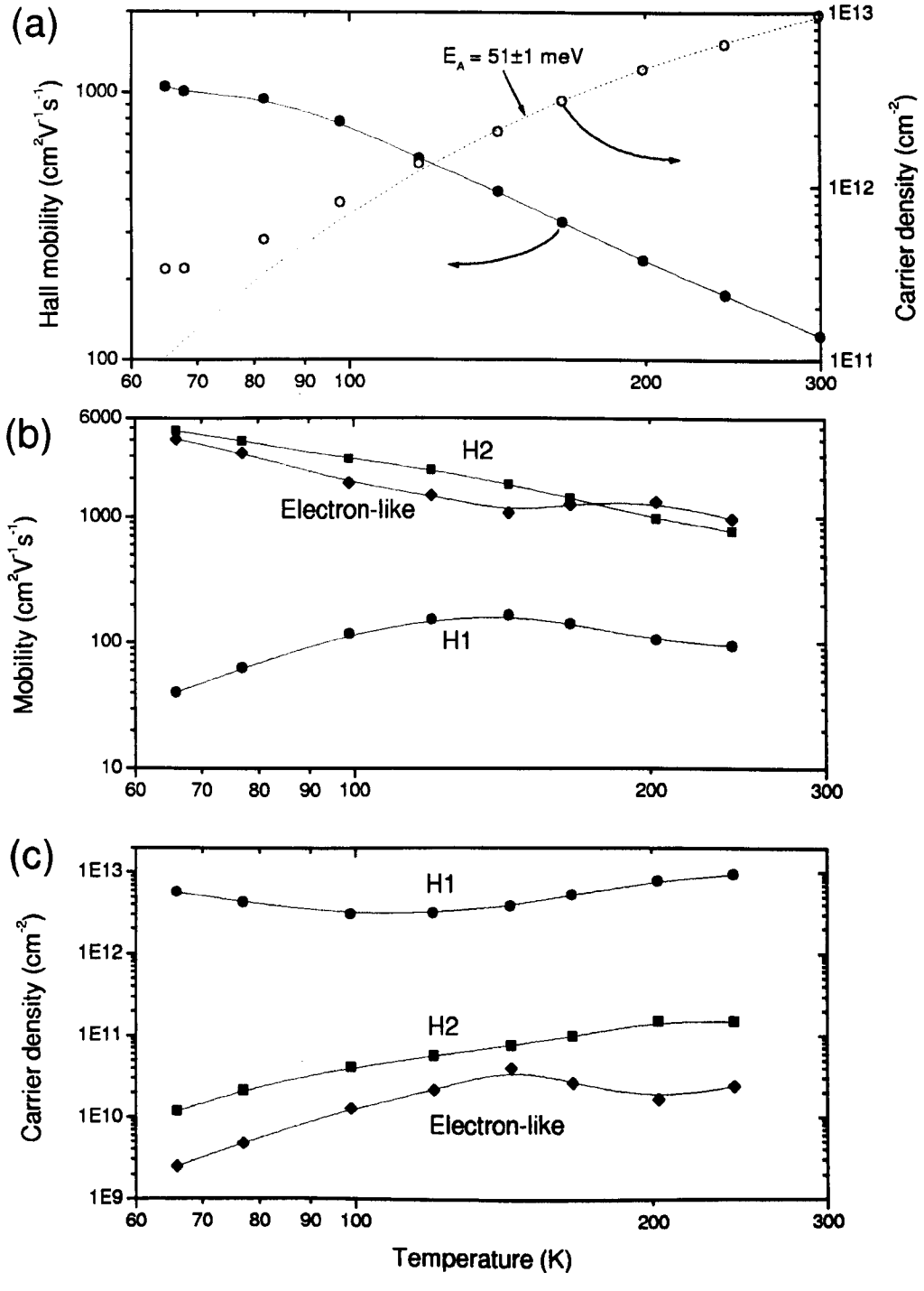

Figure 6.33: (a) The Hall mobility and carrier density of epitaxial boron-doped silicon grown on the n-type silicon substrate. (b) The mobility and (c) carrier density of each carrier species obtained from MCF.

long as the Si:B sheet conductivity is greater than 3.5×10^{-5} sq.Ω^{-1}. At the boron sheet conductivity of 2.2×10^{-5} sq.Ω^{-1}, the sheet conductivity of the 2DHG drops significantly by 50 %. The extrapolated line passes the origin which agrees with the knowledge that there is no 2DHG if the boron-cap is totally depleted. Also shown is the result after 7 minute 15 second etch at different temperatures. It can be seen that the sheet conductivity of boron increases with increasing temperature while that of the 2DHG decreases.

In addition, we have observed that the 2DHG carrier density in the 7-minute-15-second etched sample decreased monotonically with increasing temperatures, that is 1.28×10^{11} cm^{-2} at 44 K and 8.08×10^{10} cm^{-2} at 215 K. We also found that by chemical etching, the 2DHG peak in the maximum-entropy mobility spectrum can be enhanced because the boron-doped silicon peak is reduced. The example is shown in Fig. 6.35 which compares the MEMS before and after chemical etching at the temperature around 260 K. We can see that 2DHG peak starts to apprear as a shoulder to the main boron-doped silicon peak. However, we did not attempt to etch until the Si:B and 2DHG peaks are clearly separated because of time-consuming issues.

6.8 The Interpretation of Temperature-Dependent Sheet Resistivity

After all preceding analyses, the temperature dependence of the sheet resistivity can now be explained. In Figs.6.36 and 6.37, we plot the sheet resistivity at zero magnetic field and the sheet resistivity corresponding to each carrier species in $Si_{0.9}Ge_{0.1}$/Si and $Si_{0.64}Ge_{0.36}$/Si-(a), respectively. It should be recalled that the former has only one sheet resistivity maximum while the latter has two such maxima. The sheet resistivity of each carrier species is calculated from the inverse of the sheet conductivity. In both figures, we can see that the sheet resistivity of 2DHG increases monotonically

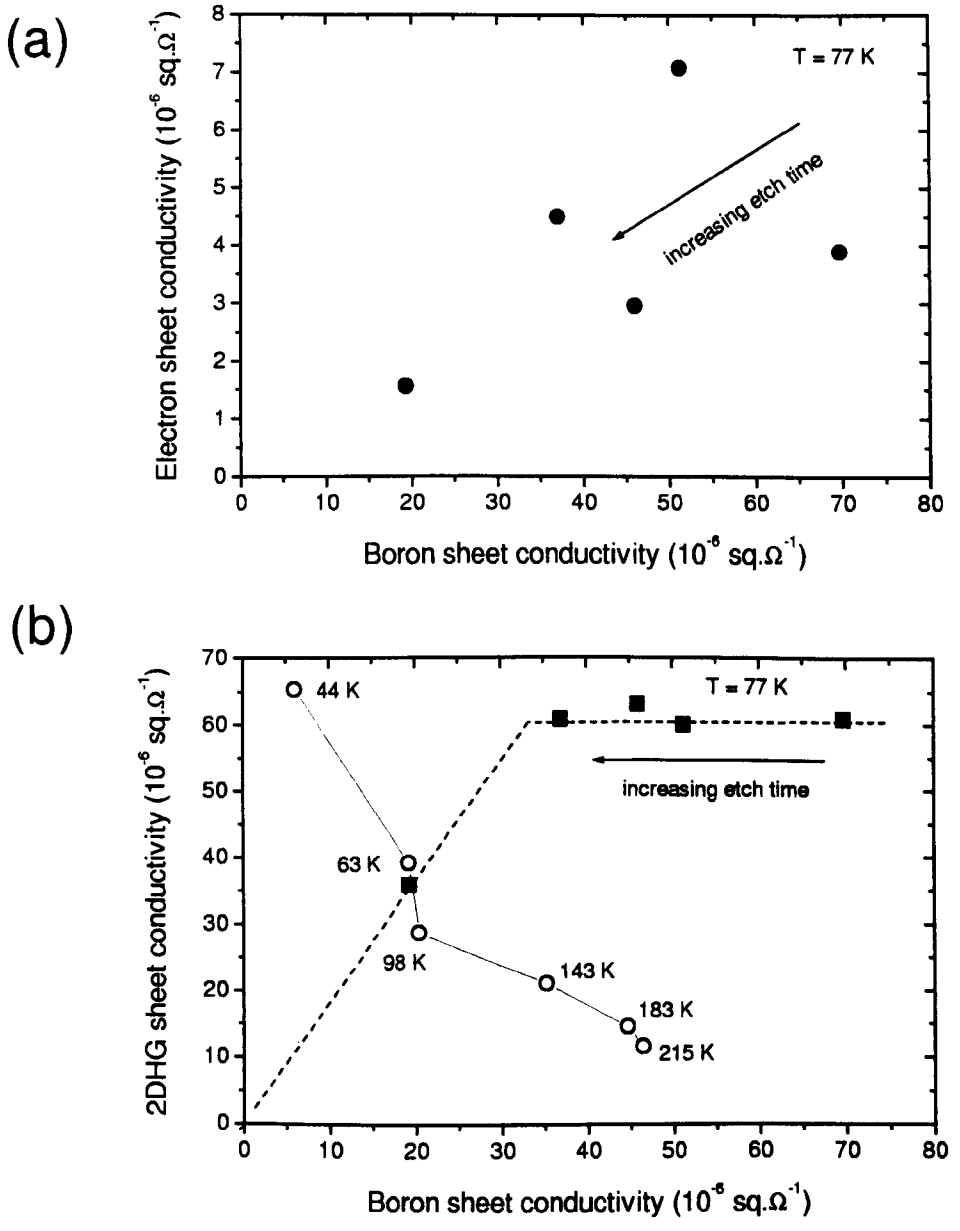

Figure 6.34: The sheet conductivity of each carrier species in $Si_{0.9}Ge_{0.1}/Si$, obtained from MCF. (a) The plot between the boron-doped silicon and electron-like carrier species at 77 K, and (b) the plot between boron-doped silicon and 2DHG at 77 K with different etch times (solid squares) and after 7-minute-15-second etch at different temperatures (open circles).

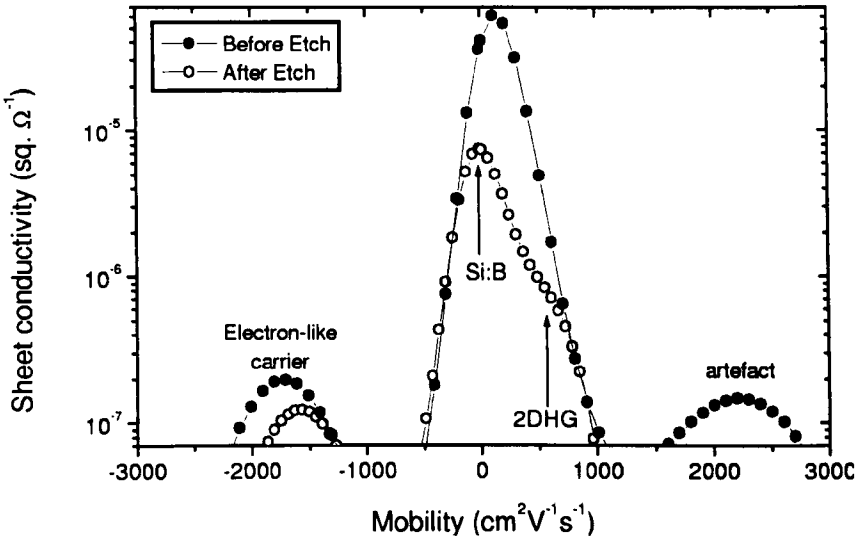

Figure 6.35: MEMS of $Si_{0.9}Ge_{0.1}$/Si sample before and after 7-minute-15-second chemical etching at temperatures around 260 K.

with increasing temperatures while that of Si:B decreases. They cross over in the temperature range 70–100 K and this causes the maximum. For the second maximum as presented in Figs. 6.37 at temperatures around 260 K, this is due to the decreasing of 2DHG carrier density and hence further increasing in the 2DHG sheet resistivity. In the temperature range 150–300 K of Figs. 6.36 and 6.37, the sheet resistivity of 2DHG in the $Si_{0.9}Ge_{0.1}$/Si sample increases less progressively than in the $Si_{0.64}Ge_{0.36}$/Si-(a) sample. The former has $T^{1.65}$ dependence while the latter has $T^{3.04}$ dependence.

6.9 Hall Factor

The Hall factor of the two-dimensional hole gas (2DHG) is calculated by using Eq.2.50 for the peaks which are associated with the 2DHG. In most cases where three peaks are clearly resolved, the 2DHG peak can be easily determined as the peak at highest positive mobility. For MEMS with either 2, 4, or 5 peaks, the sources of these peaks are still unclear at present. Therefore, the Hall factor will be calculated for 2DHG

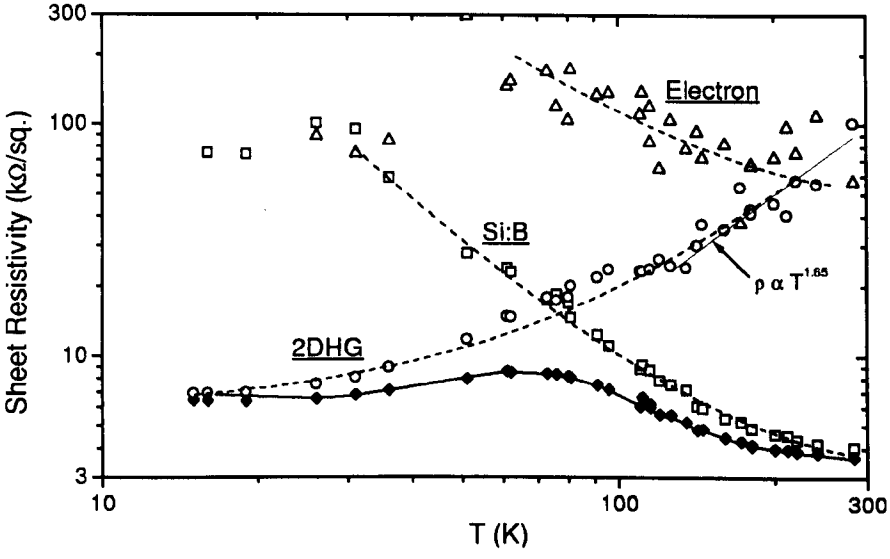

Figure 6.36: The sheet resistivity of each carrier species in $Si_{0.9}Ge_{0.1}$/Si sample.

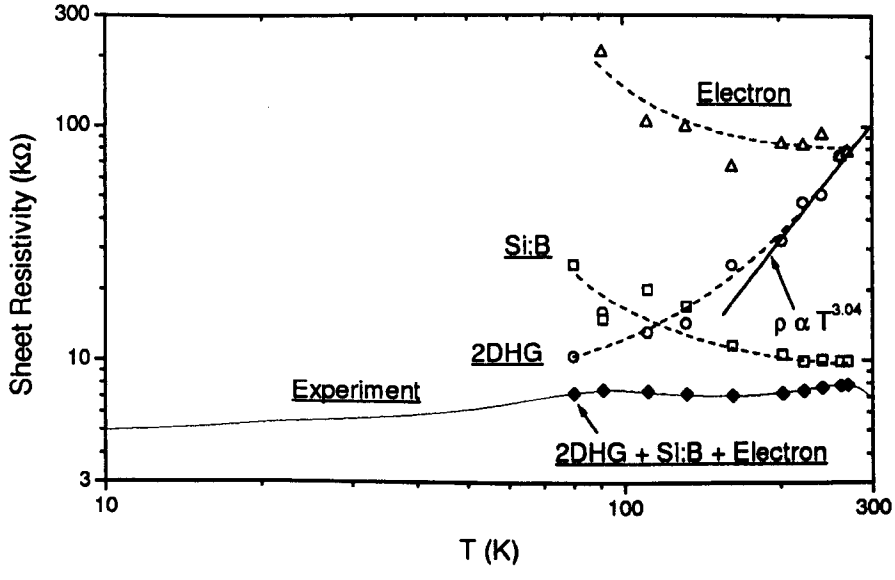

Figure 6.37: The sheet resistivity of each carrier species in $Si_{0.64}Ge_{0.36}$/Si-(a) sample.

from MEMS which shows clearly the 2DHG, the cap layer, and one electron-like carrier species.

In the calculation, the Hall factor of the 2DHG will be computed with and without the electron-like peak despite its unknown source, except for $Si_{0.64}Ge_{0.36}$/Si-(b) which has no electron-like peak. This is because, without the negative mobility, the Hall factor of the 2DHG will be always greater than unity (see section 2.5.2) while with the negative mobilities, the Hall factor can be lowered toward unity or even less than unity. Therefore, the result will be an envelope of possible Hall factors of the 2DHG as function of temperature and germanium content. It should be recalled that if the electron-like carrier could be proved to associate with the 2DHG, it would represent the anisotropy of the band structure in the undoped SiGe alloy; the further away the energy contour is from the sphere, the more the electron-like contribution is.

The Hall factors for 2DHG in $Si_{0.9}Ge_{0.1}$/Si, $Si_{0.64}Ge_{0.36}$/Si-(b), and $Si_{0.55}Ge_{0.45}$/Si samples are shown in Fig. 6.38. The Hall factor of $Si_{0.8}Ge_{0.2}$/Si sample is calculated using the data from the pulsed-magnetic field measurement at 41 T. Also shown are the Hall factors of $Si_{0.8}Ge_{0.2}$/Si sample obtained by Hall and Strip technique [McGregor et al. (1999)] and by the combination of Capacitance-Voltage (CV) and Hall measurements [Lander et al. (1997)]. We can see that the minimum of Hall factor in $Si_{0.8}Ge_{0.2}$/Si sample obtained by MEMS technique agrees well with those thechniques within their scattering range. Because the source of electron-like carrier is not verified, we shall not attempt to compare our result with those in literature, but only to summarise the current work on the Hall factor as follows.

The Hall factor in undoped strain SiGe alloy may be constructively considered from the pure Si and Ge. In Fig. 6.39, the Hall factor of highly pure p-type Si and Ge are shown [Blood and Orton (1992)]. Without the ionized impurity scattering, the Hall factor in both cases tends to merge into the same value of ~ 1 at low temperature. As the temperature increases, the phonon scattering becomes dominant and this

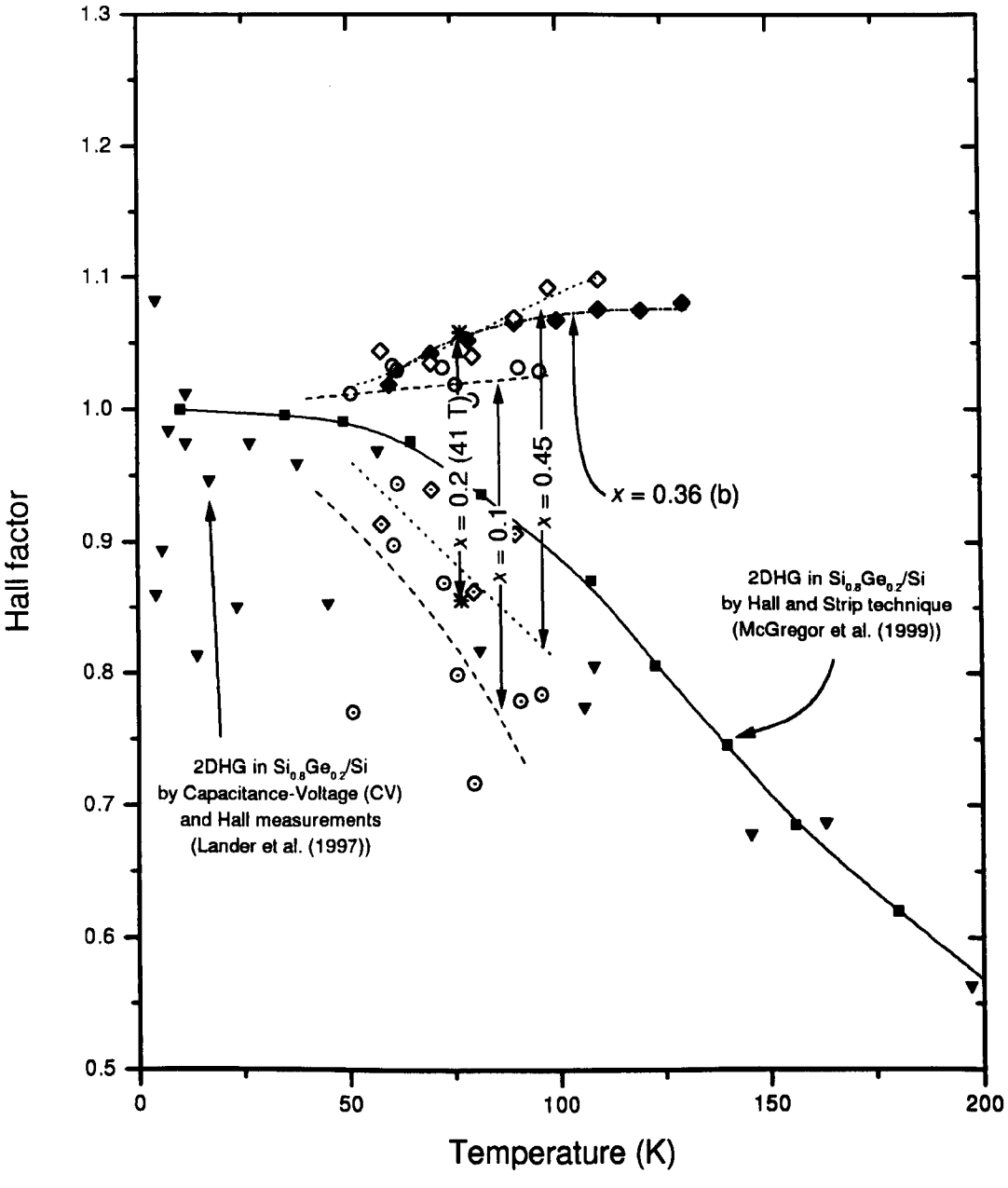

Figure 6.38: The Hall factor of the two-dimensional hole gas in the modulation-doped p-type $Si_{1-x}Ge_x/Si$ heterostructures for $x = 0.1$, 0.2, 0.3, and 0.45. The Hall factor for each sample is determined from the 2DHG peak in MEMS and is given in the form of the enevelope, the possible range of Hall factor, as a function of temperature.

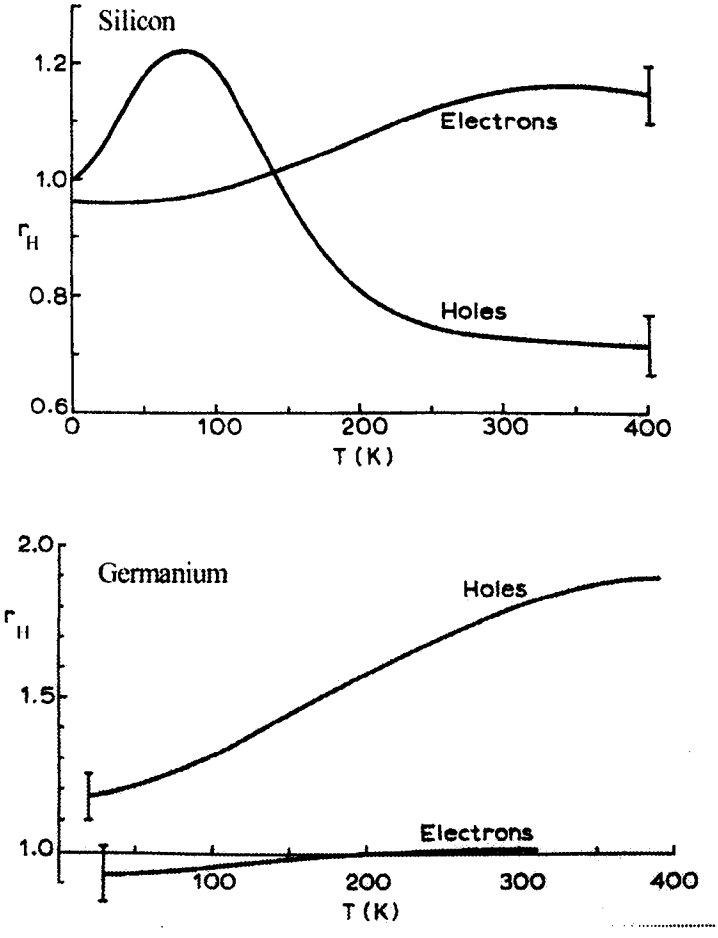

Figure 6.39: The Hall factor of pure (10^{14}–10^{15} cm^{-3}) Si and Ge versus temperature (taken from Blood and Orton (1992)).

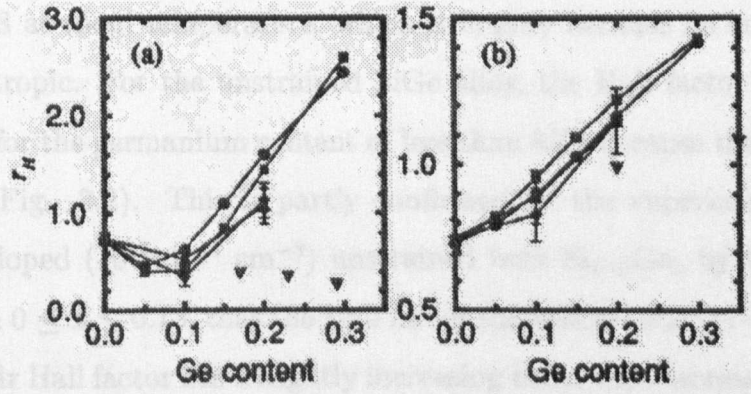

Figure 6.40: Hall factor in (a) strained and (b) unstrained $Si_{1-x}Ge_x$ calculated for different alloy scattering potentials (0–0.8 eV) (after Dijkstra and Wenckebach (1999)). The experimental data of heavily boron-doped strained (after Joelsson et al. (1997)) and unstrained $Si_{1-x}Ge_x$ (after Chen et al. (1994)) are shown as down triangles.

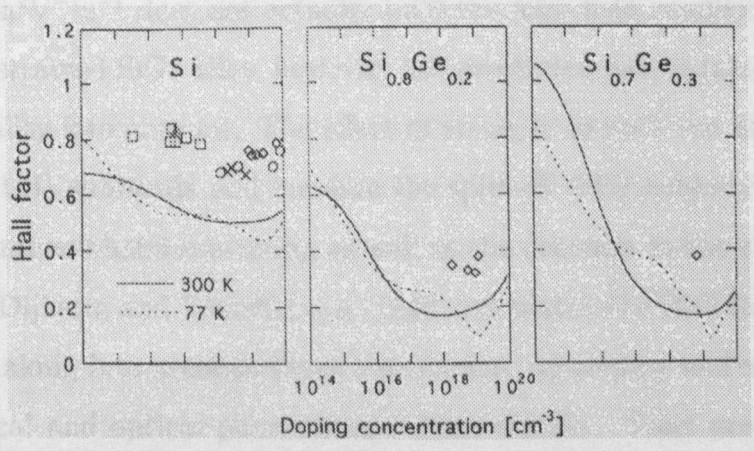

Figure 6.41: Calculated Hall factors of strained-$Si_{1-x}Ge_x$ alloy grown on (001) Si for x = 0, 0.2, and 0.3 (lines). The experimental results are showns as symbols (after Fu et al. (1996)).

increases the Hall factor of pure Ge to a well-established value of 1.8. However, that of pure silicon increase to 1.2 at around 100 K and then decreases monotonically to the value of 0.8 at room temperature, which is mainly because its energy surface is strongly anisotropic. For the unstrained SiGe alloy, the Hall factor is the same as that of silicon for the germanium content of less than 85% because the bandstructure is Si-like (see Fig. 2.2). This is partly confirmed by the experimental results on lightly boron-doped (10^{15}–10^{16} cm^{-3}) unstrained bulk $Si_{1-x}Ge_x$ by Gaworzewski et al. (1998) with $0 \leq x \leq 0.13$, that the Hall factor scatters around 0.7–0.8. In fact, we notice that their Hall factor has a slightly increasing trend with increasing germanium contents, a result which is theoretically predicted by Dijkstra and Wenchebach (1999) (see Fig. 6.40). Chen et al. (1994) measured the Hall factor of boron-doped (10^{17} cm^{-3}) relaxed $Si_{1-x}Ge_x$ grown on a Si substrate using a high magnetic field of 10 T. In the limit $\mu_H B \gg 1$, the Hall mobility equals the drift mobility which can be used as a reference point for comparison with low field measurements. The resultant Hall factors are 0.8 for $x = 0.22$ and 1.1 for $x = 0.35$ (see Fig. 6.40(b)). Even though this result seems to follow the prediction, the magnetic field of 10 T and the Hall mobility of 100–1,000 $cm^2V^{-1}s^{-1}$ does not actually fulfil the high field condition ($\mu_H B \gg 1$).

For the strained SiGe alloy, however, the prediction has to take the strain and the dimensionality into account. The effect of strain is to split the heavy-hole (HH) and ligh-hole (LH) subbands and increase the split-off (SO) subbands energy. This results in less intersubband scattering as well as the decrease in the effective mass of the HH band. Dijkstra and Wenchebach (1999) calculated the Hall factor of strained SiGe alloy by taking into account those 3 subbands, anisotropy and nonparabolicity, strain, acoustical and optical phonons, and alloy disoder. They predicted that the Hall factor will initially decrease from 0.8 for $x = 0$ to ~ 0.4 at $x = 0.1$, and then monotonically increase to unity at $x \sim 0.16$, and 2.4–2.6 at $x = 0.3$ (see Fig. 6.40(a)). The reason that the Hall factor decrease initially is because of the effect of strain. As the Ge contents rises, the valence band become more Ge-like which has less anisotropy

and therefore the Hall factor increases to the value greater than 1. The less anisotropy might be indirectly linked to the fact that the ratio of sheet conductivity of electron-like carrier species to 2DHG in our $Si_{0.9}Ge_{0.1}$/Si sample is significantly higher than that in other samples. On the other hand, Fu et al. (1996) calculated the Hall factor in strained SiGe with an additional ionized-impurity scattering and shows that for a fixed germanium content and temperature, the Hall factor decreases dramatically with increasing doping concentration (see Fig. 6.41). For very low doping-concentration ($\sim 10^{14}$ cm^{-3}), their result can be treated as the undoped strained SiGe alloy case. It shows that at 300 K, the Hall factor drops slighly from 0.66 for $x = 0$, to 0.62 for $x = 0.2$, and then increases to 1.05 for $x = 0.3$. A similar trend is also evident at 77 K. Even though the 300K Hall factor of undoped strained SiGe (Fig. 6.40(a)) and of lightly doped strained SiGe (Fig. 6.41) are different in magnitude, both results produce the similar trend that the Hall factor will decrease intitially with increasing germanium contents, and reach the minimum at $x \sim 0.1$–0.2 and then monotonically increase to a value close to or higher than 1.

6.10 Energy Dependence of the Relaxation Time

One objective of developing MEMS is that the smooth peak shape will enable us to calculate the power of energy dependence of the relaxation time accurately by using Eq.2.40. Because the peak shape can be affected by various factors, i.e. the number of iterations, the range of magnetic fields, and the range of mobilities, we therefore need to establish the condition where the peak shape will be independent from these factors.

We measured the sheet resistivity and Hall coefficient of the $Si_{0.9}Ge_{0.1}$/Si sample as functions of 1025 magnetic field points up to 12 Tesla at 27 K. We performed the calculation at this temperature because the transport can be treated classically and the Hall mobility is very high ($\sim$ 6,000 cm^{2}V^{-1}s^{-1}). The magnetic field depen-

dence effect was examined by choosing 36 magnetic field points equally spaced up to different maximum magnetic fields and performing the maximum-entropy mobility spectrum calculation for 200 mobility points (100 positive and 100 negative mobility points) for 200,000 iterations. The iteration dependence of the peak shape has already been observed in Fig. 6.11 and we will not repeat it here. We estimate that the use of 200,000 iterations would produce the uncertainty of about 5% in α which is much less than the variation of α on other factors, i.e. the range of magnetic fields and the number of data points.

The result, as illustrated in Fig. 6.42, shows that the spectrum is significantly distorted when $\mu B_{max} < 2.37$, where μ is the Hall mobility of the sample. That is the boron-doped silicon peak disappears and the two-dimensional hole gas peak broadens and shifts. The fit of Eq.2.40 to the two-dimensional hole gas peak yields parameters α and μ_0, which are shown in Fig. 6.44(a). The broadening can be seen from the increase in α while the shift in mobility is seen from the changes in μ_0. The broadening is theoretically due to the lowering of magnetic field dependency. Having less magnetic field strength means that one has less information about the sample; the situation in which the maximum-entropy approach is more reluctant to draw any conclusion about that carrier and can only give as broad a peak as possible.

The number of data points also affects the spectrum. We shows this by increasing the number of data points (M) (or decreasing the number of mobility points (N)) for the case of $\mu B_{max} = 1.37$. The results are shown in Fig. 6.43 in which the recovery of the two-dimensional hole gas peak is observed as its peak gets sharper with increasing number of data points (M). The μ_0 and α of two-dimensional hole gas are plotted in Fig. 6.44(b), both of which saturate at 5,074 $cm^2V^{-1}s^{-1}$ and 0.1 respectively for $M/N \geq 1$.

In Fig. 6.45, we summarize qualitatively the resolving power of the MEMS technique in order to yield a peak at the mobility μ accurately as a function of μB_{max} and M/N. The quantitative picture must await thorough mathematical investigation.

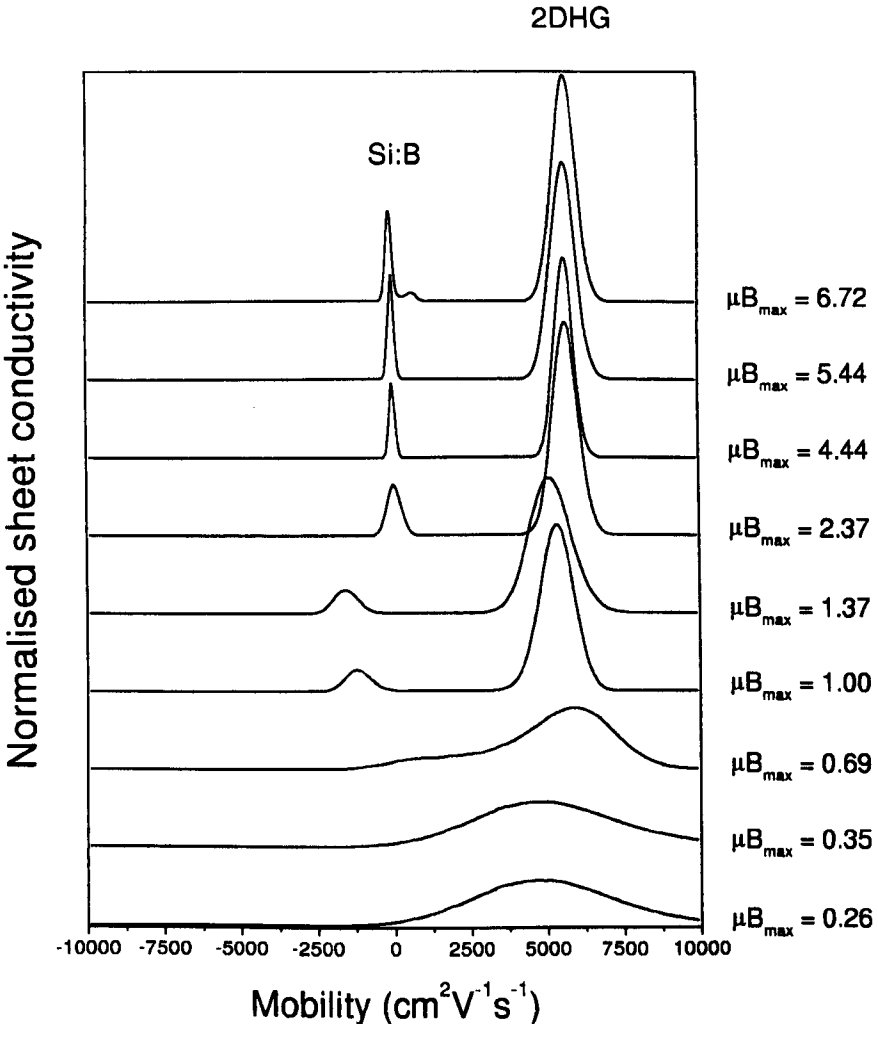

Figure 6.42: The dependence of MEMS on the product μB_{max} using the data of $Si_{0.9}Ge_{0.1}/Si$ at 27 K. The mobility μ is the Hall mobility of the sample while B_{max} is the maximum magnetic field.

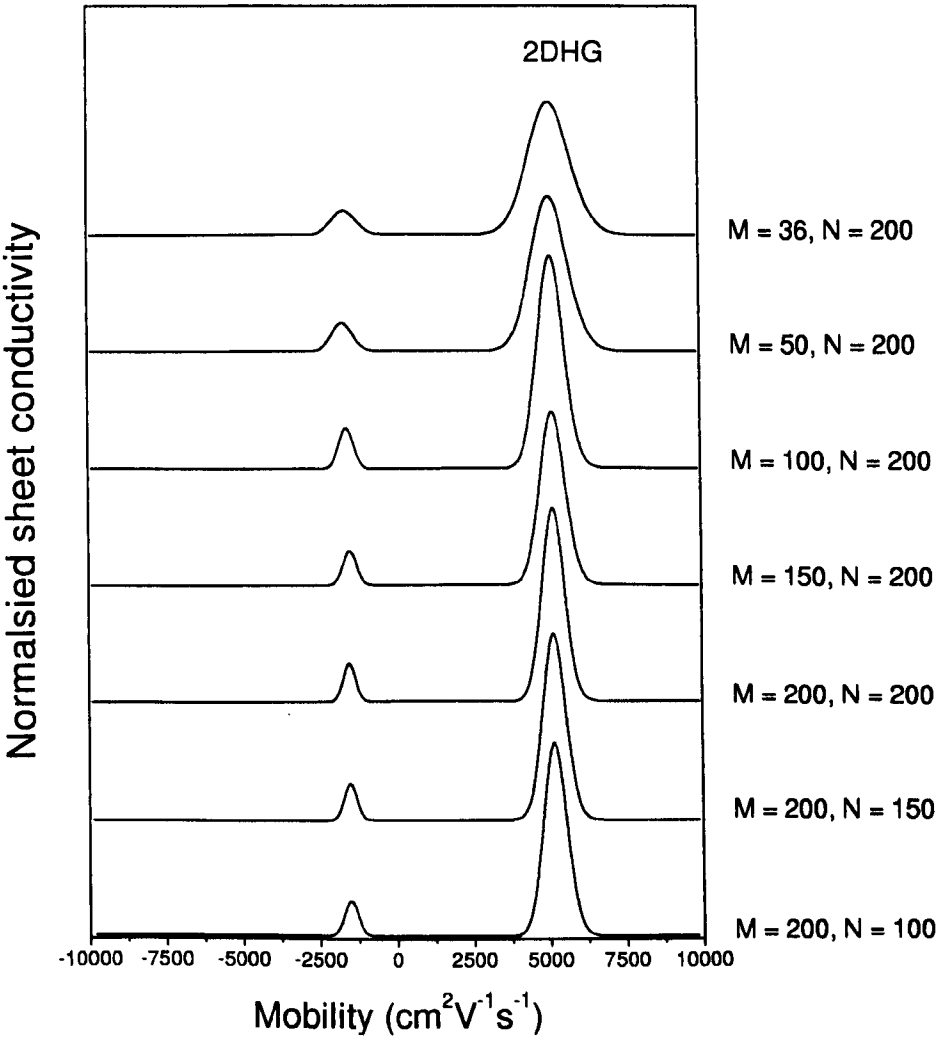

Figure 6.43: The dependence of MEMS on the number of magnetic field points (M) and that of the mobility points (N).

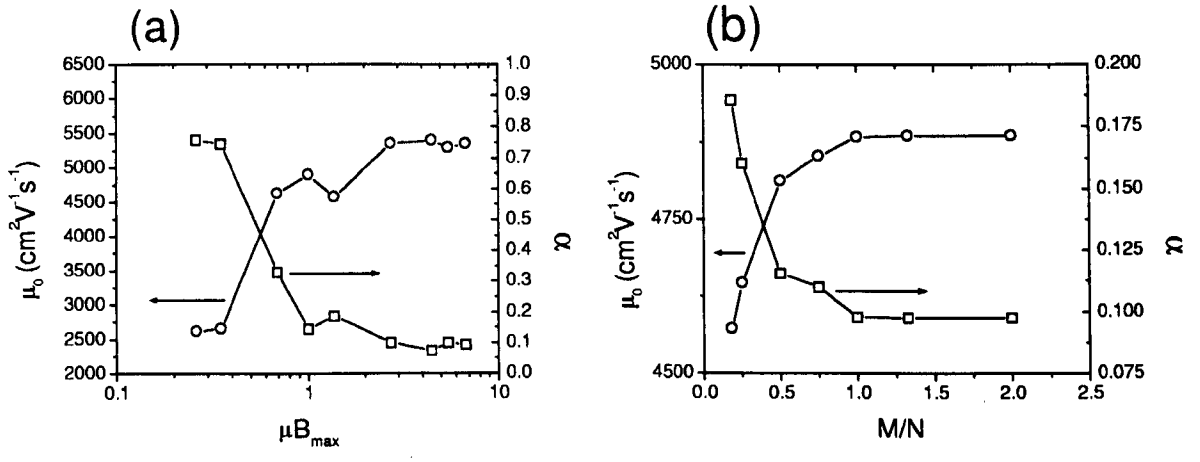

Figure 6.44: Parameters μ_0 and α from the fits of Eq. 2.40 to 2DHG peaks in Fig. 6.42 and Fig. 6.43 which are shown in (a) and (b), respectively.

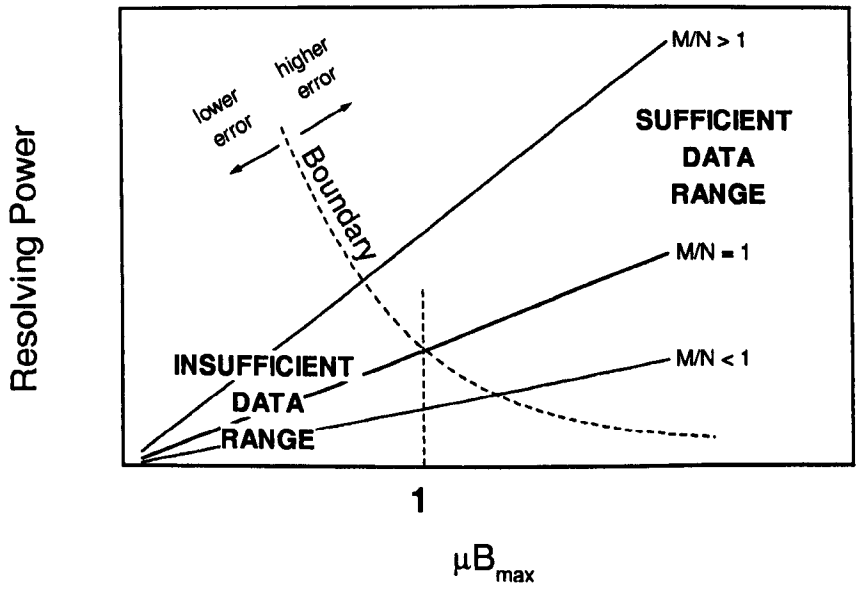

Figure 6.45: The schematic picture of relation between resolving power, the maximum magnetic field, and the ratio of the number of data points (N) to the number of magnetic field points (M).

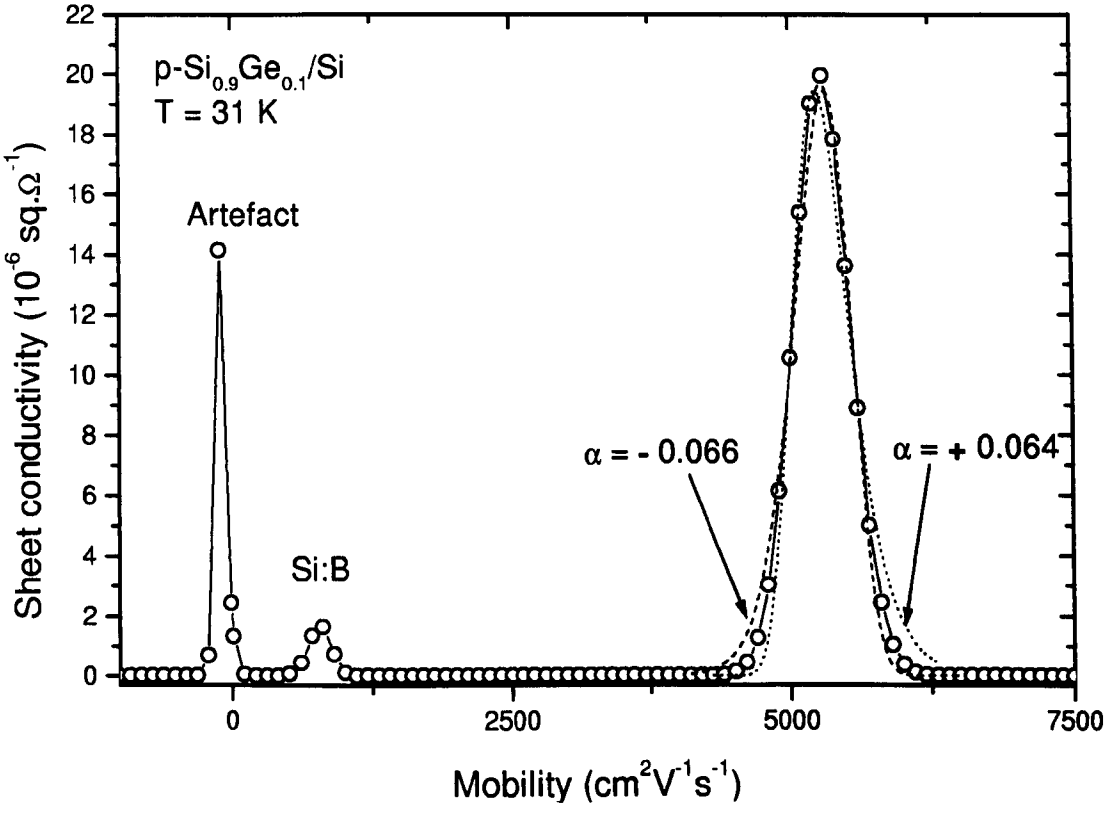

Figure 6.46: The fit of Eq.2.40 to 2DHG peak of MEMS of $Si_{0.9}Ge_{0.1}/Si$ at 31 K, for positive and negative values of α.

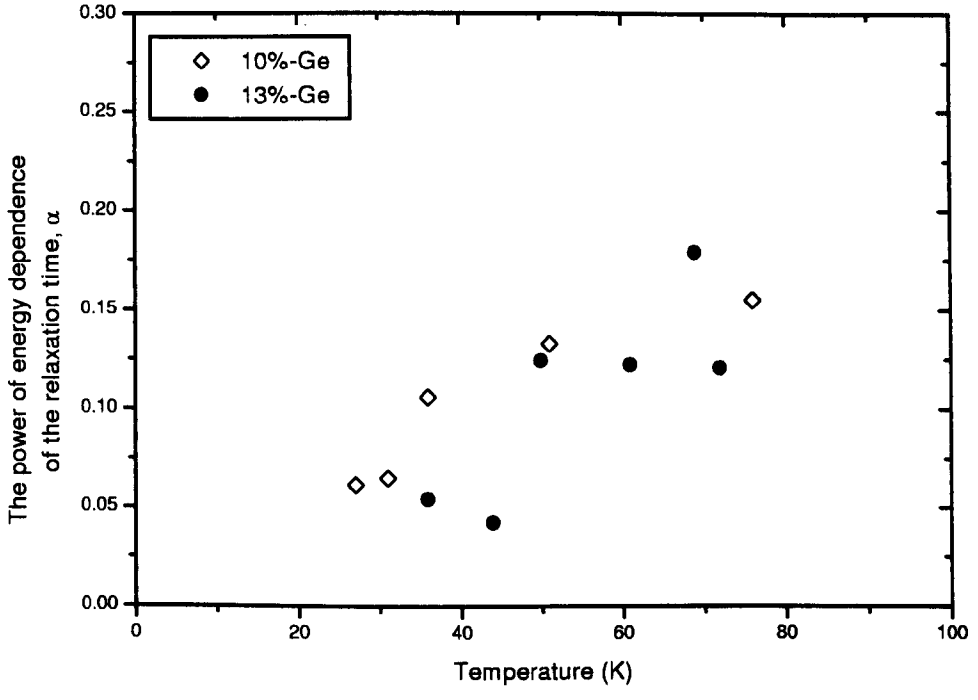

Figure 6.47: The absolute power of energy dependence of the relaxation time versus temperature for 2DHG of the modulation-doped $Si_{0.9}Ge_{0.1}/Si$ and $Si_{0.87}Ge_{0.13}/Si$ samples.

The peak shape of 2DHG for $Si_{0.9}Ge_{0.1}$/Si and $Si_{0.87}Ge_{0.13}$/Si with mobilities higher than 2,500 $cm^2V^{-1}s^{-1}$ is fitted by Eq.2.40 which yields s_0, μ_0 and α at different temperatures. The most important parameter is α because it relates to the power of energy dependence of the relaxation time. We note that the peak of 2DHG is quite symmetric while Eq.2.40 is the unsymmetric function around μ_0. Moreover, there are two equally good fits to the 2DHG peak with opposite signs of α. For example, Fig. 6.46 shows the fit results to the 2DHG peak of $Si_{0.9}Ge_{0.1}$/Si sample at 31 with α of -0.066 and $+0.064$. However, we would like to stress that these fits are much better than that reported by Reginski et al. (1997) who employed the iterative technique.

In order to decide which sign is more suitable, the temperature dependence of the mobility is considered. In table 6.4, we summarize the α, K (Hall scattering factor), and power of temperature dependence of the mobility for 3D and 2D cases, for various scattering mechanisms. In comparison with 3D case, the power of temperature dependence of 2D is higher by 0.5 because the relaxation time in a 2D gas acquires the additional $T^{\frac{1}{2}}$ factor [Shik (1997)], which comes from the difference in the density of states (see Eq.2.44). Because the mobility of 2DHG has the negative temperature dependence for 31 K and the thermal energy is much smaller than the optical phonon energy, which is 61 meV for Si and 37 meV for Ge [Fischetti and Laux (1996)], it is then justified to chose the positive α for these temperatures, and higher.

Figure 6.47 shows the α versus temperature for 2DHG in $Si_{0.9}Ge_{0.1}$/Si and $Si_{0.87}Ge_{0.13}$/Si samples within the temperature range 25–80 K. Below 25 K, Eq.2.40 is inapplicable because it is formulated for nondegenerate carriers. For temperatures higher than 80 K, the mobility of 2DHG is less than 2,300 $cm^2V^{-1}s^{-1}$ and the calculated α will be inaccurate. From this figure, we can see that α tends to decrease with decreasing temperature and seems to be zero at around 0–10 K. The increase in α (either positive or negative value) can be qualitatively seen from the broadening in the 2DHG peak in Figs. 6.12 and 6.13. The Hall scattering factor calculated from Eq. 2.50 increases with increasing $|\alpha|$ and the Hall scattering factor calculated with

Table 6.4: α of Eq.2.35, the calculated values of the Hall scattering factor K in the relaxation time approximation, and the power of temperature dependence of the mobility, for various scattering mechanisms (compiled from Nag (1980), Blood and Orton (1992), and Shik (1997)).

Mechanism	α ($\tau \propto E^{-\alpha}$)	**K** (Hall scattering factor in 3-D)	Power of temperature dependence of μ	
			for 3-D	for 2-D
Ionized impurities	$-\frac{3}{2}$	$\frac{315\pi}{512} = 1.93$	$\frac{3}{2}$	2
Neutral impurities	0	1	0	$\frac{1}{2}$
Acoustic phonons (deformation potential)	$+\frac{1}{2}$	$\frac{3\pi}{8} = 1.18$	$-\frac{3}{2}$	-1
Optical phonons (polar materials)				
(a) Low T ($k_BT \ll \hbar\omega_{opt}$)	0	1	N/A	N/A
(b) High T ($k_BT \gg \hbar\omega_{opt}$)	$-\frac{1}{2}$	$\frac{45\pi}{128} = 1.10$	$-\frac{3}{2}$	-1
Piezoelectric (by acoustic phonons in polar materials)	$-\frac{1}{2}$	$\frac{45\pi}{128} = 1.10$	$-\frac{1}{2}$	0
Alloy disorder	$+\frac{1}{2}$	$\frac{3\pi}{8} = 1.18$	$-\frac{1}{2}$	0

Table 6.5: The power of energy dependence of the momentum relaxation time for scattering mechanisms occuring in Si MOSFET (after Gallagher et al. (1990)).

Mechanism	α ($\tau \propto E^{-\alpha}$)
Ionized impurities	$\sim$ -1
Remote impurities	-1.5
Interface roughness	2

positive α is slightly higher than with negative α. From table 6.4, the same trend is also seen, i.e. the Hall scattering factor for $\alpha = +\frac{1}{2}$ is 1.18 while that for $\alpha = -\frac{1}{2}$ is only 1.10. α is estimated to increase to 0.5 at temperatures around 150 K, where the phonon scatterings are dominant.

α is believed to be zero for the extremely degenerate gas because the $\frac{\partial f_0}{\partial E}$ in Eq.2.33 behaves as a delta function with argument $E - E_f$. The integral equation (Eq. 2.33) may thus be obtained straightaway by replacing E in the integral by the Fermi energy E_f [Nag (1980)]. However, it should be pointed out that there is still the dependence of mobility on the carrier density, even at this low temperature. Gallagher et al. (1990) suggested that

$$\alpha \equiv -\left.\frac{d\ln\tau}{d\ln E}\right|_{E=E_F} \cong -\frac{d\ln\tau}{d\ln E_F} \equiv -\frac{d\ln\mu}{d\ln n_s}, \tag{6.10}$$

where μ is the mobility and n_s is the carrier density. In table 6.5, the α for some scattering mechanisms in a Si-MOSFET are given.

6.11 Conclusion

In this chapter, we have studied the magnetotransport of several modulation-doped p-type $Si_{1-x}Ge_x/Si$ ($0.10 \leq x \leq 0.45$) and $Si_{0.35}Ge_{0.65}/Si_{0.65}Ge_{0.35}$ samples. For the first time, we have obtained the temperature dependendence of the mobility and carrier

density of the two-dimensional hole gas (2DHG) without the parallel conduction, in the temperature range 0.3–300 K. It was found that, with increasing temperature, the 2DHG carrier density remains approximately constant for $x = 0.1$, increases for $x = 0.13$, or decreases for $x \geq 0.2$. The power of temperature dependence of 2DHG mobility in the temperature range 100-300 K reveals the influence of phonon and alloy scatterings. The mobility and carrier density of the boron-doped supply layer were also extracted but found to be quite inconsistent, varying from sample to sample. We have observed the electron-like carrier species in most samples, the source of which has not yet been identified. The Hall factor of the 2DHG were also determined in the temperature range 50–100 K but in the form of envelope because of the unknown electron-like carrier.

Chapter 7

Conclusions and Suggestions for Further Work

In this thesis, the magnetotransport properties of modulation-doped p-type $Si_{1-x}Ge_x/Si$ and $Si_{1-x}Ge_x/Si_{1-y}Ge_y$ heterostructures have been studied, in the magnetic field range 0–12 T and in the temperature range 0.35–300 K. The magnetic-field-dependent sheet resistivity and Hall coefficient are analysed by 3 methods of calculation for comparison. The first technique is the Beck and Anderson (BA) analysis which yields the number of carrier species, and a rough estimate of the mobility and carrier density of each carrier species. The second one is known as multicarrier fitting (MCF) which further optimises the Beck and Anderson result. The third technique, which is the concern of the major part of this thesis, is called mobility spectrum analysis. This kind of analysis can be viewed as generalised multicarrier fitting in which the possible number of carrier species is initially set to be considerably high (100–200) and subsequently reduced. In contrast to MCF, where a prior assumption is made about the number of carrier species, the mobility spectrum analysis attempts to determine this number, as well as to estimate the mobility and carrier density of each carrier species. The author has developed a novel mobility spectrum calculation, based on the concept of maximum entropy. This new calculation technique has overcome sev-

eral drawbacks or limitations in other mobility spectrum calculation techniques. The main achievements of the Maximum-Entropy Mobility Spectrum (MEMS) analysis can be summarised as follows.

1. The sheet conductivity is mathematically defined to be nonnegative at all iterations. Other techniques have to manually set the sheet conductivity to be nonnegative.

2. The number of mobility points in the spectrum can be higher than the number of magnetic field points. Other techniques usually perform an interpolation of data, to increase the number of magnetic field points to match that of the mobility points.

3. The sheet conductivity of low-mobility carriers with $\mu < B_{max}^{-1}$ can be recovered more satisfactorily than other mobility spectrum techniques, without resorting to extrapolation to higher magnetic fields. However, the accuracies of its mobility and carrier density could still be poor because this mobility is below the limit set by B_{max}.

4. The biggest advantage is that the mobility spectrum produced by this new technique is extremely smooth. This should provide the first steps toward utilising the peak shape to determine the energy dependence of the relaxation time or the wave vector dependence of the constant-energy contour, as predicted by Beck and Anderson (1978). It should be noted that the peak shape also depends on the number of iterations, the number of data points, the number of mobility points, and the product μB. Further study should be done to clarify all these dependences before coming to the conclusion of the energy dependence of the relaxation time from the peak shape.

Several modulation-doped structures ($0.1 \leq x \leq 0.65$) have been measured and analysed by these three techniques. We found that the Beck and Anderson

analyses yield mostly 3 carrier species which are the 2DHG, carriers in the Si:B (or $Si_{0.65}Ge_{0.35}$:B), and an electron-like carrier species. MCF has used 3 carrier species at all temperatures and for all samples. The results from MEMS are similar to the MCF and BA used in combination in general, but it has been seen that 2 closely spaced peaks may not be separated by MEMS. Moreover, MEMS sometimes gives 4 or 5 peaks, and it is not clear at present whether the additional peaks are real or artefacts. Therefore, the interpretation of magnetotransport has been based on 3 carrier species only.

The first species is the two-dimensional hole gas which exists for the whole temperature range. The measured carrier density varies with temperature for $x \geq 0.13$; increasing with temperature for $x = 0.13$, and decreasing monotonically for $x \geq 0.2$. The decrease is very unexpected for the 2DHG and might suggest either defect or impurity states in the Si capping layer close to the SiGe valence band edge. The 2DHG mobility in the temperature range 100–300 K follows the formula $AT^{-\gamma}$ closely. The germanium-content dependence of γ revealed that it has the bowl shape with the minimum at $x \sim 0.25$–0.3. This might suggest the influence of alloy scattering.

The second carrier species is in the boron-doped silicon (or SiGe) cap layer. We found that the activation energies, extracted from the temperature dependence of its carrier density, vary between samples even though they have the same nominal doping concentration. Discrepancies also occur in the temperature dependence of the mobility which has values from 100 to 800 $cm^2V^{-1}s^{-1}$. The measurement of a Si control sample also reveals a maximum mobility of around 1,000 $cm^2V^{-1}s^{-1}$. BA, MCF, and MEMS analyses of this control sample confirmed that there are 2 hole-like carriers, one with a mobility around 100 $cm^2V^{-1}s^{-1}$ and another with more than an order of magnitude higher mobility. This high mobility carrier can be estimated to correspond to a bulk doping concentration of around 10^{16}–10^{17} cm^{-3} and this might be the boron-spike at the Si/Si-substrate interface, shown in Fig. 6.30. Therefore, it

is likely that what we have observed is the resultant behaviour of the Si:B doping slab and the boron-spike. Moreover, because the boron-spike is usually not under control, the variation in the sum will also be random.

The third carrier species observed is an electron-like carrier. The source of this carrier within the modulation-doped p-type $Si_{1-x}Ge_x/Si$ and $Si_{1-x}Ge_x/Si_{1-y}Ge_y$ heterostructures is presently unknown. From McClure's formalism, this electron-like carrier could be either the "real" carrier, i.e. from the n-type substrate or the unintentionally n-type background doping, or the mobility harmonics of "real" hole-like carriers (2DHG or Si:B).

The Hall factor and the power (-α) of energy dependence of the relaxation time in the 2DHG were extracted from MEMS. The Hall factor in the 2DHG, however, cannot be determined accurately because this electron-like carrier is currently unknown. If it could be identified unambiguously with the 2DHG, it should be included into the Hall factor calculation for the 2DHG. α was calculated for $x = 0.1$ and 0.13 in the temperature range 30–80 K. We found that $|\alpha|$ decreases monotonically with decreasing temperature and tends to be zero at T $\sim$ 0–10 K. This is as expected because the Fermi temperature for both samples are around 20–30 K. Below these temperatures, 2DHG can be regarded as degenerate carrier and its mobility has no temperature dependence ($\alpha = 0$). It should be noted that the dependence of mobility on carrier density at very low temperature has not been taken into account.

For the future improvement in MEMS calculation, the author suggests to replace $\sigma_{xx} + \sigma_{xy}$ by other functions which are more sensitive to σ_{xx} and σ_{xy}. For the completeness of the mobility spectrum approach, the relaxation time as a function of carrier density should be taken into consideration and might be investigated by performing a MEMS analysis on an MOS device.

So far, the theory of McClure, which the MEMS analysis is based on, has not been experimentally proved by using the existing samples because the source of electron-like carrier has not been verified. Moreover, the number of peaks in the

mobility spectrum is sometimes more than 3 which is not according to the design of the modulation-doped structure and therefore unexplainable. The first priority towards the verification of the theory is to identify the source of such a carrier whether it is the "real" one (n-type carrier) or the mobility harmonics of the p-type carrier (2DHG or Si:B). An ideal experimental setup would be to design a p-type modulation-doped SiGe/Si on a p-type substrate. If the electron-like carrier does not exist in this particular sample, it would mean that this carrier in our existing samples comes from the n-type substrate. However, if it still occurs, the author suggest to use other semiconductors which has the spherical constant-energy surface, so that the mobility harmonics of p-type carrier should not appear theoretically.

It should be aware that the work of maximum-entropy mobility spectrum analsis development done by the author still needs more critically mathematical investigation. One of the most important aspect is how the experimental error influences the spectrum, i.e. the number of peaks and the shape of each peak, and whether the artefact peak could occur, and if so, under which circumstances.

Bibliography

[Abstreiter et al. (1985)] **Abstreiter G., Brugger H., Wolf T., Jorke H., and Herzog H.J.**, Phys. Rev. Lett. 54, 2441 (1985).

[Achard et al. (1999)] **Achard J., Guillot C., Barbarin F., Dugay M., and Goumet E.**, Applied Surface Science 142, 455 (1999).

[Agmon et al. (1979)] **Agmon N., Alhassid Y., and Levine R.D.**, J. Comput. Phys. 30, 250 (1979).

[Allgaier (1967)] **Allgaier R.S.**, Phys. Rev. 158, 699 (1967).

[Ando et al. (1982)] **Ando T., Fowler A.B., and Stern F.**, Rev. Mod. Phys. 54, 437 (1982).

[Antoszewski et al. (1995)] **Antoszewski J., Seymour D.J., Faraone L., Meyer J.R., and Hoffman C.A.**, J. Electron. Mater. 24, 1255 (1995).

[Antoszewski and Faraone (1996)] **Antoszewski J., and Faraone L.**, J. Appl. Phys. 80, 3881 (1996).

[Antoszewski et al. (1997)] **Antoszewski J., Dell J.M., Faraone L., Tan L.S., Raman A., Chua S.J., Holmes D.S., Lindemuth J.R., and Meyer J.R.**, Material Science and Engineering B44, 65 (1997).

[ASTM (1976)] **ASTM**, "Annual Book of ASTMS Standards" Vol. 43, 343, American society for testing and material standards, Philadelphia (1976).

[Basaran et al. (1994)] **Basaran E., Kubiak R.A., Whall T.E., and Parker E.H.C.**, Appl. Phys. Lett. 64, 3470 (1994).

[Bean et al. (1984)] **Bean J.C., Sheng T.T., Feldman L.C., Fiory A.T., and Lynch R.T.**, Appl. Phys. Lett. 44, 102 (1984).

[Beck and Anderson (1987)] **Beck W.A., and Anderson J.R.**, J. Appl. Phys. 62, 541 (1987).

[Beck et al. (1988)] **Beck W.A., Crowne F., Anderson J.R., Gorska M., and Dziuba Z.**, J. Vac. Sci. Technol. A 6, 2772 (1988).

[Beer (1963)] **Beer A.C.**, "Galvanomagnetic Effects in Semiconductors", Academic Press (1963).

[Bhaumik et al. (1993)] **Bhaumik K., Ridley B.K., and Shacham-Diamand Y.**, J. Appl. Phys. 74, 5546 (1993).

[Blakemore (1974)] **Blakemore J.S.**, "Solid State Physics" 2nd ed., Philadelphia; London : Saunders (1974).

[Blood and Orton (1992)] **Blood P., and Orton J.W.**, "The Electrical Characterization of Semiconductors: Majority Carriers and Electron States", Academic Press (1992).

[Brighten et al. (1993)] **Brighten J.C., Hawkins I.D., Peaker A.R., Kubiak R.A., Parker E.H.C., and Whall T.E.**, Semicond. Sci. Technol. 8, 1487 (1993)

[Bube (1974)] **Bube R.H.**, "Electronic Properties of Crystalline Solids," Academic Press : New York (1974).

[Carns et al. (1994)] **Carns T.M., Chun S.K., Tanner M.O., Wang K.L., Kamins T.I., Turner J.E., Lie. D.Y.C., Nicolet Marc-A., and Wilson R.G.**, IEEE. Trans. Electron. Devices 41, 1273 (1994)

[Chandra et al. (1979)] **Chandra A., Wood C.E.C., Woodard D.W., and Eastman L.F.**, Solid-State Electronics 22, 645 (1979).

[Chen et al. (1993)] **Chen Y.F., Dai Y.T., Chou H.P., Chang D.C., Chang C.Y., and Wang P.J.**, Appl. Phys. Lett. 62, 2713 (1993).

[Chen et al. (1994)] **Chen Y.C., Li S.H., Bhattacharya P.K., Singh J., and Hinckley J.M.**, Appl. Phys. Lett. 64, 3110 (1994).

[Cheng et al. (1994)] **Cheng J.-P., Kesan V.P., Grutzmacher D.A., and Sedgwick T.O.**, Appl. Phys. Lett. 64, 1681 (1994)

[Chu and Dowsett (1997)] **Chu D.P., and Dowsett M.G.**, Phys. Rev. B 56, 15167 (1997).

[Colvard et al. (1989)] **Colvard C., Nouri N., Ackley D., and Lee H.**, J. Electrochem. Soc. 136, 3463 (1989).

[Cyca et al. (1997)] **Cyca B.R., Robins K.G., Tarr N.G., Xu D.X., Noel J.-P., Landheer D., and Simard-Normandin M.**, J. Appl. Phys. 81, 8079 (1997).

[Dexter (1955)] **Dexter R.N.**, Phys. Rev. 98, 1560 (1955).

[Dijkstra and Wenckebach (1999)] **Dijkstra J.E., and Wenckebach W.Th.**, J. Appl. Phys. 85, 1587 (1999).

[Dingle et al. (1978)] **Dingle R., Stormer H.L., Gossard A.C., and Wiegmann W.**, Appl. Phys. Lett. 33, 665 (1978)

[Dresselhaus et al. (1954)] **Dresselhaus G., Kip A., and Kittel C.**, Phys. Rev. 95, 568 (1954).

[Dresselhaus et al. (1955)] **Dresselhaus G., Kip A., and Kittel C.**, Phys. Rev. 98, 368 (1955).

[Dziuba (1991)] **Dziuba Z.**, Acta Phys. Pol. (a) 80, 827 (1991).

[Dziuba (1996)] **Dziuba Z.**, Phys. Stat. Sol. (a) 153, 445 (1996).

[Dziuba and Gorska (1992)] **Dziuba Z., and Gorska M.**, J. Phys. III France 2, 99 (1992).

[Dziuba et al. (1997)] **Dziuba Z., Antoszewski J., Dell J.M., Faraone L., Kozodoy P., Keller B., Den-Baars S.P., and Mishra U.K.**, J. Appl. Phys. 82, 2996 (1997).

[Dziuba et al. (1999)] **Dziuba Z., Przeslawski T., Dybko K., Gorska M., Marczewski J., and Reginski K.**, J. Appl. Phys. 85, 6619 (1999).

[Emeleus et al. (1993)] **Emeleus C.J., Whall T.E., Smith D.W., Kubiak R.A., Parker E.H.C., and Kearney M.J.**, J. Appl. Phys. 73, 3852 (1993).

[Feenstra et al. (1995)] **Feenstra R.M., Lutz M.A., Stern F., Ismail K., Mooney P.M., LeGoues F.K., Stanis**

C., Chu J.O., and Meyerson B.S., J. Vac. Sci. Technol. B 13, 1608 (1995).

[Fischer et al. (2000)] **Fischer H., Risch L., Kearney M.J., Horrell A.I., Parker E.H.C., and Whall T.E.**, to be submitted.

[Fischetti and Laux (1996)] **Fischetti M.V., and Laux S.E.**, J. Appl. Phys. 80, 2234 (1996).

[Fu et al. (1996)] **Fu Y., Joelsson K.B., Grahn K.J., Ni W.-X, Hansson G.V., and Willander M.**, Phys. Rev. B 54, 11317 (1996).

[Gallagher et al. (1990)] **Gallagher B.L., Oxley J.P., Galloway T., Smith M.J., and Butcher P.N.**, J. Phys.: Condens. Matter 2, 755 (1990).

[Garchery et al. (1995)] **Garchery L., Sagnes I. Warren P., Dupuy J.-C., and Badoz P.A.**, J. Crystal Growth 157, 367 (1995).

[Gaworzewski et al. (1998)] **Gaworzewski P., Tittelbach-Helmrich K., Penner U., and Abrosimov N.V.**, J. Appl. Phys. 83, 5258 (1998).

[Gerald and Wheatley (1994)] **Gerald C.F., and Wheatley P.O.**, "Applied Numerical Analysis" (1994), Addison-Wesley.

[Glicksman (1958)] **Glicksman M.**, Phys. Rev. 111, 125 (1985).

[Gold (1987)] **Gold A.**, Phys. Rev. B 35, 723 (1987).

[Gold and Dolgopolov (1986)] **Gold A., and Dolgopolov V.T.**, Phys. Rev. B33, 1076 (1986).

[Goldberg et al. (1957)] **Goldberg C., Adams E.N., and Davis R.E.,** Phys. Rev. 105, 865 (1957).

[Gossman et al. (1992)] **Gossman H.-J., Asoka-Kumar P., Leung T.C., Nielsen B., Lynn K.G., Unterwald F.C. and Feldman L.C.,** Appl. Phys. Lett. 61, 540 (1992).

[Grasby (2000)] **Grasby T.J.,** private communication (2000).

[Grasby et al. (1999)] **Grasby T.J., Parry C.P., Phillips P.J., McGregor B.M., Morris R.J.H., Braithwaite G., Whall T.E., Parker E.H.C., Hammond R., Knights A.P., and Coleman P.G.,** Appl. Phys. Lett. 74, 1848 (1999).

[Gui et al. (1997)] **Gui Y.S., Zheng G.Z., Chu J.H., Guo S.L., Zhang X.C., Tang D.Y., and Cai Y.,** J. Appl. Phys. 82, 5000 (1997).

[Gui et al. (1998)] **Gui Y., Li B., Zheng G., Chang Y., Wang S., He L. and Chu J.,** J. Appl. Phys. 84, 4327 (1998).

[Hinckley et al. (1989)] **Hinckley J.M., Sankanran V., and Singh J.,** Appl. Phys. Lett. 59, 2008 (1989).

[Hock et al. (1998)] **Höck G., Glück M., Hackbarth T., Herzog H.-J., and Kohn E.,** Thin Solid Films 336, 141 (1998).

[Hollis et al. (1992)] **Hollis J.M., Dorband J.E., and Yusef-Zadeh F.,** The Astrophysical Journal 386, 293 (1992).

[Hwang et al. (1991)] **Hwang S., Lansari Y., Yang Z., Cook Jr.**

J.W., and Schetzina, J. Vac. Sci. Technol. B 9, 1799 (1991).

[Ismail et al. (1994)] **Ismail K., Chu J.O., and Meyerson B.S.**, Appl. Phys. Lett. 64, 3124 (1994).

[Jaynes (1957)] **Jaynes E.T.**, Phys. Rev. 106, 620 (1957).

[Joelsson et al. (1997)] **Joelsson K.B., Fu Y., Ni W.-X., and Hansson G.V.**, J. Appl. Phys. 81, 1264 (1997).

[Jones et al. (1994)] **Jones H., Jenkins R.G., Cleemput M.V., Nicholas R.J., Siertsema W.J., van der Burgt M.**, Physica B201, 546 (1994).

[Kawaji (1969)] **Kawaji S.**, Journal of the Physical Society of Japan 27, 906 (1969).

[Kearney and Horrell (1998)] **Kearney M.J., and Horrell A.I.**, Semicond. Sci. Technol. 13, 174 (1998)

[Kim et al. (1993)] **Kim J.S., Seiler D.G., and Tseng W.F.**, J. Appl. Phys. 73, 8324 (1993).

[Konig and Schaffler (1993)] **Koning U., and Schaffler F.**, IEEE Trans. Electron. Dev. Lett. 14, 205 (1993).

[Konig and Dambkes (1995)] **Konig U., and Dambkes H.**, Solid State Electron. 18, 1595 (1995).

[Kolodziejczak (1961)] **Kołodziejczak J.**, Acta Physica Polonica Vol. XX, 379 (1961).

[Koser et al. (1994)] **Koser H. Vollinger O., and Brugger H.**, Inst. Phys. Conf. Ser. No. 136 (1994), Chapter 11, pp. 789.

[Krein (1962)] **Krein M.**, in "Some Questions in the Theory of Moments", edited by Aheizer N.I. (or Akheizer) and Krein M., Vol. 2 of Translaton of Mathematical Monographs (American Mathematical Society, Providence, RI, 1962), p.129.

[Kubiak et al. (1988)] **Kubiak R.A., Parker E.H.C., and Iyer S.S.**, in "Silicon Molecular Beam Epitaxy: Volume I", ed. Kasper and Bean (CRC Press), 1988.

[Laikhtman and Kiehl (1993)] **Laikhtman B., and Kiehl R.A.**, Phys. Rev. B 47, 10515 (1993).

[Lander et al. (1997)] **Lander R.J.P., Emeleus C.J., McGregor B.M., Parker E.H.C., Whall T.E., Evans A.G.R., and Kenedy G.P.**, J. Appl. Phys. 82, 5210 (1997).

[Leu and Neugroschel (1993)] **Leu I.Y., and Neugroschel A.**, IEEE Trans. Electron Devices 40, 1872 (1993).

[Levitas (1955)] **Levitas A.**, Phys. Rev. 99, 1810 (1955).

[Li (1978)] **Li S.S.**, Solid-State Electronics 21, 1109 (1978).

[Lu et al. (1996)] **Lu Q., Sardela M.R., Jr., Bramblett T.R., and Greene J.E.**, J. Appl. Phys. 80, 4458 (1996).

[Manku and Nathan (1991)] **Manku T., and Nathan A.**, Phys. Rev. B 43, 12634 (1991).

[Manzini and Modelli (1989)] **Manzini S., and Modelli A.**, J. Appl. Phys. 65, 2361 (1989).

[Marquardt (1963)] **Marquardt D.W.**, J. Soc. Indust. Appl. Math. 11, 431 (1963).

[McClure (1956)] **McClure J.W.**, Phys. Rev. 101, 1642 (1956).

[McGregor et al. (1993)] **McGregor J.M., Manku T., Noël J.P., Roulston D.J., Nathan A., and Houghton D.C.**, J. Electron. Mater. 22, 319 (1993).

[McGregor (1997)] **McGregor B.M.**, "Structural and Electrical Characterisation of Si:B/$Si_{1-x}Ge_x$/Si(001) Heterostructures" Ph.D. Thesis, Department of Physics, University of Warwick (1997).

[McGregor et al. (1999)] **McGregor B.M.M., Lander R.J.P., Phillips P.J., Parker E.H.C., and Whall T.E.**, Appl. Phys. Lett. 74, 1245 (1999).

[Meyer et al. (1988)] **Meyer J.R., Hoffman C.A., Bartoli F.J., Perez J.M., Furneaux J.E., Wagner R.J., Koestner R.J., and Goodwin M.W.**, J. Vac. Sci. Technol. A6, 2775 (1988).

[Meyer et al. (1993)] **Meyer J.R., Hoffman C.A., Bartoli F.J., Arnold D.A., Sivananthan S., and Faurie J.P.**, Semicond. Sci. Technol. 8, 805 (1993).

[Meyer et al. (1997)] **Meyer J.R., Hoffman C.A., Antoszewski J., and Faraone L.**, J. Appl. Phys. 81, 709 (1997).

[Morin (1954)] **Morin F.J.**, Phys. Rev. 93, 62 (1954).

[Morin and Maita (1954)] **Morin F.J., and Maita J.P.**, Phys. Rev. 96, 28 (1954).

[Morris (2000)] **Morris R.**, private communication (2000).

[Nag (1980)] **Nag B.R.**, "Electron Transport in Compound Semiconductors", Berlin : Springer-Verlag (1980).

[Nelson et al. (1993)] **Nelson S.F.,Ismail K., Jackson T.N., Nocera J.J., Chu J.O., and Meyerson B.S.**, Appl. Phys. Lett. 63, 794 (1993)

[Norton et al. (1973)] **Norton P., Braggins T., and Levinstein H.**, Phys. Rev. B 8, 5632 (1973).

[Panaev et al. (1993)] **Panaev I.A., Studenikin S.A., Lubyshev D.I., and Migal' V.P.**, Semicond. Sci. Technol. 8, 1822 (1993).

[Panaev et al. (1996)] **Panaev I.A., Studenikin S.A., Tkachenko V.A., Tkachenko O.A., Heremans J.P., Partin D.L., Morelli D.T., and Thrush C.M.**, Semicond. Sci. Technol. 11, 1857 (1996).

[Parker (1977)] **Parker R.L.**, Ann. Rev. Earth. Sci. 5, 35 (1977).

[Parry (1991)] **Parry C.P.**, "Incorporation of elemental boron during Silicon and Germanium molecular beam epitaxy" Ph.D. Thesis, Department of Physics, University of Warwick (1991).

[Pawlowicz et al. (1998)] **Pawlowicz C., Tarr N.G., Berndt L.P., Williams R.L., Landheer D., Xu D.-X.,**

Abid R., and McAlister S.P., J. Vac. Sci. Technol. A16, 864 (1998).

[Pearson and Bardeen (1949)] **G.L. Pearson, and J. Bardeen**, Phys. Rev. 75, 865 (1949).

[People et al. (1984)] **People R., Bean J.C., Lang D.V., Sergent A.M., Störmer H.L., Wecht K.W., Lynch R.T., and Baldwin K.**, Appl. Phys. Lett. 45, 1231 (1984).

[People (1985)] **People R.**, Phys. Rev. B 32, 1405 (1985).

[Penner et al. (1998)] **Penner U., Rücker H., and Yassievich I.N.**, Semicond. Sci. Technol. 13, 709 (1998).

[Plews et al. (1997)] **Plews A.D, Mattey N.L., Phillips P.J., Parker E.H.C., and Whall T.E.**, Semicond. Sci. Technol. 12, 1231 (1997).

[Prest (2000)] **Prest M.J.**, private communication (2000).

[Press et al. (1992)] **Press W.H., Teukolsky S.A., Vetteling W.T., and Flannery B.P.**, in "Numerical Recipes in C" 2nd Ed., Cambridge University Press (1992).

[Reginski et al. (1997)] **Reginski K., Marczewski J., Dziuba Z., and Grodzicka E.**, J. Appl. Phys. 82, 6102 (1997).

[Rice (1981)] **Rice J.R.**, in "Matrix Computations and Mathematical Software", New York : McGraw-Hill (1981).

[Rothwell and Drachman (1989)] **Rothwell E., and Drachman B.**, International

Journal for Numerical Methods in Engineering, vol. 28, 609-620 (1989).

[Sakaki et al. (1987)] **Sakaki H., Noda T., Hirakawa K., Tanaka M., and Matsusue T.**, Appl. Phys. Lett. 51, 1934 (1987).

[Schaffler (1997)] **Schaffler F.**, Semicond. Sci. Technol. 12, 1515 (1997).

[Schlaf et al. (1999)] **Schlaf R, Hinogami R., Fujitani M., Yae S., and Nakato Y.**, J. Vac. Sci. Technol. A10, 164 (1999).

[Schoenberg (1984)] **Schoenberg D.**, "Magnetic Oscillations in Metals", Cambridge: Cambridge University Press (1984).

[Shaw (1953)] **Shaw F.S.**, "Introduction to Relaxation Methods", (1953).

[Shik (1997)] **Shik A.**, "Quantum Wells: physics and Electronics of Two-Dimensional Systems", Singapore: World Scientific (1997).

[Singh (1993)] **Singh J.**, "Physics of Semiconductors and Their Heterostructures", Singapore: McGraw-Hill (1993).

[Skilling (1984)] **Skilling J.**, Nature 309, 748 (1984).

[Smith (1978)] **Smith R.A.**, "Semiconductors" 2nd ed., Cambridge University Press (1978).

[Snyder et al. (1992)] **Snyder C.W., Mansfield J.F., and Orr B.G.**, Phy. Rev. B 46, 9551(1992).

[Svensson et al. (1991)] **Svensson S.P., Beck W.A., Martel D.C., Uppal P.N., and Cooke D.C.**, Journal of Crystal Growth 111, 450 (1991).

[Swanson (1955)] **Swanson J.A.**, Phys. Rev. 99, 1799 (1955).

[Sze (1981)] **Sze S.M.**, "Physics of Semiconductor Devices" 2nd ed., John Wiley & Sons (1981).

[Tan et al. (1990)] **Tan I-H., Snider G.L., Chang L.D., and Hu E.L.**, J. Appl. Phys. 68, 4071 (1990).

[Timbrell et al. (1990)] **Timbrell P.Y., Baribeau J. M., Lockwood D.J., and McCaffrey J.P.**, J. Appl. Phys. 67, 6269 (1990).

[Van der Pauw (1958)] **Van der Pauw L.J.**, Philips Research Reports 13, 1 (1958).

[Venkataraman et al. (1993)] **Venkataraman V., Liu C.W., and Sturm J.C.**, Appl. Phys. Lett. 63, 2795 (1993).

[Verdonckt et al. (1991)] **Verdonckt S., Crabbe E.F., Meyerson B.S., Harame D.L., Restle P.J., Stork J.M.C., Megdanis A.C., Stanis C.L., Bright A.A., Kroesen G.M.W., and Warren A.C.**, IEEE Electron. Device Lett. 12, 447 (1991).

[Versnel (1979)] **Versnel W.**, Solid-State Electronics 22, 911 (1979).

[Voinigescu et al. (1994)] **Voinigescu S.P., Salama C.A.T., Noel J.-P., and Kamins T.I.**, Proc. 24th European Solid State Device Research Conference, p. 43 (1994).

[Vurgaftman et al. (1998)] **Vurgaftman I., Meyer J.R., Hoffman C.A., Redfern D., Antoszewski J., Faraone L., and Lindemuth J.R.**, J. Appl. Phys. 84, 4966 (1998).

[Wang et al. (1995)] **Wang K.L., Thomas S.G., and Tanner M.O.**, Journal of Material Science : Materials in Electronics 6, 311 (1995).

[Whall et al. (1993)] **Whall T.E., Smith D.W., Plews A.D., Kubiak R.A., Phillips P.J., and Parker E.H.C.**, Semicond. Sci. Technol. 8, 615 (1993).

[Whall et al. (1994)] **Whall T.E., Mattey N.L., Plews A.D., Phillips P.J., Mironov O.A., Nicholas R.J., and Kearney M.J.**, Appl. Phys. Lett. 64, 357 (1994).

[Whall (1997)] **Whall T.E.**, Thin Solid Films 294, 160 (1997).

[Whall and Parker (1998)] **Whall T.E., and Parker E.H.C.**, J. Phy. D: Appl. Phys. 31, 1397 (1998).

[Whall and Parker (1999)] **Whall T.E., and Parker E.H.C.**, (to be published).

[Wilson (1953)] **Wilson A.H.**, "The Theory of Metals", The Cambridge University Press (1953).

[Xiao et al. (1992)] **Xiao X., Liu C.W., Sturm J.C., Lenchyshyn L.C., Thewalt M.L.W., Gregory R.B., and Fejes P.**, Appl. Phys. Lett. 60, 2135 (1992).

[Yamanaka et al. (1996)] **Yamanaka T., Fang S.J., Lin H.C., Snyder**

J.P., and Helms C.R., IEEE Electron. Device Letters 17, 178 (1996).

[Young (1971)] **Young D.M.**, in "Iterative Solution of Large Linear Systems", edited by Rheinboldt W., Computer Science and Applied Mathematics : A series of Monographs and Textbooks, Academic Press (1971).

[Yutani and Shiraki (1996)] **Yutani A., and Shiraki Y.**, Semicond. Sci. Technol. 11, 1009 (1996).

Appendix A

Beck and Anderson Algorithm

There are three steps in generating a Beck and Anderson mobility spectrum as follows.

1. Construction of matrix **A** : The experimental results provide the N pair of magnetoconductivity $((\sigma_{xx})_k,(\sigma_{xy})_k; k = 1 \ldots N)$ at different magnetic fields B_k. An element of matrix **A** denoted by $A_{\gamma\beta}$ is calculated from

$$A_{\gamma\beta} = \begin{cases} \sum_{k=1}^{N} \left[(\sigma_{xx})_k (C_R^{-1})_{k,(\gamma+\beta)/2}\right], (\gamma+\beta)\ even \\ \sum_{k=1}^{N} \left[(\sigma_{xy})_k (C_I^{-1})_{k,(\gamma+\beta-1)/2}\right], (\gamma+\beta)\ odd \end{cases} \tag{A.1}$$

   $\gamma, \beta = 1 \ldots 2N$. Constants C_R^{-1} and $C_I^{-1}$are inverse of matrices C^R and C^I where C^R is defined by

$$\sum_{j=1}^{N} C_{jk}^R x^{2(j-1)} = \prod_{\rho=1,\rho\neq k}^{N} (1 + x^2 B_\rho), \tag{A.2}$$

   which can be expanded in terms of the polynomial of variable x, and

$$C_{jk}^I = -C_{jk}^R B_k. \tag{A.3}$$

2. Physical test : Matrix **A** is required to be non-negative definite following their model. A method to check this property is to investigate its eigenvalues because a matrix is non-negative definite if and only if it is Hermitian and all eigenvalues are non-negative [Young (1971)]. In this circumstance, matrix **A** is Hermitian

because its elements are all real and symmetric ($A_{\gamma\beta} = A_{\beta\gamma}$). If some eigenvalues are negative, then matrix **A** is not non-negative definite and such magnetoconductivity data is discarded. An algorithm "tqli( )" [Press et al. (1992)] is used to evaluate eigenvalues and eigenvectors associated with each eigenvalue which will be used for the next step.

3. Determination of an envelope : Starting from a set of physical data, a conductivity density s' is guessed at a mobility μ' and original magnetoconductivity data is subtracted by this contribution and tested via a physical test. At some value of s', subtracted data changes from being physical to unphysical and this value is the maximum conductivity of carrier having mobility μ' . Analytical formula has shortened this procedure and such maximum can be obtain directly following

$$s' = \frac{\left|v_{\mu'}\right|^2}{\alpha_{\mu'}} \left[\sum_{i=1}^{N} \frac{\left(\sum_{j=1}^{N} Q_{ji}(v_{\mu'})_j\right)^2}{\lambda_i} \right]^{-1}, \tag{A.4}$$

$$\alpha_{\mu'} = \frac{\sigma_0}{\prod_{\rho=1}^{N} \left(1 + (\mu')^2 B_\rho^2\right)} \left[\sum_{j=0}^{N-1} \left(\mu'\right)^{2j} \right], \tag{A.5}$$

where vector $v_{\mu'} = (1, -\mu', \mu'^2, -\mu'^3, \ldots, (-\mu')^{N-1})$, $Q_{ji}$is an element of column eigenvectors of matrix A corresponding to an eigenvalue λ_i.

Appendix B

Condition Number of Square Matrix

A system of M linear equations with M variables can be represented in a matrix and vectors notation as

$$\mathbf{A} \cdot x = b. \tag{B.1}$$

$\mathbf{A}$ is a coefficient matrix size $M \times M$, x is a column vector of variables and b is a known vector (i.e. the magnetoconductivity). Let's define a residule vector $R = \mathbf{A} \cdot x^* - b$. The best solution will minimise the residual vector close or equal to a zero vector depending on consistency of vector b. Solving by a matrix inversion, $x^* = \mathbf{A}^{-1} \cdot b$ and error in $x^* = \|\mathbf{A}^{-1} \cdot R\|$ can be estimated as [Gerald and Wheatley (1994)]

$$\frac{1}{\|\mathbf{A}\| \, \|\mathbf{A}^{-1}\|} \frac{\|R\|}{\|b\|} \leq \frac{\|\mathbf{A}^{-1} \cdot R\|}{\|x^*\|} \leq \|\mathbf{A}\| \left\|\mathbf{A}^{-1}\right\| \frac{\|R\|}{\|b\|}. \tag{B.2}$$

The quantity $\|\mathbf{A}\| \, \|\mathbf{A}^{-1}\|$ is called the *condition number*. It is equal to 1 if $\mathbf{A}$ is an identity matrix and increases toward ∞ as $\mathbf{A}$ moves toward the singularity. For an ill-conditioned matrix, the corresponding condition number is so high that the relative error can be very big despite a small residual vector. In other words, the residual vector or fitness gives very little information about the goodness of x.

Appendix C

Singular Value Decomposition

Any $M \times N$ matrix **A** whose number of rows M is greater than or equal to its number of column N, can be written as the product of an $M \times N$ column-orthogonal matrix **U**, an $N \times N$ diagonal matrix **W** with positive or zero elements (the singular values), and the transpose of an $N \times N$ othogonal matrix **V**.

$$A = U \cdot [diag(w_j)] \cdot V^T. \tag{C.1}$$

An inversion of matrix A is

$$A^{-1} = V \cdot [diag(1/w_j)] \cdot U. \tag{C.2}$$

For ill-condition matrices, there are some value of w_j that are zero or close to zero. Replacement of any $1/w_j$ that are close to ∞ by zero will reduce the condition number of the matrix and is equivalent to throwing away an equation that is linearly dependent on other equations.